



UNIVERSITÀ DEGLI STUDI DI PADOVA

Sede Amministrativa: Università degli Studi di Padova

Dipartimento di GEOSCIENZE

SCUOLA DI DOTTORATO DI RICERCA IN: SCIENZE DELLA TERRA
CICLO XXIV

ORIGIN AND ENVIRONMENTAL IMPACT OF THE CENTRAL ATLANTIC MAGMATIC PROVINCE

Direttore della Scuola: Ch.mo Prof. Massimiliano Zattin

Supervisore: Ch.mo Prof. Andrea Marzoli

Dottorando: Sara Callegaro

*Blue Ridge Mountains, Shenandoah River
Life is old there, older than the trees
Younger than the mountains
Growin' like a breeze.*

J. DENVER

Take me home, Country Roads

TABLE OF CONTENTS

ABSTRACT	p. 7
RIASSUNTO	p. 9
INTRODUCTION	p. 11
1.1. Large Igneous Provinces	
1.2. The Central Atlantic Magmatic Province	
PART I: Geochemistry of CAMP dykes and sills from eastern North America	p. 17
1 EARLIER STUDIES	p. 19
2 GEOLOGY OF EASTERN NORTH AMERICA	p. 23
2.1 The Grenville Province	
2.2 The Appalachians	
2.2.1 Orogenic phases	
2.2.2 Physiographic and lithotectonic domains	
3 SAMPLING	p. 37
4 MAJOR ELEMENTS	p. 41
5 COMPATIBLE TRACE ELEMENTS	p. 45
6 INCOMPATIBLE TRACE ELEMENTS	p. 47
6.1 Incompatible trace element ratios	
7 ISOTOPES	p. 55
7.1 Methods	
7.2 Sr-Nd-Pb isotopes	
7.3 Os isotopes	
8 MINERALOGICAL COMPOSITIONS (EMPA)	p. 67
8.1 Olivine	
8.2 Pyroxenes	
8.3 Plagioclase	
8.4 Oxides	
9 GEOTHERMOBAROMETRY	p. 83
10 PETROGRAPHY	p. 87
11 OBSERVATIONS ON THE DATA	p. 91
12 CLOSED-SYSTEM MAGMATIC DIFFERENTIATION	p. 93

13 MANTLE MELTING	p. 97
14 OPEN-SYSTEM MAGMATIC DIFFERENTIATION	p. 103
15 ENA DYKES AND NEWARK SUPERGROUP BASINS CAMP FLOWS: A COMPARISON	p. 115
16 DISCUSSION	p. 123
17 CONCLUSIONS	p. 129
REFERENCES (PART I)	p. 131

PART II: Latest Triassic Marine Sr isotopic variations p. 143

1 OVERVIEW	p. 145
2 METHODS	p. 147
3 RESULTS	p. 149
4 DISCUSSION	p. 153
5 EVIDENCES FOR A RHAETIAN ONSET OF THE CAMP	p. 155
REFERENCES (PART II)	p. 157

APPENDICES	p. 161
APPENDIX I – Methods	p. 163
APPENDIX II – Samples coordinates	p. 169
APPENDIX III – Data tables	p. 171
APPENDIX IV – CIPW normative compositions	p. 177
APPENDIX V – Petrographic tables	p. 179
APPENDIX VI – EMPA analyses of conodont samples	p. 181

ABSTRACT

The Central Atlantic Magmatic Province (CAMP), associated with the breakup of Pangea and straddling the Triassic-Jurassic boundary, has been recognized as one of the largest Phanerozoic igneous provinces. Its volcanogenic gas outpurs possibly led to global climatic perturbations that in turn have been suggested to have had a trigger role on the end-Triassic biotic crisis.

To further test this causal link, several aspects need to be investigated, through a multidisciplinary approach. In particular, eruptive style and rate as well as chemistry of the outpurred volcanics may influence the quantity and modality of the outgassing, thus determining either a severe or weak environmental impact of a Large Igneous Province. Additionally, precise (isotopic and bio-chronostratigraphic) geochronological investigations are required to unravel the time relationship between CAMP onset and other events documented in the global stratigraphic record, such as the end-Triassic biological turnover.

In the first part of this thesis, new sampling and geochemical data are reported and interpreted for the south-eastern North American intrusive (dykes and sills) occurrences of the CAMP. Previous studies had attempted discerning the mantle source of these tholeiitic suites, leaning toward either a mantle-plume or a lithospheric mantle origin. Our combined new major and trace element and Sr-Nd-Pb-Os isotopic analyses on more than 70 rock samples and detailed electron microprobe mineral data provide further insights into the petrogenesis of eastern North American (ENA) CAMP dykes and sills. Ranging in composition from Olivine/Hyperstene- to Quartz-normative, the low-Ti (TiO_2 0.36-1.35 wt%) sampled tholeiites show large variations in major elements (e.g., MgO 17-5 wt%; CaO 12-7 wt%) that are interpreted to derive from closed-system fractional crystallization, starting from (at least) two different parental magma-types: high- and low-Fe olivine-normative basalts. ENA diabases show uniform, rather depleted trace element contents, decoupled from Sr-Nd-Pb isotopic systematics that in turn are generally enriched and show a large spread of values ($^{87}\text{Sr}/^{86}\text{Sr}_{200\text{Ma}}$ 0.70438-0.70880; $^{143}\text{Nd}/^{144}\text{Nd}_{200\text{Ma}}$ 0.5120-0.5125; $^{206}\text{Pb}/^{204}\text{Pb}_{200\text{Ma}}$ 17.41-18.61; $^{207}\text{Pb}/^{204}\text{Pb}_{200\text{Ma}}$ 15.54-15.63; $^{208}\text{Pb}/^{204}\text{Pb}_{200\text{Ma}}$ 37.32-38.38). In particular, $^{206}\text{Pb}/^{204}\text{Pb}$ ratios reach very low values, that are not observed on low-Ti basalts from the rest of CAMP, and extending towards

signatures typical of the Enriched Mantle-I pole. On the contrary, $^{187}\text{Os}/^{188}\text{Os}_{200\text{Ma}}$ isotopes are homogeneously low, showing mantle signatures, and not correlated with other isotopic compositions. Consistently, numerical modeling of assimilation processes constrains the role of crustal contamination to be no larger than 3-10%. Thus, the heterogeneous and enriched signatures are interpreted to reside in the mantle-source, which in turn is suggested to consist of sub-continental lithosphere enriched with an EMI component by ancient subductions. This EMI-flavored component is suggested to be conveyed by sediments-bearing recycled oceanic crust, incorporated as pyroxenitic veins within the lithospheric mantle.

In the second part, the results of applying the high resolution of marine biostratigraphy to constrain the detailed timing of the CAMP onset are presented. Analyses of biogenic apatite from 19 stratigraphically well-constrained conodont samples from the Tethyan realm indicate two significant shifts of the oceanic $^{87}\text{Sr}/^{86}\text{Sr}$ composition during the latest Triassic: a rapid drop of $^{87}\text{Sr}/^{86}\text{Sr}$ during the lower Rhaetian, followed by an increase during the upper Rhaetian. These shifts are positively correlated with synchronous variations of oceanic $^{187}\text{Os}/^{188}\text{Os}$ and they may be attributed to a rapid emplacement and erosion of the CAMP, followed by a prompt increase of continental weathering. These interpretations back-position the first onset of the CAMP around the Norian-Rhaetian boundary, hence implying a short duration for the Rhaetian stage (<2 Ma). Volcanogenic triggering of end-Triassic climatic perturbations is thus plausible, with bearings on the biotic crisis starting from the Norian-Rhaetian and culminating at the Triassic-Jurassic boundary. The hypothesis of a step-wise character previously suggested for this mass extinction is also reinforced by these new data.

RIASSUNTO

La Central Atlantic Magmatic Province (CAMP), legata al breakup del supercontinente Pangea, e messa in posto a cavallo del limite Triassico-Giurassico, è stata riconosciuta come una delle più grandi province magmatiche del Fanerozoico. L'emissione di gas vulcanici da parte della CAMP ha potenzialmente avuto un impatto considerevole sul clima globale, tale da essere stata una possibile causa dell'estinzione di massa di fine Triassico.

Per testare l'effettiva consistenza di questo rapporto di causa-effetto, è necessario indagare la CAMP sotto diversi aspetti, attraverso un approccio di tipo multidisciplinare. In particolare, lo stile e la frequenza eruttiva, così come il chimismo delle intrusioni e delle vulcaniti messe in posto possono influenzare la quantità e la modalità del degassamento, determinando quindi un impatto ambientale forte o blando da parte di una provincia magmatica. Inoltre, si rendono necessarie precise analisi geocronologiche (isotopiche e biocronostratigrafiche) per dipanare le relazioni temporali di dettaglio tra magmatismo CAMP e altri eventi riscontrati nel record stratigrafico, come il turnover biologico osservato alla fine del Triassico.

Nella prima parte di questa tesi vengono presentati e interpretati nuovi dati ottenuti da un recente campionamento di dicchi e sill appartenenti alla CAMP e affioranti nell'area sud-orientale del Nord America. Studi precedenti hanno affrontato il problema di determinare la sorgente di mantello di questi corpi intrusivi tholeiitici, propendendo alternativamente per un'origine determinata dall'arrivo di un mantle-plume, o per una provenienza di questi magmi dal mantello litosferico. I nuovi dati ottenuti (elementi maggiori e in traccia e analisi isotopiche di Sr-Nd-Pb-Os su oltre 70 campioni di roccia totale e analisi dettagliate dei fenocristalli da microsonda elettronica) forniscono una migliore comprensione della petrogenesi di questa parte della CAMP. I campioni mostrano un ampio range composizionale, variando da Olivin/Hyperstene-normativi a Quarzo-normativi. Generalmente basse in Ti (TiO_2 0.36-1.35 wt%), le doleriti campionate mostrano abbondanti variazioni in elementi maggiori (es. MgO 17-5 wt%; CaO 12-7 wt%), che sono state interpretate derivare da processi di cristallizzazione frazionata a partire da magmi parentali di (almeno) due diverse composizioni: basalti Olivin-normativi alti e bassi in Fe. Contrariamente agli elementi in traccia, che mostrano com-

posizioni uniformi e tendenzialmente impoverite, i rapporti isotopici (Sr-Nd-Pb) presentano valori molto eterogenei e signature arricchite ($^{87}\text{Sr}/^{86}\text{Sr}_{200\text{Ma}}$ 0.70438-0.70880; $^{143}\text{Nd}/^{144}\text{Nd}_{200\text{Ma}}$ 0.5120-0.5125; $^{206}\text{Pb}/^{204}\text{Pb}_{200\text{Ma}}$ 17.41-18.61; $^{207}\text{Pb}/^{204}\text{Pb}_{200\text{Ma}}$ 15.54-15.63; $^{208}\text{Pb}/^{204}\text{Pb}_{200\text{Ma}}$ 37.32-38.38). In particolare, i rapporti $^{206}\text{Pb}/^{204}\text{Pb}$ raggiungono valori molto bassi, mai riscontrati prima in rocce CAMP basse in Ti., estendendosi verso il campo composizionale dell'Enriched Mantle I (EMI). Viceversa, i valori di $^{187}\text{Os}/^{188}\text{Os}_{200\text{Ma}}$ risultano omogenei, con firme isotopiche basse, tipiche del mantello, e non correlati con altri isotopi. In accordo con tali dati, la modellizzazione numerica dei processi di assimilazione limita la contaminazione crostale tra il 3 e il 10 %. Quindi, l'elevata variabilità e la firma isotopica arricchita sono caratteristiche ereditate dalla sorgente, interpretata come un mantello litosferico sub-continentale, arricchito di una componente EMI da un'antica subduzione. La componente con firma isotopica tipica dell'EMI si suppone fornita da crosta oceanica riciclata (e relativi sedimenti oceanici), incorporati come vene pirossenitiche all'interno del mantello litosferico.

Nella seconda parte vengono presentati i risultati dell'applicazione della biostratigrafia marina e della sua alta risoluzione temporale a una definizione di dettaglio della messa in posto della CAMP. L'analisi di 19 campioni di conodonti (apatite) da sezioni del reame tetideo stratigraficamente ben calibrate ha portato al riconoscimento di due shift nella composizione isotopica dell'acqua oceanica. Una rapida caduta del rapporto $^{87}\text{Sr}/^{86}\text{Sr}$ durante il Retico inferiore è seguita da un aumento nel Retico superiore. Queste variazioni isotopiche sono positivamente correlate con perturbazioni nel rapporto $^{187}\text{Os}/^{188}\text{Os}$ in acqua oceanica, e possono essere imputate a una rapida messa in posto ed alterazione della CAMP, seguite da un veloce aumento del tasso di erosione continentale. Questa interpretazione implica un riposizionamento della prima messa in posto della CAMP intorno al limite Norico/Retico, cui consegue necessariamente un limite massimo per la durata del Retico (<2 Ma). Un rapporto di causa/effetto tra vulcanismo CAMP e perturbazioni climatiche è quindi plausibile. A sua volta, il mutamento del clima può aver potenzialmente innescato la crisi biologica globale culminata al limite Triassico/Giurassico. Questa nuova interpretazione appoggia inoltre il carattere graduale dell'estinzione di fine Triassico, descritta da autori precedenti come un'escalation progressiva di estinzioni iniziata al limite Norico/Retico e culminata al Triassico/Giurassico.

INTRODUCTION

I.1 LARGE IGNEOUS PROVINCES

The geologic history has been punctuated by the outpour of Large Igneous Provinces (LIPs), major geodynamic events constituted by emplacement of giant volumes of magmatic rocks in within-plate tectonic settings during geologically brief to nearly instantaneous periods. Extruded volumes of the order of 1 million km³ extending on a surface of the order of 1 million km² are typically observed in LIPs (e.g.; Mahoney et al., 1997), and both acid and mafic magmatism may constitute LIPs. Continental flood basalts (CFBs) or oceanic plateaus (OP) are included in the definition (e.g. Ernst et al., 2005) of LIPs, and the first are often linked to continental breakup either as a cause or as a consequence of it (Courtilot et al., 1999). Unraveling this causal relationship requires further insights into the processes originating these large scale events. In particular, LIPs have been variably attributed, with strong debate, either to a (active) mantle plume origin (e.g. Morgan, 1971; Campbell, 2005) or a (passive) derivation from adiabatic melting following extensional thinning of the lithosphere (e.g. White and McKenzie, 1989; Anderson, 1998). Many different features have also been appealed to represent straightforward evidences of a LIP being generated through one of the two models, e.g. high-rate magmatic production, geochemically enriched signatures, high-T rocks (picrites), domal uplift and the presence of hot spot tracks are viewed as unequivocally reflecting a mantle plume origin.

Secondly, a growing body of evidences has recently been calling for a time-correspondence between Large Igneous Provinces and other global scale events such as mass extinctions (Courtilot and Renne, 2003). In particular, Courtilot and Renne (2003) showed that the most recent 12 LIPs preserved in the global geological record (covering a good portion of the Phanerozoic, from 300 Ma to the present) do not show any periodicity in their timing of emplacement, and that four of them correspond in time (to the best resolution available) to the 4 major mass extinctions of the last 260 Ma (Raup and Sepkowski, 1984). This temporal correspondence has thus led to infer a general causal relationship between LIPs and mass extinctions, where the connection between the two would be represented by catastrophic climatic perturbations driven by the volcanism (e.g. Wignall,

2001). This causal relationship is however still debated, drawbacks including the existence of LIPs unrelated to extinction events (e.g. ~133 Ma Parana-Etendeka CFBs; Ernesto et al., 1999) or related to minor biotic turnovers (e.g. ~183 Ma Karoo-Ferrar province; Jourdan et al., 2008). Furthermore, precise estimates of the atmospheric load of outpoured volcanic gases (CO_2 , S and Cl) are still sparse (e.g. McHone, 2002; Self et al., 2008), and climatic response models to volcanic perturbation still unclear (Rampino et al., 1988; McElwain, 1999). However, even if a triggering role of LIPs on environmental perturbations seems likely, the highest accuracy of radiogenic isotope geochronology yet lacks the necessary resolution to assess exact time-relationships between CFBs and mass extinctions. In this context, the application of precise bio- and chronostratigraphic tools, and of new analytical methods to assess the extent of volcanic gas emissions are required.

The Central Atlantic Magmatic Province (CAMP) has not been spared debates concerning a) its geodynamic origin (DeBoer and Snider, 1979; McHone, 1999), b) its possible causal link to the end-Triassic global biotic crisis (Pálffy et al.; 2000; Wignall et al., 2001; Marzoli et al., 2004; Whiteside et al., 2007) and c) its atmospheric burden of volcanic gases (Grossmann et al., 1991; McHone, 2002).

Along this thesis two of the above presented main topics will be addressed, with the contribution of newly obtained data.

Part I will deal with new geochemical data (major and trace elements, Sr-Nd-Pb-Os isotopes) on eastern North American CAMP dykes and sills, sampled along the Piedmont area of the southern Appalachians, aiming to depict the petrogenetic processes and the mantle source residing at the base of this part of the province.

On **Part II** the onset of CAMP is constrained with the unprecedented precision of marine biostratigraphy to the Late Triassic. $^{87}\text{Sr}/^{86}\text{Sr}$ data obtained on conodont samples highlight variations in seawater Sr isotopic curve, directly recording the isotopic fingerprint of CAMP emplacement and weathering. Through this newly applied biostratigraphic tool, onset of the CAMP is re-positioned around the Norian-Rhaetian boundary, with major implications for the duration of the Rhaetian stage (c. 1.7 Ma).

I.2 THE CENTRAL ATLANTIC MAGMATIC PROVINCE

Late Triassic-Early Jurassic (~ 200 Ma) breakup of Pangea has been accompanied by the emplacement of tholeiitic basaltic and basaltic-andesitic dykes, sills, lavas and minor intrusive bodies over a vast area surrounding the present Central Atlantic Ocean. Overall synchrony of the magmatism over four continents has allowed its grouping under the common definition of Central Atlantic Magmatic Province (CAMP; Marzoli et al., 1999; Fig. A). Emplaced over an area exceeding 10^7 km², from Brazil to Nova Scotia and from Mali to France, CAMP is the largest LIP documented so far, though perhaps not being the most voluminous (a possible estimate of erupted magma volume sums up to $\sim 2 \times 10^6$ km³; Marzoli et al., 1999; McHone, 2002).

The majority of investigated CAMP rocks are low in Ti ($\text{TiO}_2 < 2$ wt%) and crop out all over the province, whereas a minor occurrence of high-Ti volcanics ($\text{TiO}_2 > 2$ wt%) is recorded in palaeogeographically central areas of the CAMP (e.g. Brazil, Guyana, Surinam, Liberia). Different geochemical classifications have been applied to CAMP volcanics, following recognition of different units in lava piles from eastern North America and Morocco (Bertrand et al., 1982; Puffer, 1992; Marzoli et al., 2004) and uniform geochemical characteristics in other groups of CAMP tholeiites (e.g., Wiegand and Ragland, 1971). In general, the first CAMP volcanics emplaced appear to belong to a rather common quartz-normative, geochemically enriched group, intermediate in Ti (TiO_2 1-2 wt%). A general geochemical depletion is observed with time in CAMP lava piles, e.g. a decrease in La/Yb ratio and in Ti (Marzoli et al., 2004). Eventually, late-stage magmatism (namely the Recurrent Unit in Morocco and the Hook Mt. basalts in the eastern North American basins) with geochemical traits resembling those of E-MORBs (e.g. higher Ti contents and flatter REE-patterns) followed, and has been addressed to reflect an increasing contribution of the asthenosphere, linked to the incipient continental separation. An overall isotopically enriched signature is recorded for low-Ti CAMP tholeiites, while high-Ti ones cluster on a more restricted (and depleted) field (Alibert, 1985; Dupuy et al., 1988; Greenough et al., 1989; Mauche et al., 1989; Heatherington and Mueller, 1991; Puffer, 1992; Dostal and Durning, 1998; Heatherington and Mueller, 1999; De Min et al., 2003; Jourdan et al., 2003; Deckart et al., 2005; Verati et al., 2005; Merle et al., 2011). Though a mantle-plume origin for the CAMP has been tentatively addressed in the past (May, 1971; DeBoer and Snider, 1979; Hill, 1991; Wilson, 1997), there is general tendency to support a (metasomatized)

lithospheric origin for CAMP magmatism (e.g. Pegrarn, 1990; Heatherington and Mueller, 1999; McHone, 2000) and to limit the possible involvement of a mantle plume essentially as a heat supplier (Cebria et al., 2003; Merle et al., 2011).

High-precision geochronology (mostly $^{40}\text{Ar}/^{39}\text{Ar}$ ages, filtered for data quality, and few U/Pb dates) for CAMP rocks, recently reviewed by Marzoli et al. (2011) and recalculated after newly-established ^{40}K decay constant (Renne et al., 2010), allows constraining the main peak of CAMP activity at c. 201.5 Ma, i.e. comparable to the single-zircon U/Pb age of the Triassic–Jurassic boundary (201.58 ± 0.17 ; Schaltegger et al., 2008; 201.31 ± 0.43 Ma, Schoene et al., 2010). Furthermore, geochronologic evidences support stratigraphic and palaeomagnetic data in constraining the main pulse of CAMP volcanism to be brief (<1 Ma; ~ 600 ka, Olsen et al., 2003; Knight et al., 2004). A second, minor pulse of CAMP magmatism (corresponding to the Recurrent Unit basalts, Morocco) appears however to have occurred between 198 and 192 Ma (Verati et al., 2007). Basalts of the North American margin volcanic wedge have been interpreted to be CAMP-related and in this sense they would represent the final stages of CAMP activity, marking the rift-to-drift transition (Withjack et al., 1998). However, recently obtained ages of ~ 170 Ma (Hames et al., 2010) cast doubts to their actual CAMP-affinity (Heffner et al., 2012).

Time-relationship between CAMP and Triassic–Jurassic boundary (TJB) has long been debated. Olsen et al. (2003) placed the TJB below the oldest CAMP volcanics in the Newark basins (eastern North America, ENA), thus constraining the CAMP to be entirely Early Jurassic, at least in North America. However, geochemistry and geochronology support a slightly older onset of CAMP lava piles in Morocco (Marzoli et al., 2004; 2011) with respect to eastern North America. Moreover, recent biostratigraphic data (palynology and conchostracan biostratigraphy) constrain oldest ENA CAMP lava piles (from the Fundy basin) to be Latest Triassic in age (Cirilli et al., 2009; Kozur and Weems, 2010). In this sense, CAMP activity was demonstrated to have straddled the TJB.

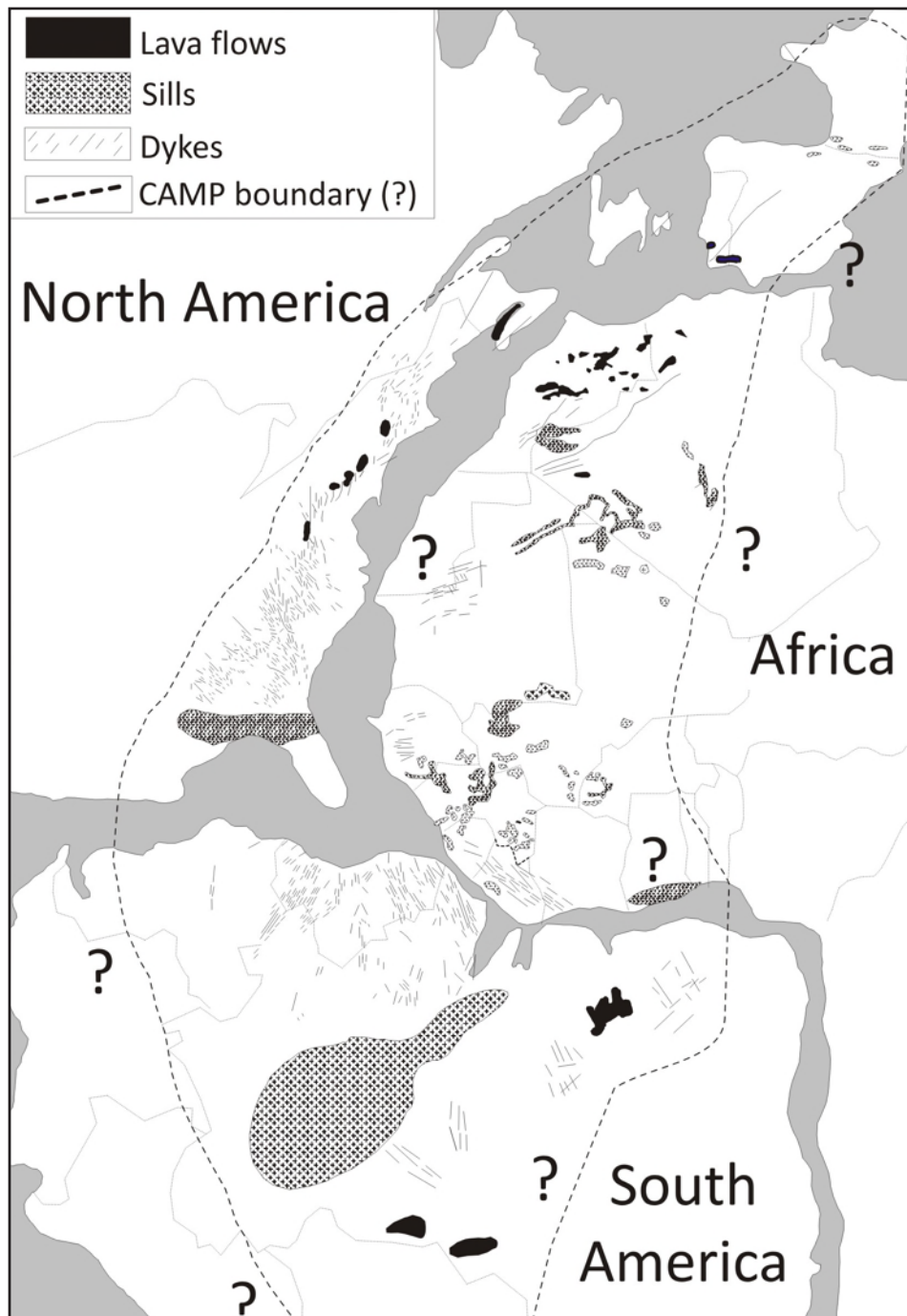


Figure I.1: Schematic map of the CAMP on a palinspastic reconstruction of Pangea. Modified after Marzoli et al. (2011)

PART I

GEOCHEMISTRY OF **CAMP** DYKES AND SILLS FROM EASTERN **NORTH AMERICA**

1 EARLIER STUDIES

The North American portion of the Central Atlantic magmatic province encompasses volcanics and magmatic bodies outcropping along the Eastern, coastal states of the U.S.A and Canada. Magmatism in this area has long been referred as eastern North American (ENA) Mesozoic magmatism (e.g., Puffer and Ragland, 1992), a definition that incorporates four different episodes during the entire Mesozoic. In particular, the second of these episodes (latest Triassic-earliest Jurassic) is linked to the lithospheric thinning that led to the breakup of Pangea and the opening of the Atlantic ocean. Intrusion and outpour of tholeiitic magmas along a discontinuous network of rift- and transform-related structures along the entire extent of the Appalachian Mountain system is now straightforwardly related to the CAMP (Marzoli et al., 1999, 2011).

CAMP magmatism in the Southern Appalachians comprises a) numerous diabase dykes, in NW to NE trending swarms (King, 1961; Ragland, 1983), which can be followed from Georgia to Pennsylvania (i.e. cropping out also in the northern Appalachians) and are not directly related to (feeding) preserved lava flows; b) sub-horizontal intrusions (doleritic sills) within sedimentary basins (e.g. within Durham basin, NC); c) diabase dykes and possibly basaltic flows and dacitic ash fall tuffs within sedimentary basins (e.g. the Tallahassee basin; Heatherington and Muller, 1999) of Florida, Georgia (South Georgia rift; McBride et al., 1989) and Alabama; d) wedge-shaped basaltic bodies offshore of eastern North America (Holbrook and Kelemen, 1993; Oh et al., 1995; McHone, 1996; Hames et al., 2010; Heffner, 2011). Among the thickest (up to 450 m; Tollo and Gottfried, 1992; Marzoli et al. 2011) basaltic lava piles of the entire CAMP crop out in the northern Appalachians, within sedimentary basins of the Newark Supergroup (Schlische, 2003; Olsen et al, 2003). Emplacement of CAMP flows in these basins was constrained through geochronology, cyclo- and magnetostratigraphy to have been briefer than 1 Ma (~ 600 ky; Olsen et al., 2003). Here, the Triassic-Jurassic boundary had long been located below the oldest CAMP flows (e.g. Whiteside et al., 2007), but has recently been demonstrated to occur above the oldest CAMP flows (Cirilli et al., 2009; Kozur and Weems, 2010). Up to three different basaltic units were emplaced in the Newark basins (Culpeper, Gettysburg, Newark, Hartford, Deerfield, Fundy) from Virginia to Nova Scotia

(Puffer and Student, 1992; Kontak, 2008; Jourdan et al., 2009; Fig.1.1) and precise chemo-, magne- to- and biostratigraphic analyses allow inter-basinal correlations. Intrusive and sub-volcanic bodies are present in the northern Appalachians as well, being either feeder-dykes of the main flows or independent bodies (Higganum, Fairheaven, Butress, Bridgeport and Shelburne dykes and Belmont, Rapidan, Palisades and French King sills; e.g. Philpotts and Asher, 1993).

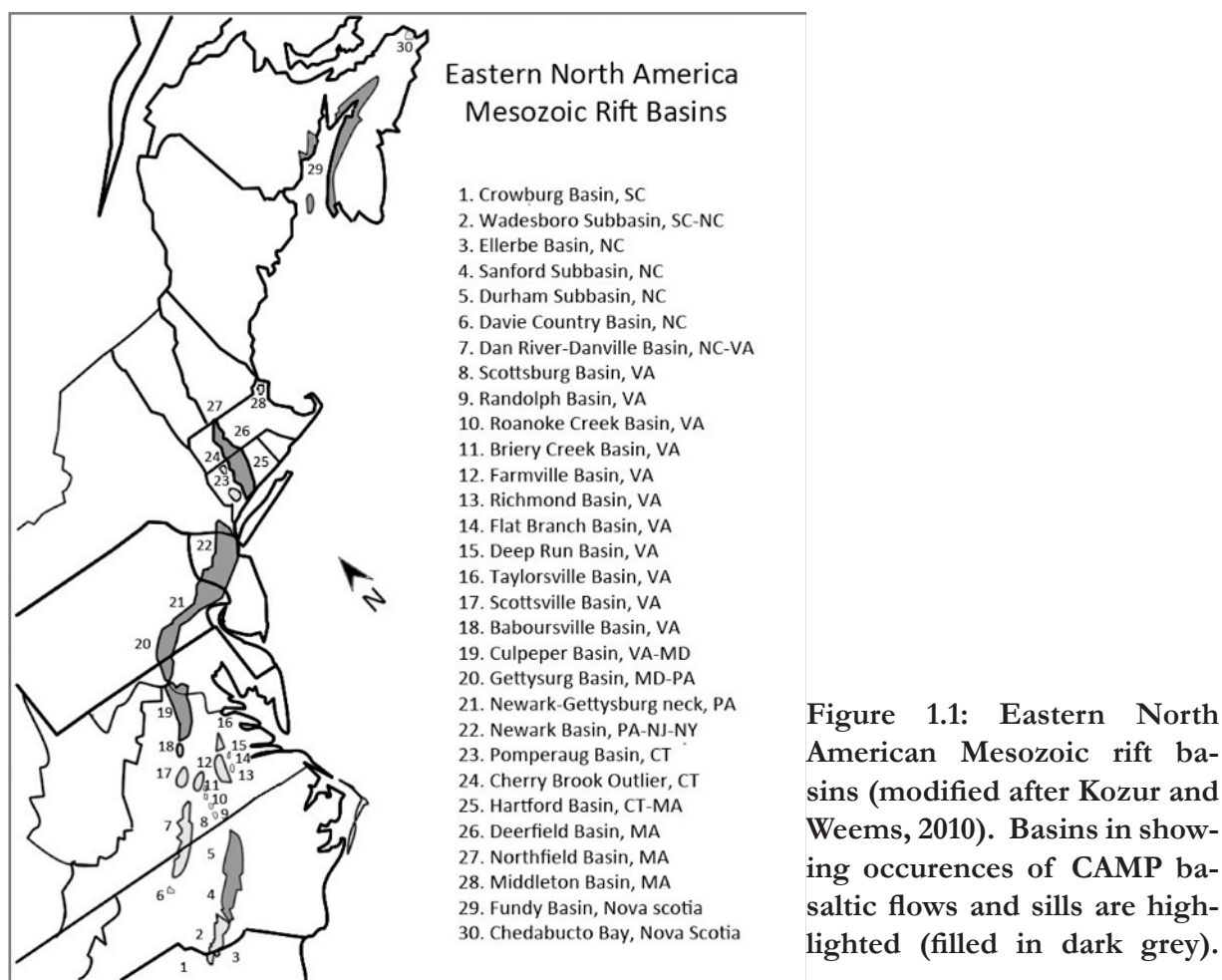


Figure 1.1: Eastern North American Mesozoic rift basins (modified after Kozur and Weems, 2010). Basins in showing occurrences of CAMP basaltic flows and sills are highlighted (filled in dark grey).

Few U/Pb ages exist for ENA CAMP rocks. Baddeleytes from the Gettysburg sill and from the Palisades sill yielded ages of 201.3 ± 1.0 Ma and 200.9 ± 1.0 Ma, respectively (Dunning and Hodych, 1990). Zircons from pegmatitic layers within the North Mountain basalt in the Fundy basin resulted in a U/Pb age of 201.7 ± 1.4 Ma (Hodych and Dunning, 1992), of 201.3 ± 0.3 Ma (Schoene et al., 2006) and 201.38 ± 0.31 Ma (Schoene et al., 2010). On the contrary, a fair number of $^{40}\text{Ar}/^{39}\text{Ar}$ dates are now available for ENA CAMP rocks, since the dataset has been increased by geochronologic data recently obtained by Jourdan et al. (2009) and Marzoli et al. (2011). Moreover, Marzoli et al. (2011) reviewed pre-existing $^{40}\text{Ar}/^{39}\text{Ar}$ ages on ENA CAMP rocks, i.e. data were carefully

filtered with quality criteria and recalculated with the new decay constant after Renne et al. (2010), thus being now directly comparable with U/Pb ages. CAMP dykes from the Carolinas yielded (recalculated) $^{40}\text{Ar}/^{39}\text{Ar}$ ages between 202.1 ± 1.5 Ma and 195.2 ± 2.0 Ma (Hames et al., 2000; Beutel et al., 2005; Nomade et al., 2007). Dates from bitoite and plagioclase separates from ENA CAMP lava piles and sills within Newark supergroup basins range instead from 202.9 ± 1.4 (Fundy basin; Jourdan et al., 2009) to 195.1 ± 2.1 Ma (Palisades sill; Marzoli et al. 2011). The recalculated mean $^{40}\text{Ar}/^{39}\text{Ar}$ age for CAMP peak activity in North America (201.5 ± 0.9 Ma; Marzoli et al., 2011) is thus indistinguishable from the U/Pb age of the Triassic-Jurassic boundary (201.31 ± 0.43 Ma; Schaltegger et al., 2008; Schoene et al., 2010). Hames et al. (2010) obtained $^{40}\text{Ar}/^{39}\text{Ar}$ crystallization ages (on plagioclases and whole rock) between 172.35 ± 0.80 Ma and 169.1 ± 2.0 Ma from basalts of the South Georgia Rift (from a core of the Clubhouse Crossroads basalts and one from Dorchester County, SC). Given this c. 30 Ma age difference, Hames et al. (2010) hypothesized a different origin for these rocks, casting doubts on their CAMP affinity. Basalts forming the wedge-shaped seaward dipping reflector sequences of the eastern North American margin have been seismically correlated to flood basalts of the Clubhouse Crossroads and South Georgia rift (Hamilton et al., 1983; McBride et al., 1989). Thus, this age discrepancy led Heffner et al. (2011) to question CAMP affiliation of the entire basaltic coastal wedge as well.

ENA CAMP tholeiites have been prevalently described with a classification based on major elements geochemistry, i.e. on CIPW-normative compositions (Wiegand and Ragland, 1970; Ragland et al., 1983). Quartz-normative rocks are common in the northern part of ENA, i.e. CAMP flows cropping out in the Newark Supergroup basins all belong to the quartz-normative group, as well as numerous dykes. Olivine/Hyperstene-normative basalts occur instead mostly in the South (Ragland et al., 1983). Quartz-normative rocks were further classified into High Ti (HTQ, $\text{TiO}_2 > 1$ wt%), High Fe (HFQ; $\text{Fe}_2\text{O}_{3\text{tot}} > 13$ wt%) and Low Ti (LTQ, $\text{TiO}_2 < 1$ wt%).

An alternative classification (Cummins et al. 1992), based on TiO_2 -MgO relations, subdivided ENA tholeiites into enriched and depleted magma types, i.e. at a given MgO content, the enriched magma type shows higher TiO_2 (and trace elements) content. Applied to the entire ENA CAMP, this criterion marked that despite the widespread occurrence, tholeiites belonging to the enriched group showed a considerable chemical uniformity. On the contrary, though more geographically localized,

depleted magmas displayed a wider geochemical heterogeneity. Such differences were related by Cummins et al. (1992) to different plumbing systems feeding rocks of different chemical groups, i.e. deep rift-flank (slow ascending rate for the magmas) and shallow rift-axial sources (fast magma emplacement, no ponding or fractionation) would have originated depleted and enriched magmas, respectively. This feature is reflected by the HTQ basaltic magma type, which includes each of the initial lava flows in the ENA Mesozoic basins and is the most chemically uniform throughout eastern North America (Wiegand and Ragland, 1970). This led Puffer and Student (1992) to propose that the rifting of Pangea triggered a decompression melting acting uniformly on Pangean lithosphere and producing a “common”, primary, HTQ magma type in eastern North America, which successively underwent a rapid emplacement, with limited ponding or fractionation (e.g. Philpotts and Asher, 1993). Isotopic data for ENA tholeiites (Pegram, 1990; Puffer and Student, 1992; Tollo and Gottfried, 1992; Heatherington and Muller, 1999) appear to mostly support this hypothesis, yielding signatures that are consistent with a subcontinental lithospheric mantle (SCLM) source. However, other geochemical traits disagree with this interpretation (e.g. enriched Pb signatures, convergent margin-like trace element ratios; Pegram, 1990) and have led to different models to unravel the origin of these tholeiites. Different mechanisms have been claimed to supply the heat necessary to cause widespread partial melting of the SCLM under Pangea and to produce ENA CAMP magmatism, as a) the impingement of a hot mantle plume head under the Carolinas (e.g., DeBoer and Snider, 1979); b) delamination of the lithospheric mantle after the Alleghanian orogeny (cf. Chapter 2) may have brought in contact the hot convecting asthenosphere with the cold SCLM, which in turn underwent partial melting (Nelson, 1992; Levin et al., 2000); c) convection cells beneath the rift zone, possibly influenced by pre-existing lithospheric structures, may have created both ENA Mesozoic rift basins and produced tholeiitic magmas by decompressional melting that followed lithospheric thinning (McHone, 2000); d) heat accumulation driven by thermal insulations under Pangea supercontinent (following to the model proposed by Coltice et al., 2007).

2 GEOLOGY OF EASTERN NORTH AMERICA

An appraisal of the eastern North America geology helps understanding the context in which volcanics and intrusives of the Central Atlantic Magmatic Province (CAMP) were emplaced. Information about crustal lithotectonic units allows to constrain geochemical flavors potentially inherited via crustal contamination processes, while the reconstruction of geodynamic events may help outlining the characteristics of the lithospheric mantle. In particular, differences between the geology of northern and southern portions of eastern North America may account for observed (e.g. isotopic) differences between CAMP magmatism emplaced on different areas (cf., Pegram, 1990). Furthermore, geochemical comparison between mafic or bimodal magmatic provinces emplaced in the same area in different ages (e.g. Badger and Sinha, 1988; Murphy and Dostal, 2011) may provide a proxy to understand mantle evolution below an area as eastern North America, which underwent a complex geodynamic history.

The geological history and evolution of eastern North America are envisaged through the development of more than one entire Wilson cycle (Fig. 2.3), from the formation of Rodinia supercontinent (Mesoproterozoic) to the breakup of Pangaea (Early Jurassic). These complex, world-wide scale events resulted in the formation of two main orogenic belts in the eastern North America (ENA), i.e. the Grenville province and the Appalachians.

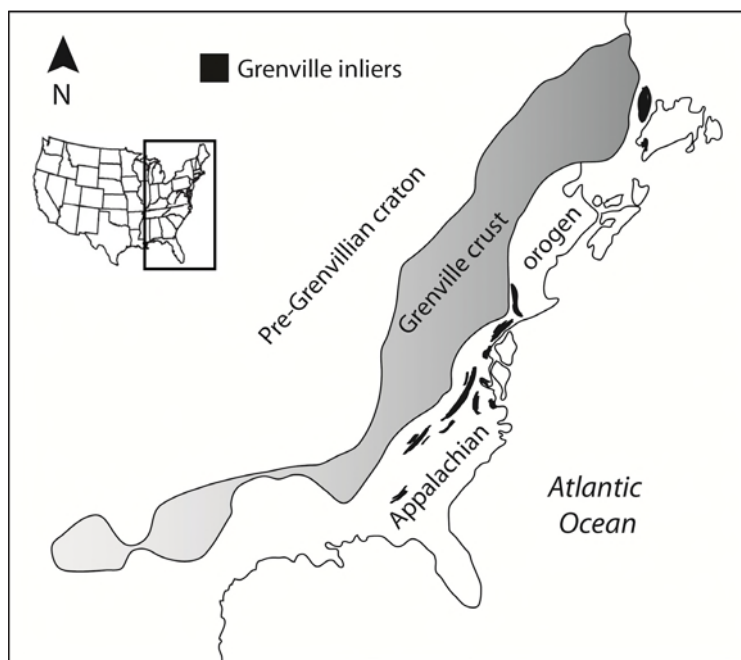


Figure 2.1: Generalized geological outline of the eastern North America, indicating geographic extent of cratonic terrains and of Grenvillian and Appalachian orogens. Grenville inliers within Appalachian terrains are shown in black. (Modified after McLelland et al., 2010).

2.1 THE GRENVILLE PROVINCE

Grenvillian terrains witnessed metamorphism and tectonic deformation during the Grenville orogeny (1190-990 Ma; Gower and Krogh, 2002), which led to the collision between Laurentia with Baltica (and other continental masses) and to the assemblage of Rodinia supercontinent. They mainly constitute the northern part of ENA (Nova Scotia, Adirondack Mountains and surrounding areas) and the immediate western hinterland of the Appalachian orogen. Nevertheless, portions of Grenville crust are present also as inliers cropping out in tectonic windows within Appalachian terrains (Fig. 2.1), while Appalachian outliers overrode and crop out on Grenvillian domains.

Grenville Province rocks have been thrust over their foreland along a series of ductile to brittle shear zones and faults that truncate the structural trends of the proto-Laurentian craton (Ludden & Hynes, 2000). Allochthonous and parautochthonous crustal nappes were transported to the NW and are now stacked above basement rocks of the pre-Grenvillian Laurentian margin, resulting in an overthickened crust of 36-42 km (as seismic profiles reveal; e.g. Carr et al., 2000). High-grade metamorphic terranes of the Grenville Province are considered a complex juxtaposition of Andean-type plutonic and volcanic arc environments. The ENE-trending and SE-dipping Grenville Front is a shear zone marking the boundary between the Grenville province and the older structural, cratonic provinces to the NW, i.e. it is a NW limit for Grenville orogeny-linked tectonic reworking of rocks belonging to the older provinces. These faults and shear zones occasionally reactivate pre-existing Archean to Proterozoic structures that acted as persistent crustal weaknesses, while in other cases truncate pre-existing lithotectonic boundaries. Three principal tectonic units constitute the Grenville Province: a) the Parautochthonous Belt, b) the Allochthonous Polycyclic Belt, and c) the Allochthonous Monocyclic Belt (Rivers et al., 1989; Rankin et al., 1993). The Parautochthonous Belt (Davidson and van Breemen, 2001), adjacent to the Grenville Front, includes reworked Archean to Mesoproterozoic rocks of the Superior Province foreland (that were the southern margin of Laurentia during the Mesoproterozoic), deformed by NW thrusting of the multiply metamorphosed Allochthonous Polycyclic Belt. This overlies the Parautochthonous belt along the Allochthon Boundary Thrust and is composed of transported Paleoproterozoic and Mesoproterozoic rocks. The Allochthonous Monocyclic Belt consists of rocks younger than ca. 1.35 Ga, which thus underwent a single metamorphic event. Allochthonous lithologies were emplaced during the

closure of an oceanic basin (Martignole & Pouget 1994). During the Grenvillian Himalayan-type orogeny, extensive crustal thickening and tectonic extrusion led to widespread high-grade metamorphism (Ludden and Hynes, 2000) and anatectic magmatism.

2.2 THE APPALACHIANS

2.2.1 OROGENIC PHASES

The Appalachian system stretches for c. 3000 km in a NE-SW orientation along the eastern margin of North America (Fig. 2.2), from Newfoundland (Canada) to Alabama (USA). This marginal position is a reflection of the fact that during the Mesozoic breakup of Pangaea, North America separated from Europe and Africa along approximately the same line as that marking earlier continental collisions (Hatcher, 2010). The geological history of the Appalachians can be tracked back to 1.3-1.1 Ga, when the Grenville orogeny deformed and metamorphosed (up to the granulite facies) the eastern part of Laurentia, a proto-American continental mass, during the assemblage of the supercontinent Rodinia (Tollo et al., 2004). Crystalline rocks cropping out in several tectonic windows along the Appalachians (i.e. Sauratown Mountains window; Wright Horton and McConnel, 1991) testify this event. The rifting phase marking Rodinia breakup (Mesoproterozoic, 750-700 Ma) led to the opening of the Iapetus ocean and separated Laurentia from Baltica and Siberia continents broadly along the present North American margin (Scotese et al., 1979). Lithospheric thinning associated to continental rifting in eastern North America allowed the intrusion of peralkaline granites (Odom and Fullagar, 1984) as well as the emplacement of the Bakersville tholeiitic dyke swarm (Goldberg et al., 1986) and of a bimodal, rift-related, volcanic suite (Rankin, 1975; Hibbard et al., 2002). The opening of the Iapetus ocean led to the Cambrian-early Ordovician inundation of Laurentia (500-450 Ma), testified by a deepening upward facies transition from continental sediments to shelf carbonates, i.e. eastern North America was then the southern passive margin of Laurentia (Schwab, 1972). A transient uplift phase (Penobscottian orogeny) is recorded in the Early Ordovician by the post-Knox-Beekmantown unconformity, of nearly worldwide occurrence (Hatcher and Repetski, 2007). The Iapetus ocean, opened in late Proterozoic-Cambrian times, began to close in Middle Ordovician times with a compressional orogenic phase named Taconic orogeny. Decoupling between southern and northern Appalachian domains is already visible at this time, i.e. while northern Appalachians witnessed the obduction of ophiolitic complexes, the southern area devel-

oped as a foredeep environment, interested by sedimentation of different character (Hatcher, 2010; Pollock and Hibbard, 2010). Accretion of volcanic arcs is the trade-mark of the Taconic phase. A complex arc system (Piedmont arc) had formed off shore of present day Newfoundland in the Ordovician, and was accreted to Laurentia through W and E-vergent subduction of the Iapetus oceanic crust (van Staal et al., 2007). This Taconic allochthons are not present in the southern Appalachians, interested on the other hand by mafic and ultra-mafic ophiolitic complexes (Hatcher et al, 1984). The peak of the Taconic regional metamorphism, up to the upper-amphibolite facies, is diachronous, proceeding from North to South, i.e. dating back to 495-455 Ma in the North, 480-455 Ma in New England and 460-455 Ma in the southern Appalachians (van Staal et al., 2004). A Late Ordovician-Early Silurian molasse was deposited unconformably throughout the orogeny, above the Taconic unconformity (Rodgers, 1971).

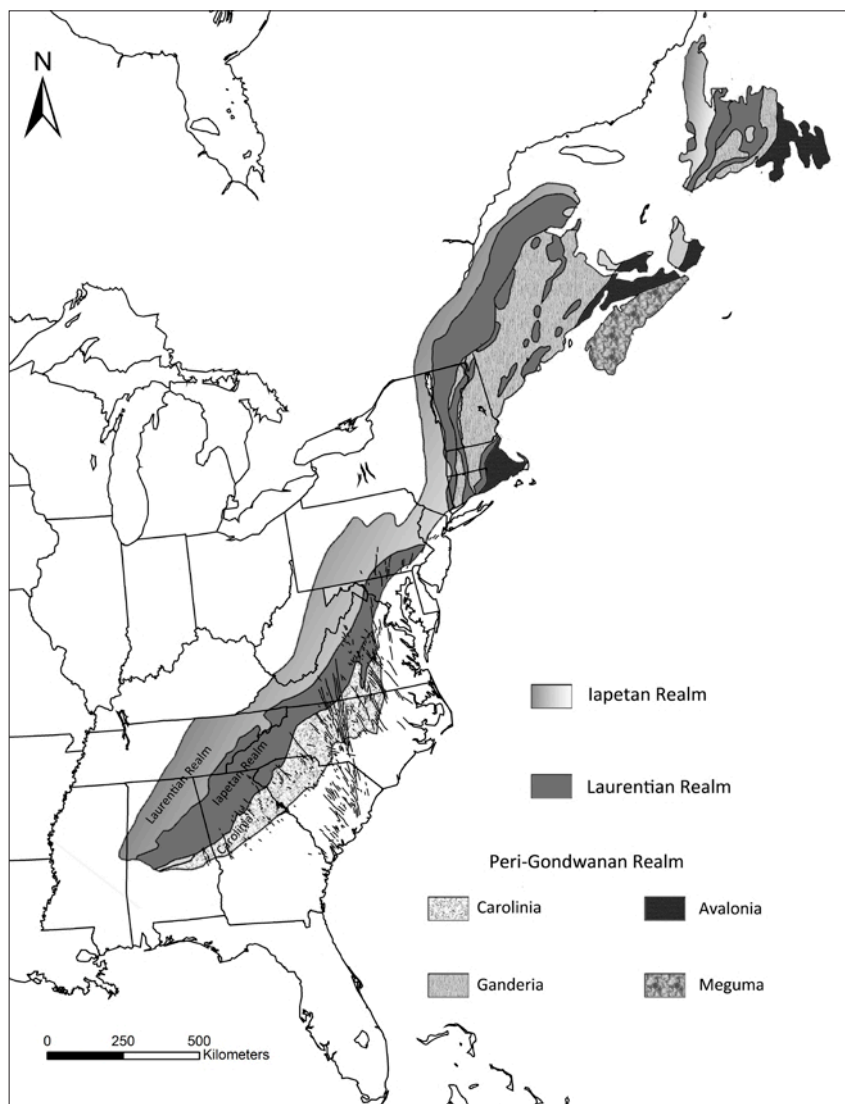


Figure 2.2: Principal lithotectonic units (left, modified after Hibbard, 2007) and geologic-physiographic subdivision (right, modified after Holm-Denoma and Das, 2010) for the Appalachians.

A collisional phase started in the Late Devonian (c. 410 Ma), named Acadian orogeny in the North and Neoacadian orogeny from New England southward (ending here around 345 Ma, early Carboniferous; Hatcher, 2010). A rotational (zippered; Hatcher, 2010) north-to-south closing of the Rheic ocean resulted in collision between Laurentia and microcontinents (superterrane) of Gondwanan affinity, i.e. Carolina, Avalon, Ganderia and Meguma allochthonous terranes (e.g. Ingle et al., 2003). Plutonism of essentially mafic chemistry accompanies the Acadian orogeny and is widespread in the North (New England and Canadian Maritimes; e.g. Ayuso and Bevier, 1991; Hibbard et al., 2010), but sparse in the South (e.g. Butler and Fullagar, 1978; McSween et al., 1991). This marked difference may be due opposite directions of Acadian subduction, i.e. westward from New England to the North, eastward in the central and southern Appalachians, as suggested by Hatcher (2010). A possibly limited amount of available oceanic crust in the South led to a) sparse suprasubduction-zone plutons and b) subduction of continental crust that totally shut off plutons emplacement (Hatcher, 2010; Hibbard, 2010). This decoupling may be supportive of chemical differences in the lithospheric mantle from North to South inherited during the Acadian orogeny and eventually resulting in different isotopic signatures of mantle derived mafic magmatism that involved the same area, i.e. tholeiites emplaced before the Acadian event display depleted signatures (e.g. Badger and Sinha, 1989), while those emplaced after it show isotopic enrichment (Pegram, 1990, and data from this work).

Closure of the Rheic ocean during the following Alleghanian (late Carboniferous-Permian) orogeny eventually resulted in the continental collision between Laurentia and Gondwanaland, leading to the assemblage of the supercontinent Pangaea (Bradley, 1982). This last orogenic phase was the most prominent for the southern and central Appalachians, resulting in pervasive deformation of the molasse deposits in the west (Appalachian Plateau) and of the sedimentary series of the Valley and Range. Evidences of this major continental collision are represented by (Hercynian) S-type granitic intrusions pervading the area SE of the Brevard fault zone (Sinha & Zietz, 1982), amphibolite-facies regional metamorphism and deformation in belts of the Appalachian Piedmont (Secor et al., 1986) and westward transportation and stacking of the crystalline thrust sheets now forming the Piedmont and Blue Ridge areas.

The Appalachian orogen was subsequently intersected by the Late Triassic continental rifting phase

that led to the opening of the Atlantic Ocean, an event witnessed by the formation of NE-trending sedimentary basins filled by the rift-facies deposits of the Newark Supergroup (Olsen et al., 2003; Schlische, 2003). Attendant Triassic-Jurassic magmatism occurred as 1) differently trending diabase dyke swarms penetrating the Piedmont and Coastal Plain areas (being the main topic of the present work), 2) intrusions of diabase sills in the Late Triassic sedimentary basins (e.g. the sampled Durham sill, NC) and 3) onset of lava piles in the basins, interlayered by the rift-facies deposits. Attendant felsic magmatism possibly accompanied CAMP mafic volcanism, and is represented by dykes of porphyritic rhyolite, cropping out along in the eastern Piedmont and dated between 202 ± 5 Ma (Stoddard et al., 1986; Stoddard, 1992), and 196.3 ± 0.7 Ma (Ganguli et al., 1995). However, at present, evidences for a straightforward connection between CAMP and this felsic magmatism are still lacking.

The prosecution of the extensive regime resulted in tilting of the basinal sedimentary series and Early Jurassic opening of the Atlantic Ocean, with the initial seafloor spreading phase marked by the emplacement of extensive basalt flows and sills offshore of the post-rift margin (even if their link with CAMP magmatism has recently been questioned; Heffner et al., 2012).

A physiographic approach has been applied to describe the Appalachians and to divide them into several provinces. Thus, according to the common USGS definition, the Appalachians encompass five regions: 1) the Appalachian Plateau, 2) the Valley and Ridge, 3) the Blue Ridge, 4) the Piedmont Province and 5) the New England Province (Fig. 2.4).

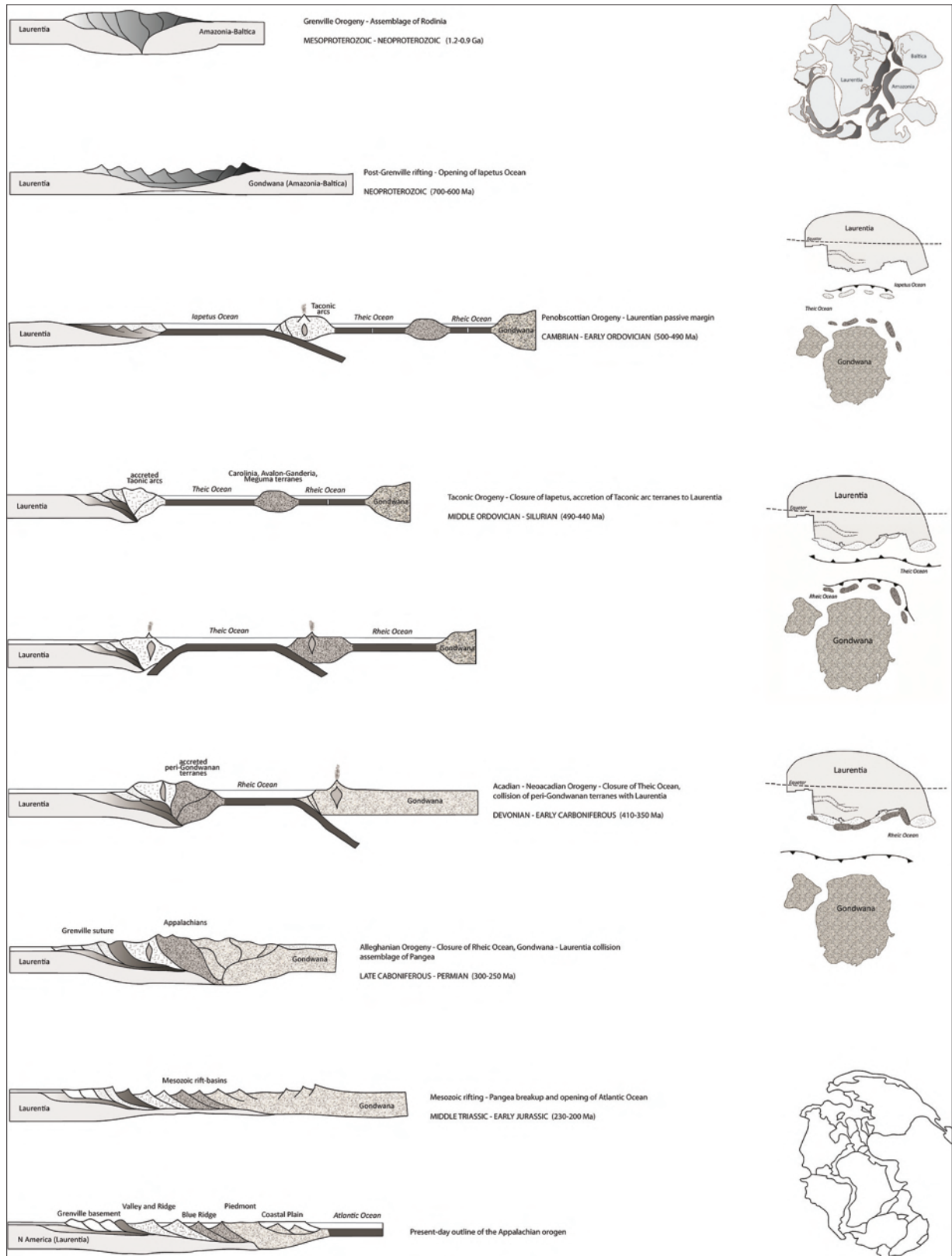


Figure 2.3: Schematic sequence of development of the Appalachian orogen from 1.2 Ga to the present. The geodynamic evolution of the Laurentian (North American) eastern margin is highlighted throughout the major orogenic phases seen in profiles (left column) and in schematic maps (right column). Paleotectonic reconstructions and figures modified after Hatcher and Goldberg, 1991 (profiles) and Hatcher, 2010 (maps). Rodinia supercontinent reconstruction from Carrigan et al. (2003), Pangea from Scotese et al. (1979).

2.2.2 PHYSIOGRAPHIC AND LITHOTECTONIC DOMAINS

A first geological assessment of the Appalachian range sees it subdivided into **Sedimentary** and **Crystalline** Appalachians. The **Appalachian Basin** constitutes the foreland basin of the Appalachians, flanking the chain on the western side, and representing the Sedimentary portion of the range. Two sub-regions are here recognizable: the Appalachian (or Cumberland) Plateau to the west and the Valley and Ridge to the east. Early Cambrian to Early Permian shallow sea sediments (c. 540-300 Ma) characterize the **Plateau**, where the bland deformation associated to the following uplift resulted at most in giant-radius folds involving both the Mississippian limestones and the younger Pennsylvanian shales and sandstones. The terrigenous sediments organized in clastic wedges represent a flysch sequence derived from the early erosion of the rising Appalachians farther east. The **Valley and Ridge**, the eastern portion of the Appalachian Basin, encompasses the same sedimentary series, though showing a stronger deformation, with Alleghenian-driven imbricate thrusting and folding. Boarding the Valley and Ridge to the east, the Blue Ridge fault system (composed by Holston-Iron Mountain, Cartersville and Great Smoky faults) separates the Sedimentary from the Crystalline Appalachians, and represents the thrust level over which Piedmont and Blue Ridge crystalline nappes (composed by Precambrian basement, late Proterozoic-early Paleozoic metasediments and metavolcanics, and Paleozoic plutons) north-westerly overrode the sedimentary series of the Valley and Ridge (Cook, 1983).

The **Blue Ridge**, lying between the Valley and Ridge and the Piedmont, is NW bounded by the Blue Ridge fault system and SE by the Brevard fault zone. The Blue Ridge consists of several stacked thrust sheets, formed by NE-trending thrust faults that were activated by the compressive phase of Iapetus ocean closure (Hatcher and Goldberg, 1991). The stacked sheets were subsequently obducted during the Alleghanian continental collision (Samson et al., 1995) around 300 km to the NW and this tectonic phase imprinted deformation on the Valley and Ridge sedimentary series to the west. Differences in lithologies, deformational and metamorphic history allows the distinction among different nappes, originally discovered in several tectonic windows in the area. The province was primarily physiographically described, but a geological approach further subdivides it into western and eastern Blue Ridge, with the Hayesville-Gossan Lead (Fries) faults marking this separation. Rocks of the Blue Ridge most thoroughly record the entire Proterozoic-Paleozoic Wilson cycle

from the opening of Rodinia to the formation of Pangaea supercontinent. The western Blue Ridge is dominated by the late Proterozoic low- to high-grade metamorphosed sedimentary rocks of the Ocoee Supergroup, which represent the continental rift-facies clastic filling of troughs and basins formed during the extensional phase associated to the breakup of Rodinia and subsequent opening of the Iapetus Ocean (c. 700 Ma). Subsequent units bear both mafic and felsic metavolcanics, that are absent in the Ocoee Supergroup (Goldberg et al., 1986). Lower Cambrian platform and rifted continental margin deposits of the Chilhowee Group overlie conformably the late-Proterozoic metasedimentary series. In the western Blue Ridge sedimentary covers lie in nonconformity (or tectonic contact) upon the crystalline continental Grenvillian basement of 1.2-0.9 Ga, composed by granitic and quartz-monzonitic gneisses (metamorphosed in amphibolite to granulite phase), migmatites, paragneisses and schists, i.e. western Blue Ridge is formed by obducted sediments that were deposited all along the Laurentian passive margin. The eastern Blue Ridge is markedly different, containing fewer lithologies and very minor occurrences of North American continental basement, with (meta)-sedimentary series resting nonconformably over oceanic (ophiolitic) basement.

Eastern Blue Ridge terranes yield a variety of allochthonous igneous and high-grade metamorphic rocks, including numerous granite bodies. A minor portion of these rock units were already metamorphosed, originally belonging to the Precambrian basement, others were volcanic and sedimentary rocks deposited partly on continental and partly on oceanic crust during the Iapetan closure in the early Paleozoic. Rocks as quartzites and migmatites testify the high temperatures reached during the metamorphic phase that interested the eastern Blue Ridge during the late Proterozoic. Partial melting in this phase led to the intrusion of several granitic plutons now constellating the region.

The **Piedmont area**, though broadly constituted by the same rock types of the Blue Ridge, is characterized by milder relief shapes and is bounded to the E by the Fall line and to the NW by the Brevard fault zone. NE trending and SE dipping, the Brevard fault is a mylonitic and cataclastic splay of the major flat decollement underlining the allochthonous crystalline units of both the Blue Ridge and the Piedmont (Cook, 1983; Dallmeyer et al., 1986; Carrigan et al., 2003). According to seismic reflections, the deep structure of the Piedmont consists of a thin nappe that was thrust a great distance from the SE onto the North American continent. Major, long inactive fault zones striking mostly NE divide the Piedmont into several belts and blocks, that were either defined basing on the

metamorphic grade, or on tectonic boundaries, thus setting confusion on the descriptive attempts of the area (e.g. from NW to SE: Inner Piedmont block, Kings Mountain Belt, Charlotte Belt, Milton Belt, Carolina Slate Belt). A different approach to the geologic outline of the Piedmont starts from the physiographic observation of the relief variance across the province: the higher relief Inner Piedmont to the west (more resistant metamorphics alternate with more erodible lithologies to form the monadnocks), and the lower relief Outer Piedmont to the east (Bell et al., 1974). The Inner Piedmont block is a composite stack of thrust sheets containing gneisses, schists, amphibolites, sparse ultramafic and granitic bodies. The Outer Piedmont is instead an upland where indications of the folded bedrock have been obliterated by erosion. In a general view, also the geology of the Piedmont recorded the evolution of eastern North America from the Middle Proterozoic to the Mesozoic. The basement rocks cropping out in the Sauratown Mountains and in other tectonic windows in the Piedmont area show at least two metamorphic phases, a) a Middle Proterozoic, high-grade event associated to the Grenville orogeny and b) a second one, of Paleozoic age, occasionally resulting in late-stage retrogressive metamorphism. In the Western Piedmont an inverted pattern of metamorphic zones can be observed for the Paleozoic phase, in which allochthonous, high-grade (sillimanite-facies) metamorphic units overlie lower-grade (kyanite-facies) rocks. In the Inner Piedmont the thermal peak of regional metamorphism did not affect granitic intrusions aging around 450 Ma (Horton et al., 1989), thus it is constrained to the Ordovician Taconic orogeny, even if its associated anatectic plutonism lingered well into the Silurian. Sediments deposited along the outer continental shelf of the western passive margin of the Iapetus Ocean were folded and metamorphosed during the continental collision phase and now constitute part of the Piedmont rock formations. Granitic intrusions and major amphibolitic metamorphic bodies (ophiolites) occur in these belts, as well as remnants of severely deformed pillow lavas, indicative of submarine extrusions. In particular, the Carolina Slate belt, whose name marks its low metamorphic grade, contains the remains of shallow subvolcanic intrusions, volcanic sediments, and extrusive rocks, typical of the explosive volcanism and hydrothermal activity of volcanic island systems. In this subregion long, narrow rift valleys started forming from the Carnian (Olsen et al., 2003). These Triassic basins are filled with the sandstones and siltstones of the Newark Supergroup, of lacustrine and fluvial environment. Intercalated with these continental sediments are basaltic flows of the Central Atlantic Magmatic Province, cropping out in several of these basins, not only restricted to the Piedmont

area. Diabase dyke swarms crop out instead in the Piedmont and the Blue Ridge areas, constituting the sampling regions of this work.

Marking the eastern border of the Piedmont area and its transition to the Coastal Plain, the **Fall Line** is a low east-facing cliff paralleling the Atlantic coastline from New Jersey to the Carolinas. It separates the hard Proterozoic and Paleozoic metamorphic rocks of the Appalachian Piedmont to the west from the softer Mesozoic and Tertiary sedimentary series of the Coastal Plain. This erosional scarp was thus named after the alignment of many rapids and waterfalls it marks.

The wide **Coastal Plain** belt, extending from New Jersey to Texas, encompasses Triassic to Holocene deposits. Coastal Plain sediments overlap the Paleozoic and Precambrian basement rocks (Dennis et al., 2003) cropping out immediately to the north and west, and occurring deeper and deeper toward the south and east, reaching depths of up to 3000 m b.s.l. beneath the modern Georgia coast. Coastal Plain sequences, then, essentially form a large, wedge-shaped body, which is thickest along the modern Atlantic coast and the Florida state line and thinnest along the edge of the Fall Line. These sedimentary sequences were later uplifted and tilted, and now dip seaward (part of them forming the broad Atlantic continental shelf). Due to their attitude, the oldest Coastal Plain rocks are on the proximity of the Fall Line, and outcropping sediments grow younger eastward. These sediments recorded sea level variations and show that the Coastal Plain was submerged and emerged several times during the last 100 Ma. Marine transgressions are marked by shallow marine sediments, whereas regressive periods were characterized by the deposition of continental sediments, with riverine and floodplains facies. In proximity of the Fall Line, sedimentary facies shift to the ones typical of coastal environments, such as estuaries, deltas, barrier islands, coastal mud flats, and sandy beaches.

The Coastal Plain characteristically alternate basement downwarps called embayments and major upwarps termed arches. The embayments are areas of major subsidence, where the weaker basement could sink under the sediments burden offering more accommodation space and marked by thicker sedimentary strata. The arches are instead areas of stronger basement offering no space to new sediments, and resulting in thinner stratification and reduced sediment thickness. Rift basins opened during the Triassic distensive phase and hosted the deposition of thick layers of coarse red sandstones, conglomerates, shales, and other non-marine sediments. Similar sediment-filled troughs

occurred all along North America east coast, from Georgia to Nova Scotia (Canada).

The Crystalline Appalachians include also the northernmost part of the chain, the **New England Appalachian province** (Ayuso and Bevier, 1991). Late Cambrian-Early Ordovician foundering of the Laurentian passive margin and ophiolite obduction was here followed by Late Ordovician–Devonian collisions between Laurentia and several micro plates (including the Avalon and Meguma terranes) and by the terminal (Alleghanian) collision that formed Pangaea (Dorais et al., 2008). There is evidence that the eastern Avalonian terranes of the New England region have underthrust the central Acadian terranes during the Pennsylvanian-Permian Alleghanian collisional orogeny (the thrust boundary is a ductile shear zone, the Putnam-Nashoba belt). Alleghanian phase constituted essentially a metamorphic event in the New England province, originating plutonism, and a kyanite-facies metamorphism overprinting the Acadian one (of sillimanitic facies). The Meguma terrane, south of the Avalon terrane, consists of a Cambrian-Ordovician continental-rise prism overlain by Late Ordovician bimodal volcanic rocks, and Silurian-earliest Devonian shallow-marine rocks fading upward into continental deposits of Early-Middle Devonian age (Schenk, 1997). The onset of the Acadian orogeny (c. 410 Ma) was associated with oblique convergence between Avalon and Meguma terranes during or following the collision of the Meguma terrane with Laurentia (Clarke et al., 1997; Murphy et al., 1999). Polyphase deformation and regional metamorphism within Meguma terrane rocks testify this event. Moreover, Silurian arc-related magmatism in adjacent Maine and New Brunswick suggests the existence of a northward-dipping subduction zone at that time.

The **Adirondack Mountains**, a roughly circular dome about 200 km in diameter in northern New York State surrounded by the Carthage-Colton Mylonite Zone, are a main subregion of the New England Appalachian domain, and represent a tectonic window exposing older, Grenvillian terranes (McLelland et al., 2010). A Tertiary tectonic phase uplifted the area, leading to erosive removal of the metasedimentary and metavolcanic late Proterozoic and sedimentary Paleozoic covers. The Grenvillian continental basement thus crops out in the Adirondacks, with lithologies varying from metasediments (marbles, quartzites, paragneisses), metavolcanics and metaplutons (granitic gneisses, metanorthosites, metanorites).

Differences in the geologic evolution of the northern and southern part of the Appalachians are thoroughly depicted in the recent reviews by Hibbard et al. (2010) and Hatcher (2010).

Northern Appalachians extend farther northward to Canada. Newfoundland Appalachians will summarize this long geological history through their three main subregions. The Humber Zone to the W, that constitutes the North American continental margin; the Central Mobile Belt, containing various tectonic units associated with the formation and destruction of Iapetus Ocean, and the Avalon terrane that is an accreted continental block that flanked the southern side of Iapetus (Cawood, 1994; Van Der Pluijm et al., 1990).

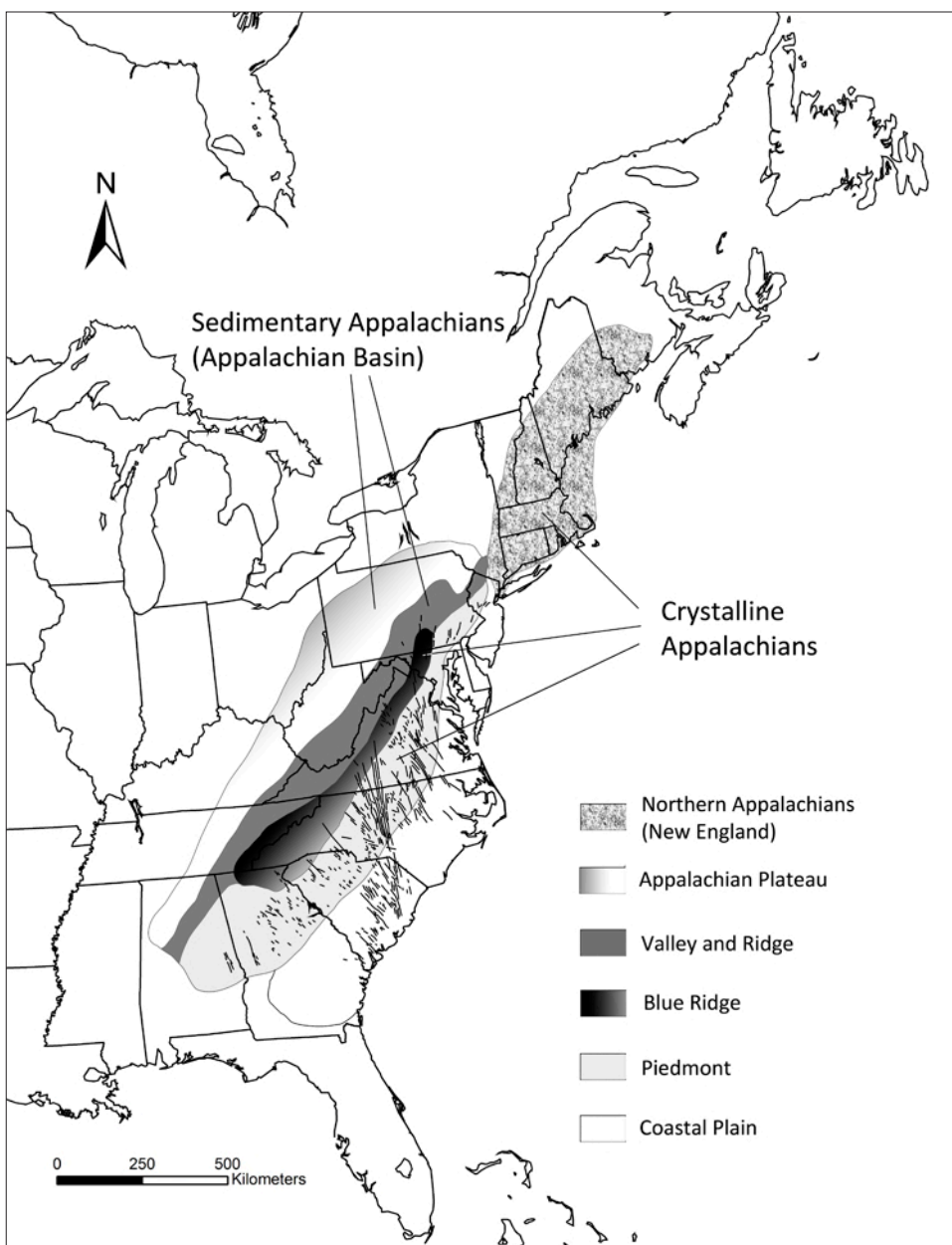


Figure 2.4: Physiographic domains of the Appalachians (modified after Holm-Denoma and Das, 2010). Eastern North American CAMP dykes are shown in black (after Ragland, 1983).

3 SAMPLING

Seventy-four samples were collected along the Piedmont area of Georgia, South Carolina, North Carolina and Virginia (USA), following previously published maps of the dyke swarms and sills, obtained prevalently from aeromagnetic surveys (e.g. Burt et al., 1978; Ragland et al. 1983). Given their magnetic properties, many of these dykes have been discovered with airborne and ground magnetometer surveys both in the subsurface of the Coastal Plain and in Piedmont outcrops (e. g. Bell et al., 1974; Popenoe e Zeitz, 1977; Fig. 3.1). Previously $^{40}\text{Ar}/^{39}\text{Ar}$ dated dykes (Hames et al., 2000; Beutel et al., 2005; Nomade et al., 2007) were re-sampled and the sampling was extended to as much dykes and sills as possible in the surroundings. The sampling strategy consisted in sampling dykes of all the different orientations even if scarce and difficult outcropping of these magmatic bodies represented a major hinder to the measurement of the dykes trend. A very limited number of dykes and sills were observed in clear outcrops where trend, thickness and, if present, petrographic variations were recognizable. More samples per site were collected where the good outcrop exposure allowed the macroscopic recognition of different petrofacies or textures. All the directly sampled rocks are intrusive, i.e. a sill was sampled in the Durham basin area (the Durham sill; Ackerman et al., 1976), while all the other sampled bodies were sub-vertical dipping (as confirmed by field observation and symmetrical ground magnetic profiles), variously trending dykes (e.g. Ragland et al. 1983).

The sampled eastern North America diabase dykes vary in thickness from few decimetres to several tenths of meters (Pageland dyke reaches a thickness as high as 150 m), and show maximum elongation of 250 km (King, 1961; Ragland et al., 1983; McHone, 1996). Initially, a radial pattern was recognized (King, 1961) observing the directions of these dykes, as they vary in trend from NW (N 10° - 30° W) in the South, to N-S, to mostly NE (N 30° E) in the North. Minor occurrences of E-W dykes are also reported (and were sampled). Though previously considered the upwarping effect of a mantle plume emplaced under the Carolinas (De Boer and Snider, 1979), recent geochronological and paleomagnetic studies link this different trends to a rapidly changing stress field (Beutel et al. 2005). Cross-cutting relationships and paleomagnetic data show that the N-S swarm is slightly

younger (Smith and Hare, 1983; Ragland et al. 1983; Beutel et al. 2005). All dykes cropping out in Georgia and most of those from South Carolina are NW trending, whereas moving northward also dykes of N-S and NE directions were sampled in North Carolina and Virginia, with the NW trend remaining the most frequent. This pattern in dykes orientations was recognized by Ragland et al. (1983), and in particular, he described four directional domains in the Piedmont area of North Carolina, proceeding roughly from SW to NE, i.e. domain I, dominated by NW trends; domain II, N-S dominated, with dykes radiating northward into Virginia and converging southward under the Coastal Plain; domain III, NW dominated with some minor N-S trends and domain IV, NW dominated. Dykes apparently occur in tight sets alternated by areas with low density of dykes (Bell, 1988), a feature that is confirmed by aeromagnetic surveys, thus not representing merely a mapping bias. No straightforward explanation for this distribution exists yet, but several hypotheses have been presented, either dealing with the structural concept of dykes being emplaced along inherited weakness zones, or with alternating brittle and ductile behaviours in the lower crust, or with more lithologically resistant crustal plutons controlling dykes trends (Ragland et al., 1983). An evident example of this juxtaposed different dyke densities is observed in correspondence of the well developed Pageland dyke, which shows few smaller satellite dykes in its direct proximity, but no other important dyke for broad areas on each side. In any case, regardless these regional scale differences in dyke density, with respect to the entire CAMP, eastern North America presents one of the largest and densest dyke swarms of the province.

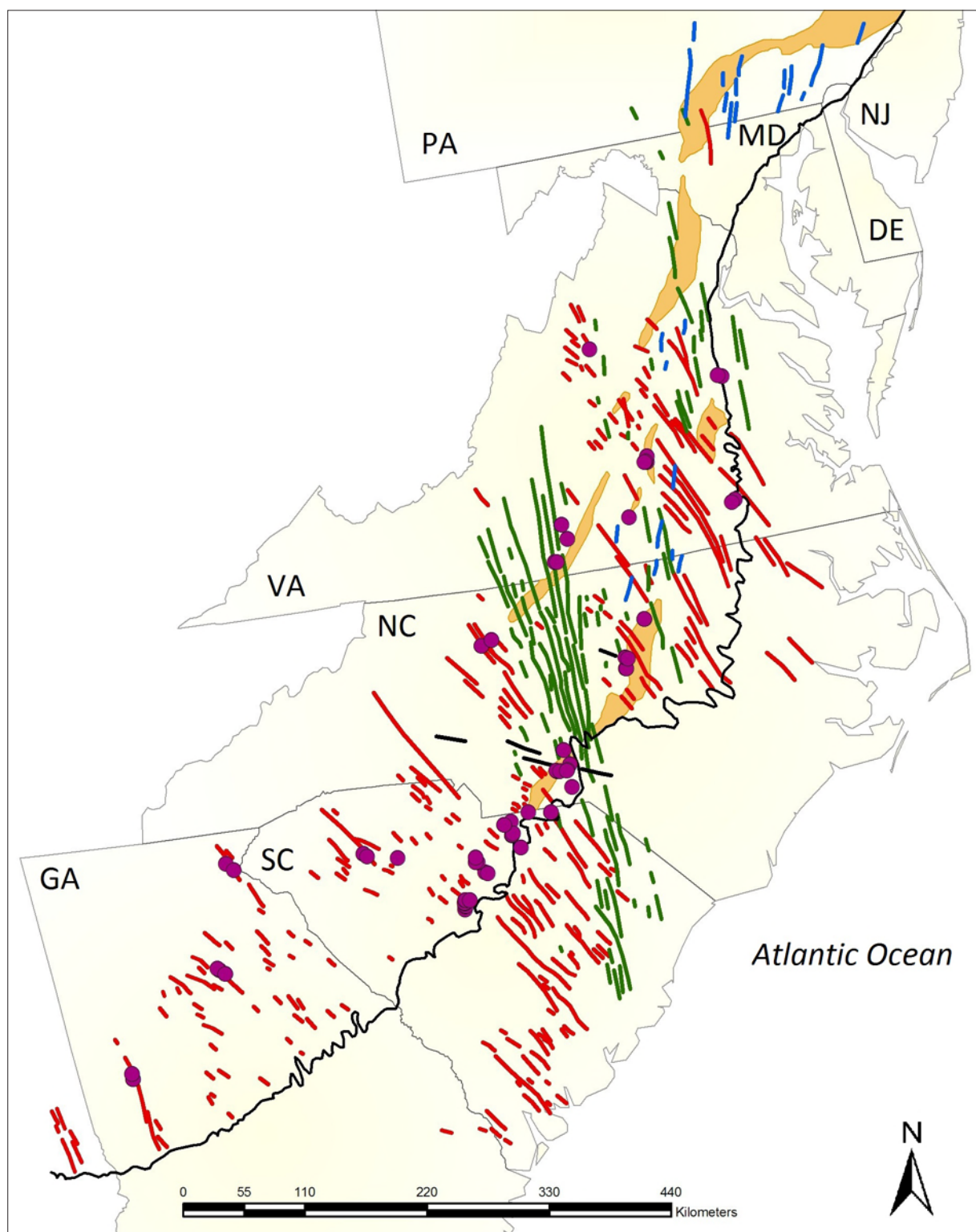


Figure 3.1: Sample sites (purple dots) plotted on an overview map of the eastern North America diabase dyke swarm as it results from the compilation of Ragland et al. (1983), based on aeromagnetic mapping (King, 1961). NW-trending dykes were color coded in red, N-S in green, NE in blue and E-W in black. Triassic rift basins indicated as orange outlined areas. Black line marks the limit between Appalachian Piedmont area (NW) and Coastal Plain (SE).

4 MAJOR ELEMENTS

XRF (WDS Philips PW2400) analyses for major elements were performed on 74 samples at the University of Padova. SiO_2 (46.2-54.3 wt%) and $\text{Na}_2\text{O}+\text{K}_2\text{O}$ (1.2-4.3 wt%) contents classify the sampled ENA dykes and sill as basalts and basaltic andesites (Le Maitre et al. 1989; Fig. 4.1) while CIPW-normative compositions (either Olivine/Hypersthene, Ol-Hy-, or Quartz, Q-normative) define their sub-alkaline character. On an AFM plot (Irvine and Baragar, 1971) all the samples fall on the tholeiitic compositional field (Fig. 4.2).

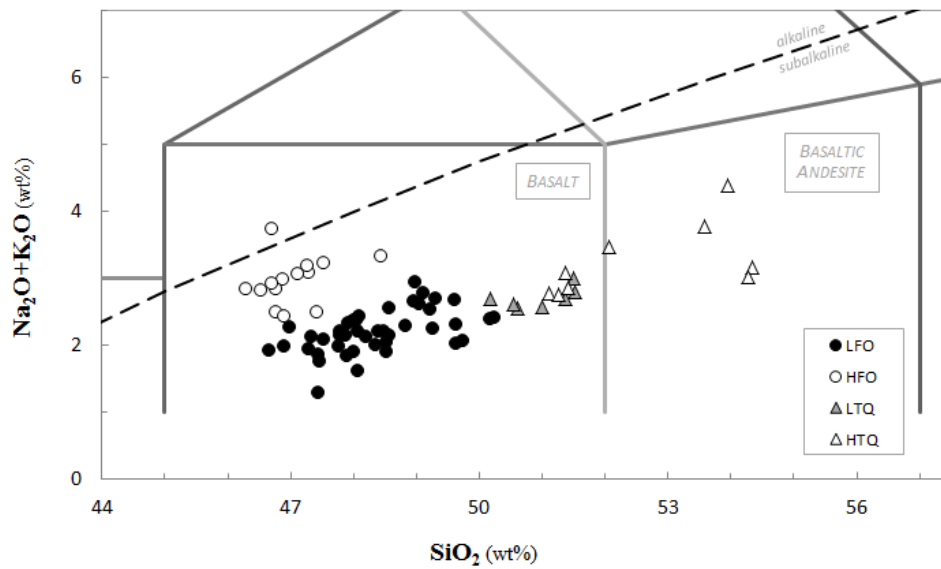


Figure 4.1: Total Alkali versus Silica (TAS) classification diagram of the 74 sampled ENA dykes and sills. Grey lines mark the boundaries between compositional fields as in LeMaitre et al. (1989). The black dashed line separating alkaline from subalkaline compositions is drawn after Irvine and Baragar (1971).

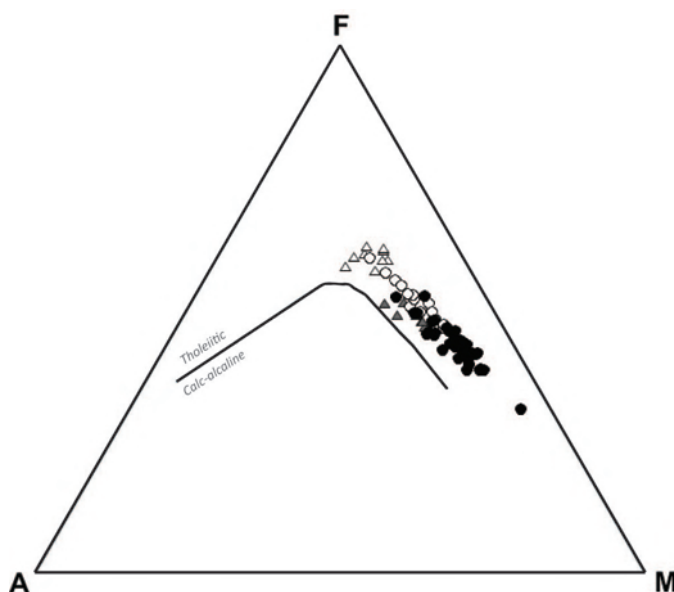
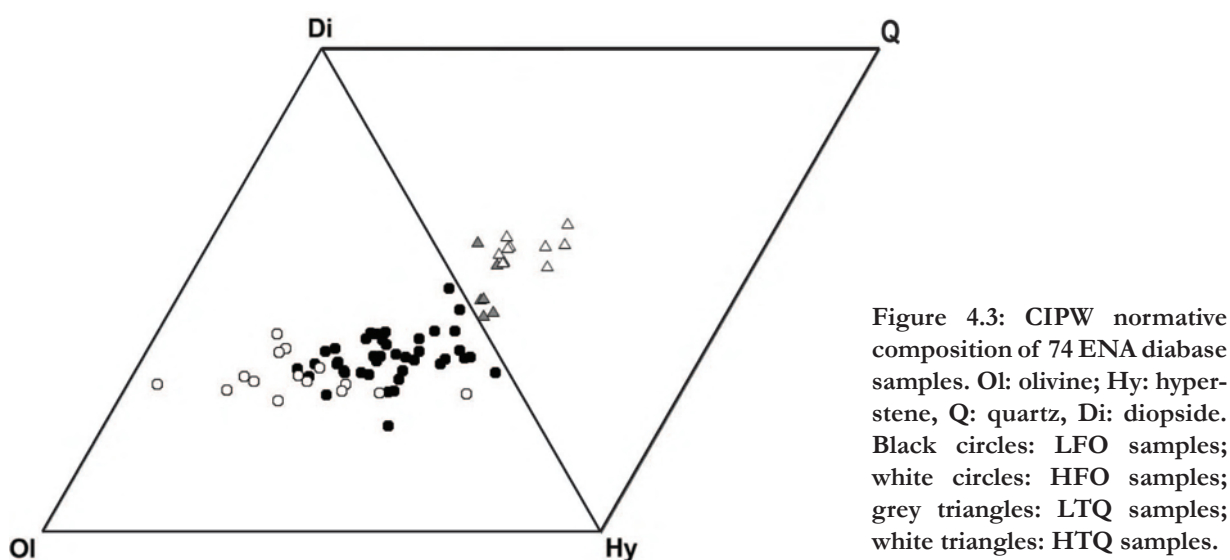


Figure 4.2: AFM diagram with A marking the total-alkali content, F the total iron expressed as FeO, and M the MgO content. All 74 samples plot on the tholeiitic compositional field (boundary between tholeiitic and calc-alkaline series drawn after Irvine and Baragar, 1971). Black circles: OLN samples; grey circles: LTQ samples; white circles: HTQ samples.

A wide range in MgO (16.9-4.7 wt%), Al₂O₃ (12.9-18.6 wt%) and TiO₂ (0.36-1.35 wt%) contents is observed, with Mg numbers [$Mg\# = 100 * Mg / (Mg + Fe^{2+})$, Fe^{2+} being $0.87 * Fe_{tot}$] varying from 77.3 to 43.4. (Fig. 4.3, Tab. 4a. In general, Ol/Hy-normative rocks are higher in MgO and lower in SiO₂ compared to Q-normative ones. Ol/Hy-normative rocks appear to be split into two groups, defined by their distinct Fe₂O₃ contents: low-Fe olivine normative samples (hereafter, LFO) yield less than 13 wt% Fe₂O₃, while high-Fe samples (HFO) show more than 13 wt% Fe₂O₃. Similarly, a further subdivision of the quartz -normative group is established considering TiO₂ contents, that is, rocks with less than 1.00 wt% TiO₂ are classified as low-Ti quartz normative (LTQ), while rocks yielding more than 1.00 wt% TiO₂ are high-Ti quartz normative (HTQ). The differences among the four groups are well highlighted also by the SiO₂ vs Fe₂O₃ diagram of Fig. 4.4 e.



However, all the sampled rocks can be classified as low-Ti tholeiites ($TiO_2 < 2$ wt%; e.g. Marzoli et al., 1999), with TiO₂ showing no correlation with MgO in the quartz-normative and in the LFO samples, while HFO rocks, enriched in Ti with respect to LFO, show a neat negative co-variance of TiO₂ with MgO. Very limited overlap is observed between the four chemical groups in a TiO₂ vs MgO plot (Fig. 4.4 a). SiO₂ varies between 46.3-54.3 wt% and shows no clear correlation with MgO for the olivine normative samples. Rocks of the HFO group appear depleted in SiO₂ with respect to the LFO ones. A rapid increase in SiO₂ with decreasing MgO is observed for quartz-normative ENA diabases, which are clearly higher in SiO₂ compared to olivine-normative ones (Fig. 4.4 b). CaO varies significantly (7.7-12.1 wt%), showing a shallow negative correlation with MgO in LFO samples, and a relative depletion in HFO samples, that in turn do not plot in any co-varying trend

in the CaO-MgO space. HTQ samples broadly follow the negative trend on the Ca-rich end member of LFO array. Conversely, LTQ diabases are aligned to form a steep positive correlation at generally lower CaO and MgO contents (Fig. 4.4 c).

LFO, HFO and LTQ samples are aligned along a negative trend in a Al-Mg variation diagram, i.e. Al_2O_3 increases with decreasing MgO. HTQ rocks instead cluster at significantly lower Al_2O_3 (12.9-14.1 wt%), and low MgO (Fig. 4.4 d). Total iron expressed as Fe_2O_3 is negatively correlated with SiO_2 for olivine-normative samples. The gap in data distribution around 13 wt% Fe_2O_3 suggests the distinction between low-Fe and high-Fe olivine normative samples. HFO samples plot on the high- Fe_2O_3 , low- SiO_2 end-member of the olivine-normative compositional array. LTQ samples parallel the trend described by the OLN, plotting on its high SiO_2 side. Totally separated from the olivine-normatives compositional field, the HTQ samples plot at higher Fe_2O_3 and SiO_2 values (13.7-16.3 wt% and 46.4-48.4 wt%, respectively), defining a linear negative trend, shallower than that shown by the olivine normatives (Fig. 4.4 e).

HFO rocks define a linear positive array shifted to higher alkali content on the TAS diagram (Fig. 4.1), though remaining within the tholeiitic compositional field. This higher alkalinity of the HFO samples is given by an enrichment in Na_2O content (total range 3.21-1.20 wt%; Fig. 4.4 f). A clear negative correlation between Na_2O and MgO is shared by LFO and LTQ groups, while HFO data points plot in a more scattered, negatively correlated cluster, shifted to higher Na_2O contents. HTQ rocks show different Na_2O composition at broadly constant low MgO. K_2O ranges between 0.08 and 0.89 wt% in the sampled ENA diabases (Fig. 4.4 g), lower values belonging to olivine normative samples and higher ones to quartz-normative. A good overlap is visible between LFO and HFO, thus K appears not to contribute to the higher alkalinity of the latter group. If the entire dataset is observed, a broad and scattered negative correlation between K_2O and MgO is observed accounting for the incompatibility of K, but co-variations are not visible for each of the different chemical groups. Slightly less incompatible, P (expressed as P_2O_5) ranges between 0.03 wt% and 0.27 wt% (Fig. 4.4 h). In a P_2O_5 vs MgO diagram, a shallow negative correlation is shown by the olivine-normative samples and by LTQ rocks. On the contrary, HTQ samples yield a significant scatter in P_2O_5 at nearly constant, low MgO values.

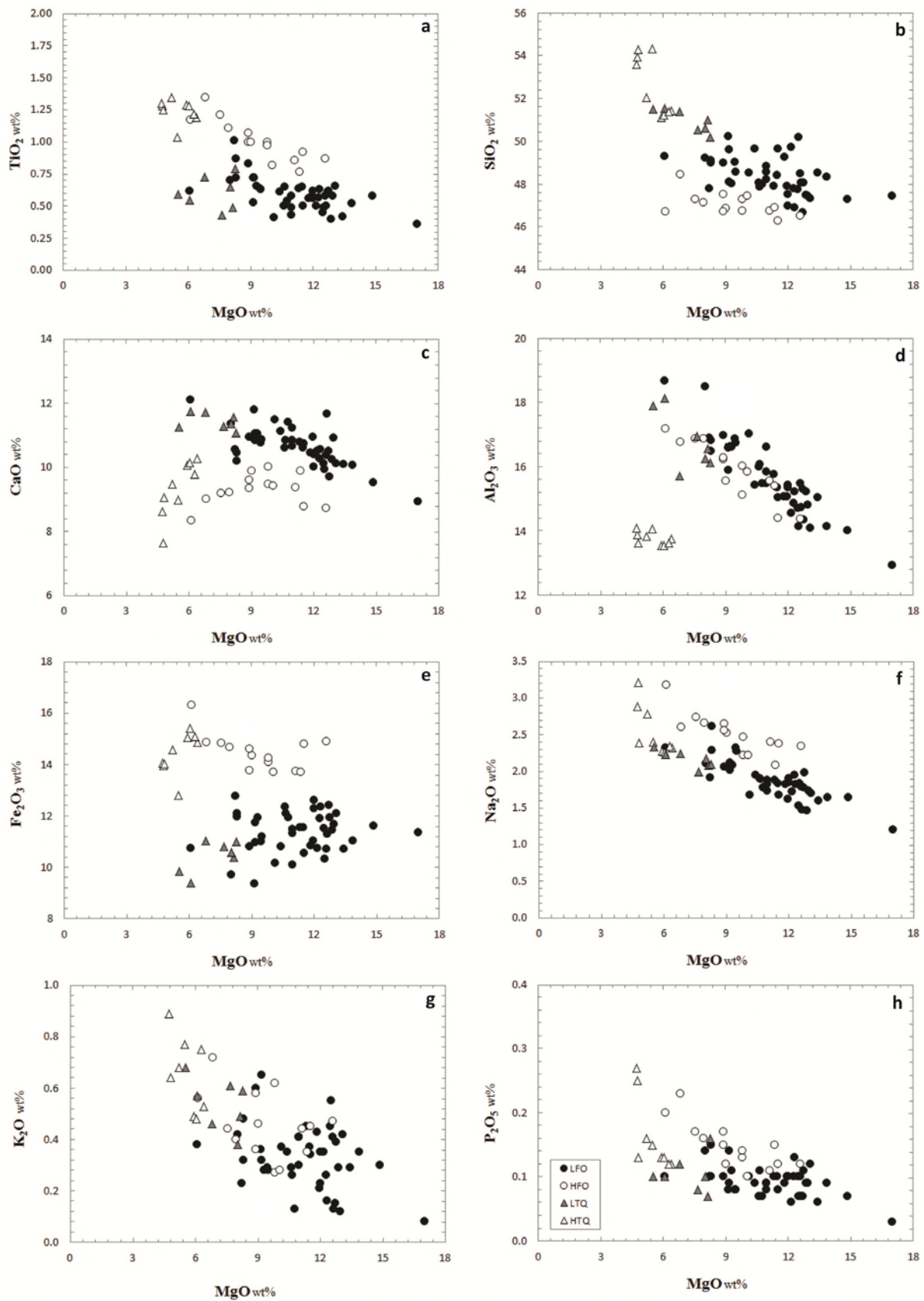


Figure 4.4, a-h: Major elements variation diagrams for 74 ENA diabase samples. Black circles: LFO samples; white circles: HFO samples; grey triangles: LTQ samples; white triangles: HTQ samples.

5 COMPATIBLE TRACE ELEMENTS

Compatible trace elements were analysed with XRF (WDS Philips PW2400) at the University of Padova for all the 74 sampled rocks.

A strong positive linear correlation with MgO is observed for Ni (varying from 747 to 10 ppm), and it is shared by all the four chemical groups (Fig. 5.1 a). Cr instead ranges between 1983 and 22 ppm and behaves differently depending on the normative character of the samples (Fig. 5.1 b). LFO rocks show a steep linear correlation between Cr and MgO. Less steep is the positive correlation trend described by HFO samples. Quartz-normative samples define two even shallower, parallel trends, the LTQ one yielding the higher Cr contents and the HTQ the lower (lowest within all the data set). No correlation is observed between V and MgO for olivine-normative and LTQ samples (Fig. 5.1 c), which show a restricted variability in V (157-264 ppm) for different MgO contents. Two anomalous HFO samples however plot apart from this main group, at low V (79 and 136 ppm). HTQ rocks cluster at distinctly higher V (379-433 ppm) and low MgO (4.76-5.93) showing absolutely no overlap with the former group. A Sc versus MgO variation diagram (Fig. 5.1d) separates efficiently quartz- and olivine-normative samples, the former describing a large variation of Sc (19-53 ppm) at near-constant MgO, and the latter forming a scattered cluster (8-36 ppm). In particular, LFO samples show no correlation at all between Sc and MgO, while HFO data points are aligned (not without some scatter) in a trend of positive co-variation. Quartz normative samples, taken as a whole, draw a steep negatively sloping trend in which a small decrement in MgO is accompanied by a significant increase in Sc. Precisely, this behaviour is mostly shown by HTQ samples, while LTQ ones do not describe any clear trend.

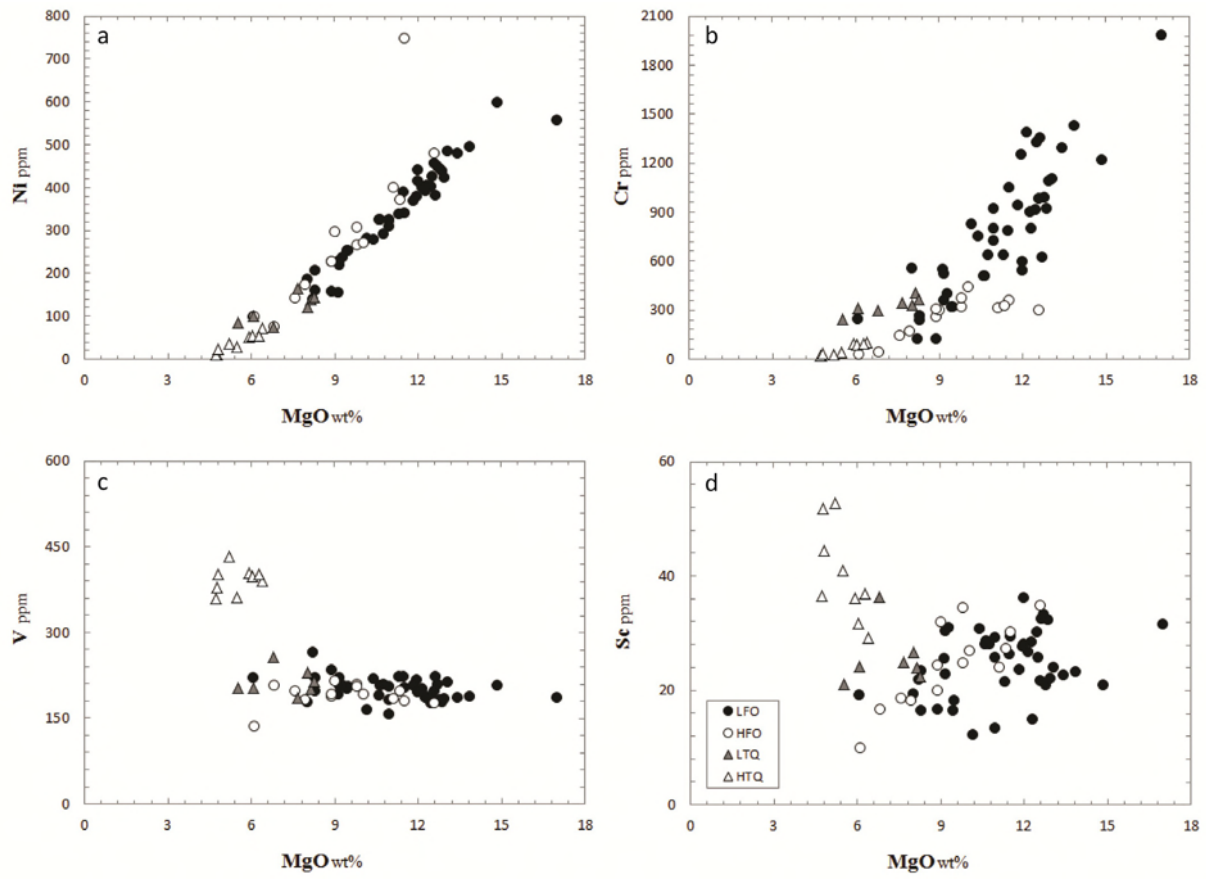


Figure 5.1 a-d: Compatible trace elements variation diagrams plotted versus MgO for 74 ENA diabase samples.

6 INCOMPATIBLE TRACE ELEMENTS

Trace elements were measured on 39 whole rock samples by ICP-MS at the Washington State University laboratory. Normalized to primitive mantle compositions (Sun and McDonough, 1989) and plotted on spidergrams (Fig. 6.1), ENA diabases display moderately enriched incompatible elements (IE), comparable with E-MORB compositions (Sun and McDonough, 1989). A considerable spread in primitive mantle-normalized compositions is observed for different samples, but all the rocks broadly share similar trends. No pronounced differences in compositions are observed between quartz- and olivine-normative, with the only exceptions of Rb, Th, U, Nb e Ta being significantly more depleted in ol/hy-normative rocks. All the samples share some common IE features such as negative Nb, Ta and Ti anomalies (Nb/Nb^* : 0.25-0.89, Ta/Ta^* : 0.26-0.74, calculated as deviation from the trend between K and La; Ti/Ti^* : 0.46-0.71, calculated between Tb and Dy). The vast majority of the samples display as well a positive Pb anomaly (Pb/Pb^* : 0.91-2.88, calculated as deviation from the trend between Ce and Sr). Though broadly similar in concentrations, E-MORB differ profoundly from ENA diabases with regard to these anomalies, as they in turn display positive Nb and Ti anomalies and negative Pb anomaly (e.g. McDonough and Sun, 1989). The widest compositional variation is shown by Th and U, ranging between respectively 1.6-35 and 1.3-40 times the concentration in the primitive mantle.

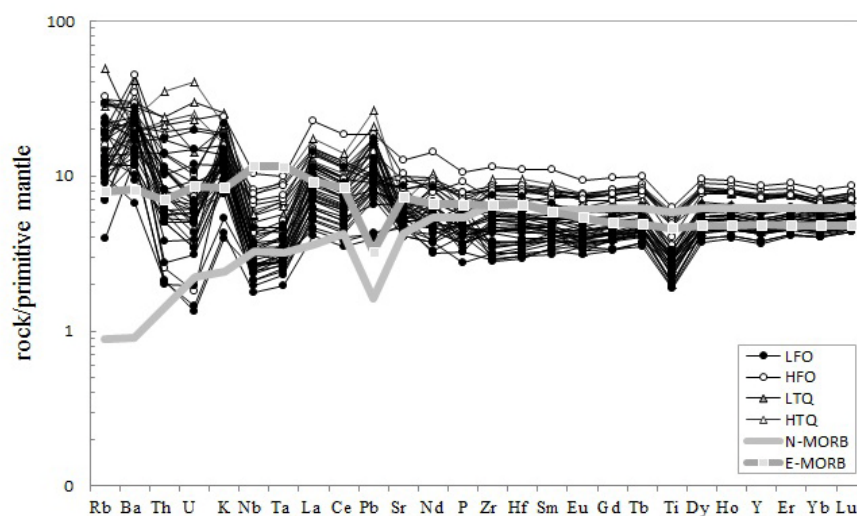


Figure 6.1: Spider diagram showing primitive mantle normalized (Sun and McDonough, 1989) incompatible trace elements contents for 39 ENA CAMP sampled tholeiites. I.E. are ordered on the x-axis for increasing compatibility in basaltic systems from left to right. For comparison, N-MORB and E-MORB compositions are shown (data from Sun and McDonough, 1989).

Rocks from each chemical (normative) group share very similar IE compositions, showing narrow ranges in IE contents and similar patterns. Along with their more evolved character, quartz-normative samples yield higher IE contents. HTQ rocks show the most uniform and slightest Ti/Ti* negative anomalies among the entire dataset (Fig.6.3). HFO samples are slightly more I.E. enriched with respect to LFO samples.

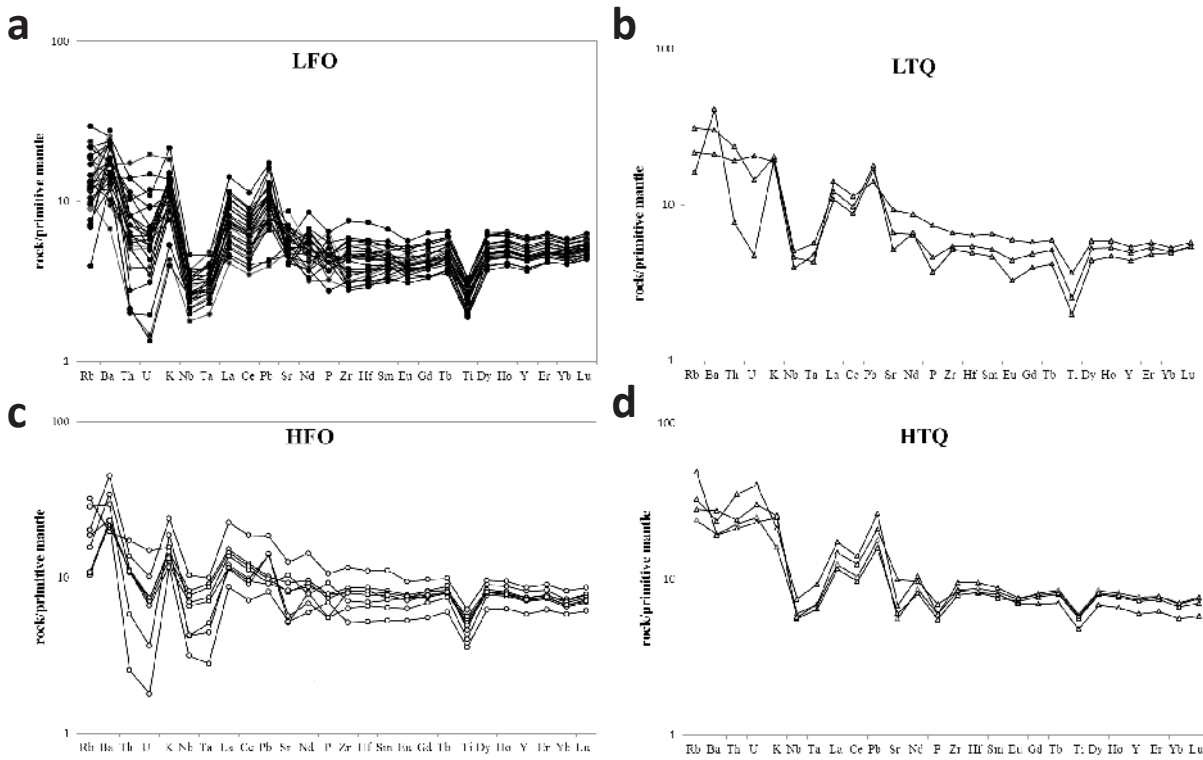


Figure 6.2 a-d: Spider diagrams showing primitive mantle-normalized (Sun and McDonough, 1989) incompatible trace elements contents for a) LFO, b) HFO, c) LTQ and d) HTQ samples. Incompatible elements are ordered on the x-axis basing on increasing compatibility in basaltic systems from left to right.

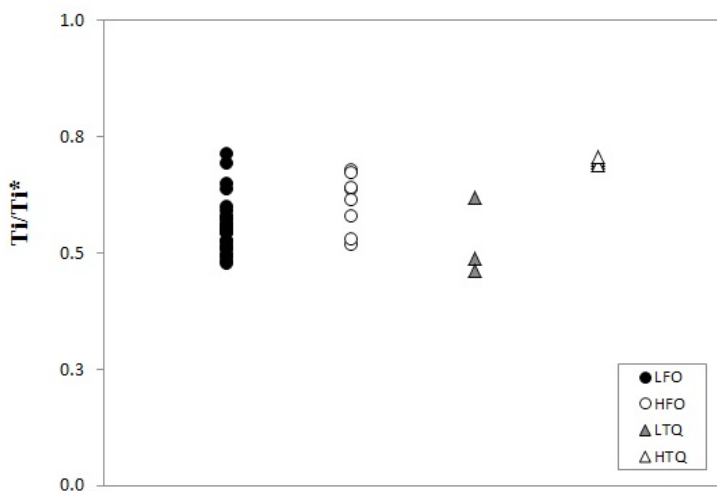


Figure 6.3: Ti negative anomaly displayed for each sample from the four different normative-groups.

Rare Earth Elements (REE) concentrations are moderately enriched compared to chondritic values (McDonough and Sun, 1995) and their patterns range from poorly fractionated to depleted (i.e. La_{Ch}/Yb_{Ch} : 0.54-2.60; La_{Ch}/Sm_{Ch} : 1.18-2.53; Sm_{Ch}/Yb_{Ch} : 0.42-1.40). Broad overlap exists between REE patterns of quartz- and olivine-normative ENA diabases, but with the quartz-normatives yielding generally both more enriched compositions and the most fractionated patterns (Fig. 6.4).

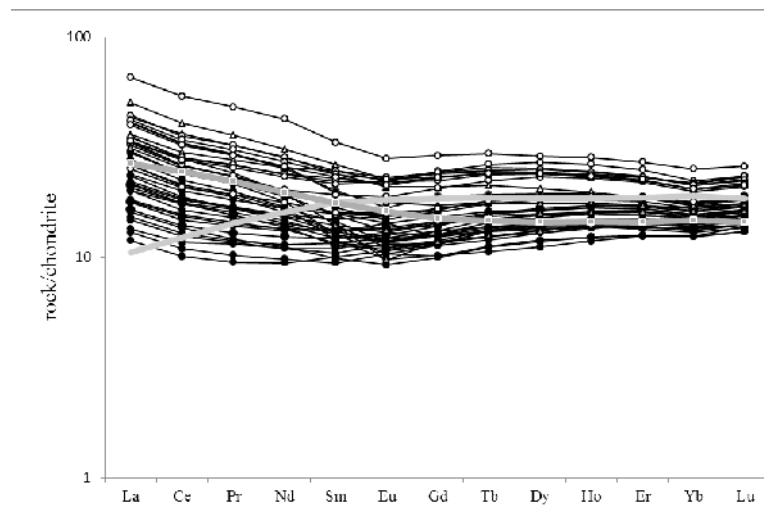


Figure 6.4: Spider diagram displaying chondrite-normalized (McDonough and Sun, 1995) REE contents for 39 ENA CAMP sampled tholeiites (black lines). For comparison, N-MORB and E-MORB compositions from Sun and McDonough (1989) are shown.

Again, REE patterns and contents are very uniform within each normative group, showing poorly fractionated LREE/MREE trends and nearly flat HREE/MREE.

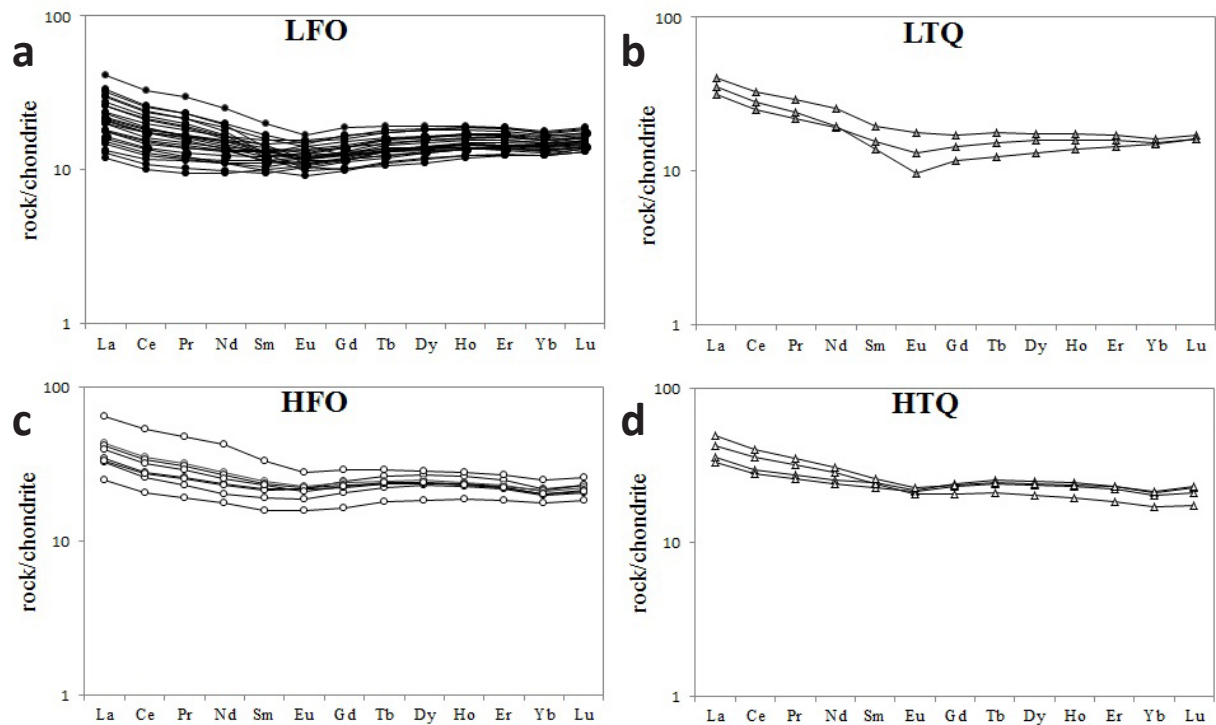


Figure 6.5 a-d: Spider diagrams showing chondrite-normalized (McDonough and Sun, 1995) REE contents for a) LFO, b) HFO, c) LTQ and d) HTQ samples.

No conspicuous either positive or negative Eu-anomaly is observed (Eu/Eu^* : 0.85-1.13), with the only partial exception of sample CS77 (Eu/Eu^* : 0.76). No link exists between Al_2O_3 content, degree of evolution or CIPW-normative character and Eu-anomalies (Fig. 6.6 a and 6.6 b), arguing against a significant control of plagioclase fractionation (cf. De Paolo and Sims, 1997).

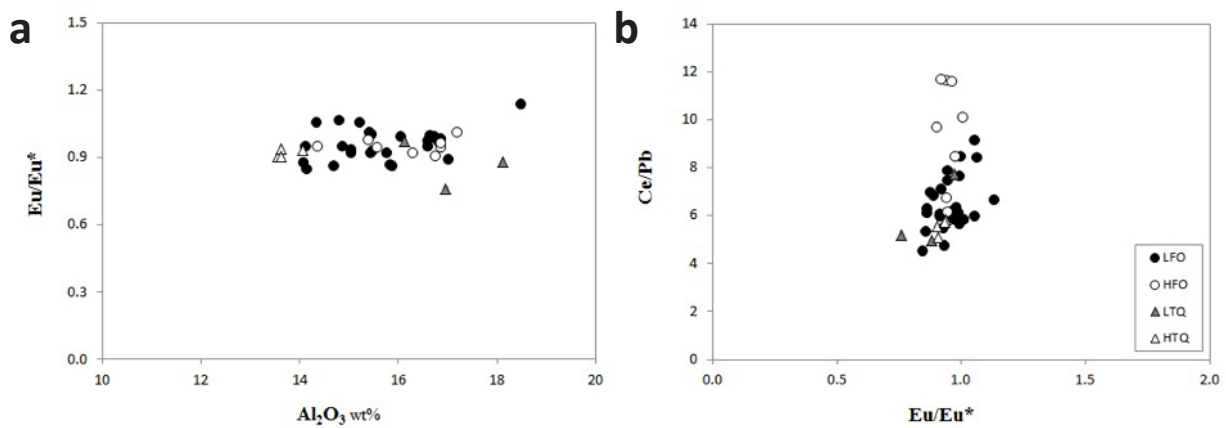


Figure 6.6 a-b: Variation diagrams of Eu anomalies (Eu/Eu^*) plotted against Al_2O_3 wt% (a) and Ce/Pb (b).

6.1 INCOMPATIBLE TRACE ELEMENTS RATIOS

Observations on incompatible elements ratios can help constraining the mantle source of the ENA tholeiites, as well as correlating dykes and sills from the Southern part of the ENA province with the CAMP lava flows cropping out in the northern ENA.

On a La/Yb versus La (7-65 ppm) diagram (Fig. 6.7 a), all the samples trend along positive arrays, but LFO and LTQ samples more steeply than HFO and HTQ ones (which in turn reach the highest La contents). La/Nb is positively correlated with La for LFO samples, whereas the other normative-groups are all overlapped and plot along a scattered and broadly negative trend (Fig. 6.7 b). HFO samples show rather stable La/Yb compositions at varying La contents

The same general pattern is obtained for, respectively, Zr/Y vs Zr and Zr/Nb vs Zr: while in the first diagram all the samples broadly plot along the same positively correlated trend, the second marks a distinction between LFO samples and the other three normative groups (Fig. 6.7 c-d).

U (ppm) plotted against La content (ppm) shows two differently sloping positive arrays of LFO samples. The steeper array continues with HTQ samples, which fall in the high-U, high-La area of the diagram, whereas the second array, much shallower, is continued by HFO samples (Fig. 6.7 e).

Limited overlap is shown between LFO and HFO samples in a Ce/Pb vs Ce diagram, LFO samples clustering rather tightly on the low-Ce, low-Ce/Pb quadrant, and HFO samples plotting more dispersedly on the high-Ce/Pb, high-La portion of the diagram. Contrarily, LTQ and HTQ samples show a broad overlap, both resting on a relatively low-Ce/Pb, high-Ce field (Fig. 6.7 f).

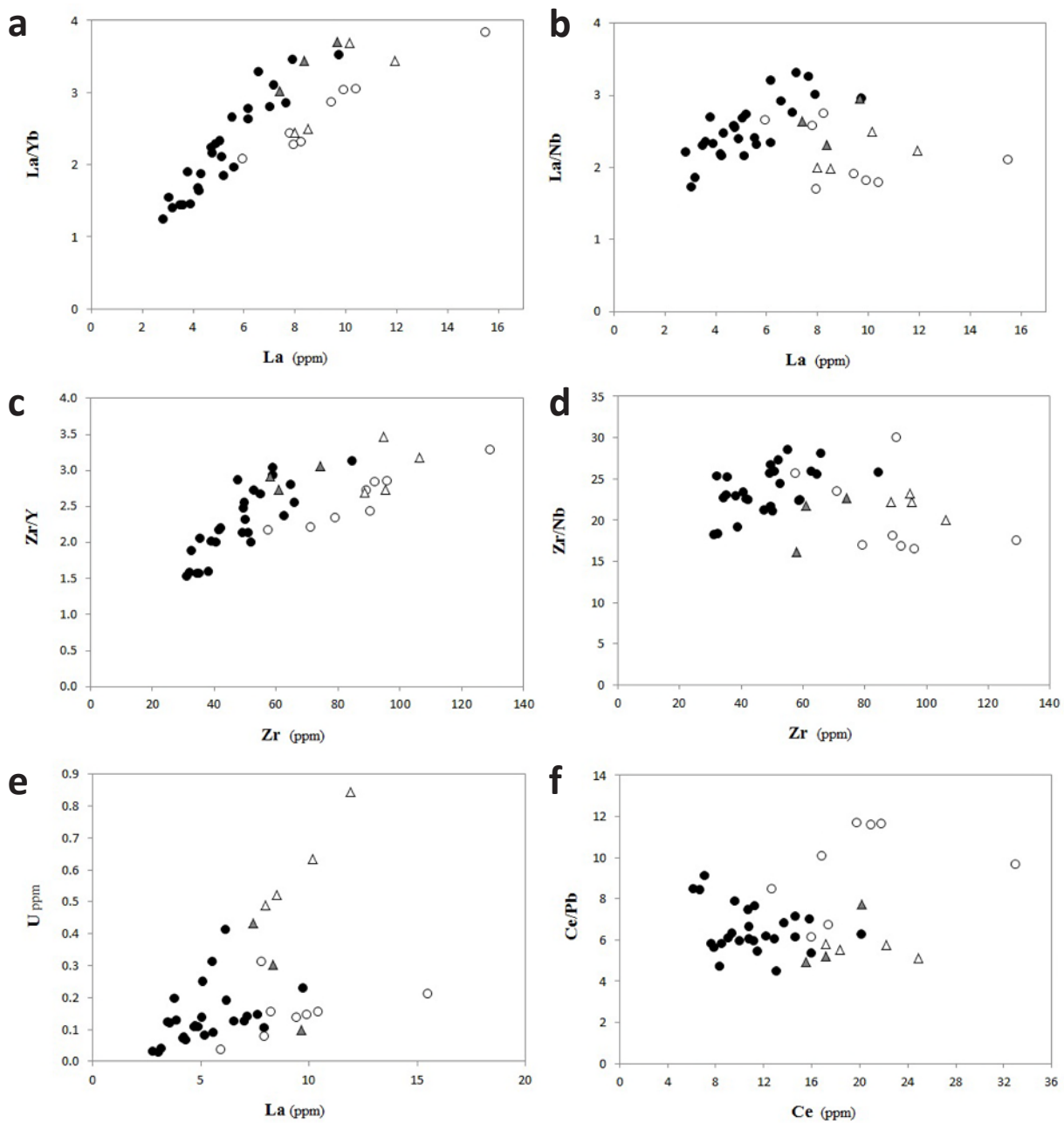


Figure 6.7 a-f: Variation diagrams between incompatible elements ratios and incompatible elements (a: La/Yb vs La; b: La/Nb vs La; c: Zr/Y vs Zr; d: Zr/Nb vs Zr; e: U vs La and f: Ce/Pb vs Ce).

Plotting IE ratios vs MgO (wt%) clearly allows to distinguish Q-normative samples from Ol/Hy-normative ones. Plots of Th/Nb, Th/Ce and U/Pb vs MgO (wt%) show consistently that all Q-normative samples (except CS44) cluster tightly on a high-IE ratio, low-MgO position. HFO samples display a reduced variability in IE ratios, with respect to LFO samples, which yield the widest range in IE ratios values (Fig. 6.8 a-c). On the contrary, in the Th/U versus MgO space, quartz-normative samples plot on the low-IE, low-Mg quadrant. HFO samples are enriched in Th/U with respect to LFO ones (Fig. 6.8 d).

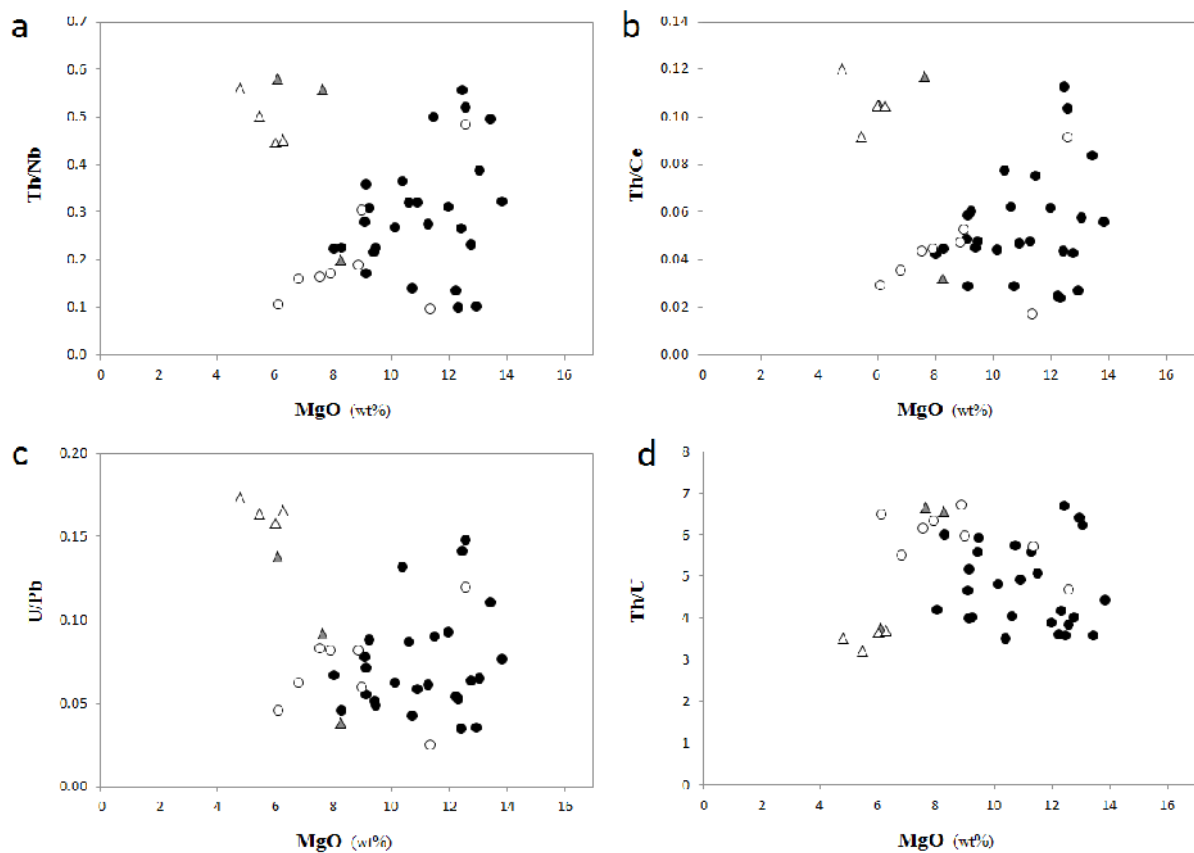


Figure 6.8 a-d: Variation diagrams between incompatible elements ratios and wt% MgO. a: Th/Nb vs MgO; b: Th/Ce vs MgO; c: U/Pb vs MgO; d: Th/U vs MgO.

7 ISOTOPES

7.1 METHODS

Isotopic analyses for Sr, Nd and Pb were carried out on a subset of 24 whole rock samples at the University of Geneva (on a Thermo Finnigan Triton TIMS). All the isotopic ratios were back corrected to initial values using a 200 Ma age, and starting from trace elements contents obtained by ICP-MS (at the Washington State University laboratory).

$^{87}\text{Sr}/^{86}\text{Sr}_{\text{measured}}$ ratios vary between 0.704719-0.710105. Initial ratios were calculated using the decay-ing equation:

$$(^{87}\text{Sr}/^{86}\text{Sr})_{200\text{Ma}} = (^{87}\text{Sr}/^{86}\text{Sr})_{\text{measured}} - [(^{87}\text{Rb}/^{86}\text{Sr}) * (e^{\lambda t} - 1)],$$

where ^{87}Rb decays to ^{87}Sr with a decay constant $\lambda = 1.42 * 10^{-11} \text{ yr}^{-1}$. [Rb] in these rocks varies between 4.4-20.4 ppm and [Sr] between 87-265 ppm, and the ratio $^{87}\text{Rb}/^{86}\text{Sr}$ was estimated as :

$$^{87}\text{Rb}/^{86}\text{Sr} = (\text{Rb}/\text{Sr}) * \{2.692938345 + [0.2830396178 * (^{87}\text{Sr}/^{86}\text{Sr})_{\text{measured}}]\}.$$

Similarly, $^{143}\text{Nd}/^{144}\text{Nd}_{\text{measured}}$ ratios range between 0.512222 and 0.512759. An analogous equation was used for the age correction of Nd isotopic ratios:

$$(^{143}\text{Nd}/^{144}\text{Nd})_{200\text{Ma}} = (^{143}\text{Nd}/^{144}\text{Nd})_{\text{measured}} - [(^{147}\text{Sm}/^{144}\text{Nd}) * (e^{\lambda t} - 1)],$$

where ^{147}Sm decays to ^{143}Nd with $\lambda = 6.54 * 10^{-12} \text{ yr}^{-1}$, and the ratio $^{147}\text{Sm}/^{144}\text{Nd}$ was estimated as:

$$^{147}\text{Sm}/^{144}\text{Nd} = (\text{Sm}/\text{Nd}) * \{0.149957 * [532.9463529 + (142.90982 * (^{143}\text{Nd}/^{144}\text{Nd})_{\text{measured}})] / 150.36556\},$$

with [Sm] ranging between 1.39-4.91 ppm, and [Nd] between 4.47-19.43 ppm.

Nd isotopic ratios were then translated into $(\epsilon_{\text{Nd}})_{200\text{Ma}} = [(^{143}\text{Nd}/^{144}\text{Nd})_{200\text{Ma}} / \text{CHUR}_{200\text{Ma}}] - 1] * 10000$. $(\epsilon_{\text{Nd}})_{200\text{Ma}}$ were calculated related to the CHUR at 200 Ma using the present day values for CHUR: $(^{143}\text{Nd}/^{144}\text{Nd})_{\text{CHUR}} = 0.512638$, and $^{147}\text{Sm}/^{144}\text{Nd} = 0.1967$ (Hamilton, 1983).

Measured lead isotopic ratios yielded ranges of $^{206}\text{Pb}/^{204}\text{Pb}_{\text{measured}}$: 17.462-18.847, $^{207}\text{Pb}/^{204}\text{Pb}_{\text{measured}}$: 15.539-15.649, $^{208}\text{Pb}/^{204}\text{Pb}_{\text{measured}}$: 37.469-38.764. To back correct these values to 200 Ma, the three different decaying systems must be taken into account, that is, ^{238}U decaying to ^{206}Pb , ^{235}U to ^{207}Pb and ^{232}Th to ^{208}Pb with, respectively,

$$\lambda^{238}\text{U} = 1.551 \times 10^{-10} \text{ yr}^{-1},$$

$$\lambda^{235}\text{U} = 9.849 \times 10^{-10} \text{ yr}^{-1},$$

$$\lambda^{232}\text{Th} = 4.948 \times 10^{-11} \text{ yr}^{-1}.$$

Trace elements concentrations in the analyzed samples range between [Pb]: 0.79-3.86 ppm, [U]: 0.03-0.63 ppm, [Th]: 0.18-2.04 ppm. ^{204}Pb is calculated as:

$$[\text{Pb}_{\text{tot}}] / (1 + ^{206}\text{Pb}/^{204}\text{Pb}_{\text{measured}} + ^{207}\text{Pb}/^{204}\text{Pb}_{\text{measured}} + ^{208}\text{Pb}/^{204}\text{Pb}_{\text{measured}}).$$

^{206}Pb was calculated as $^{204}\text{Pb} * (^{206}\text{Pb}/^{204}\text{Pb}_{\text{measured}})$, and the same was done for ^{207}Pb and ^{208}Pb . A $^{238}\text{U}/^{235}\text{U}=137.88$ ratio is assigned, thus allowing the separation between ^{235}U and ^{238}U starting from the total U measured with the ICP-MS. Every radioactive/radiogenic species ratio ($^{238}\text{U}/^{204}\text{Pb}$, $^{235}\text{U}/^{204}\text{Pb}$, $^{232}\text{Th}/^{204}\text{Pb}$) was thus calculated and utilized in the decaying equation.

The same approach was used for recalculating Os isotopic ratios to the initial values at 200Ma, with:

$$(^{187}\text{Os}/^{188}\text{Os})_{200\text{Ma}} = (^{187}\text{Os}/^{188}\text{Os})_{\text{measured}} - [(^{187}\text{Re}/^{188}\text{Os}) * (e^{\lambda t} - 1)],$$

where ^{187}Re decays to ^{187}Os by β^- with a $\lambda=1.666 \times 10^{-11} \text{ yr}^{-1}$ (Smoliar et al., 1996). Os concentrations were measured by isotopic dilution and N-TIMS, Re concentrations by isotopic dilution and ICP-MS, and ranged, respectively, between 0.13-0.92 ppb and 0.50-1.37 ppb. Measured $^{187}\text{Os}/^{188}\text{Os}$ ratios varied between 0.1435 and 0.2656.

7.2 Sr-Nd-Pb ISOTOPES

Samples selected for Sr-Nd-Pb isotopic analyses were 24, i.e. fourteen from the LFO group (CS14, CS28, CS31, CS41, CS48, CS49, CS51, CS55, CS57, CS60, CS62, CS64, CS73), six from the HFO group (CS7, CS9, CS17, CS22, CS26, CS32), three belonging to the LTQ group (CS23, CS44, CS77) and two to the HTQ group (CS2 and CS46). Measured isotopic ratios were recalculated to 200 Ma to get initial values.

A wide range is observed for $^{87}\text{Sr}/^{86}\text{Sr}_{200\text{Ma}}$ (0.70438-0.70880) and $^{143}\text{Nd}/^{144}\text{Nd}_{200\text{Ma}}$ (0.51251-0.51204; $\epsilon_{\text{Nd-200Ma}}$ from +2.42 to -6.67) (Fig.7.1). Negative correlation exists between Sr and Nd isotopic ratios, broadly parallel to the mantle array on the enriched quadrant of the Nd-Sr space. Samples from the various normative groups show total overlap in Sr and Nd isotopic compositions, but LFO samples show the greatest variation in both Sr and Nd isotopes.

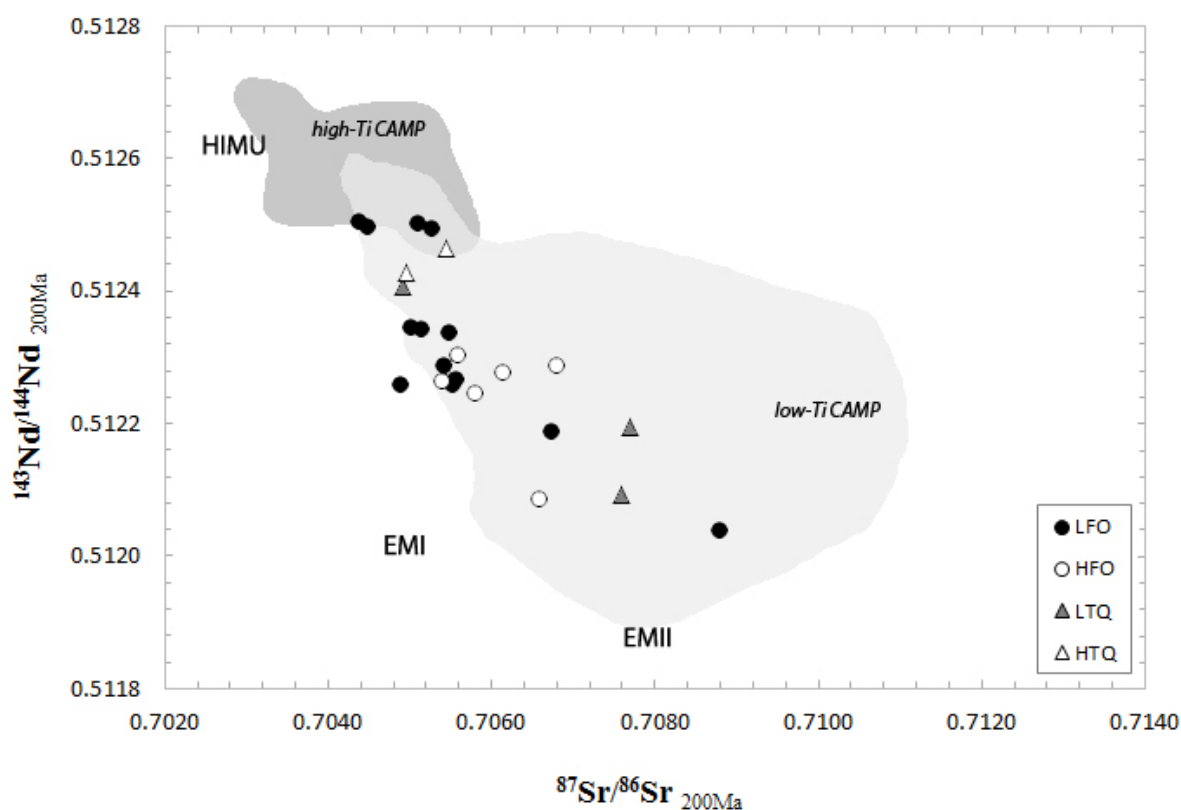


Figure 7.1.: Initial (200 Ma) Sr and Nd isotopic compositions of ENA tholeiites. Fields for low-Ti and high-Ti CAMP rocks were drawn for comparison. Data for compositional fields were taken from: Alibert, 1985; Dupuy et al., 1988; Greenough et al., 1989; Mauche et al., 1989; Heatherington and Mueller, 1991; Puffer, 1992; Dostal and Durning, 1998; Heatherington and Mueller, 1999; Cebria et al., 2003; De Min et al., 2003; Jourdan et al., 2003; Deckart et al., 2005; Verati et al., 2005; Merle et al., 2011).

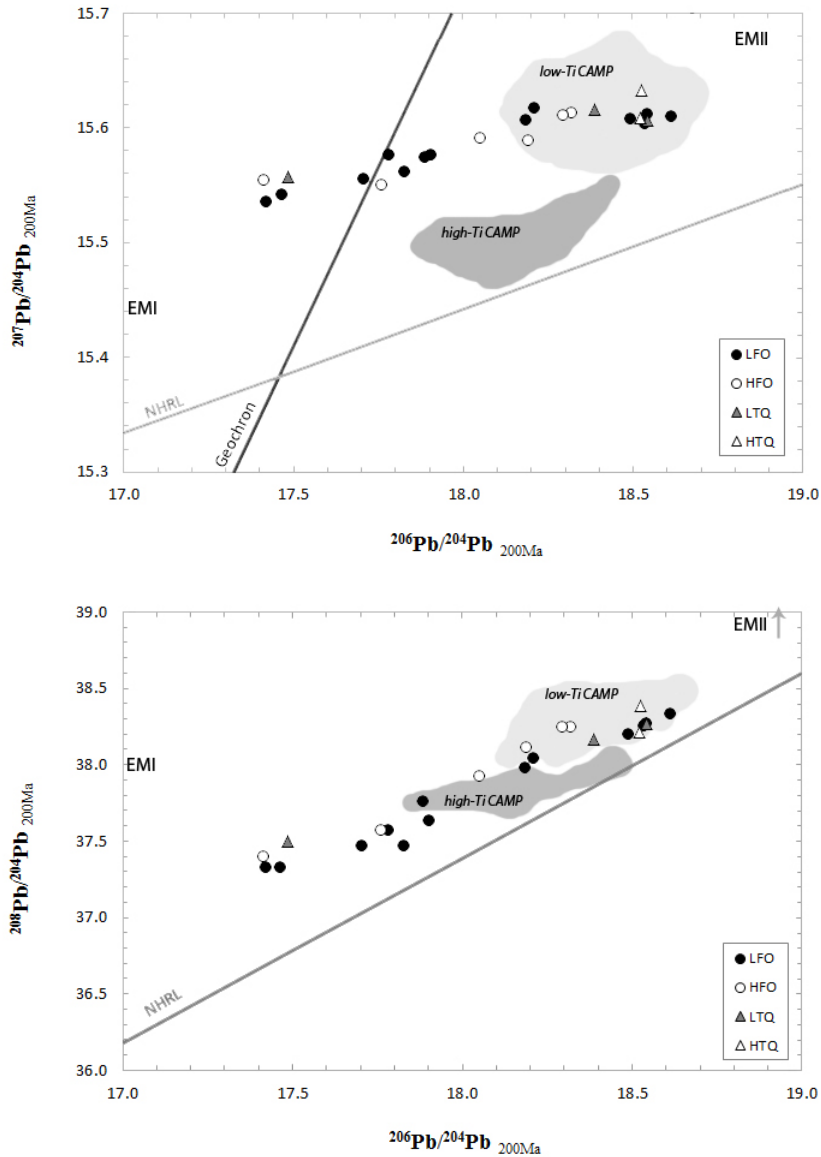


Figure 7.2 a-b: Isotopic data back corrected to 200 Ma are plot on $^{207}\text{Pb}/^{204}\text{Pb}_{200\text{Ma}}$ versus $^{206}\text{Pb}/^{204}\text{Pb}_{200\text{Ma}}$ space (a) and $^{208}\text{Pb}/^{204}\text{Pb}_{200\text{Ma}}$ versus $^{206}\text{Pb}/^{204}\text{Pb}_{200\text{Ma}}$ (b). A measure of the vertical displacement from the NHRL in the above diagrams is shown in Fig. 7.3 by $\Delta 7/4$ (e) and $\Delta 8/4$ (f), as a function of $^{206}\text{Pb}/^{204}\text{Pb}_{200\text{Ma}}$.

Pb isotopic signatures of the sampled ENA tholeiites show a high variability ($^{206}\text{Pb}/^{204}\text{Pb}_{200\text{Ma}} = 17.46-18.85$, $^{207}\text{Pb}/^{204}\text{Pb}_{200\text{Ma}} = 15.54-15.65$, $^{208}\text{Pb}/^{204}\text{Pb}_{200\text{Ma}} = 37.47-38.76$). The less radiogenic samples plot to the left of the Geochron and the most radiogenic ones well to the right. In particular, both on a $^{207}\text{Pb}/^{204}\text{Pb}_{200\text{Ma}}$ versus $^{206}\text{Pb}/^{204}\text{Pb}_{200\text{Ma}}$ (Fig. 7.2 a) and on a $^{208}\text{Pb}/^{204}\text{Pb}_{200\text{Ma}}$ versus $^{206}\text{Pb}/^{204}\text{Pb}_{200\text{Ma}}$ plot (Fig. 7.2 b), all the samples form a positive trend displaced towards higher $^{207}\text{Pb}/^{204}\text{Pb}_{200\text{Ma}}$ and $^{208}\text{Pb}/^{204}\text{Pb}_{200\text{Ma}}$ values with respect to the Northern Hemisphere Reference Line (NHRL), thus trending roughly between EMI and EMII compositions (Zindler and Hart, 1986).

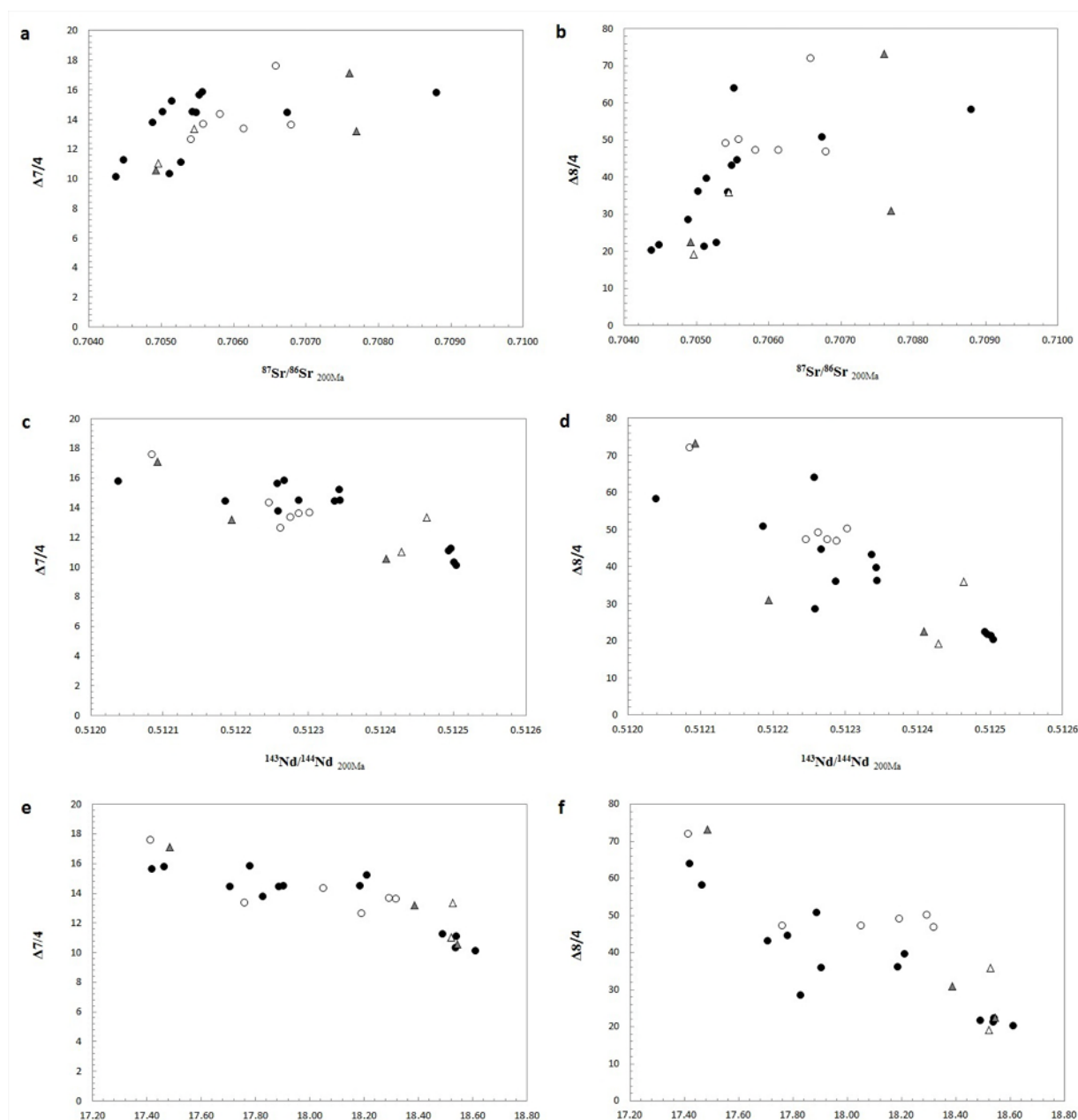


Figure 7.3 a-f: A measure of the vertical displacement from the NHRL in the above diagrams is given by $\Delta 7/4$ and $\Delta 8/4$, here plot as a function of $^{87}\text{Sr}/^{86}\text{Sr}_{200\text{Ma}}$ (a-b), $^{143}\text{Nd}/^{144}\text{Nd}_{200\text{Ma}}$ (c-d) and $^{206}\text{Pb}/^{204}\text{Pb}_{200\text{Ma}}$ (e-f).

A measure of this displacement is given by $\Delta 7/4$, (calculated as $[(^{207}\text{Pb}/^{204}\text{Pb})_{\text{sample}} - (^{207}\text{Pb}/^{204}\text{Pb})_{\text{NHRL}}] * 100$; varying between 10 and 18) and $\Delta 8/4$, (calculated as $[(^{208}\text{Pb}/^{204}\text{Pb})_{\text{sample}} - (^{208}\text{Pb}/^{204}\text{Pb})_{\text{NHRL}}] * 100$; ranging between 19 and 73). The trend formed by ENA isotopic data is not parallel to the NHRL and this is shown by the negative correlation between $\Delta 7/4$ and $\Delta 8/4$ and $^{206}\text{Pb}/^{204}\text{Pb}_{200\text{Ma}}$, i.e. samples yielding the less radiogenic $^{206}\text{Pb}/^{204}\text{Pb}_{200\text{Ma}}$ signatures display the highest deviation from NHRL values (Fig. 7.2 a-b). Both $\Delta 7/4$ and $\Delta 8/4$ are positively correlated with Sr isotopic ratios and negatively correlated with Nd isotopic values (Fig. 7.3 a-d).

A $^{143}\text{Nd}/^{144}\text{Nd}_{200\text{Ma}}$ versus $^{206}\text{Pb}/^{204}\text{Pb}_{200\text{Ma}}$ isotopic space sees the samples plotting along a broadly positive correlation, although with significant scatter. Similarly, a broad but scattered negative correlation is visible in a $^{87}\text{Sr}/^{86}\text{Sr}_{200\text{Ma}}$ vs $^{206}\text{Pb}/^{204}\text{Pb}_{200\text{Ma}}$ plot. HFO samples, though with some scatter, yield more radiogenic Sr and less radiogenic Nd signatures than LFO, while sharing similar $^{206}\text{Pb}/^{204}\text{Pb}_{200\text{Ma}}$ values (Fig. 7.4 a-b)

A good overlap exists between samples from the different normative groups, but while Ol/Hy-normative samples display the maximum observed variation, the two analyzed HTQ samples occupy the most radiogenic position in both the Pb-Pb isotopic spaces, while yielding among the least radiogenic initial Sr isotopic signatures and the highest initial $^{143}\text{Nd}/^{144}\text{Nd}$.

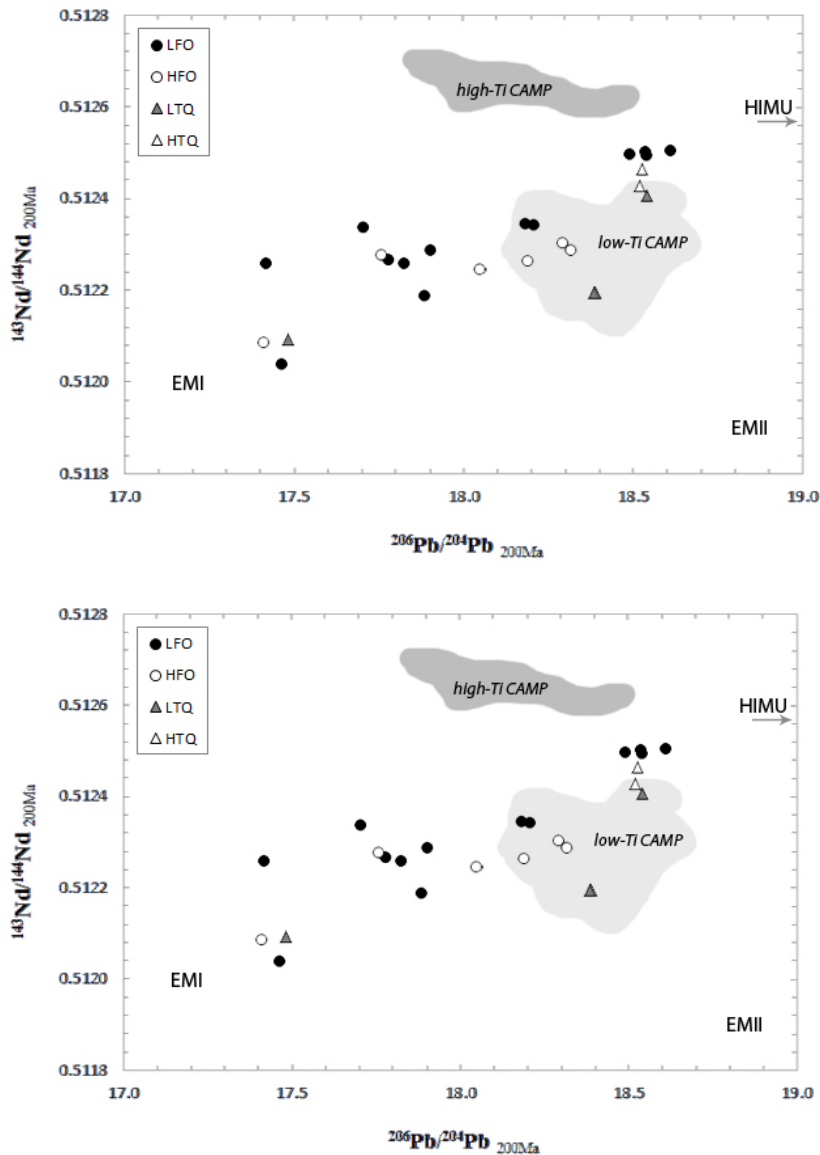


Figure 7.4 a-b. Initial (200 Ma) Sr and Nd isotopic compositions of ENA tholeiites plot as a function of $^{206}\text{Pb}/^{204}\text{Pb}_{200\text{Ma}}$.

Our new isotopic data are in agreement with those obtained by Pegrarn (1990) on dykes (mostly Ol/Hy-normative) cropping out in North and South Carolina. Nd and Sr isotopic values from Pegrarn (1990) were back corrected to 200 Ma instead of 180 Ma (Fig. 7.5 a). Pb isotopic data from Pegrarn (1990) cannot be corrected to initial values, but a comparison between uncorrected values shows an excellent concordance between new and previous data (Fig. 7.5 c-d). The same concordance is shown by Nd initial isotopic compositions and $^{206}\text{Pb}/^{204}\text{Pb}$ uncorrected values, where the most radiogenic data from Pegrarn (1990) overlap our quartz-normative samples in a short vertical alignment (Fig. 7.5 b).

7.3 Os ISOTOPES

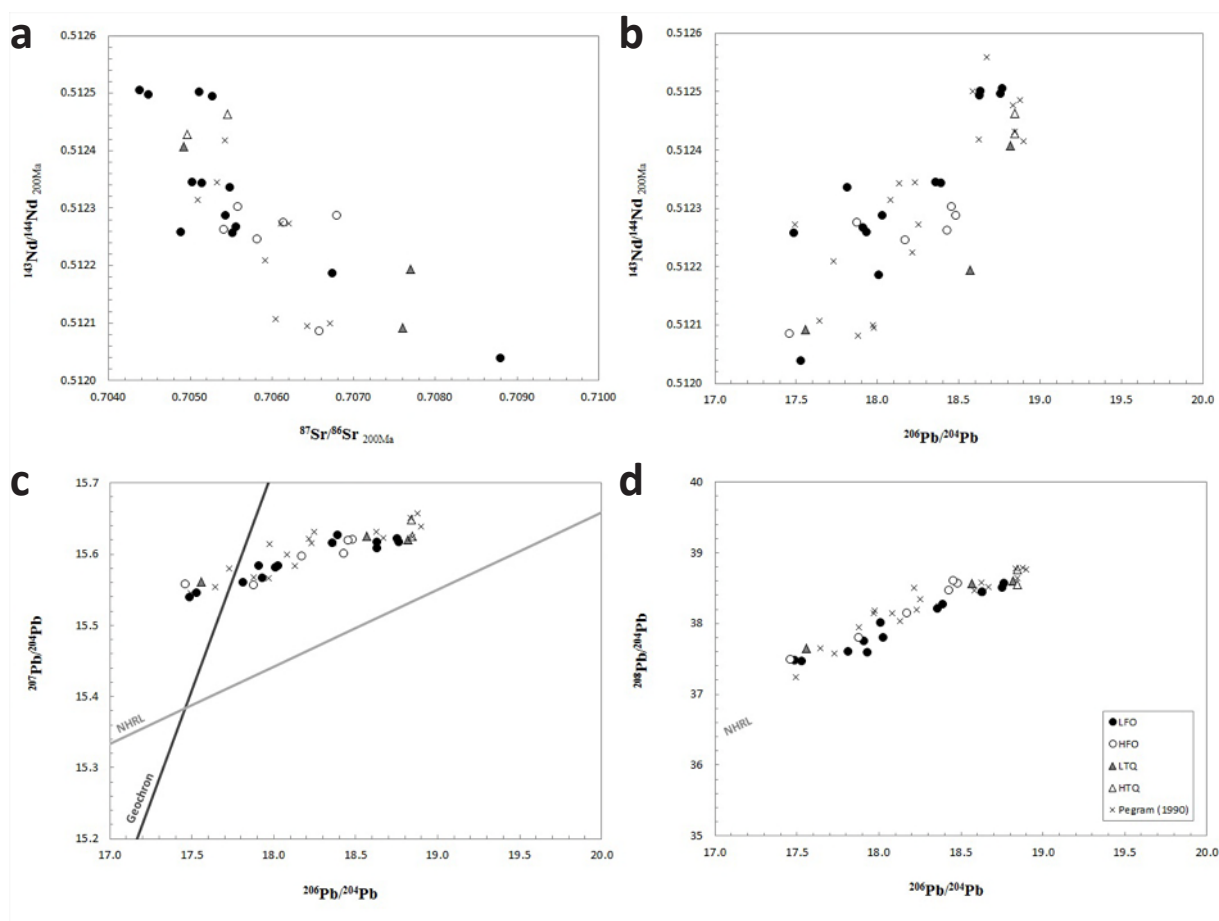


Figure 7.5 a-d: Data from Pegrarn (1990) back corrected to 200 Ma are shown in a) along with ENA tholeiites data from the present work. In b) initial (200 Ma) Nd isotopic ratios are plotted as a function of uncorrected $^{206}\text{Pb}/^{204}\text{Pb}$. c) and d) show uncorrected Pb isotopes for our data and those from Pegrarn (1990).

A subset of 12 samples taken from those analyzed for Sr-Nd-Pb isotopes was selected for whole-rock Re-Os chemical and isotopic analyses. Samples were chosen basing on the highest possible MgO content. Therefore, all the selected samples belong to Ol/Hy-normative LFO (CS14, CS28,

CS31, CS41, CS49, CS55, CS57, CS60, CS64, CS73) and HFO (CS9, CS26) groups.

Analyses were carried out at the CRPG-CNRS of Nancy (FR), where chemical extraction of Re and Os in the clean lab (cf. Methods on Appendix 2) from 0.5 g of powdered whole-rock samples was followed by determination of Re concentrations by isotope dilution and Re isotopic ratios by peak jumping using a Daly detector on a Micromass Isoprobe ICP-MS. Os concentrations were determined by isotope dilution, and Os isotopes were measured by Negative Thermal Ionization Mass Spectrometry (N-TIMS) (Creaser et al., 1991; Volkening et al., 1991) in ion counting mode, using a Finnigan MAT262 mass spectrometer. The average measured Os blank was 13 ppt, and Re blank 370 ppt, while uncertainties on $^{187}\text{Os}/^{188}\text{Os}$ initial signatures range between 0.3 and 0.05%. Measured Os concentrations range from 0.13 to 0.92 ppb, while [Re] varies between 0.5 and 1.4 ppb, with uncertainties of, respectively 0.1 and 1.9 % and 1.06-1.56%.

Measured $^{187}\text{Os}/^{188}\text{Os}$ ratios range between 0.1435 and 0.2656, and plotted against $^{187}\text{Re}/^{188}\text{Os}$ resulted in apparent isochron yielding an age of 201 ± 40 Ma (MSWD=406), with initial $^{187}\text{Os}/^{188}\text{Os}$ of 0.137 ± 0.012 (Fig.7.6 a). This age, although obviously very imprecise, is comparable to the $^{40}\text{Ar}/^{39}\text{Ar}$ ages of the samples (201.4-195.2 Ma, Hames, 2000; Beutel, 2005; Nomade et al., 2007; all data recalculated after Renne et al. 2010;) suggesting that the Re–Os system was not disturbed significantly after dykes (and sill) emplacement and supporting the significance of recalculating initial ratios to 200 Ma.

Sample CS31 yielded a result that is distinctly higher than all the others, probably due to a laboratory bias, thus it is not considered further in the results discussions. Eliminating CS31 from the $^{187}\text{Os}/^{188}\text{Os}$ - $^{187}\text{Re}/^{188}\text{Os}$ diagram brings to a cleaner apparent isochron with a different age of 211 ± 22 Ma (MSWD=56), that is nevertheless still comparable, within error, with the $^{40}\text{Ar}/^{39}\text{Ar}$ ages of ENA CAMP dykes. In this case the initial $^{187}\text{Os}/^{188}\text{Os}$ calculated from the regression is 0.1319 ± 0.0066 (Fig. 7.6 b).

$^{187}\text{Os}/^{188}\text{Os}_{200\text{Ma}}$ of sampled ENA diabases display a restricted compositional range (0.1278 ± 0.0011 - 0.1442 ± 0.0015), with HFO and LFO samples sharing similar Os isotopic traits. There is no correlation between [Re] and initial Os isotopic ratios. The two HFO samples display higher Re concen

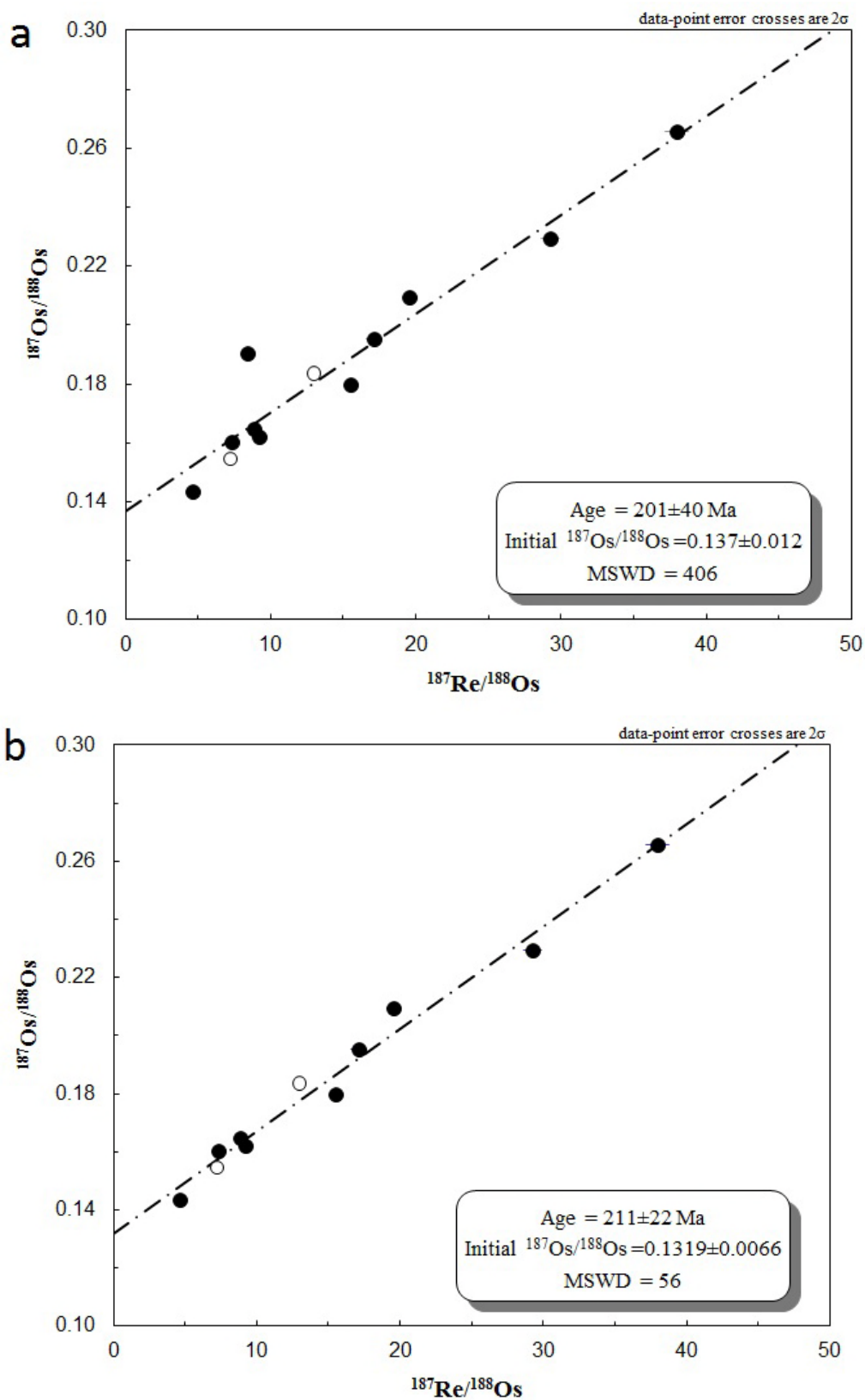


Figure 7.6 a-b: Re–Os isochron plot of 12 ENA CAMP tholeiites. Age and uncertainties were calculated using the Isoplot software (Ludwig, 2003). Line is regressed through all 12 analysed HFO and LFO samples in a), while sample CS31 was eliminated from regression in b). Uncertainties on each data point are 2σ and include in-run errors as well as blank and weighing uncertainties.

trations than the LFO ones (Fig. 7.7 a). No correlation is observed between initial $^{187}\text{Os}/^{188}\text{Os}$ and [Os] as well, but the two samples showing distinctly higher [Os] (CS9, HFO: 0.90 ppb and CS14, LFO: 0.92 ppb; Fig. 7.7 b) are among the least radiogenic ones.

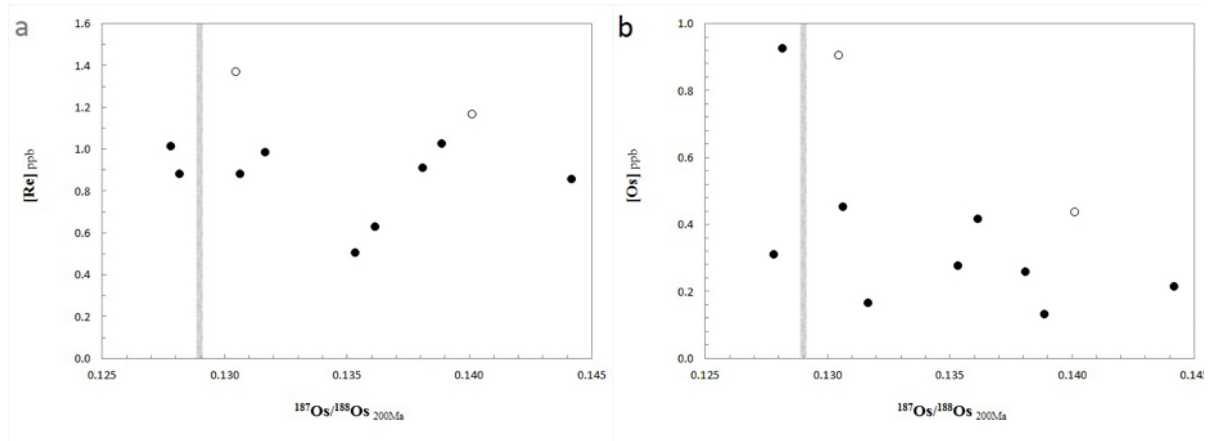


Figure 7.7 a-b: Re (a) and Os (b) concentration (in ppb) plot as a function of $^{187}\text{Os}/^{188}\text{Os}_{200\text{Ma}}$ for 12 ENA CAMP tholeiites. Grey belt in A and B marks the Os isotopic composition of PUM (Meisel et al., 2001).

Os isotopic compositions for ENA CAMP tholeiites vary from values close to the estimated $^{187}\text{Os}/^{188}\text{Os}$ composition of the Primitive Upper Mantle (0.1281 ± 0.0008 , recalculated to 200 Ma after the present-day ratio from Meisel et al., 2001), to slightly more radiogenic ones (up to 0.1441 ± 0.0015) and plot, in Sr–Os and Nd–Os isotopic spaces among DMM, EMI and EMII compositions (Shirey and Walker, 1998). Os isotopic ratios are poorly correlated with Sr–Nd–Pb ones, even though the sample with the most radiogenic Os signature shows also the highest $^{87}\text{Sr}/^{86}\text{Sr}_{200\text{Ma}}$ and lowest Nd (Fig. 7.8 a-b). Similarly, $\Delta 7/4$ and $\Delta 8/4$ signatures appear uncorrelated with $^{187}\text{Os}/^{188}\text{Os}$ initial ratios (Fig. 7.9 a-b).

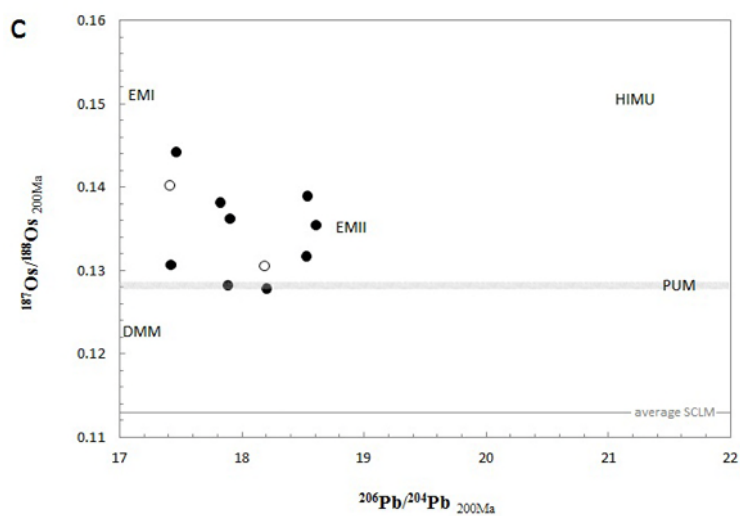
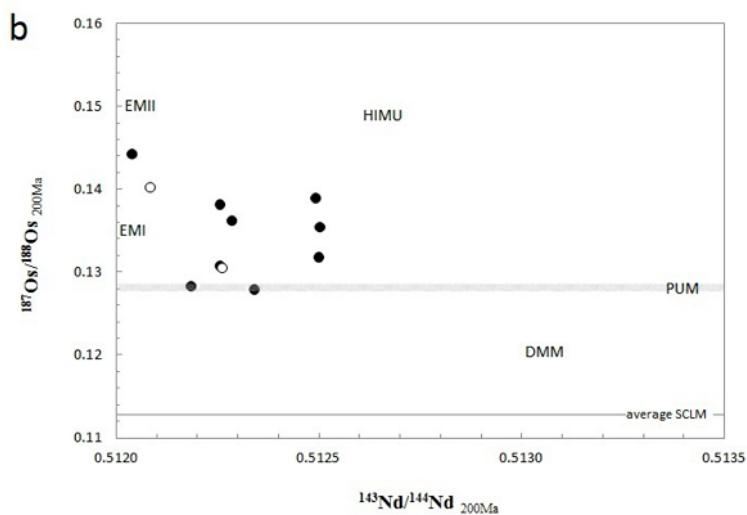
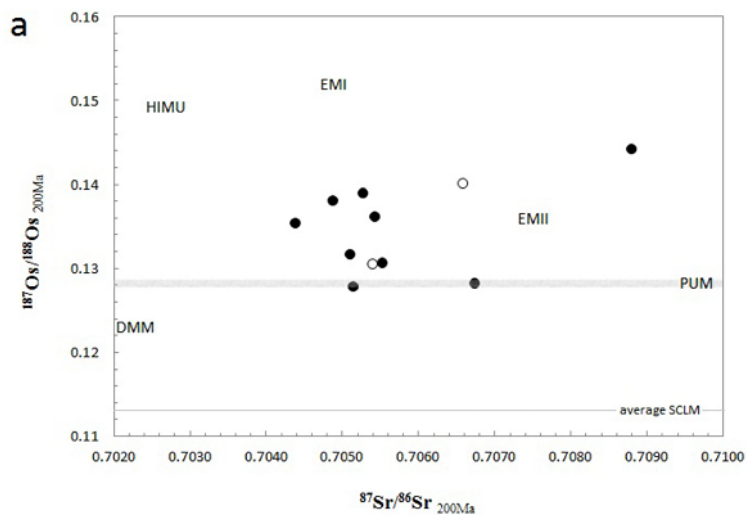


Figure 7.8 a-c: Initial Os vs Sr–Nd–Pb isotopic ratios for ENA CAMP tholeiites. Os ratios for mantle poles from Shirey and Walker (1998) and primitive upper mantle (PUM) from Meisel et al. (2001). Sr, Nd and Pb mantle reservoirs values are from Zindler and Hart (1986). All mantle reservoirs are back-corrected to 200Ma (present-day PUM values from Meisel et al. 2001: $^{187}\text{Os}/^{188}\text{Os}=0.1296\pm 0.0008$; $^{87}\text{Re}/^{188}\text{Os}=0.4353$).

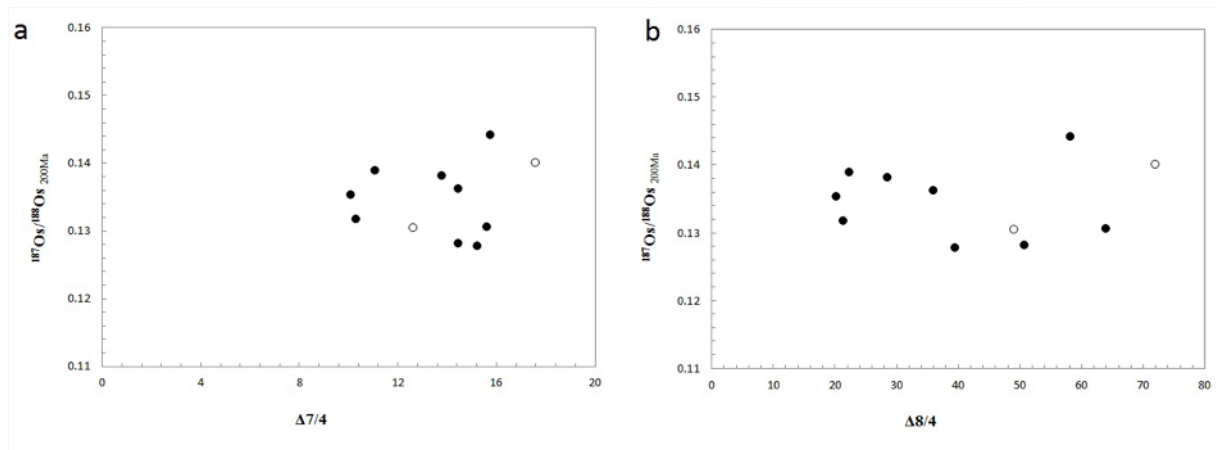


Figure 7.9 a-b: Initial Os compositions for ENA tholeiites plotted as a function of $\Delta 7/4$ (a) and $\Delta 8/4$ (b).

8 MINERALOGICAL COMPOSITIONS (EMPA)

Phenocryst compositions and their variations can help defining the processes that occurred during the magmatic evolution of ENA tholeiites. Electron Micro Probe Analyses (EMPA) for major elements on phenocrysts from the sampled rocks were obtained with a CAMECA SX50 at the IGG-CNR of Padova. Analytical procedures are described in Appendix. Detailed core-rim traverses were analyzed on olivine, pyroxene, plagioclase and oxide crystals.

8.1 OLIVINE

The vast majority of the olivine/hyperstene-normative samples also show modal olivine, and, unlike CAMP basalts from other areas (e.g. Morocco, Marzoli et al., 2004), crystals appear unaffected or only partially altered by hydrothermal processes. Olivine phenocrysts mostly occur in porphyritic rocks, but also in texturally different rocks. 18 olivine crystals were analyzed from 6 different samples (CS6, CS28, CS31, CS49, CS57 and CS77), of which CS6 belongs to the HFO normative group, while all the others are LFO, except for CS77, a quartz-normative sample (LTQ). Analyzed crystals range in size between 200 and 1500 μm , and analytical spots along the transects were spaced by 6 to 20 μm , making up total transect lengths ranging from 100 to 500 μm . Olivine compositions ranging between Fo_{56} and Fo_{89} were obtained.

All analyzed olivine crystals are either unzoned or normally zoned. Olivines in porphyritic samples (CS28 and CS57) are normally zoned and yield high-Fo cores (up to Fo_{89}) which are close to equilibrium with the host whole-rock compositions, for a $^{olivine/melt}K_D(\text{Fe}/\text{Mg})$ of 0.30 ± 0.03 (Roeder and Emslie, 1970; Ulmer, 1989). Also the olivine crystal analyzed for CS77 is unzoned and rather primitive, with core composition around Fo_{81} close to equilibrium with the whole-rock. On the contrary, ophitic rocks (CS6, CS31, CS49) show unzoned low-Fo olivines (Fo_{70-65}) which would be in equilibrium with a less Mg-rich melt than their whole-rocks. In sample CS6, two distinct generations of olivine were analyzed, i.e. relatively high Fo (Fo_{70}) unzoned skeletal olivines enclosed in augites and uniform, low Fo (Fo_{60}) olivines hosted among plagioclase and groundmass.

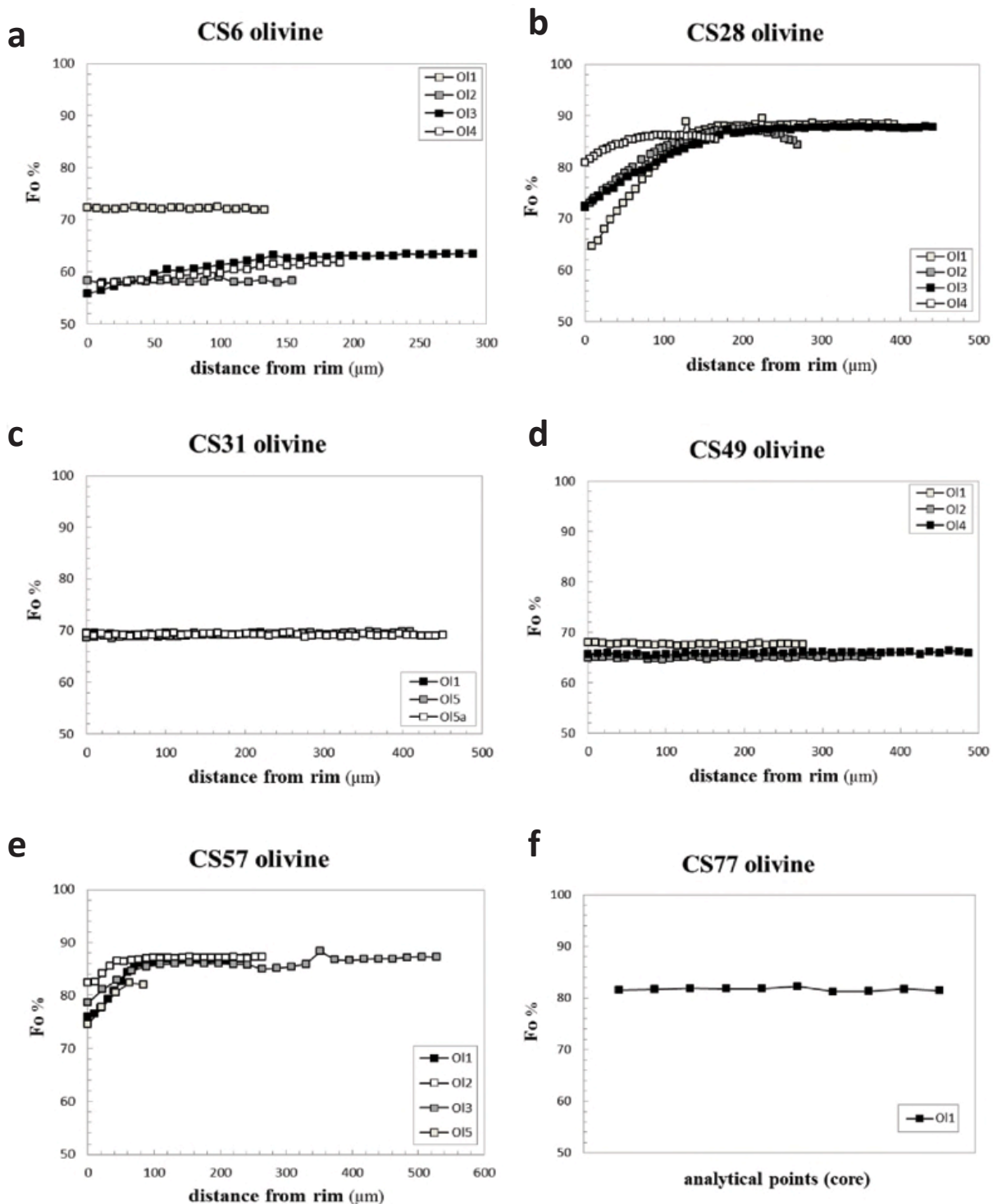


Figure 8.1: a-e) Fo content (in %) for 18 olivines analyzed from 5 OI-Hy-normative ENA diabases. Squares mark punctual analyses, plotted as a function of the distance (in μm) from the crystal rim. f) Fo content (in %) from 10 analytical points from the core portion in olivine phenocryst from CS77 (LTQ).



Figure 8.2: Microphotographs (crossed polars) of the analyzed olivines in thin sections from 6 ENA diabases. Analytical paths are marked by straight line and letters (c:core, r:rim, a-b: random points).

There is no systematic negative correlation between Fo content in olivine cores and Mg# or total FeO wt% in the whole rocks. Thus, as observed by Warner et al. (1992), the presence of low-Fo olivine (under Fo_{80}) is either linked to 1) whole rock composition, i.e. these olivines crystallized from relatively MgO-poor melts (as observed for sample CS6, 13.78 wt% Fe_2O_{3tot}) or 2) the grain size, i.e. in coarser grained samples slower cooling allowed re-equilibration between olivine and melt (as visible in samples CS31 and CS49). However, Warner et al. (1992) observed that the second situation is attended by the presence of low-Ca pyroxenes (either pigeonite or orthopyroxene) in the diabase, and low-Ca pyroxene are lacking in CS31 and CS49, except for a pigeonitic rim (Wo_{\cdot}) in an augite crystal from sample CS31. To draw the rock-olivine equilibrium curves, a $K_D(Fe-Mg)^{olivine/liquid}$ of 0.30 ± 0.03 was used (Roeder and Emslie, 1970; Ulmer, 1989), and Fo content in olivines and Mg# of the whole rock were considered.

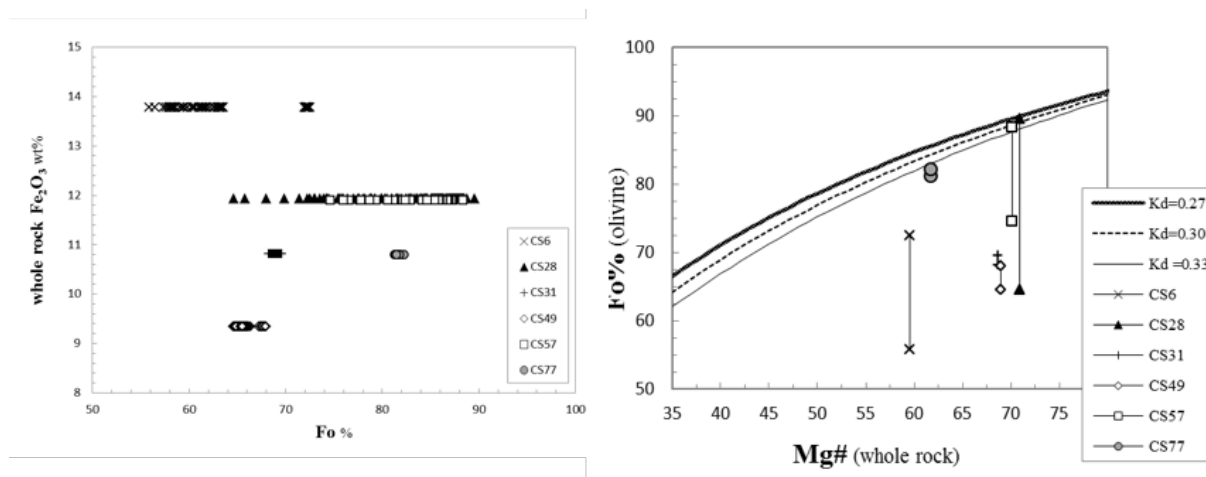


Figure 8.3: a) Fo content (in %) for all analytical points in olivines, plotted against total Fe_2O_3 (wt%) in the respective whole rocks. b) Rhodes diagram for analyzed olivines, with olivine/melt equilibrium curves drawn with a $K_D(Fe-Mg)^{olivine/liquid}$ of 0.3 ± 0.03 (Roeder and Emslie, 1970; Ulmer, 1989).

The partition coefficient was chosen to best fit the petrologic conditions of ENA tholeiites, i.e. poor hydration (<1 wt% H_2O), fO_2 around the Quartz-Fayalite-Magnetite (QFM) buffer and low crystallization pressure (5-9 kbar). Olivines from CS6, CS31 and CS49 (ophitic, coarse grained rocks sampled from thick dykes and sill) show disequilibrium with the rock (Fo content below the equilibrium curve) that possibly suggests olivine accumulation.

In general, all the analyzed olivines show a good positive correlation between Ni (varying between 473 and 3344 ppm) and Fo, and a negative correlation between Mn (708-5275 ppm) and Fo (Fig. 8.4, a-b).

Olivines from ENA tholeiites are generally Ni-rich and Mn-poor, comparable to those of within plate magmas possibly issued from a pyroxenitic mantle source (cf. Sobolev et al., 2007).

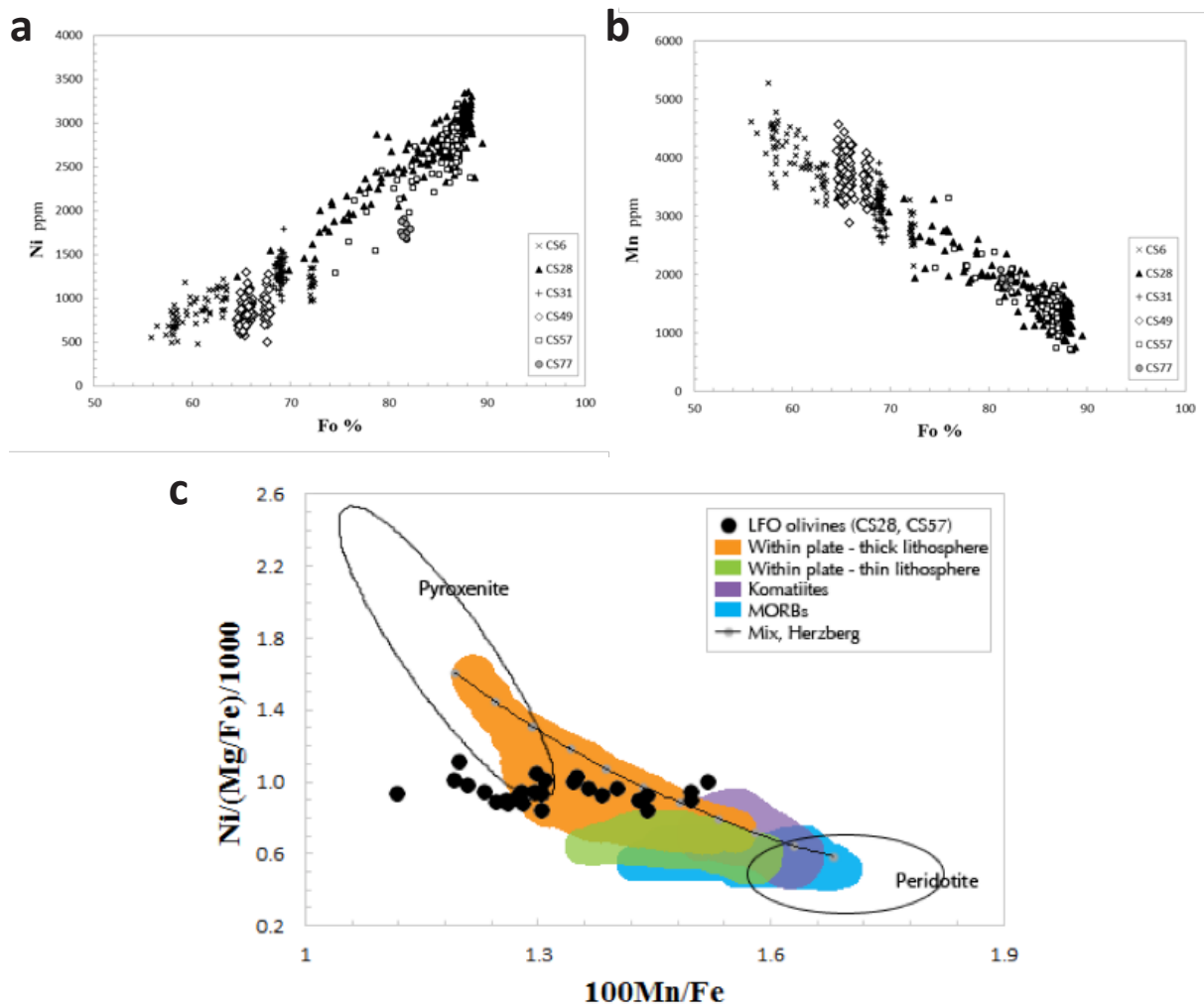


Figure 8.4. Ni (a) and Mn (b) concentrations (ppm) in olivines from ENA tholeiites, plotted against Fo%. c) Compositions of olivine cores from CS28 and CS57 are compared with those from different tectonic settings (modified after Sobolev et al., 2007).

	SiO ₂ wt%	Al ₂ O ₃ wt%	FeO wt%	MnO wt%	MgO wt%	CaO wt%	NiO wt%	Total	Fo %	Fa %	Teph %
CS6 ol1	37.46	0.01	25.21	0.36	37.26	0.28	0.15	100.75	72.2	27.4	0.4
CS6 ol3 core	36.66	0.02	32.17	0.42	31.83	0.35	0.15	100.33	63.5	36.0	0.5
CS6 ol3 rim	35.41	0.00	37.45	0.57	27.65	0.31	0.09	101.47	56.5	42.9	0.7
CS28 ol1 core	40.17	0.04	11.15	0.16	48.55	0.29	0.42	100.83	88.4	11.4	0.2
CS28 ol1 rim	36.89	0.02	30.44	0.43	33.32	0.24	0.15	101.06	65.8	33.7	0.5
CS28 ol4 core	40.16	0.03	13.74	0.16	46.72	0.29	0.36	101.19	85.7	14.1	0.2
CS28 ol4 rim	39.68	0.07	17.41	0.23	43.70	0.29	0.27	101.73	81.5	18.2	0.2
CS31 ol1	37.51	0.02	27.81	0.41	35.25	0.19	0.17	101.37	69.0	30.5	0.5
CS49 ol1	37.08	0.01	28.94	0.46	34.41	0.15	0.11	101.17	67.6	31.9	0.5
CS49 ol2	36.67	0.01	30.90	0.48	32.80	0.15	0.10	101.14	65.1	34.4	0.5
CS57 ol2 core	40.88	0.07	12.31	0.21	47.89	0.25	0.33	101.68	87.2	12.6	0.2
CS57 ol2 rim	39.58	0.07	16.68	0.27	44.37	0.24	0.30	101.78	82.3	17.4	0.3
CS57 ol4 core	40.25	0.02	12.20	0.19	47.73	0.24	0.35	100.31	87.3	12.5	0.2
CS57 ol4 rim	38.47	0.04	20.01	0.25	41.90	0.21	0.20	100.86	78.7	21.1	0.3
CS77 ol1 core	39.02	0.02	16.90	0.25	43.33	0.29	0.22	100.03	81.8	17.9	0.3

Table 8a: Representative compositions (EMPA, in wt% oxides) of analyzed olivines.

8.2 PYROXENES

From the same Ol-Hy-normative samples analyzed for olivine compositions, 11 pyroxenes were selected for EMPA, and 10 more were analyzed from Q-normative samples, i.e. CS23 (HTQ) and CS67 (LTQ). Punctual analyses were plotted on the compositional quad (Morimoto, 1988). Clinopyroxenes of augitic composition are the most frequent pyroxenes to crystallize in ENA diabases. A good overlap exists among compositions of pyroxenes analyzed from HFO and LFO rocks, while quartz-normative samples yielded pyroxenes of more variable compositions (Fig. 8.5). Representative EMPA data for some of the analyzed crystals are shown in Table 8b.

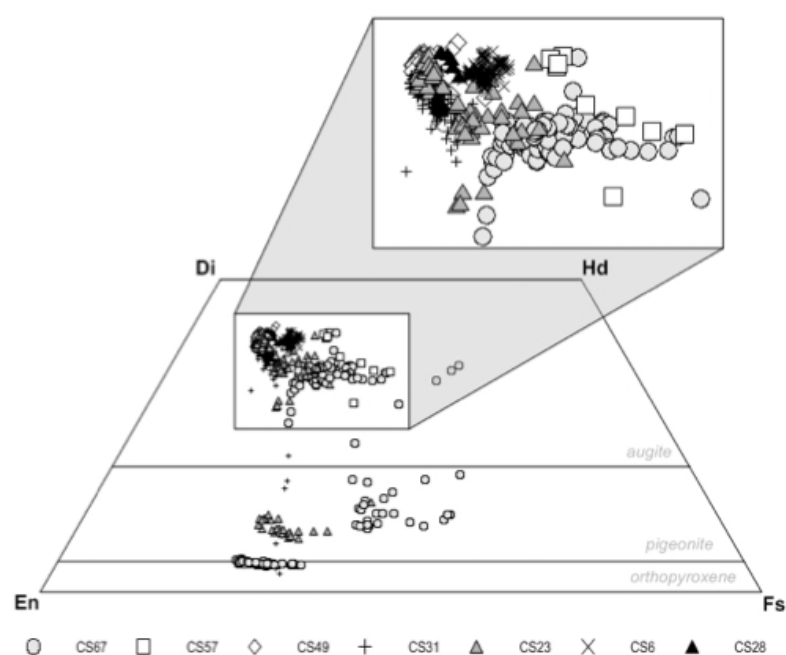


Figure 8.5: EMPA data points for each analyzed pyroxene crystal plotted on the pyroxene compositional quad. (Di: diopside, Hd: hedbergite; En: enstatite; Fs: ferrosilite). Magnifier field for most frequent augitic compositions.

Coarse-grained, ophitic rocks yielded large crystals (up to 800 μ m), either unzoned or slightly normally zoned (i.e. Mg# and CaO decreasing towards the crystal rim, Fig.8.8), while small, rather uniform pyroxene microphenocrysts were analyzed from the groundmass of porphyritic rocks. Ol-Hy-normative rocks (CS6, CS28, CS31, CS49 and CS57) all crystallized augites, whose compositions cluster in Ca component (wollastonite) around 27 and 43% (Wo_{27-43}), and range from 24 to 52% in enstatite (En_{24-52} , Mg component). Augite microphenocrysts from CS57 show the highest content in ferrosilite (Fe component, Fs_{58-66}). A large augite from CS31 showed a decrease in wollastonite (and Mg#) towards the rim, reaching compositions typical of low-Ca pyroxenes (Wo_{4-18} , orthopyroxene and pigeonite). CS67 (LTQ) showed, along with augite ($Wo_{24-43}En_{23-52}$), orthopyroxene (hypersthene, $Wo_{4-5}En_{62-72}$) rimmed by pigeonite ($Wo_{10-19}En_{32-52}$), while sample CS23 (HTQ) crystallized augite

($\text{Wo}_{29-43}\text{En}_{40-53}$) and pigeonite ($\text{Wo}_{8-13}\text{En}_{55-65}$). Variations in Wo component are positively correlated with variations in Mg# and Cr_2O_3 , and inversely linked to those in TiO_2 .

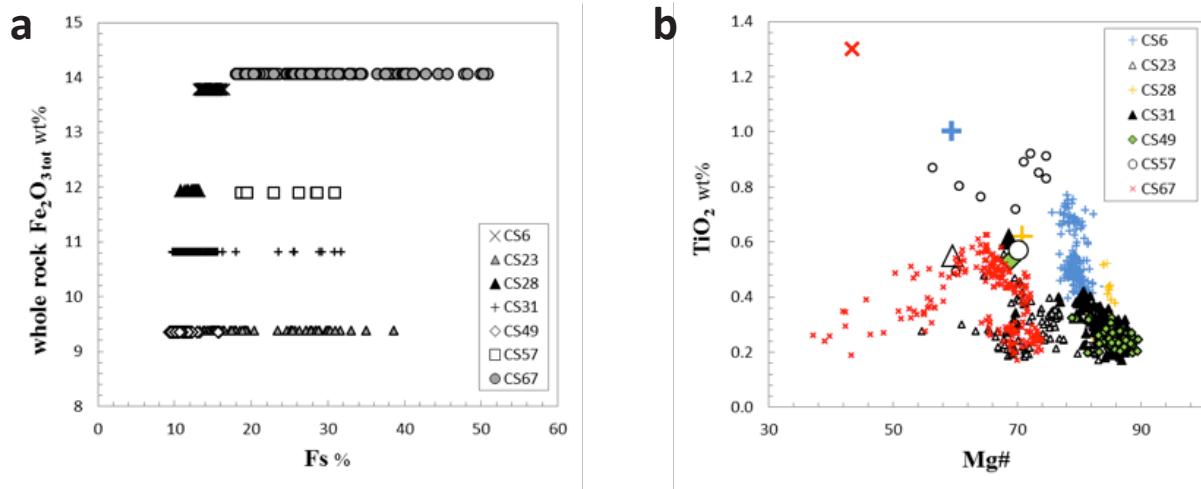


Figure 8.6: a) Fs content (in %) for all analytical points in pyroxenes, plotted against total Fe_2O_3 (wt%) in the respective whole rocks. b) TiO_2 content plotted versus Mg# for both pyroxenes compositions (small symbols) and whole rocks (big symbols).

Pyroxenes either show a Fe-enrichment trend, or a Ca-depletion one (or both, as observed in CS23 and CS67; Fig. 8.5). In CS57 and CS67, more ferrosilitic compositions are coupled with a relatively high total Fe_2O_3 in the whole rock (12 and 14 wt%, respectively), but for the other samples there is no correlation between Fe content in pyroxenes and whole rock. TiO_2 content in pyroxenes is roughly correlated with the whole rock composition, with the only exception of sample CS57, whose pyroxenes are richer in TiO_2 than the whole rock (0.7-0.9 wt% and 0.57 wt%, respectively). This is probably due to augites from CS57 having crystallized during a late stage, from a more evolved (and TiO_2 -rich) melt. Plotted on a Rhodes diagram (Fig.8.7) to investigate their equilibrium with the whole rock, pyroxenes from ENA diabases show different situations, i.e. augitic cores from phenocrysts in CS6, CS31 and CS49 (that is, from Ol-Hy-normative, coarse grained, ophitic rocks) appear in equilibrium with the melt when a $K_D(\text{Fe-Mg})^{\text{clinopyroxene/liquid}}$ of 0.25 (Kinzler, 1997; Gaetani and Grove, 1998) is used. On the contrary, augites from porphyritic samples (CS28 and CS57) have a lower Mg# than the whole rocks, addressing crystallization from a more evolved melt (thus being possibly in equilibrium with the mesosthesis even if not with the whole rock) and Mg-enrichment of the whole rock probably due to accumulation of Mg-bearing minerals (high-Fo olivines). In Q-normative samples clinopyroxene cores of augitic compositions are in with the equilibrium with the whole rock, while pigeonites (much lower Mg#) are not. Disequilibrium of the pigeonites supports

a late crystallization of these phenocrysts. Orthopyroxenes appear in equilibrium with the whole rock if a lower $K_D(\text{Fe-Mg})^{\text{orthopyroxene/liquid}}$ is considered (i.e., 0.20, black curve in Fig.8.7). A lower $K_D(\text{Fe-Mg})^{\text{orthopyroxene/liquid}}$ for orthopyroxene with respect to coexisting clinopyroxene is plausible in basaltic systems according to e.g. Villiger et al. (2004).

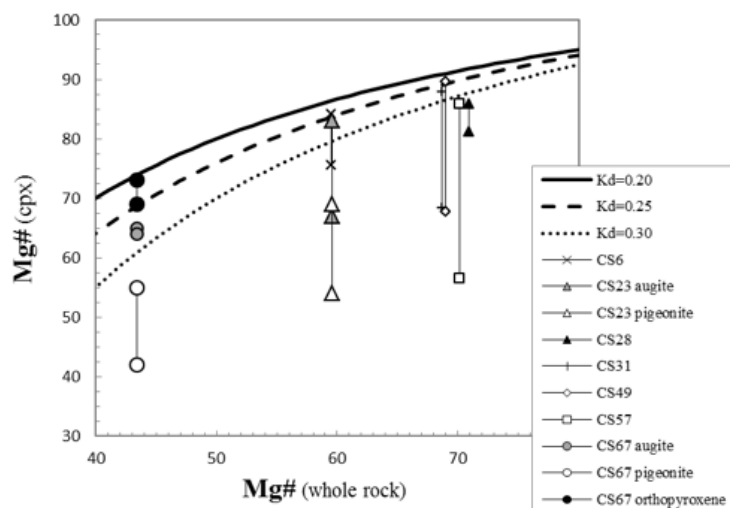


Figure 8.7: Rhodes diagram with clinopyroxene/melt equilibrium curves drawn with a $K_D(\text{Fe-Mg})^{\text{pyroxene/liquid}}$ of 0.25 ± 0.5 (Gaetani and Grove, 1998).

	SiO ₂ wt%	TiO ₂ wt%	Al ₂ O ₃ wt%	FeO wt%	MnO wt%	MgO wt%	CaO wt%	Na ₂ O wt%	Cr ₂ O ₃ wt%	Total	Wo %	En %	Fs %	Mg#
CS6 cpxC core	49.77	0.60	4.33	8.24	0.15	15.10	19.53	0.39	1.01	99.11	41.5	44.6	13.9	81.4
CS6 cpxC rim	51.26	0.50	2.62	8.84	0.21	15.72	19.27	0.40	0.24	99.06	40.0	45.4	14.7	80.1
CS23 cpx2 core	51.70	0.23	2.49	7.31	0.17	17.54	18.94	0.18	0.83	99.40	38.4	49.4	11.6	81.0
CS23 cpx2 rim	51.55	0.38	1.72	11.05	0.26	16.15	17.96	0.19	0.15	99.41	36.4	45.5	17.5	72.3
CS23 cpx7 augite	51.25	0.31	1.94	10.24	0.27	17.14	17.12	0.18	0.07	98.52	34.7	48.4	16.2	74.9
CS23 prx7 pigeonite	52.53	0.21	1.07	15.87	0.42	22.93	5.82	0.05	0.02	98.91	11.6	63.6	24.7	72.0
CS28 cpxB	51.10	0.41	2.84	7.11	0.20	16.37	19.99	0.26	0.90	99.19	41.2	47.0	11.8	84.7
CS28 cpxC	52.62	0.30	1.73	7.83	0.19	17.50	18.62	0.23	0.58	99.61	37.8	49.5	12.7	82.0
CS31 cpxA core	52.90	0.22	1.80	6.14	0.18	18.14	19.55	0.25	0.68	99.86	39.3	50.8	9.9	87.2
CS31 cpxA rim	52.86	0.27	0.72	20.06	0.42	23.65	1.46	0.01	0.03	99.49	2.9	65.3	31.7	68.3
CS49 cpx1	51.39	0.26	3.02	5.83	0.16	17.35	19.66	0.25	1.09	99.02	40.6	49.8	9.6	88.0
CS57 cpxA	49.64	0.72	3.08	13.82	0.32	13.69	18.07	0.33	0.05	99.73	37.5	39.5	22.9	69.8
CS67 cpx2	50.56	0.50	2.08	13.42	0.40	15.34	16.78	0.27	0.02	99.36	34.2	43.5	21.3	67.1
CS67 prx2a	52.55	0.27	1.75	16.49	0.33	25.61	2.31	0.04	0.00	99.35	4.5	70.0	25.3	73.5
CS67 prx3 opx	52.90	0.21	1.01	19.39	0.34	24.09	2.22	0.02	0.08	100.27	4.4	65.8	29.7	68.9
CS67 prx3 pigeonite	50.83	0.34	1.02	25.20	0.69	17.25	5.16	0.07	0.00	100.56	10.5	49.0	40.2	55.0

Table 8b: Representative EMPA data points (expressed in wt% oxides) for analyzed pyroxenes.

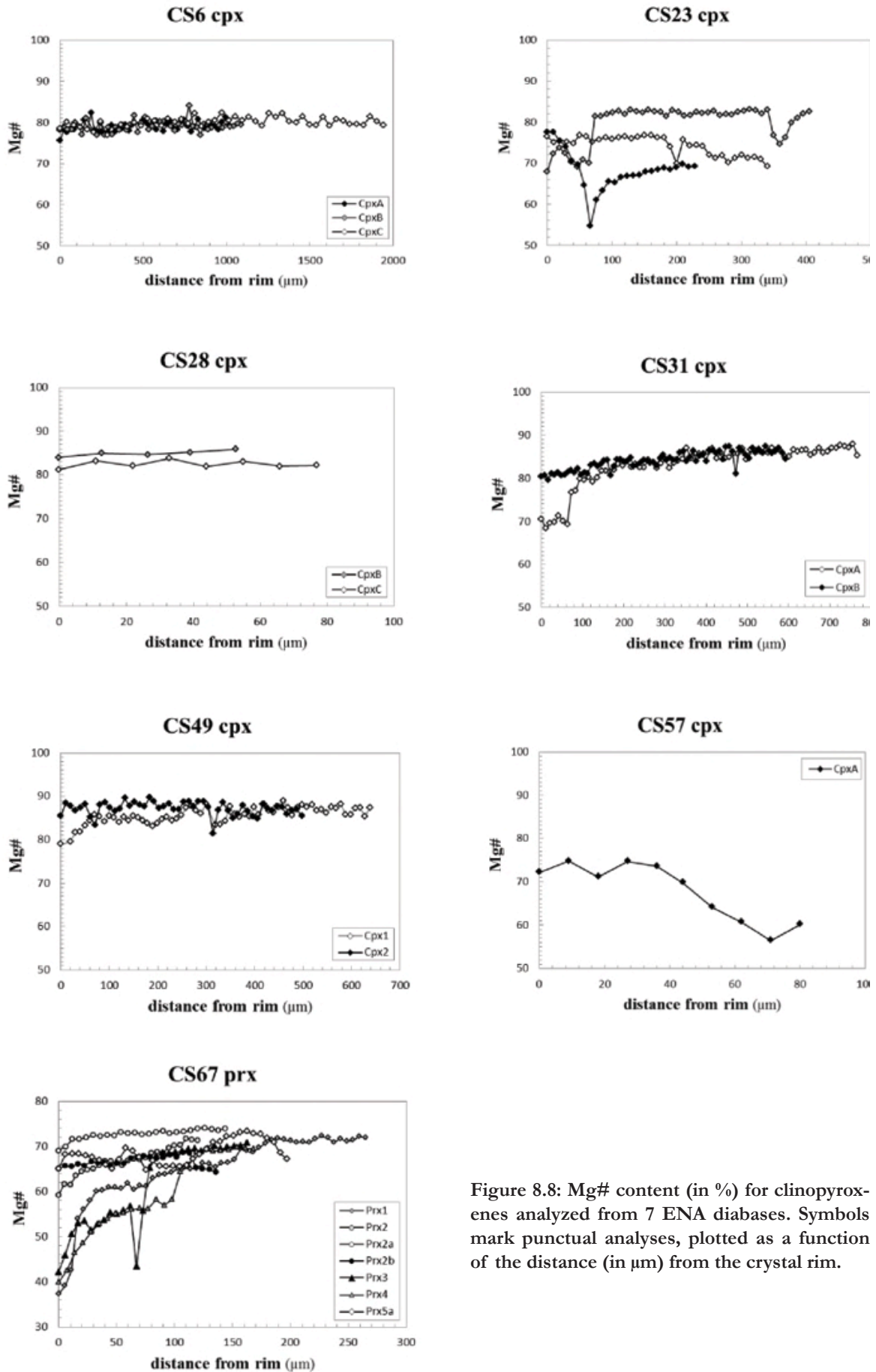


Figure 8.8: Mg# content (in %) for clinopyroxenes analyzed from 7 ENA diabbases. Symbols mark punctual analyses, plotted as a function of the distance (in μm) from the crystal rim.

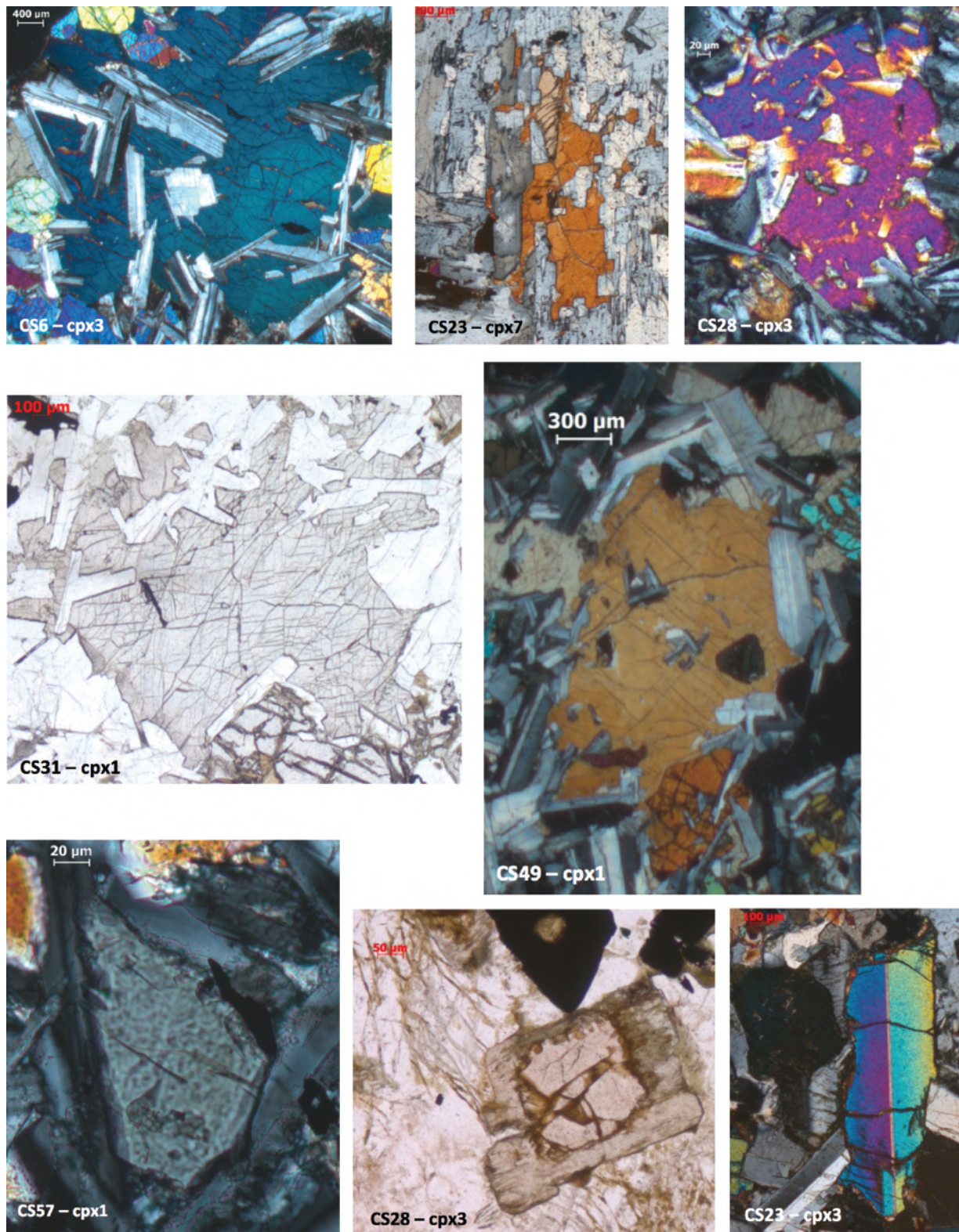


Figure 8.9: Microphotographs (crossed polars, except for CS31-cpx1 and CS28-cpx3, parallel polars) of the analyzed pyroxenes in thin sections from 7 ENA diabases.

8.3 PLAGIOCLASE

Plagioclase crystals were selected from 5 samples, of which CS6, CS31 and CS49 were also chosen to be dated with $^{40}\text{Ar}/^{39}\text{Ar}$ geochronology. Data points of representative compositions for each crystal were calculated and reported in Table 8c. Plotted on the feldspar triangular diagram, plagioclases show a labradoritic-bytownitic composition, ranging from An_{55} to An_{77} .

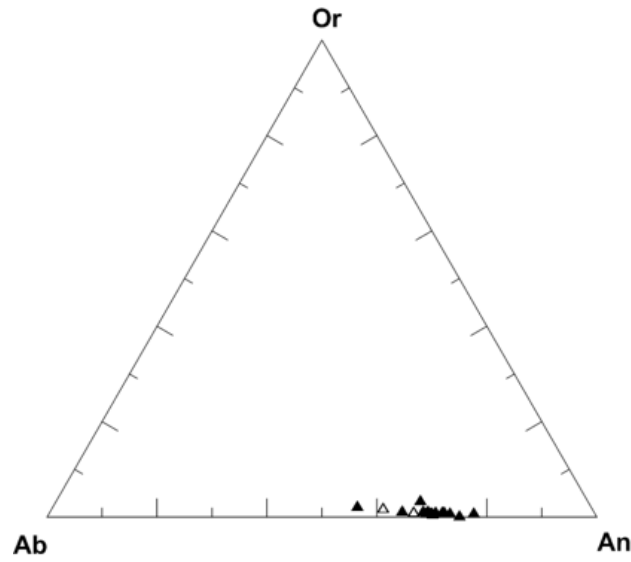


Figure 8.10: Triangular diagram for feldspars (averaged compositions), classifying plagioclases from ENA tholeiites as labradorites and bytownites. Black triangles for crystals from LFO rocks, white for HFO. Or: orthoclase, Ab: albite, An: anorthite.

	SiO ₂ wt%	Al ₂ O ₃ wt%	FeO wt%	MgO wt%	CaO wt%	Na ₂ O wt%	K ₂ O wt%	Total	Ab%	An%	Or%
CS6 plgA avg	49.90	31.63	0.49	0.09	14.50	3.11	0.18	99.90	27.6	71.3	1.1
CS6 plgD core	51.91	29.97	0.44	0.08	12.76	3.88	0.31	99.36	34.9	63.3	1.8
CS6 plgD rim	55.75	27.65	0.58	0.07	10.16	5.47	0.47	100.14	48.0	49.3	2.7
CS28 pl2 core	48.97	28.15	3.44	2.12	14.81	2.32	0.16	99.96	21.9	77.2	1.0
CS28 pl8	51.58	30.29	0.87	0.21	13.03	3.91	0.24	100.14	34.7	63.9	1.4
CS31 plgC core	47.23	33.97	0.70	0.00	17.12	1.74	0.09	100.85	15.4	84.0	0.5
CS31 plgC rim	55.35	27.96	0.69	0.34	9.97	5.15	0.47	99.93	47.0	50.2	2.8
CS49 plg4 avg	49.55	31.56	0.82	0.16	14.62	2.92	0.18	99.82	26.2	72.7	1.0
CS57 plgB avg	49.38	31.90	0.50	0.29	15.19	2.79	0.07	100.13	24.9	74.7	0.4

Table 8c: Significant EMPA data points (expressed in wt% oxides) for analyzed plagioclases.

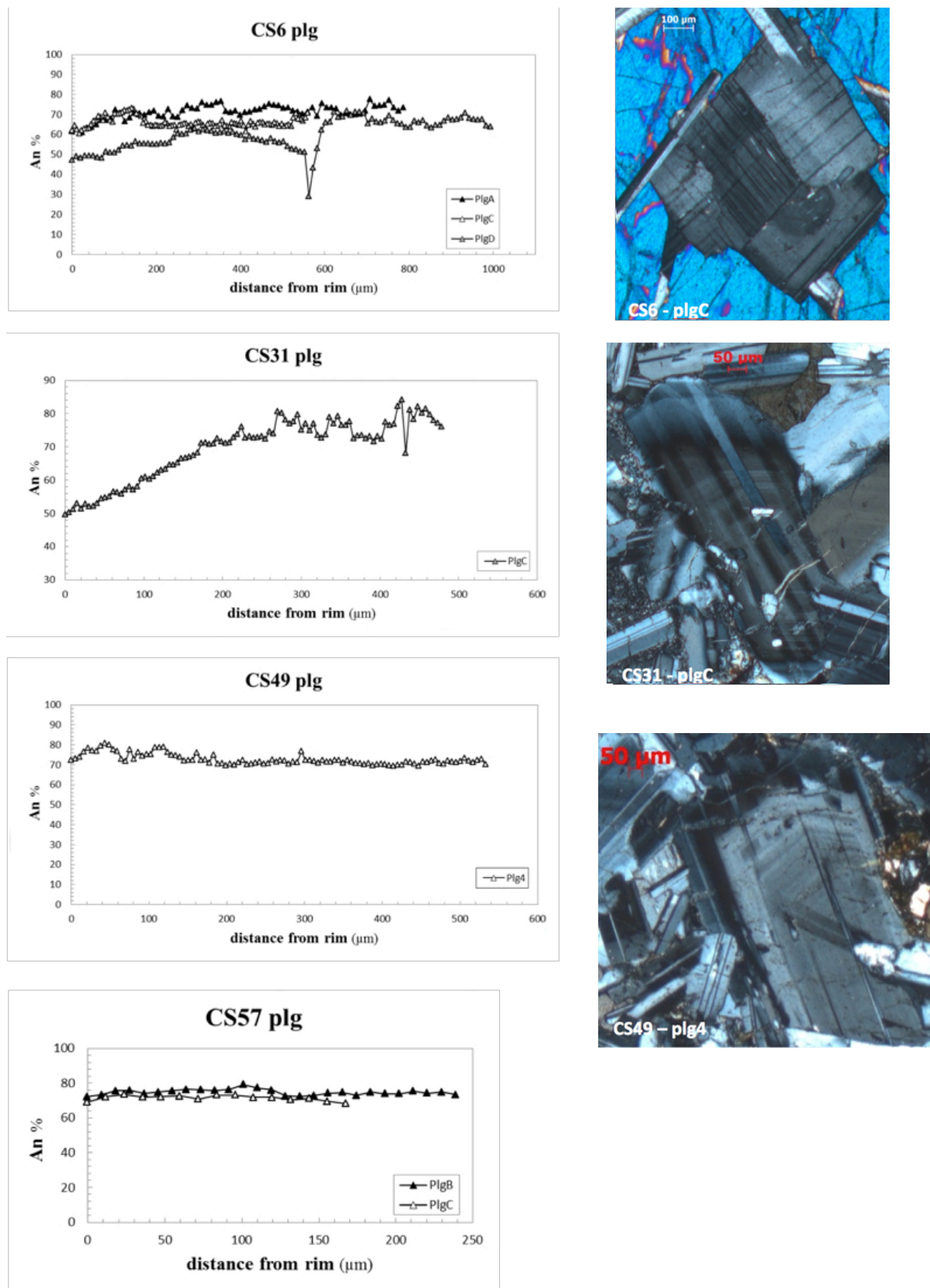


Figure 8.11: Anorthite content (in %) for 7 plagioclases analysed from 4 ENA diabbases. Triangles mark punctual analyses, plotted as a function of the distance (in μm) from the crystal rim. Microphotographs on the right side (crossed polars) show examples of analyzed plagioclases from three coarse grained samples.

Analyzed plagioclase crystals from CS49 and CS57 are very uniform, containing around 70% Ca component, anorthite (An_{70}). Large crystals (up to 800 μm) from CS6 and CS31 show a global normal zoning, with An decreasing from core to rim from 75 to 50 % in CS31 and with crystal rims being up to 16 mol% less calcic in CS6. From this latter sample a plagioclase was analyzed with a uniform, less anorthitic core (An_{64}) surrounded by a more anorthitic rim (An_{70-73}), which in turn shows a smooth normal zoning from An_{73} to An_{62} (Fig. 8.11). Crystal cores from sample CS31 show some oscillatory zoning and its maximum range in anorthite is from An_{84} to An_{50} . Plagioclase crystals from CS28 were selected from the groundmass, and were not large enough to perform analytical traverses. Punctual analyses on 10 crystals resulted in a significant range of compositions, from An_{77} to An_{55} .

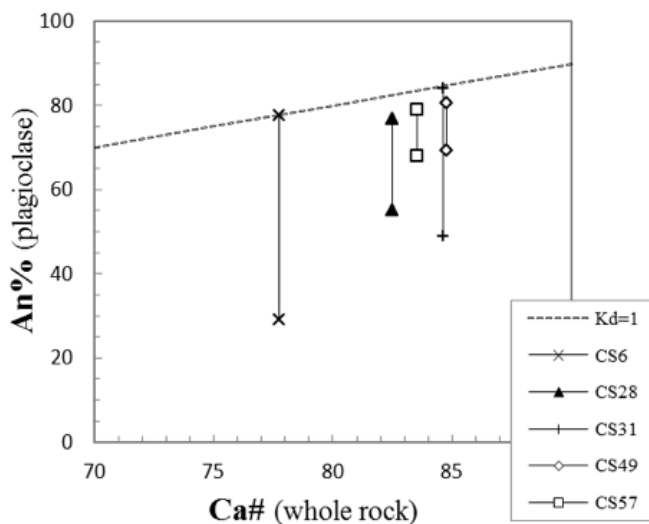


Figure 8.12: Rhodes diagram for analyzed plagioclase crystals from 5 samples. Plagioclase/melt equilibrium line drawn with a $K_D(\text{Ca-Na})_{\text{plagioclase/liquid}}$ of 1 (Aigner-Torres et al., 2007).

Plagioclase crystal cores from samples CS6 and CS31 appear in equilibrium with the melt, represented by the Ca# (calculated as $\text{Ca}/(\text{Ca}+\text{Na}) \times 100$) of the whole rock. Crystal core of plagioclase C (sample CS6) is An_{64} , thus plotting below the equilibrium line. This disequilibrium may be due to its early stage crystallization, from a melt whose composition is no more represented by the observed whole rock. The other samples, CS28, CS49 and CS57 yielded plagioclases slightly lower in anorthite than what requested by the equilibrium condition, thus implying a certain Ca enrichment of the whole rock, possibly due to plagioclase accumulation. A $K_D \text{Ca-Na}^{\text{mineral/melt}}$ of 1 was applied, in agreement with near-anhydrous character of ENA tholeiites (Aigner-Torres et al., 2007).

8.4 OXIDES

EMPA analyses of Fe, Ti and Cr oxides were performed on 6 ENA diabbases (CS15, CS26, CS28, CS49, CS59, CS77). In particular, care was taken in analyzing oxides in the groundmass as well as enclosed in other phenocrysts (olivine, clinopyroxene and plagioclase). Some representative examples of the 111 punctual analyses are listed in Table 8d. A few crystals were large enough to allow several analyses from core to rim to be performed. Crystals from CS28 were analyzed with a different setup (i.e. Ni was not analysed). Oxides from sample CS15 (LFO) enclosed in phenocrysts (orthopyroxene and olivine) are Cr-spinel (~ 30 wt% Cr_2O_3), while those selected within the groundmass are Ti-magnetites (~ 12 wt% TiO_2), while those. The same happens in sample CS26 (HFO), but with different compositions, i.e. Ti-magnetites are higher in Ti (~ 20 wt% TiO_2) and chromites are lower in Cr (~ 20 wt% Cr_2O_3). Oxides from sample CS28 (LFO) were all selected from the groundmass and show a variety of oxides, i.e. ilmenite (~ 46 wt% TiO_2), Ti-magnetite (~ 6 wt% TiO_2) and chromite (25-30 wt% Cr_2O_3). The same variety is observed for oxides from CS49 that yielded ilmenite (~ 48 wt% TiO_2), Ti-magnetite ($\sim 12\%$ TiO_2) and chromite (23-25 wt% Cr_2O_3) in the interstices between larger crystals. CS59, a LFO sample texturally intersertal, shows Ti-magnetite with variable Ti content (13-17 wt% TiO_2), and chromite (20-24 wt% Cr_2O_3) in the groundmass. Oxides were also analyzed within olivine (Ti-magnetite and chromite), in clinopyroxene (Ti-magnetite) and in plagioclase (chromite). Enclosed oxides are richer in Ti than those in the groundmass. Oxides from sample CS77 (LTQ), a porphyritic, intersertal diabase are Ti-magnetites (13 wt% TiO_2) in the groundmass, while chromites, richer in Cr than those from the other samples (35 wt% Cr_2O_3), are enclosed in plagioclase crystals.

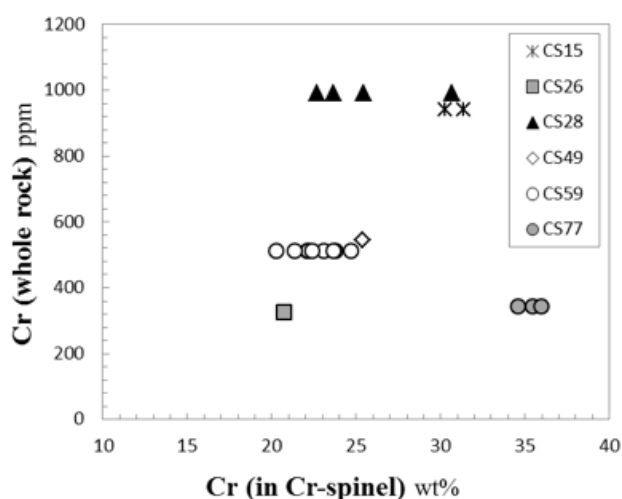


Figure 8.13: Cr_2O_3 content (in %) in Cr-spinel crystals plotted against Cr content (in ppm) in the respective whole rocks.

With the exception of sample CS77, Cr content in the Cr-spinel crystals is coupled with bulk-rock Cr, thus composition of the melt controls the composition of the oxides. CS77, though low in Cr (<400 ppm), crystallizes Cr-spinel with the highest Cr₂O₃ content (around 35%).

		MgO wt%	Al ₂ O ₃ wt%	SiO ₂ wt%	TiO ₂ wt%	V ₂ O ₅ wt%	Cr ₂ O ₃ wt%	MnO wt%	FeO wt%	NiO wt%
CS15 ox1	Ti-magnetite	0.10	2.08	0.218	12.84	0.679	0.025	1.253	77.46	0.073
CS15 ox3 in opx	chromite	12.54	29.62	0.144	0.39	0.177	31.376	0.255	25.27	0.207
CS15 ox4	Ti-magnetite	0.04	2.35	0.182	13.08	0.590	0.046	1.325	77.40	0.027
CS15 ox5	Cr-Ti spinel	0.93	2.75	0.472	9.22	0.504	8.779	0.734	71.69	0.000
CS15 ox6 in ol	chromite	13.54	29.26	0.320	0.44	0.161	30.267	0.195	24.61	0.170
CS26 ox1	Ti-magnetite	0.01	0.66	0.128	21.17	0.432	0.050	1.813	72.39	0.006
CS26 ox5	chromite	0.23	1.31	0.162	22.55	0.554	0.096	1.627	70.34	0.056
CS26 ox3 in ol	chromite	12.26	33.22	1.839	1.03	0.220	20.747	0.215	30.08	0.139
CS28 ox A	ilmenite	2.29	0.07	0.179	46.07	0.625	0.015	0.377	48.20	-
CS28 ox D	Ti-magnetite	0.17	1.08	0.084	6.41	1.343	0.042	0.778	83.75	-
CS28 ox D6	chromite	8.05	26.83	3.010	1.28	0.266	25.440	0.263	33.77	-
CS28 ox D7	chromite	12.71	30.58	0.103	0.52	0.118	30.696	0.269	25.10	-
CS49 ox1	Ti-magnetite	1.00	1.73	0.830	11.96	0.716	0.037	0.597	75.30	0.097
CS49 ox3	ilmenite	4.21	0.14	0.015	48.93	0.279	0.034	0.506	45.07	0.019
CS49 ox2 in ol	chromite	1.48	4.72	0.064	3.20	0.923	7.677	0.295	76.23	0.132
CS49 ox9	chromite	2.44	6.34	0.033	0.86	0.775	25.368	0.381	59.66	0.089
CS59 ox1 in ol1	chromite	16.19	40.08	0.140	0.27	0.069	23.803	0.252	19.74	0.299
CS59 ox2 in cpx	Ti-magnetite	0.17	3.06	0.327	18.96	0.782	0.056	1.667	71.08	0.008
CS59 ox4	Ti-magnetite	0.00	3.43	0.242	13.33	0.698	0.041	1.189	76.66	0.014
CS59 ox9 in plg1	chromite	13.46	37.55	0.767	0.35	0.147	23.107	0.288	24.45	0.223
CS59 ox12	chromite	16.57	41.72	0.206	0.22	0.104	22.153	0.210	19.35	0.323
CS59 ox14	Ti-magnetite	0.16	3.25	0.486	12.46	0.906	0.027	0.870	75.88	0.063
CS59 ox13 in ol4	chromite	16.64	37.18	2.282	0.26	0.157	23.632	0.173	20.79	0.299
CS59 ox17 in ol1	Ti-magnetite	0.01	2.77	0.198	17.49	0.703	0.057	1.444	72.82	0.037
CS59 ox18	Ti-magnetite	0.01	2.61	0.231	17.78	0.751	0.083	1.400	72.71	0.001
CS77 ox7	Ti-magnetite	0.06	2.10	0.246	12.51	0.690	0.000	1.751	77.76	0.000
CS77 ox8	Ti-magnetite	0.21	2.15	0.488	12.91	0.685	0.054	2.056	76.37	0.055
CS77 ox9	Ti-magnetite	0.00	2.26	0.209	13.15	0.741	0.007	1.947	77.14	0.000
CS77 ox10 in plg1	chromite	12.56	26.66	0.094	0.39	0.199	35.443	0.275	25.13	0.185
CS77 ox11 in plg1	chromite	12.89	27.12	0.080	0.41	0.194	34.563	0.262	24.96	0.122
CS77 ox12 in plg1	chromite	12.57	26.14	0.104	0.35	0.199	35.953	0.247	24.82	0.208

Table 8d: Representative examples of the EMPA analyses on oxides from 6 different ENA tholeiites.

9 GEOTHERMOBAROMETRY

From the Rhodes diagram clinopyroxenes cores from sample CS6, CS31 and CS49 appear in equilibrium with the whole rock, therefore they are suitable for estimating crystallization pressures and temperatures basing on the thermo-barometer of Putirka (2008). P and T are calculated starting from the composition of a clinopyroxene core and of its relative whole rock.

Crystallization T results well constrained around 1222-1237°C, while pressure varies more significantly, between 8.5 and 5 kbar.

Pressures and temperatures obtained from augites in disequilibrium with the bulk rock are less precise, in particular for samples where clinopyroxene is clearly not the first liquidus phase. Still, crystallization temperatures obtained for CS28 and CS57 (1243-1295 °C) are concordant with those obtained from augites in equilibrium. The disequilibrium is visible in the imprecise estimation of pressure (4.6-9.5 kbar for CS28, 5.4-9.6 kbar for CS57). A crystal core of an augite from CS23 is also in equilibrium with the whole rock, but results in relatively low crystallization temperature and pressure (1176°C, 3.2 kbar).

a			b				
sample	T (°C)	P (kbar)	sample		T (°C)	err	
CS6	1226	8.0	CS23	aug	pig	1047	±15
CS6	1230	8.5		aug	pig	1196	±63
CS6	1233	8.5	CS31	opx	pig	1145	±69
CS23	1176	3.2		opx	aug	1075	±29
CS28	1243	4.6		pig	aug	1079	±58
CS28	1280	9.5	CS67	pig	opx	1094	±18
CS28	1261	6.3		opx	aug	1107	±222
CS31	1236	5.3		pig	aug	917	±107
CS31	1257	5.8					
CS49	1222	5.0					
CS49	1236	7.0					
CS57	1247	5.4					
CS57	1295	9.5					

Table 9a: A) Crystallization temperatures (°C) and pressures (kbar) calculated on augite cores (on single analytical points), after Putirka (2008). B) Equilibrium temperatures calculated at 5 kbar for pyroxenes pairs with Quilf 4.0 (Andersen, 1993).

Coexisting augites and pigeonites (or orthopyroxenes) from samples CS23, CS31 and CS67 at a pressure of 5 kbar give equilibrium crystallization temperatures (after Andersen, 1993) between 917 and 1196°C (with uncertainties between ±15°C and ±222°C), i.e. 100-200°C lower than those estimated following Putirka (2008). However, since these are crystallization temperatures for low-Ca pyroxenes (i.e. pyroxenes whose crystallization starts at lower T), results from both the geothermometers are reasonable.

Starting from pressures obtained with Putirka (2008) thermo-barometer, crystallization temperatures for olivine (Fig. 9.1 a) were estimated basing on the olivine-liquid equilibrium, again following Putirka (2008). In particular, the calculation was carried out for olivine cores from samples CS28 and CS57, which are in equilibrium with the whole rock composition. Thus, crystallization temperatures of 1350 ± 15 °C and 1325 ± 15 °C were obtained for olivine cores from CS28 and CS57, on an anhydrous base and at pressures of 9 and 5 kbar, respectively.

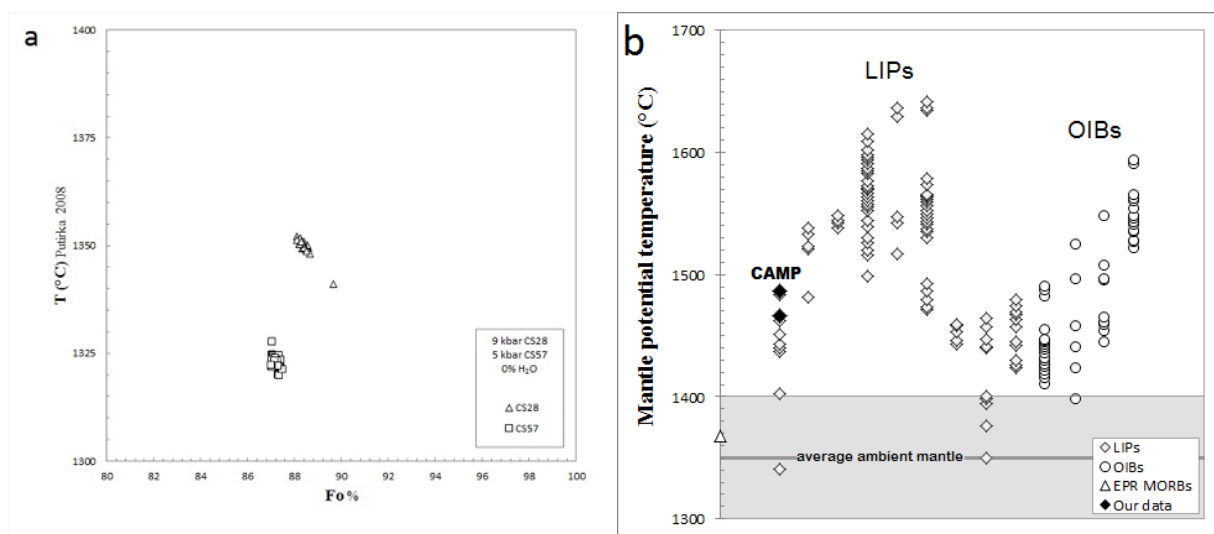


Figure 9.1 a-b: a) Crystallization temperatures (°C) calculated with Putirka (2008) thermo-barometer for 2 olivine phenocrysts from ENA tholeiites. b) TP obtained for CS28 and CS57 compared to mantle potential temperatures (T_p) obtained for different volcanic provinces by Herzberg and Gazel (2009).

Mantle potential temperature (T_p) is defined as the temperature that the solid adiabatically convecting mantle would attain if it could reach the surface without melting (McKenzie and Bickle, 1988). Using the equilibrium temperatures for olivine cores and the P conditions previously obtained from clinopyroxene compositions, a T_p of 1487 and 1466 °C is calculated after Putirka (2008), based on the approach of Roeder and Emslie (1970). These values are in agreement with those published for the CAMP by Herzberg and Gazel (2009). They calculated mantle T_p ranging between 1330 and 1480 °C for CAMP primary magmas, even though the majority of values plot on a more restricted range (1430-1480 °C; Fig. 9.1 b), entirely above the potential temperature range of the average ambient mantle (1300-1400 °C).

The ILMAT geothermometer (Lepage, 2003) was applied to the oxides analyzed from sample CS28, the only analyzed sample yielding ilmenite crystals. Magnetite-ilmenite pairs were thus used to calculate the oxygen fugacity (fO_2) and the equilibrium T between the two oxides. Resulting temperatures (following Andersen & Lindsley, 1985) are rather low (770-750°C) and on a T- $\log fO_2$ diagram oxides pairs are aligned, but do not parallel any fO_2 buffer curve (plotting at higher $\log fO_2$ and at angle to the Nickel-Nickel Oxide buffer curve, Fig. 9.2). They thus reflect a possible sub-solidus re-equilibration at still relatively high temperatures, and cannot be used to infer oxides crystallization T or fO_2 condition of the melt.

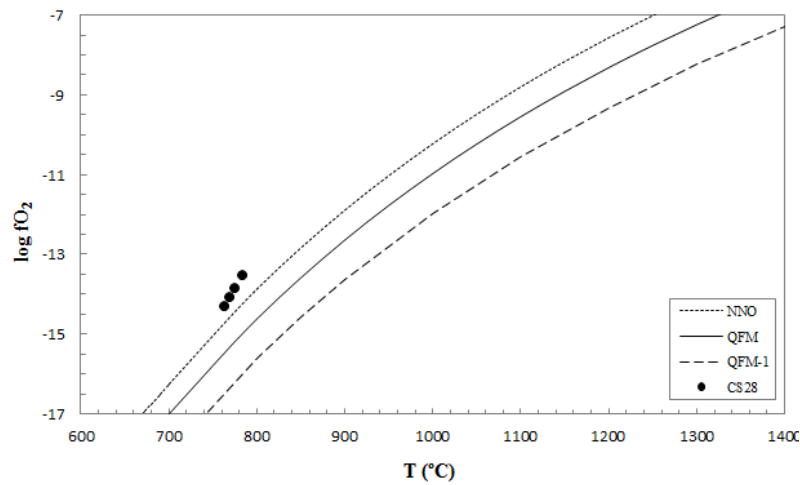


Figure 9.2: Oxygen fugacity (in \log_{10} units) vs temperature ($^{\circ}C$) values calculated with ILMAT geothermometer (Lepage, 2003) for oxides from sample CS28.

10 PETROGRAPHY

ENA dykes and sills display simple mineralogical assemblages, typical of diabasic or doleritic rocks and may be petrographically divided into two groups that broadly modally reflect their normative composition (CIPW olivine-hyperstene or quartz normative), i.e. olivine phyric and pigeonite-granophyre bearing diabases. The olivine-phyric diabases show phenocrysts of plagioclase (An_{47-84}), augite ($En_{33-56}Fs_{9-30}Wo_{17-42}$), olivine (Fo_{48-89}), orthopyroxene and oxides (Ti-magnetite, ilmenite, Cr-spinel). The others, devoid of olivine phenocrysts, contain plagioclase and augite of broadly similar compositions, as well as pigeonite, which is never present in the olivine-bearing diabases) and in some cases thin granophyric intergrowths of K-feldspar and quartz in the groundmass. Oxides are present as well in this second group. Warner & Wasilewski (1985) showed Ti-magnetite to be the main oxide phase in olivine-hyperstene normative ENA diabases, while ilmenite is more common in quartz normative diabases. Primary sulphides are also observed in some of the sampled rocks. Devitrified glass and hydrous minerals (amphibole, chlorite, biotite, zeolites) are present in the groundmass, as hydrothermal or alteration phases. Amygdules and vugs are filled in some cases with secondary zeolites or carbonates. Alteration phases such as serpentine and iddingsite on olivine crystals are observed in some rocks as well as clay minerals coating plagioclases, and amphiboles substituting pyroxenes. A broad grain spectrum is observed for these rocks, varying continuously from nearly aphyric (smaller dykes and margins of the thicker dykes) to sub-pegmatitic (Durham sill) and ranging from equigranular, to seriate, to strongly porphyritic. All textural shades are observed, from porphyritic to intersertal, from intergranular to ophitic, regardless of the different grain sizes. Porphyritic rocks show coarse grained olivine (rarely plagioclase and clinopyroxene) phenocrysts in a microcrystalline to glassy groundmass (e.g. sample CS28, Fig. 10.1 a). This texture is typically found in chilled margins or in small dykes. Alteration appears to preferentially affect the groundmass, partially eluding phenocrysts. Intersertal rocks show randomly oriented, euhedral, plagioclase and pyroxene phenocrysts, with a glassy (or devitrified) matrix filling the spaces in between (Fig. 10.1 b). Intergranular rocks show fine grained, mostly anhedral, pyroxene crystals occupying the interstices between euhedral plagioclases. In some samples intersertal portions grade to intergranular, and this change can be observed even at the thin section scale. Diabases from the thickest dykes

or from the internal, slowly solidified portion of the dykes, show ophitic textures in which coarse grained pyroxene crystals encompass plagioclase smaller laths (Fig. 10.1 c).

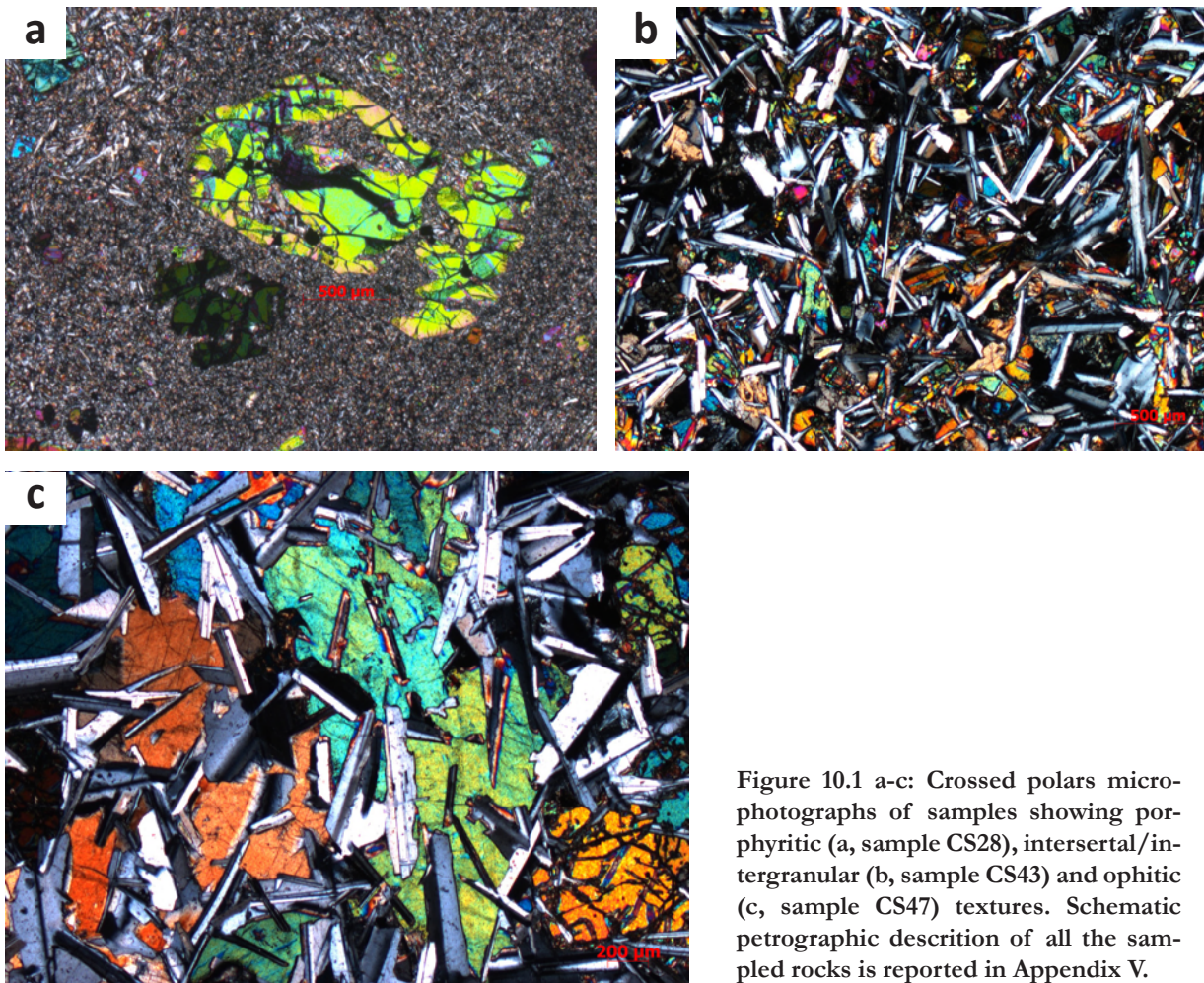


Figure 10.1 a-c: Crossed polars microphotographs of samples showing porphyritic (a, sample CS28), intersertal/intergranular (b, sample CS43) and ophitic (c, sample CS47) textures. Schematic petrographic description of all the sampled rocks is reported in Appendix V.

11 OBSERVATIONS ON THE DATA

The main whole-rock and mineral composition features of the analyzed dykes and sills from the SE-USA are listed here and will be discussed in the following chapters.

The studied diabases display decoupled major elements vs trace elements and isotopic compositions. The dykes and sill can be subdivided in four clearly distinct groups in terms of CIPW norm as well as for major (Si, Fe, Ca, Al, Ti) and compatible trace elements (Sc and V). To group samples basing on criteria other than normative composition has proven unworthy, since no systematic geochemical characteristics are observed between groups based on a) direction of the dykes or b) geographic position (including both latitude and country rock intruded, an approach followed by e.g. Pegram, 1990).

Except for U/Pb, Th/Ce, Th/Nb ratios being highest in quartz-normative diabases, all the rocks yield rather uniform, depleted incompatible element contents, show negative Ti and Nb and positive Pb anomalies on multielement diagrams and rather flat REE patterns (i.e. La_{Ch}/Yb_{Ch} : 0.54-2.60), resembling those from enriched MORBs. Sr-Nd-Pb isotopic compositions are not clearly correlated with major and trace element compositions and show a very large variability, covering the almost the entire isotopic compositional field for low-Ti CAMP rocks in Sr-Nd space (0.70438-0.70880; 0.51251-0.51204), and falling largely out of it in Pb-Pb spaces. Pb isotopic values ($^{206}Pb/^{204}Pb_{200Ma}$: 17.46-18.85, $^{207}Pb/^{204}Pb_{200Ma}$: 15.54-15.65, $^{208}Pb/^{204}Pb_{200Ma}$: 37.47-38.76) form a linear array displaced above the NHRL but not parallel to it ($\Delta 7/4$: 10-18, $\Delta 8/4$: 19-73), plotting roughly between EMI and EMII mantle poles. There is good positive correlation between Nd and Pb isotopes, while no covariance is shown by Sr and Pb isotopes. $^{187}Os/^{188}Os_{200Ma}$ are low (0.128 and 0.144) and do not correlate with either Sr, Nd or Pb isotopes. In general, the described geochemical variations are not correlated with geographic position of the dykes (or their orientation). Finally, it should be noted that olivine phenocrysts from some porphyritic samples are high in Fo (up to Fo_{89}) and yield crystallization temperatures around 1325-1350°C (at pressures of 5 or 9 kbar), addressing mantle potential temperatures of 1460°C.

12 CLOSED-SYSTEM MAGMATIC DIFFERENTIATION

The software MELTS (Ghiorso and Sack, 1995) was used to model the closed system magmatic differentiation through fractional crystallization for ENA diabbases. Starting samples were chosen to be representative of their normative groups (CS28 and CS57 for LFO, CS9 for HFO) and to best approximate primitive and near-liquidus magmatic characteristics, i.e. relatively high MgO (12-13 wt%) and porphyritic (rather than intersertal or ophitic) texture. Different pressure conditions spanning the range obtained with clinopyroxene-liquid geobarometry (CS28: 4.6-9.5 kbar; CS57: 5.4-9.6 kbar; cf. Chapter 9) and low water (H_2O : 0 wt% or 0.3 wt%) and oxygen fugacity (constrained to the Quartz Fayalite Magnetite, QFM buffer) were considered as starting conditions (Table 12a).

Liquidus temperatures at 8 kbar and 0.3 wt% H_2O range between 1343° (CS9) and 1457°C (CS28). Starting from LFO composition, fractionation of spinel is followed by an orthopyroxene + spinel assemblage and again by high-Ca clinopyroxene + spinel. Fractionation of high-Ca clinopyroxene starts at 1300°C, in agreement with crystallization T for augites (1247-1295°C) obtained following Putirka (2008).

Starting from HFO composition (with 0.3 wt% H_2O at 8 kbar), spinel is no more the first crystallizing phase, substituted by orthopyroxene. Crystallization of low-Ca clinopyroxene follows (from 1288°C), followed by an assemblage of high-Ca clinopyroxene + feldspar + spinel (Table 12a)

The smooth increase in Al_2O_3 , TiO_2 , Na_2O and P_2O_5 in the residual liquid observed for modeled fractionation at (relatively) high-pressure (8 kbar) well resembles the trends described by LFO ENA dykes compositions for these elements. However, SiO_2 and Fe_2O_3 variations for dykes are not reproduced by the modeled liquid lines of descent, i.e. at 8 kbar Fe_2O_3 should increase with fractionation and SiO_2 should decrease, while the opposite is observed for analyzed samples, suggesting that evolution of LFO dykes is not controlled by high-pressure fractionation.

The same situation is observed for HFO samples, even though, starting from CS9 composition, closed system differentiation results in a late increase in SiO_2 , as oxides (spinel) enter the fractionating assemblage. Again, HFO rocks seem not controlled by high-pressure fractionation.

Setting pressure at 3 kbar and a H₂O content of 0.3 wt% lowers liquidus temperatures to 1338° (CS9) and 1375°C (CS28). Starting from LFO compositions Cr-spinel is the first crystallizing phase, followed by olivine + spinel assemblage. Clinopyroxene starts crystallizing at 1218-1200° forming an olivine + spinel + high-Ca clinopyroxene fractionating assemblage that eventually turns to high-Ca clinopyroxene + low-Ca clinopyroxene + plagioclase. Fractionation from HFO compositions does not see the involvement of spinel, i.e. differentiation is controlled by early olivine fractionation, followed by olivine + high-Ca clinopyroxene + plagioclase fractionation (Table 12a)

For all major element vs MgO variations (Fig. 12.1 a-g), liquid lines of descent resulting from fractional crystallization at 3 kbar are broken, with kinking occurring as fractionation of Fe-Mg minerals (olivine ± spinel) ceases in favor of Ca-Al silicates. First portions of the modeled fractionation curves at 3 kbar well mimic both LFO and HFO trends. This is valid for most of the major elements oxides, with the exception of Fe₂O_{3tot}, whose evolution is not well described by the trend starting from sample CS9 (HFO), i.e. in the modeled trend Fe₂O₃ is decreasing with differentiation, while it is increasing in the analyzed samples. However, data are largely scattered in Fe₂O₃ vs MgO space, and this hinders an unmistakable definition of their co-variation trend.

There is no way to produce HFO compositions from LFO (or vice versa) by fractional crystallization, thus different parental magmas must be at the origin of the two Ol/Hy-normative groups. On the contrary, Q-normative samples plot along the 3 kbar liquid lines of descent for most major elements, thus potentially deriving from LFO or HFO magmas after fractional crystallization processes. However, marked discrepancies between calculated and observed compositions are observed for 1) SiO₂, whose concentration in Q-normative samples is too high to result from fractionation processes, i.e. LTQ and HTQ samples do not plot along the extension of any modeled liquid line of descent; 2) Al₂O₃, that is too low for LTQ samples to be reached with fractional crystallization alone, except if anhydrous conditions are considered allowing for early plagioclase saturation (cf. the liquid line of descent from CS28 at 3 kbar); 3) Na₂O and P₂O₅ in Q-normative samples, which appears too low to be achieved by fractional crystallization alone from primitive Ol/Hy-normative magmas. However, this is partly due to the fact that starting compositions are relatively Na₂O- and P₂O₅-rich. Both LTQ and HTQ samples may potentially derive for fractional crystallization from a LFO magma type. On the contrary, while HFO magmas may result in HTQ differentiated composi-

tions, they do not appear to evolve as LTQ magmas.

Starting composition	P (kbar)	Liquidus T (°C)	Fractionating minerals				(T °C)	Fractionated mass (gm)
CS9 + 0.3 wt% H ₂ O	3	1338					1313	61%
			olivine				1188	17 olivine (Fo ₈₁)
			olivine	high-Ca cpx	feldspar		1163	14 high-Ca cpx
			olivine	high-Ca cpx	low-Ca cpx	feldspar		6 low-Ca cpx 24 feldspar (An ₇₁)
CS9 anhydrous	3	1343	olivine				1318	17%
			olivine	feldspar			1218	14 olivine (Fo ₈₃) 3 feldspar (An ₇₃)
CS9 + 0.3 wt% H ₂ O	8	1388	opx				1356	72%
			low-Ca cpx				1288	13 opx
			high-Ca cpx	spinel			1238	42 high-Ca cpx
			high-Ca cpx	feldspar	spinel		1163	6 spinel 11 ol (Fo ₈₄)
CS28 + 0.3 wt% H ₂ O	3	1375	spinel				1350	58.5%
			olivine	spinel			1325	0.5 spinel
			high-Ca cpx	low-Ca cpx	feldspar	spinel	1200	11 olivine (Fo ₈₄)
								15 high-Ca cpx 13 low-Ca cpx 19 feldspar (An ₇₅)
CS28 anhydrous	3	1395	spinel				1370	3 spinel
			olivine	spinel			1345	6 olivine (Fo ₈₆)
			olivine	spinel	opx		1270.31	2 opx
			high-Ca cpx	low-Ca cpx	feldspar		1252.93	23 high-Ca cpx
			high-Ca cpx	low-Ca cpx	feldspar	spinel	1227.93	21 low-Ca cpx
			olivine	high-Ca cpx	low-Ca cpx	feldspar	spinel	1202.93
CS28 + 0.3 wt% H ₂ O	8	1457	spinel				1432	1 spinel
			opx	spinel			1357	12 opx
			high-Ca cpx	spinel			1307	28 high-Ca cpx
CS57 + 0.3 wt% H ₂ O	3	1368	spinel				1343	0.5 spinel
			olivine	spinel			1293	9 olivine (Fo ₈₄)
			olivine	spinel	high-Ca cpx		1218	23 high-Ca cpx
			high-Ca cpx	low-Ca cpx	feldspar	spinel	1193	5 low-Ca cpx 18 feldspar (An ₇₅)
CS57 + 0.3 wt% H ₂ O	8	1450	spinel				1425	1 spinel
			opx	spinel			1375	10 opx
			high-Ca cpx	spinel			1300	31 high-Ca cpx

Table 12a: Summary of the input parameters for the three starting compositions (first and second column left) and of outputs (liquidus temperature and fractionated assemblages), obtained with MELTS modeling (Ghiorso and Sack, 1995).

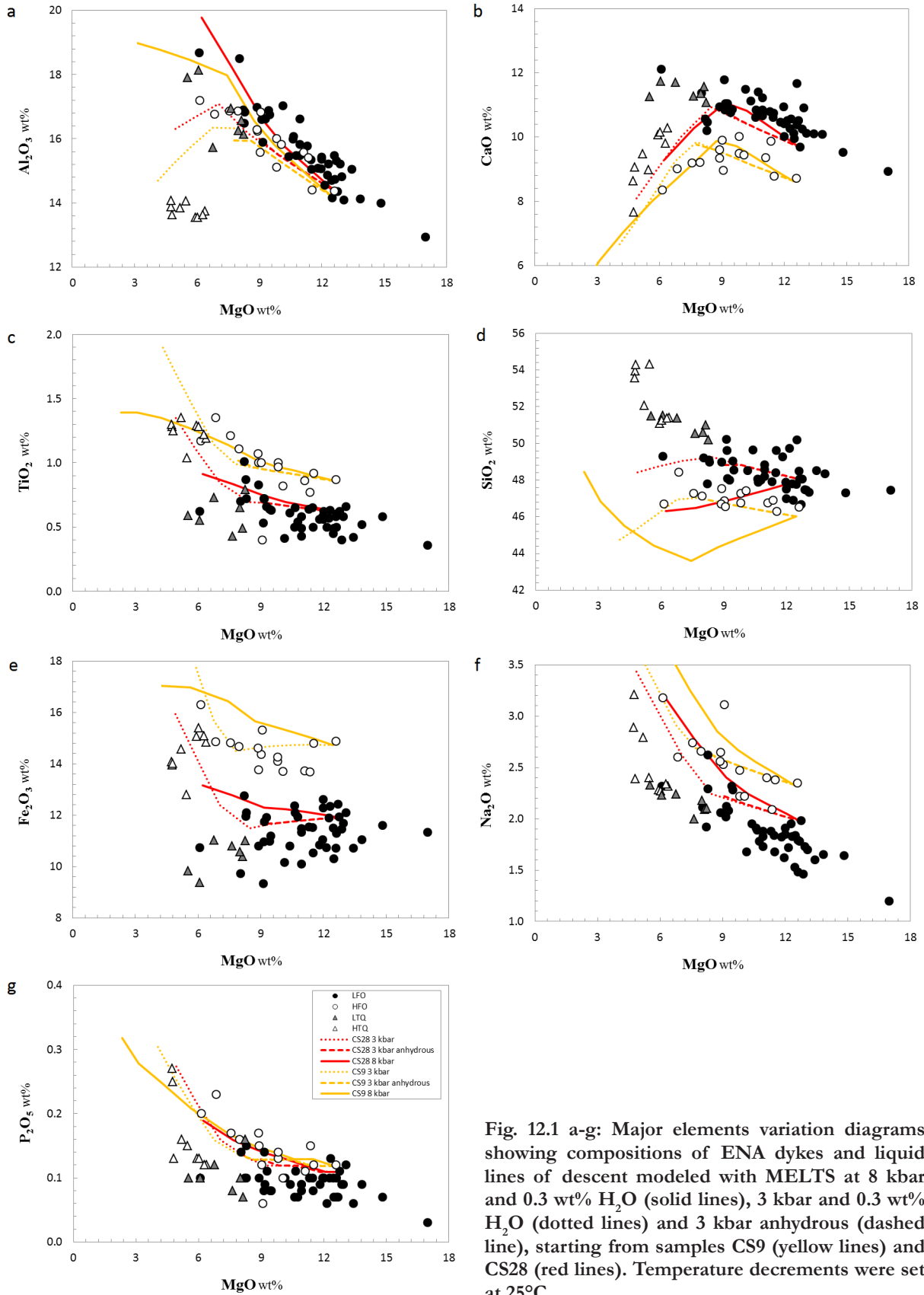


Fig. 12.1 a-g: Major elements variation diagrams showing compositions of ENA dykes and liquid lines of descent modeled with MELTS at 8 kbar and 0.3 wt% H_2O (solid lines), 3 kbar and 0.3 wt% H_2O (dotted lines) and 3 kbar anhydrous (dashed line), starting from samples CS9 (yellow lines) and CS28 (red lines). Temperature decrements were set at 25°C

13 MANTLE MELTING

As shown in Chapter 12 on shallow level closed-system differentiation processes, parental magmas of different compositions are required to explain the distinct compositions of LFO and HFO ENA diabbases, which is most evident in terms of FeO, CaO, SiO₂ and Na₂O contents. Major element compositions of ENA dykes were thus compared to those of melts obtained by experimental (near) anhydrous partial melting of spinel lherzolite and pyroxenite between 10 and 30 kbar (Fig. 13.1 a-e).

Major element compositions of high-Mg LFO samples well overlap those of melts obtained from spinel lherzolite KLB-1 between 1370°C and 1450°C at 20-25 kbar by Hirose and Kushiro (1993) or those issued from a depleted spinel lherzolite at 15 kbar at 1319-1336°C as shown by Robinson et al. (1998). On the contrary, most major element compositions for high-Mg HFO samples are comparable with experimental partial melts of HK-66 spinel olivine-websterite between 1425° and 1500°C at 25-30 kbar (Hirose and Kushiro, 1993). However, these latter experimental melts appear slightly CaO-enriched with respect to HFO diabbases. Relatively low-CaO, high-FeO compositions typical of HFO basalts resemble those of partial melts obtained at 30-50 kbar (around 1500-1600°C) from a mixture of pyrolite and MORB (representing a pyroxenitic mantle source) by Kogiso et al. (1998, 2003), but these experimental melts are in turn either too SiO₂ and Na₂O rich (at 30 kb) or too Al₂O₃ poor and CaO rich (at 50 kbar) to represent parental HFO magmas. The experimental melts best approaching HFO compositions are those obtained by Keshav et al. (2004) from a high-Mg garnet pyroxenite at 20-25 kbar, between 1340° and 1430°C.

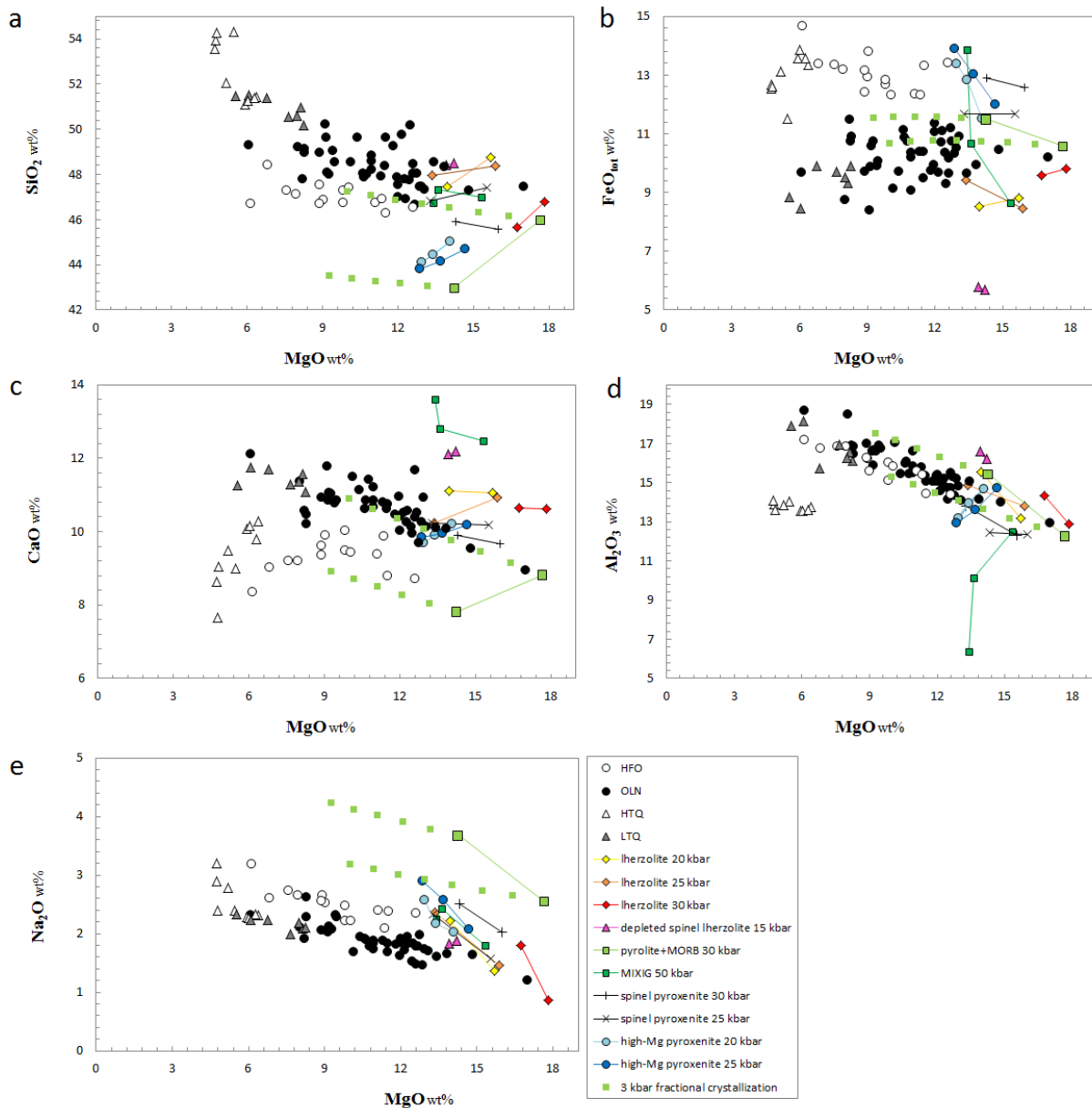


Figure 13.1 a-e: Major elements composition for ENA diabases plotted together with experimental melts of different mantle lithologies. Yellow, orange, red diamonds: experimental melting of Iherzolite and spinel pyroxenite after Hirose et al. (1993); pink triangles: depleted spinel Iherzolite after Robinson et al. (1998); light green squares: pyrolite-MORB mixed compositions after Kogiso et al. (1998); dark green squares: MIXIG low Si-garnet pyroxenite (Kogiso et al. 2003) and light and dark blue circles: high-Mg pyroxenite after Keshav et al. (2004). Small light green squares represent liquid lines of descent for fractional crystallization at 3 kbar (olivine + spinel fractionation) of melts obtained from pyrolite+MORB at 30 kbar (Kogiso et al., 1998), modeled with MELTS (Ghiorso and Sack, 1995).

According to Herzberg and Asimow (2008), a further proxy calling for a pyroxenitic mantle source for HFO ENA diabases is their low CaO content. CaO depletion can also result from removal of clinopyroxene from primitive partial melts, but if fractional crystallization occurs at low pressures (as suggested by closed-system differentiation trends modeled with MELTS, cf. Chapter 12), the drop in CaO would be evident between 10-7 wt % MgO, i.e. only quite evolved HFO magmas can be reflecting this fractionation-linked CaO depletion.

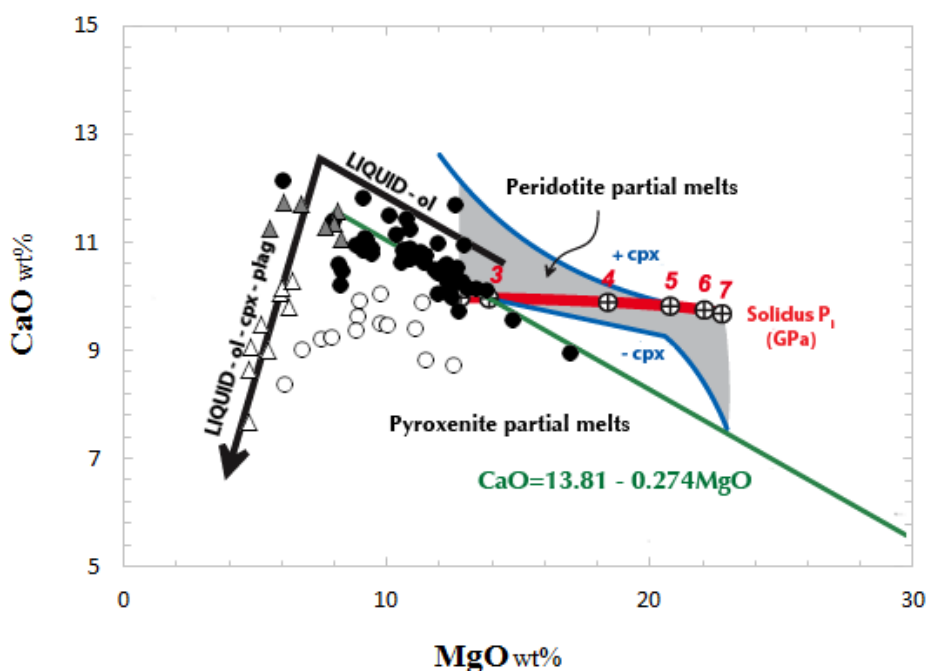


Figure 13.2: CaO and MgO contents in ENA dykes compared with primary magmas produced by accumulated fractional melting of fertile peridotite. According to Herzberg and Asimow (2008), magmas with CaO contents below the green line potentially represent pyroxenite partial melts. A liquid line of descent for crystallization of gabbro in the crust is shown in black. Gray shaded area shows computed CaO and MgO contents of accumulated fractional melts of fertile peridotite (from Herzberg, 2006). Red line joins points of near-solidus melts compositions at different initial melting pressure. Blue lines represent clinopyroxene fractionation filters (cf. Herzberg and Asimow, 2008). (Modified after Herzberg and Asimow, 2008).

Henceforth, two mantle sources of different composition appear to reside at the origin of ENA diabases, i.e. LFO magmas being most probably issued from a (dominantly) peridotitic mantle source (lherzolite) at 20-25 kbar and 1370-1450°C (consistent with estimated olivine crystallization temperatures of 1325-1350°C), and HFO from a (dominantly) pyroxenitic source between 20 and 30 kbar (1340-1500°C).

An independent indication of possible pyroxenitic source components hinges on olivine major and trace element compositions, as underlined by Sobolev et al. (2007). Pyroxenite-derived melts are enriched in SiO_2 and NiO and depleted in MgO, CaO and MnO with respect to those issued from a peridotite at given P and T, and early crystallized olivines would record these features. Primitive (Fo_{86-89}) olivines from LFO samples support a contribution of 40-70% pyroxenitic source in their genesis. This is at odds with what suggested by observations on major elements and REE data, i.e. calling for a spinel peridotitic source for LFO samples.

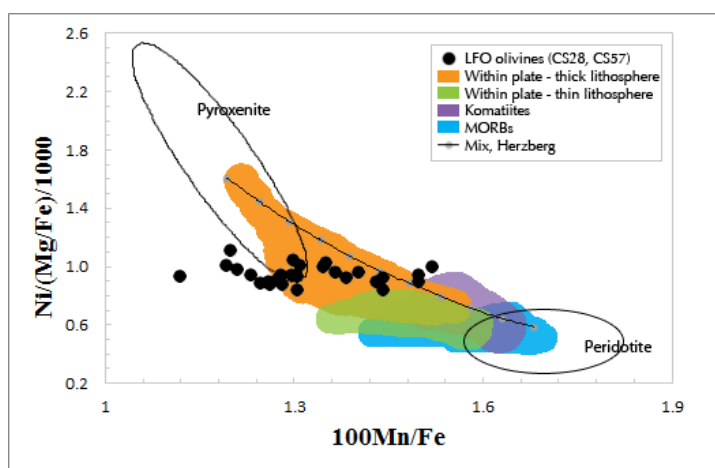


Figure 13.3: To ease the reading, here reported is again Fig. 8.4c. Compositions of high-Fo olivine phenocrysts (from LFO samples CS28 and CS57), plotted with primitive olivine compositions (colored fields) from igneous rocks from different tectonic settings. MIX Herzberg curve represents equilibrium olivine compositions calculated for mixtures (10% steps) of pyroxenite-derived and peridotite-derived melts (modified after Sobolev et al., 2007).

To further constrain the mantle source originating ENA diabases, REE behavior during non-modal partial melting of mantle lithologies was modeled in both fractional and batch mode, at different melting degrees. In particular, La/Yb was used to represent fractionation between LREE and HREE, while Sm/Yb is representative of MREE/HREE ratios. Primitive (McDonough, 1991) to depleted (Workman and Hart, 2005) mantle peridotites were considered as starting compositions, and melting was modeled either within garnet or spinel stability field. Experimental $K_D^{\text{Cpx/melt}}$ for REE measured by Chazot et al. (1996) for melts issued from a lherzolite were used. $K_D^{\text{Mineral/melt}}$ for olivine, orthopyroxene, garnet and spinel are as in Johnston et al. (1998) and references therein. Melting in presence of residual garnet appear at odds with ENA dykes REE patterns (Fig. 6.4). The melting curve best approaching the majority of ENA dykes compositions and in particular LFO samples is the one obtained by 4-10% batch melting of a depleted spinel peridotite (Fig. 13.4 a). Thus, ENA LFO dykes magmas appear to be issued from a REE-depleted mantle source at a considerable extent of melting, as also confirmed by their tholeiitic chemistry, low REE contents and near-flat REE patterns, similar to those observed in enriched-MORBs (Sun and McDonough,

1989). The presence of a (very minor) amount of residual garnet in the mantle source of HFO diabases may be revealed by the slightly higher La/Yb ratios of these samples compared to LFO ones. Indeed, 20-24% batch partial melting of a garnet-bearing peridotitic mantle source (starting from primitive mantle compositions after McDonough, 1991) approaches but does not intersect REE ratios typical of HFO samples (Fig. 13.4). In turn, modeled 10-24% partial melts of a pyroxenitic mantle source (0.4 modal fraction of clinopyroxene, 0.5 of orthopyroxene, 0.1 of either spinel or garnet; Bodinier et al., 2008) well reproduce HFO ENA dykes compositions. If a melting coefficient of 0.45 is considered for garnet, this mineral is consumed after $\sim 22\%$ partial melting, thus low LREE/HREE fractionation observed in these rocks may be due to relatively high melting fraction of a garnet pyroxenite.

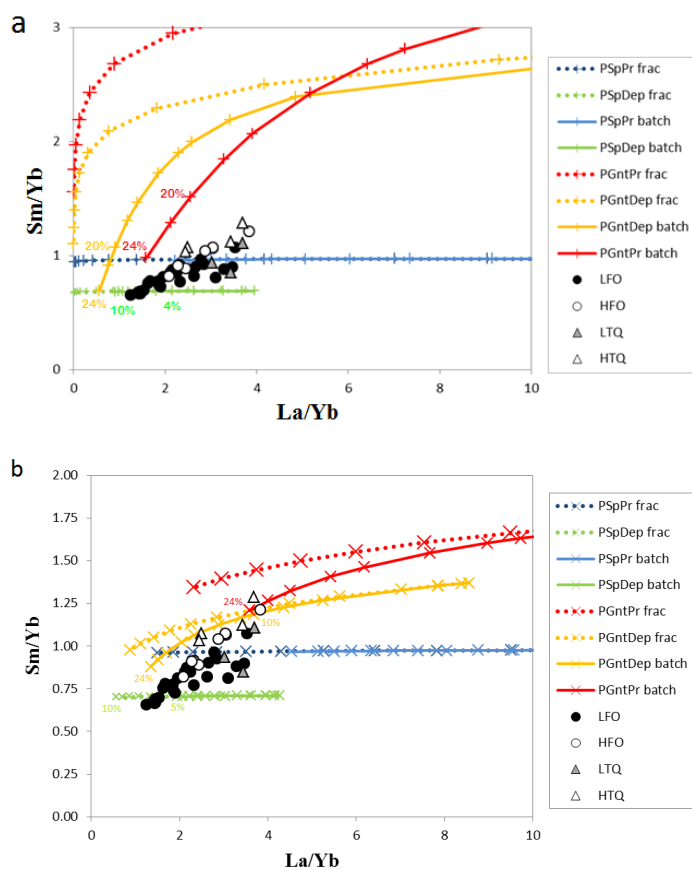


Fig. 13.4 a-b: La/Yb and Sm/Yb ratios in ENA dykes compared to those obtained by batch and fractional melting of a) garnet- and spinel-bearing mantle peridotites (primitive and depleted) and b) by garnet and spinel websterites (olivine-free pyroxenites). Modal compositions for peridotites and pyroxenites according to, respectively, Hirose et al. (1993) and Bodinier et al. (2008).

REE compositions for LFO samples are thus reproduced by partial melting of peridotitic lithologies at a lower degree than that required to replicate HFO compositions, starting from a pyroxenitic source. On the hypothesis of a mixed source partial melting, these estimates would respect the higher fertility (i.e., lower solidus temperature) of mantle pyroxenites with respect to peridotites.

14 OPEN-SYSTEM MAGMATIC DIFFERENTIATION

Despite closed-system processes (fractional crystallization) reproduce reasonably well major element trends observed for ENA dykes, their large spread in isotopic compositions suggests a possible contribution of lower and/or upper crustal contamination.

Magmatic evolution through open-system processes for ENA tholeiitic magmas was modeled for Sr-Nd-Pb and Os isotopes as simple AFC (Assimilation and Fractional Crystallization; DePaolo, 1981), and as EC-AFC (Energy Constrained Assimilation and Fractional Crystallization), following the formulation of Spera and Bohrson (2001).

To model the possible role of crustal contamination in the evolution of ENA diabases, three LFO samples were chosen to represent starting compositions (namely, CS41, CS49 and CS60), given their near-primitive character both in major and trace elements geochemistry and mantle-like isotopic signatures (i.e. low Os and Sr and high Nd ratios). Though sharing similar low $^{187}\text{Os}/^{188}\text{Os}_{200\text{Ma}}$ (1.1278-1.1354), and different but rather depleted Sr and Nd isotopic ratios (0.7043-0.7055 and 0.5123-0.5125, respectively), the three starting samples show very different initial Pb isotopic compositions ($^{206}\text{Pb}/^{204}\text{Pb}_{200\text{Ma}}$ 17.4-18.6; cf. also Table 14a to compare compositions of the three samples).

A fair amount of literature deals with Sr and Nd (and, to a lesser extent, Pb) isotopic compositions of the Eastern North American upper crust. In particular, different areas of the Appalachians were investigated by several authors (e.g. Jones and Walker, 1973; Fullagar and Butler, 1976; Sinha and Zietz, 1982; Pettinghill et al., 1984; Badger and Sinha, 1989; Holm-Denoma and Das, 2010). What arises from this dataset is the extreme variability of Appalachians upper crust in lithology and isotopic composition (e.g. $^{87}\text{Sr}/^{86}\text{Sr}_{200\text{Ma}}$ may vary from 0.7048 to 0.7622 in an area as restricted as the Central Virginia Blue Ridge). Averaging out all the available data appears however to lack geologic significance, given the impossibility to calculate a reasonably precise weighted mean of the isotopic signatures of all the different terrains. Thus the upper crust contamination was modeled starting from a “standard” upper crust with geochemical parameters as in Taylor and McLennan (1995) and with isotopic compositions as in Hoffman (1997) and in GERM (<http://earthref.org/GERM/>) and GEOROC (<http://georoc.mpch-mainz.gwdg.de/georoc/>) web databases. Analyses of lower

crustal rocks (from terrains or xenolithes) are lacking for the Southern Appalachians, thus reasonable compositions (i.e., concentration and isotopic signatures of Sr-Nd-Pb) for the lower crust were estimated following reports of Grenvillian (i.e., Meyzen et al., 2005) or different age lower crust (Bohrson and Spera, 2001; Hoffmann, 1997; Jourdan et al., 2007) from other areas. Trace element concentrations for the lower crust was taken as in Rudnick and Fountain (1995). Os compositions (concentration and isotopes) for the upper and lower crust were estimated starting from Saal et al. (1998), Shirey and Walker (1998) and Heinonen et al. (2010). Thermodynamic characteristics of the upper and lower crust were set following Bohrson and Spera (2001).

a

	CS41	CS49	CS60	ref.	UC	ref.	UC2	ref.	LC	ref.
Magma liquidus T (°C)	1380	1380	1380	estimated (MELTS)	1000	Bohrson e Spera 2001	1000	Bohrson e Spera 2001	1100	Bohrson e Spera 2001
Assimilant liquidus T (°C)					300	Bohrson e Spera 2001	300	Bohrson e Spera 2001	600	Bohrson e Spera 2001
Assimilant initial T (°C)					700	estimated	700	estimated	950	Bohrson e Spera 2001
Assimilant solidus T (°C)					1100	estimated	1100	estimated	1100	estimated
Equilibration T (°C)					1370	Bohrson e Spera 2001	1370	Bohrson e Spera 2001	1388	Bohrson e Spera 2001
Isobaric specific heat (J/kg)	1484	1484	1484		270000	Bohrson e Spera 2001	270000	Bohrson e Spera 2001	350000	Bohrson e Spera 2001
Crystallization enthalpy (J/kg)	396000	396000	396000	Bohrson e Spera 2001	350	Taylor & McLennan 1995	350	Taylor & McLennan 1995	421	Meyzen et al. 2005
Fusion enthalpy (J/kg)					0.9	GERM	0.9	GERM	0.5	GERM
Sr (ppm)	97	148	88		0.71400	GERM	0.71400	GERM	0.70800	GERM
KD (Sr)	0.5	0.5	0.5	GERM	26.0	Taylor & McLennan 1995	26.0	Taylor & McLennan 1995	21.0	Meyzen et al. 2005
(⁸⁷ Sr/ ⁸⁶ Sr) _{200Ma}	0.70552	0.70438	0.70515		0.136	GERM	0.136	GERM	0.19036	GERM
Nd (ppm)	4.5	6.5	5.0		0.5111	Bohrson e Spera 2001	0.5111	Bohrson e Spera 2001	0.5116	Meyzen et al. 2005
KD (Nd)	0.03961	0.03961	0.03961	GERM	20.0	Taylor & McLennan 1995	20.0	Taylor & McLennan 1995	2.6	Meyzen et al. 2005
(¹⁴³ Nd/ ¹⁴⁴ Nd) _{200Ma}	0.5123	0.5125	0.5123		0.56	GERM	0.56	GERM	0.45	GERM
Pb (ppm)	0.8	1.4	1.3		19.40	Hoffmann 1997	19.40	Hoffmann 1997	16.00	Meyzen et al. 2005
KD (Pb)	0.17	0.17	0.17	GERM	15.74	Hoffmann 1997	15.74	Hoffmann 1997	15.50	Meyzen et al. 2005
(²⁰⁶ Pb/ ²⁰⁴ Pb) _{200Ma}	17.421	18.612	18.211		39.00	GERM	39.00	GERM	37.00	Meyzen et al. 2005
(²⁰⁷ Pb/ ²⁰⁴ Pb) _{200Ma}	15.54	15.61	15.62		50	Saal 1998	50	Saal 1998	41	Saal 1998
(²⁰⁸ Pb/ ²⁰⁴ Pb) _{200Ma}	37.33	38.33	38.04		0.1	Heinonen 2010	0.1	Heinonen 2010	0.1	Heinonen 2010
Os (ppt)	452	276	310		1.73	estimated (Saal 1998, Shirey & Walker 1998)	0.46	estimated for 600Ma average upper crust	0.9	Saal 1998
KD (Os)	3	3	3	estimated (Saal 1998)						
(¹⁸⁷ Os/ ¹⁸⁸ Os) _{200Ma}	0.1306	0.1354	0.1278							

b

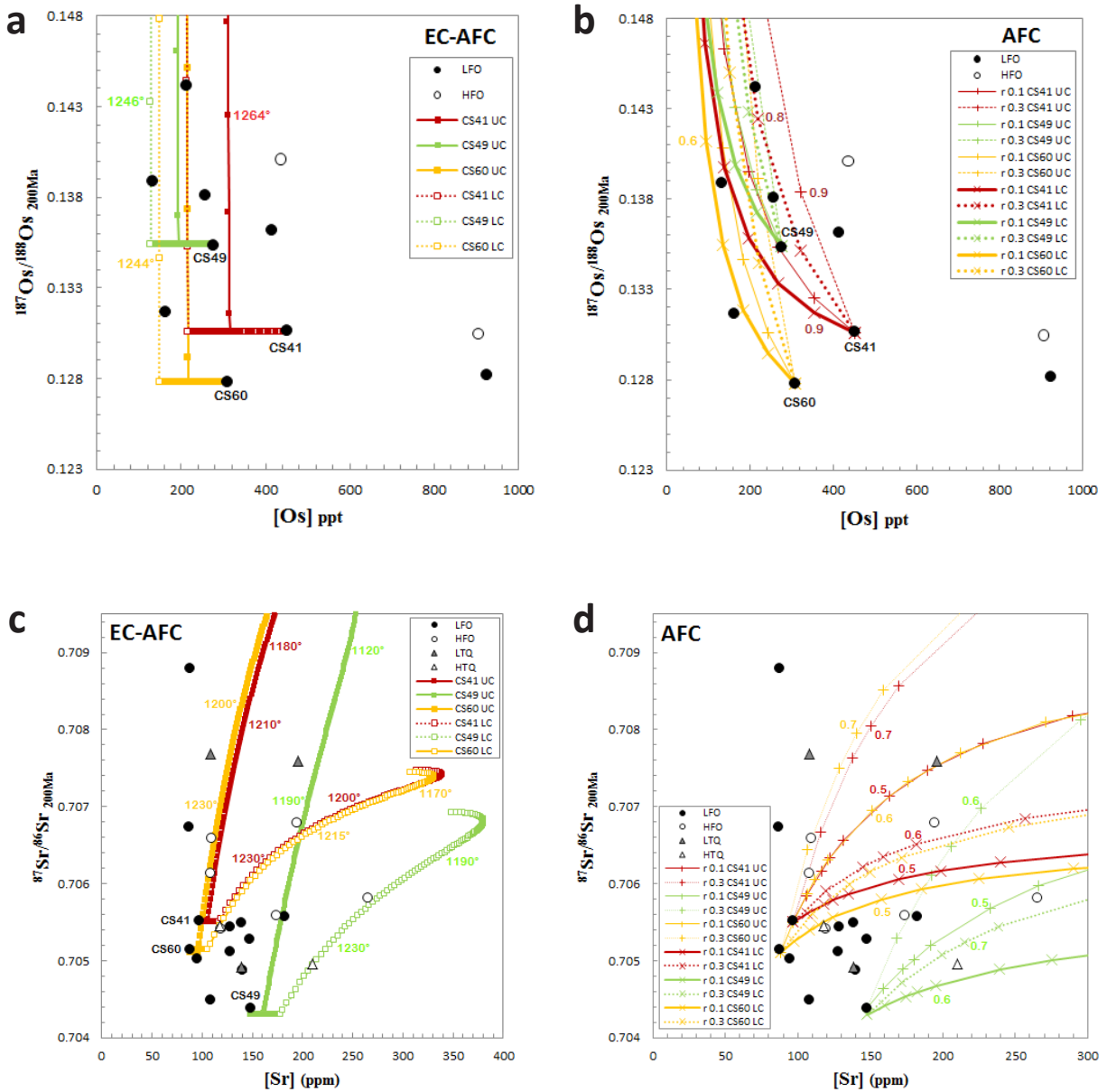
	CS41	CS49	CS60	ref.	UC	ref.	UC2	ref.	LC	ref.
r	0.1, 0.3	0.1, 0.3	0.1, 0.3							
F	0.9, 0.6	0.9, 0.6	0.9, 0.6							
Sr (ppm)	97	148	88		350	Taylor & McLennan 1995	350	Taylor & McLennan 1995	421	Meyzen et al. 2005
KD (Sr)	0.5	0.5	0.5	GERM	0.714	GERM	0.714	GERM	0.708	GERM
(⁸⁷ Sr/ ⁸⁶ Sr) _{200Ma}	0.70552	0.70438	0.70515		26.0	Taylor & McLennan 1995	26.0	Taylor & McLennan 1995	21.0	Meyzen et al. 2005
Nd (ppm)	4.5	6.5	5.0		0.5111	Bohrson e Spera 2001	0.5111	Bohrson e Spera 2001	0.5116	Meyzen et al. 2005
KD (Nd)	0.03961	0.03961	0.03961	GERM	20.0	Taylor & McLennan 1995	20.0	Taylor & McLennan 1995	2.6	Meyzen et al. 2005
(¹⁴³ Nd/ ¹⁴⁴ Nd) _{200Ma}	0.5123	0.5125	0.5123		19.40	Hoffmann 1997	19.40	Hoffmann 1997	16.00	Meyzen et al. 2005
Pb (ppm)	0.8	1.4	1.3		15.74	Hoffmann 1997	15.74	Hoffmann 1997	15.50	Meyzen et al. 2005
KD (Pb)	0.17	0.17	0.17	GERM	39.00	GERM	39.00	GERM	37.00	Meyzen et al. 2005
(²⁰⁶ Pb/ ²⁰⁴ Pb) _{200Ma}	17.421	18.612	18.211		50	Saal 1998	50	Saal 1998	41	Saal 1998
(²⁰⁷ Pb/ ²⁰⁴ Pb) _{200Ma}	15.535	15.609	15.617		0.1	Heinonen 2010	0.1	Heinonen 2010	0.1	Heinonen 2010
(²⁰⁸ Pb/ ²⁰⁴ Pb) _{200Ma}	37.329	38.332	38.039		1.73	estimated (Saal 1998, Shirey & Walker 1998)	0.46	estimated for 600Ma average upper crust	0.9	Saal 1998
Os (ppt)	452	276	310							
KD (Os)	3	3	3	estimated (Saal 1998)						
(¹⁸⁷ Os/ ¹⁸⁸ Os) _{200Ma}	0.1306	0.1354	0.1278							

Table 14a-b: Input parameters for the EC-AFC(a) and AFC (b) modeling and geochemical characteristics of the contaminants, and relative data sources. Isotopic compositions for upper and lower crust were chosen taking into account a Grenvillian to Paleozoic age (1.2-0.4 Ga) for eastern North American crust (cf. Chapter 1). ¹⁸⁷Os/¹⁸⁸Os ratio for the c. 600 Ma Appalachian continental crust at the time of ENA dykes emplacement (200 Ma) was estimated to be around 0.46 starting from a Primitive Upper Mantle isotopic composition of 0.129, a ¹⁸⁷Re/¹⁸⁸Os value of 50 and a λ of 1.666×10⁻¹¹ yr⁻¹ (Shirey and Walker, 1998).

On an EC-AFC base, starting from the above mentioned three supposedly less contaminated (or uncontaminated) samples, the isotopic compositions and Os concentrations of the most radiogenic ones (e.g., CS73: $^{187}\text{Os}/^{188}\text{Os}_{200\text{Ma}}$ 0.144, [Os] 213 ppt) is reached with a very limited amount of assimilation of either upper (0.3-0.8%) or lower (0.8-1.2%) crust, with an M_m (fraction of residual magma; Spera and Bohron, 2001) of, respectively, 0.8 and 0.7. Differences in percentage of assimilated crust rest on which starting sample is considered. Slightly higher (but still quite low) amounts of crustal contribution (ca. 3%) are obtained if a lower $^{187}\text{Os}/^{188}\text{Os}_{200\text{Ma}}$ crustal composition (0.46) is considered. Given the low partition coefficient of Os ($D_{\text{Os}}=0.1$) chosen for the crustal assimilant, and the significant difference in isotopic signatures between crust and mantle-derived magma, contamination proceeds fast, and moderately radiogenic compositions (as for CS73) are soon achieved. Modeling with simple AFC gives slightly different results, i.e. with r (the ratio between assimilation rate over crystallization rate; De Paolo, 1981) set at either 0.1 or 0.3, and F (fraction of residual magma; De Paolo, 1981) ranging between 0.9 and 0.5, 2.5% up to 9.5% assimilation of continental crust is required to reproduce the compositions of the most contaminated samples. It should be noted that crustal contamination on an EC-AFC base, starting from a lower (0.46) $^{187}\text{Os}/^{188}\text{Os}$ signature for the upper crust (reported in Table 14a as UC2) i.e. Hinging on the modeled effect of contamination on Os isotopes, the effects of a comparable amount of crustal assimilation were considered for other isotopic systems (Sr, Nd and Pb).

On element concentration versus isotopic ratio diagrams, the observed general trends and compositions for Sr and Nd are fairly reproduced with assimilation models, but the most enriched data points are reached only through a large amount of crustal contamination, which largely exceeds those derived for Os. In particular, both EC-AFC and AFC assimilation paths well represent ENA dyke trends, but to reproduce radiogenic (e.g. $^{87}\text{Sr}/^{86}\text{Sr}_{200\text{Ma}}$: 0.7067; [Sr]: 108 ppm) Sr compositions through EC-AFC modeling, an upper crustal contamination between 4 and 5% is required (a value confirmed also by AFC modeling). Though not unreasonable in itself, this amount of contamination is an order of magnitude higher than that required to reproduce Os data. The majority of ENA dykes data are intersected by assimilation trends for the upper crust, but some are better represented by lower crustal contamination trends (Fig. 14.1 a-b). Lower crustal assimilation appears to better reproduce the ENA dykes Nd elemental and isotopic compositions by simple AFC modeling, being EC-AFC paths too steep to fit them (Fig. 14.1 c-d). However, while around 3% lower crustal

assimilation is estimated with EC-AFC to reproduce less radiogenic samples (e.g. $^{143}\text{Nd}/^{144}\text{Nd}_{200\text{Ma}}$: 0.5122; [Nd]: 11 ppm), up to 16% appears necessary through AFC modeling. What appears certain, both from Sr and Nd compositions, is that the large spread of isotopic compositions observed cannot be obtained by different amounts of crustal contamination of a single parental magma. Scarce extents of assimilation starting from parental magmas of different initial isotopic compositions must instead be considered.



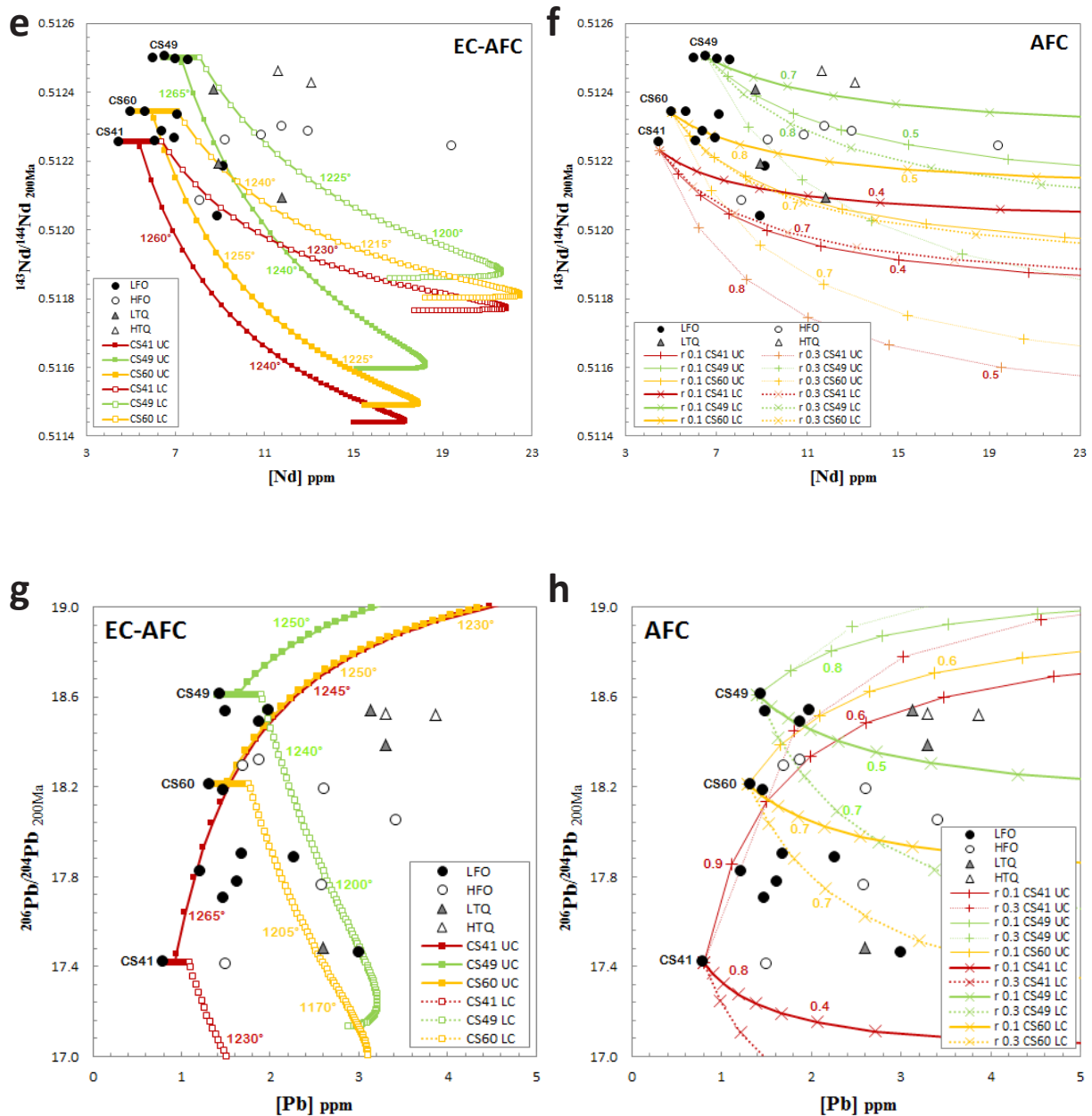


Figure 14.1 a-h: Concentration versus isotope ratios diagrams for Os (a-b), Sr (c-d), Nd (e-f) and Pb (g-h) representing ENA dykes data along with assimilation paths calculated via EC-AFC modeling (left column) and AFC modeling (right column). Tick marks on EC-AFC paths represent steps of 2°C equilibration T (T decreases moving away from starting samples). Tick marks on AFC paths represent 0.1 steps of F (fraction of residual magma). Some ticks are labeled for reference.

A different situation is shown by Pb plots (Fig. 14.1 g-h), because of a) the very different isotopic compositions of the starting samples (i.e. $^{206}\text{Pb}/^{204}\text{Pb}_{200\text{Ma}}$: 17.4-18.6) and b) the considered upper and lower crustal poles plot far apart from each other in Pb compositions, resulting in totally dif-

ferent orientations for calculated contamination paths. Nearly all the ENA dykes data plot within the space enclosed between lower and upper crustal contamination paths starting from the least radiogenic sample (CS41), but they do not plot along, or even parallel, any of the calculated paths. Starting from CS41, the most radiogenic samples (e.g. $^{206}\text{Pb}/^{204}\text{Pb}_{200\text{Ma}}$: 18.5; [Pb]: 1.98 ppm) are reached through 2.5% of upper crustal contamination (EC-AFC), or 1% if CS60 is taken as a parental magma, i.e. the amount of upper crustal contamination is comparable to that calculated for Os. We note however that the positive correlation among Pb isotopes cannot be chiefly due to crustal contamination processes, since samples with very high $^{206}\text{Pb}/^{204}\text{Pb}_{200\text{Ma}}$ (e.g., CS49) yield high Nd and low Sr and Os isotopic compositions which are hardly related to low $^{206}\text{Pb}/^{204}\text{Pb}_{200\text{Ma}}$ samples (e.g. CS41) by crustal assimilation processes. Similarly aberrant results are reached if the whole dataset of Pb isotopic compositions is modeled starting from the highest $^{206}\text{Pb}/^{204}\text{Pb}_{200\text{Ma}}$ samples (e.g., CS49) and considering assimilation of lower crust. In this case, > 20% of assimilation is required (EC-AFC and AFC), an amount totally unreasonable if other isotopic systems are considered (e.g. it would raise $^{187}\text{Os}/^{188}\text{Os}_{200\text{Ma}}$ to 0.36, and such radiogenic signatures are never reached by ENA dykes).

Similar fundamental discrepancies between modeled and observed isotopic variations are observed in combined Sr-Nd-Pb-Os isotopic space. While the general observed Sr-Nd (Fig. 14.2 a-b) or Pb-Nd (Fig. 14.2 c-d) isotopic variations seem to be reproduced at least by AFC trends, it should however be noted that the assimilated component is the upper crust in the first (Sr-Nd) and the lower crust in the second case (Pb-Nd). Furthermore, the needed amounts of crustal contribution (26% for $r = 0.3$, $F = 0.4$; 14.2 a-b and 14.2 c-d, respectively) are so high that they would result in extreme variations of Os isotopic compositions, for example, as well as in much more evolved compositions (e.g., lower MgO) than those observed. While we exclude therefore that the entire set of (isotopic) compositions of ENA-dykes can be reproduced through assimilation processes, starting from a common parental magma, we cannot rule out a moderate contribution of crustal contamination (< 3%), compatible with the observed Os isotopic variations. Such moderate amount of crustal assimilation would only slightly modify the Pb and in particular the Sr-Nd isotopic composition of the contaminated magmas. Upper crust assimilation would shift the Sr isotopic composition from, for example, 0.7043 to 0.7051, $^{143}\text{Nd}/^{144}\text{Nd}$ from 0.5125 to 0.5119 and $^{206}\text{Pb}/^{204}\text{Pb}$ from 18.61 to 18.66, whereas addition 3% of lower crust would instead shift $^{87}\text{Sr}/^{86}\text{Sr}$ from 0.7043 to

0.7049, $^{143}\text{Nd}/^{144}\text{Nd}$ from 0.5122 to 0.5125 and $^{206}\text{Pb}/^{204}\text{Pb}$ from 18.34 to 18.61. That is, shifts in Sr and Nd isotopic ratios are dampened in magnitude if lower crust is added in spite of upper crust, while shifts in Pb isotopes witness a change in direction (i.e. towards less radiogenic signatures in the second case). Another concern that should be pointed out is that while $^{206}\text{Pb}/^{204}\text{Pb}$ signatures are reasonably reproduced by AFC modeling, $^{207}\text{Pb}/^{204}\text{Pb}$ ones are not, i.e. assimilation does not proceed parallel to the ENA dyke alignment in Pb/Pb space, thus resulting in systematically higher calculated $^{207}\text{Pb}/^{204}\text{Pb}$ signatures at a given observed $^{206}\text{Pb}/^{204}\text{Pb}$.

A different situation is shown by Pb plots (Fig. 14.1 g-h), because of a) the very different isotopic compositions of the starting samples (i.e. $^{206}\text{Pb}/^{204}\text{Pb}_{200\text{Ma}}$: 17.4-18.6) and b) the considered upper and lower crustal poles plot far apart from each other in Pb compositions, resulting in totally different orientations for calculated contamination paths. Nearly all the ENA dykes data plot within the space enclosed between lower and upper crustal contamination paths starting from the least radiogenic sample (CS41), but they do not plot along, or even parallel, any of the calculated paths. Starting from CS41, the most radiogenic samples (e.g. $^{206}\text{Pb}/^{204}\text{Pb}_{200\text{Ma}}$: 18.5; [Pb]: 1.98 ppm) are reached through 2.5% of upper crustal contamination (EC-AFC), or 1% if CS60 is taken as a parental magma, i.e. the amount of upper crustal contamination is comparable to that calculated for Os. We note however that the positive correlation among Pb isotopes cannot be chiefly due to crustal contamination processes, since samples with very high $^{206}\text{Pb}/^{204}\text{Pb}_{200\text{Ma}}$ (e.g., CS49) yield high Nd and low Sr and Os isotopic compositions which are hardly related to low $^{206}\text{Pb}/^{204}\text{Pb}_{200\text{Ma}}$ samples (e.g. CS41) by crustal assimilation processes. Similarly aberrant results are reached if the whole dataset of Pb isotopic compositions is modeled starting from the highest $^{206}\text{Pb}/^{204}\text{Pb}_{200\text{Ma}}$ samples (e.g., CS49) and considering assimilation of lower crust. In this case, > 20% of assimilation is required (EC-AFC and AFC), an amount totally unreasonable if other isotopic systems are considered (e.g. it would raise $^{187}\text{Os}/^{188}\text{Os}_{200\text{Ma}}$ to 0.36, and such radiogenic signatures are never reached by ENA dykes).

Similar fundamental discrepancies between modeled and observed isotopic variations are observed in combined Sr-Nd-Pb-Os isotopic space. While the general observed Sr-Nd (Fig. 14.2 a-b) or Pb-Nd (Fig. 14.2 c-d) isotopic variations seem to be reproduced at least by AFC trends, it should however be noted that the assimilated component is the upper crust in the first (Sr-Nd) and the lower

crust in the second case (Pb-Nd). Furthermore, the needed amounts of crustal contribution (26% for $r = 0.3$, $F = 0.4$; 14.2 a-b and 14.2 c-d, respectively) are so high that they would result in extreme variations of Os isotopic compositions, for example, as well as in much more evolved compositions (e.g., lower MgO) than those observed. While we exclude therefore that the entire set of (isotopic) compositions of ENA-dykes can be reproduced through assimilation processes, starting from a common parental magma, we cannot rule out a moderate contribution of crustal contamination (< 3%), compatible with the observed Os isotopic variations. Such moderate amount of crustal assimilation would only slightly modify the Pb and in particular the Sr-Nd isotopic composition of the contaminated magmas. Upper crust assimilation would shift the Sr isotopic composition from, for example, 0.7043 to 0.7051, $^{143}\text{Nd}/^{144}\text{Nd}$ from 0.5125 to 0.5119 and $^{206}\text{Pb}/^{204}\text{Pb}$ from 18.61 to 18.66, whereas addition 3% of lower crust would instead shift $^{87}\text{Sr}/^{86}\text{Sr}$ from 0.7043 to 0.7049, $^{143}\text{Nd}/^{144}\text{Nd}$ from 0.5125 to 0.5122 and $^{206}\text{Pb}/^{204}\text{Pb}$ from 18.61 to 18.34. That is, shifts in Sr and Nd isotopic ratios are dampened in magnitude if lower crust is added in spite of upper crust, while shifts in Pb isotopes witness a change in direction (i.e. towards less radiogenic signatures in the second case). Another concern that should be pointed out is that while $^{206}\text{Pb}/^{204}\text{Pb}$ signatures are reasonably reproduced by AFC modeling, $^{207}\text{Pb}/^{204}\text{Pb}$ ones are not, i.e. assimilation does not proceed parallel to the ENA dyke alignment in Pb/Pb space, thus resulting in systematically higher calculated $^{207}\text{Pb}/^{204}\text{Pb}$ signatures at a given observed $^{206}\text{Pb}/^{204}\text{Pb}$.

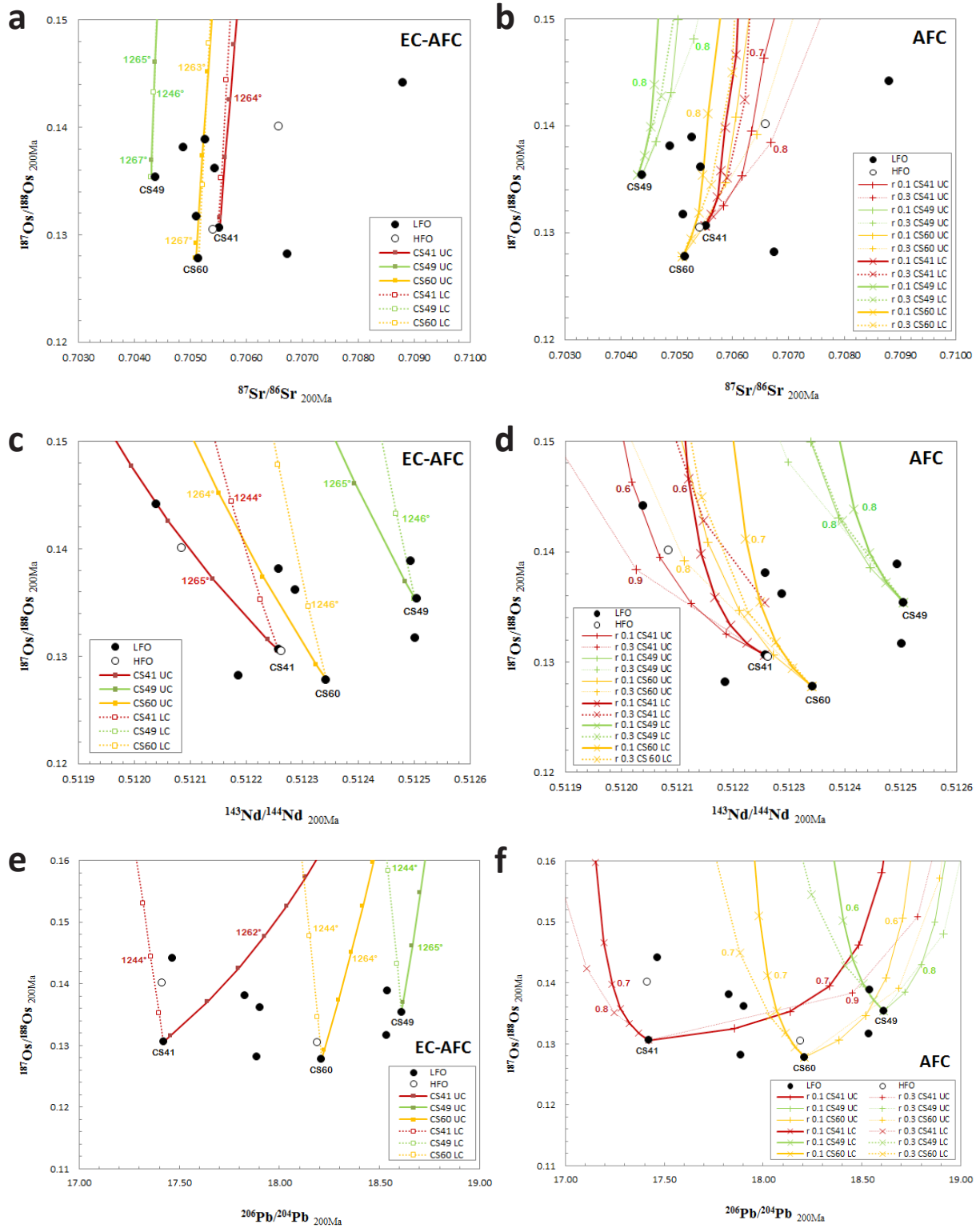
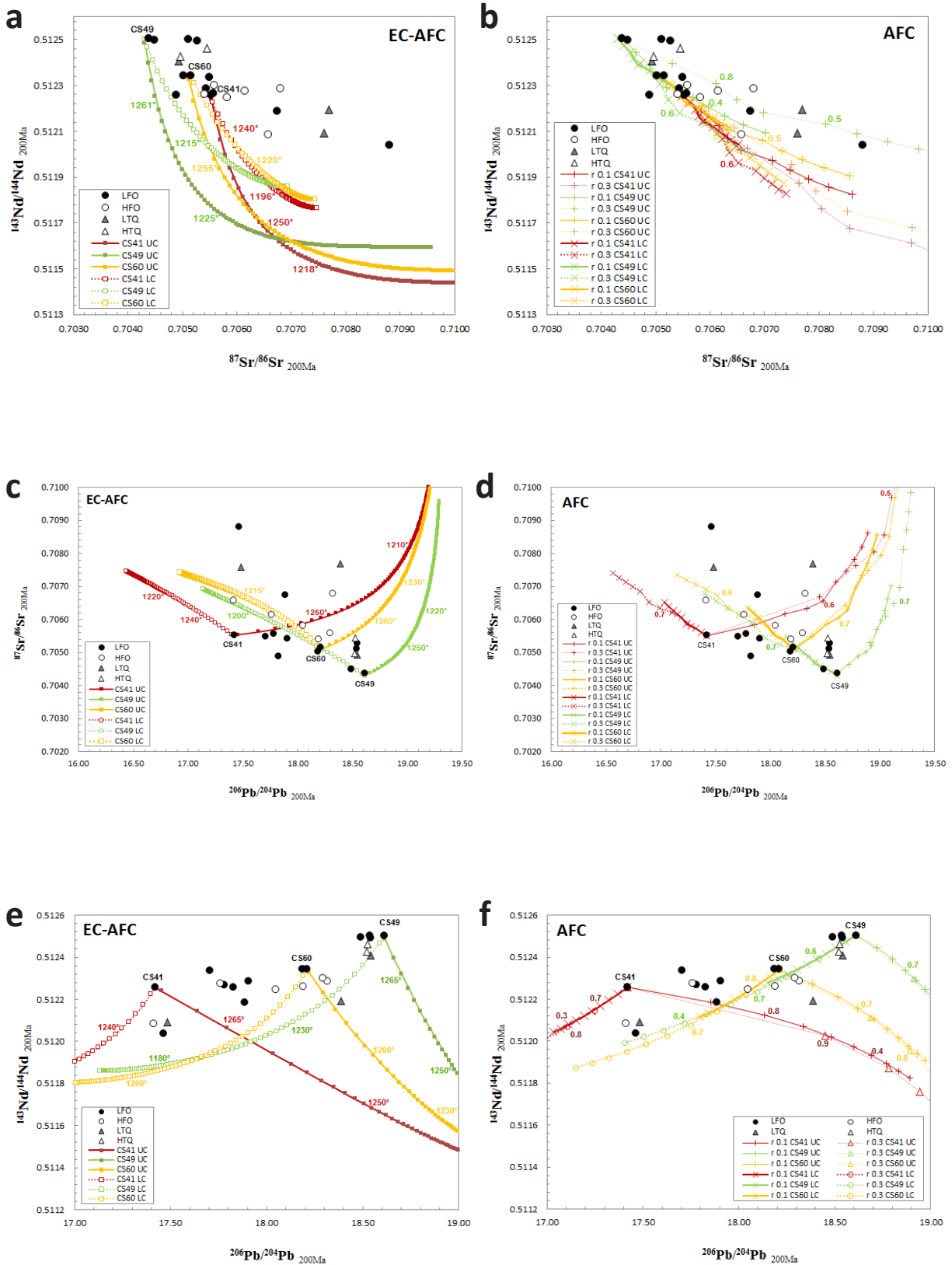


Figure 14.2 a-f: Isotopic ratios diagrams for $^{187}\text{Os}/^{188}\text{Os}_{200\text{Ma}}$, as a function of Sr (a), Nd (b) and Pb (c) isotopes, representing ENA dykes data along with assimilation paths calculated via EC-AFC modeling (left column) and AFC modeling (right column). Tick marks as in Fig.14.1.



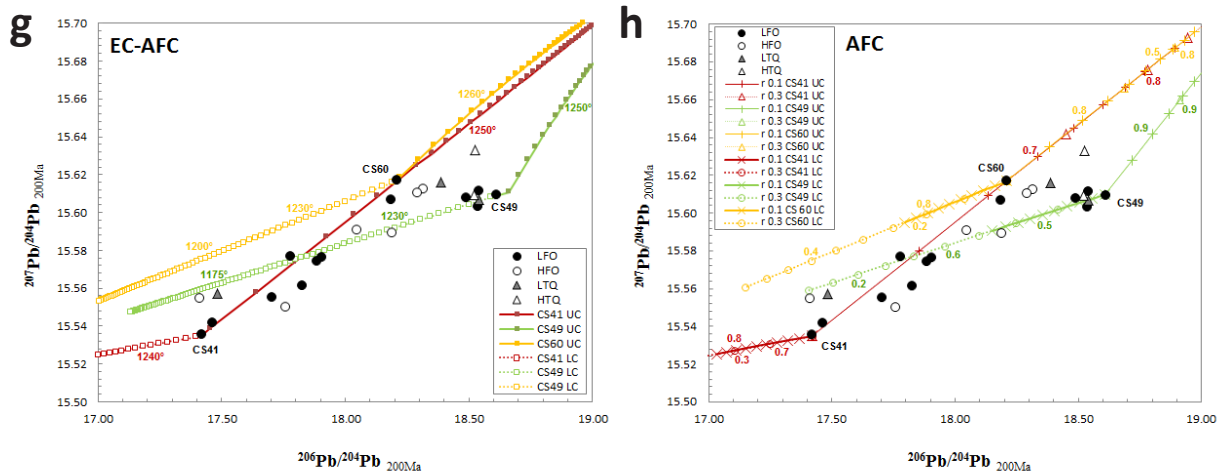


Figure 14.3 a-h: Initial isotopic ratios diagrams for $^{87}\text{Sr}/^{86}\text{Sr}$ against $^{143}\text{Nd}/^{144}\text{Nd}$ (a) and for $^{206}\text{Pb}/^{206}\text{Pb}$ as a function of Sr (b), Nd (c) and $^{207}\text{Pb}/^{204}\text{Pb}$ (d) isotopes, representing ENA dykes data along with assimilation paths calculated via EC-AFC modeling (left column) and AFC modeling (right column). Tick marks as in Fig. 14.1.

In summary, what can be deduced from AFC and EC-AFC modeling of open system differentiation rules out a massive involvement of crustal assimilation processes in producing the vast spread in isotopic compositions for ENA dykes. However, a slight amount of (presumably upper) crustal contamination is conceivable, and would explain small isotopic differences observed among several samples. An upper limit to the amount of this contamination is constrained from Os isotopes to be around 3%. This implies that the observed co-variations and the large diversity in initial isotopic signatures must reside in the mantle source of ENA dykes.

15 ENA DYKES AND NEWARK SUPERGROUP BASINS CAMP FLOWS: A COMPARISON

CAMP is represented in Eastern North America by dolerite dykes and sills and by basaltic and basaltic-andesitic flows (cf. Chapter 1). CAMP flows crop out intercalated to the fluvial-lacustrine sediments filling the rift basins of Culpeper (Virginia), Gettysburg (Maryland-Pennsylvania), Newark (Pennsylvania-New Jersey), Hartford (Connecticut, Massachusetts), Deerfield (Massachusetts), and Fundy (New Brunswick-Nova Scotia), from south to north (Fig. 1.1). A maximum of three groups of flows were recognized in each basin, and detailed geochemical and stratigraphic investigations allowed inter-basinal correlations between different units (Puffer and Student, 1992; Olsen et al. 2003). In this sense, observations referred to Newark units are also referred to correlative flows from the other basins. The Orange Mt. unit from the Newark basin correlates with Mt. Zion Church and Talcott basalts (and the basaltic unit from Gettysburg basin), the Preakness unit with Hickory Grove, Sander and Holyoke basalts, and the Hook Mt. basalts correlate with Hampden ones (Fig. 15.1). Geochemical correlations of the lava flows are mostly based upon incompatible major and trace element contents (e.g., TiO_2 , Nb and REE). A progressive decrease in La/Yb is evidenced, as well as a systematic upsection depletion in incompatible elements (e.g., Tollo and Gottfried, 1982; Marzoli et al., 2011). Geochemical correlations of Newark with the three Fundy basin basaltic lava flow units (cf. Kontak, 2008) is not straightforward (Marzoli et al., 2011), yet in general those flows resemble the Orange Mt. group.

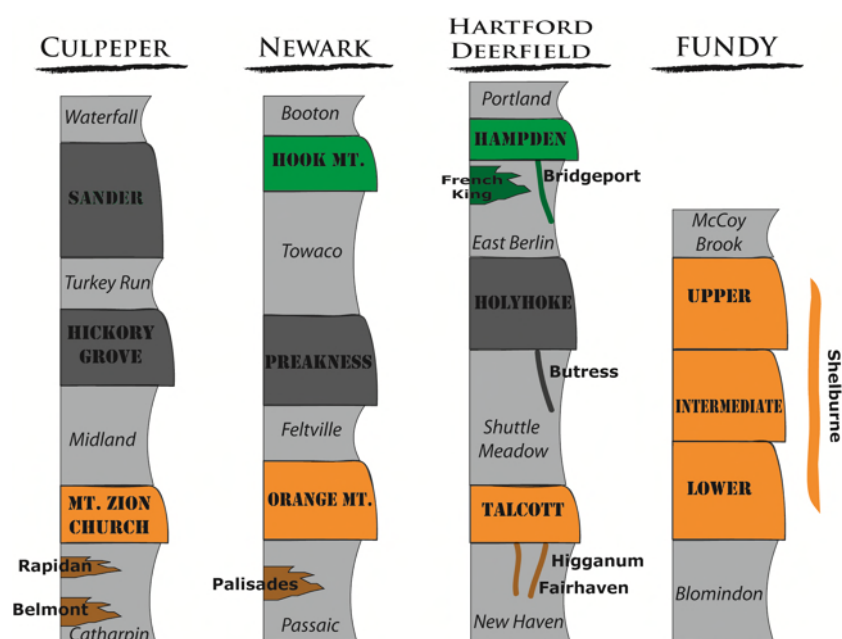


Figure 15.1: Schematic color-coded stratigraphy sequences showing correlations between lava flows in ENA Mesozoic rift basins. Left to right sequence reflects basins latitude, from S to N. Gettysburg basin not shown. (Modified after Marzoli et al., 2011).

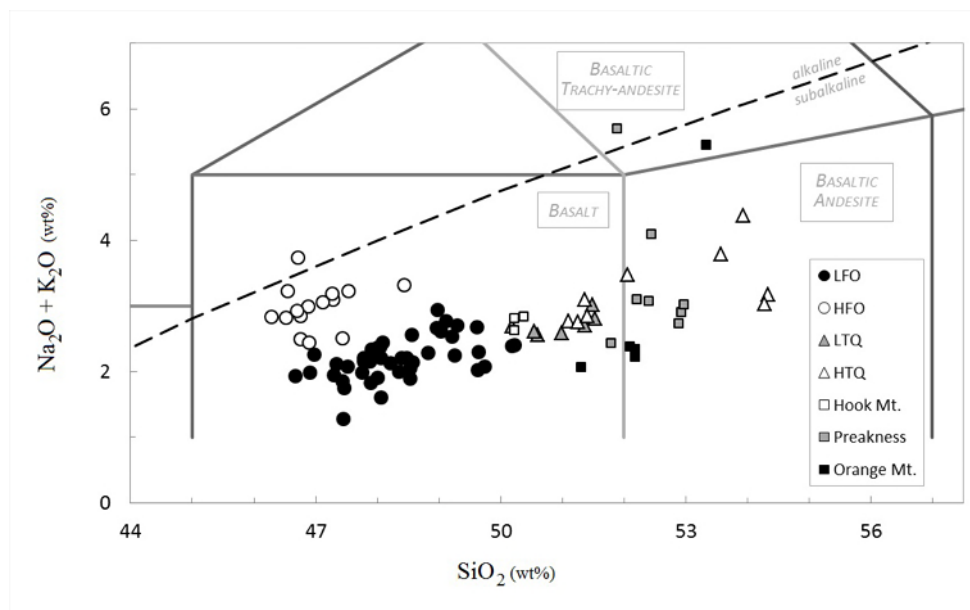


Figure 15.2: Total Alkali versus Silica (TAS; LeMaitre et al. (1989) classification diagram for 74 sampled ENA dykes and sills (circles and triangles) and Newark basins flows (squares).

Orange Mt. and Preakness tholeiites are basalts and basaltic andesites, whereas the Hook Mt. unit consists of basalts only. Newark lava flows are all Q-normative and show generally a much restricted range in major elements compositions compared to ENA dykes, i.e. MgO ranges between 5.5-8.3 wt%, and Al_2O_3 between 12.5-14.9 wt%. All the samples are strictly low-Ti tholeiites ($\text{TiO}_2 < 2$ wt%) as are ENA dykes. However, following the classification of Wiegand and Ragland (1970), both LTQ and HTQ flows are recognized, even if with a narrower compositional range with respect to the dykes (0.8-1.44 wt% vs 0.36-1.35 wt% TiO_2 for ENA dykes). Wiegand and Ragland (1970) classified Orange Mt. basalts (and correlatives) as HTQ, and Preakness lava flows as LTQ rocks, basing on the same definition here used to classify ENA dykes. A high-Ti, high-Fe character (HTFQ) is recognized instead for Hook Mt. flows, which are compositionally very uniform (SiO_2 50.3 wt%, MgO 5.6 wt%), showing the highest TiO_2 (ca. 1.4 wt%) and Fe_2O_3 (ca. 16.7 wt%). Compared to other quartz-normative rocks, Hook Mt. basalts are depleted in SiO_2 at similar MgO contents. However, there appears not to be a good correspondence between major element geochemistry of dykes and flows of the two Q-normative groups. HTQ dykes show major element compositions broadly intermediate between Preakness and Hook Mt. flows. Whereas LTQ do not match Preakness unit compositions as it would be expected. Also, Fe_2O_3 is markedly lower in Orange Mt. flows (11.0-11.6 wt%) than in (similarly classified) HTQ dykes (12.8-15.4). Orange Mt. flows overlap instead HFO dykes in Mg, Ti, K and P contents, but the two groups do not match in Si, Al, Ca, Fe and Na. ENA

flows are all depleted in Al_2O_3 with respect to LFO, HFO and LTQ dykes, i.e. all the flows show Al concentrations compatible with those of the HTQ dykes.

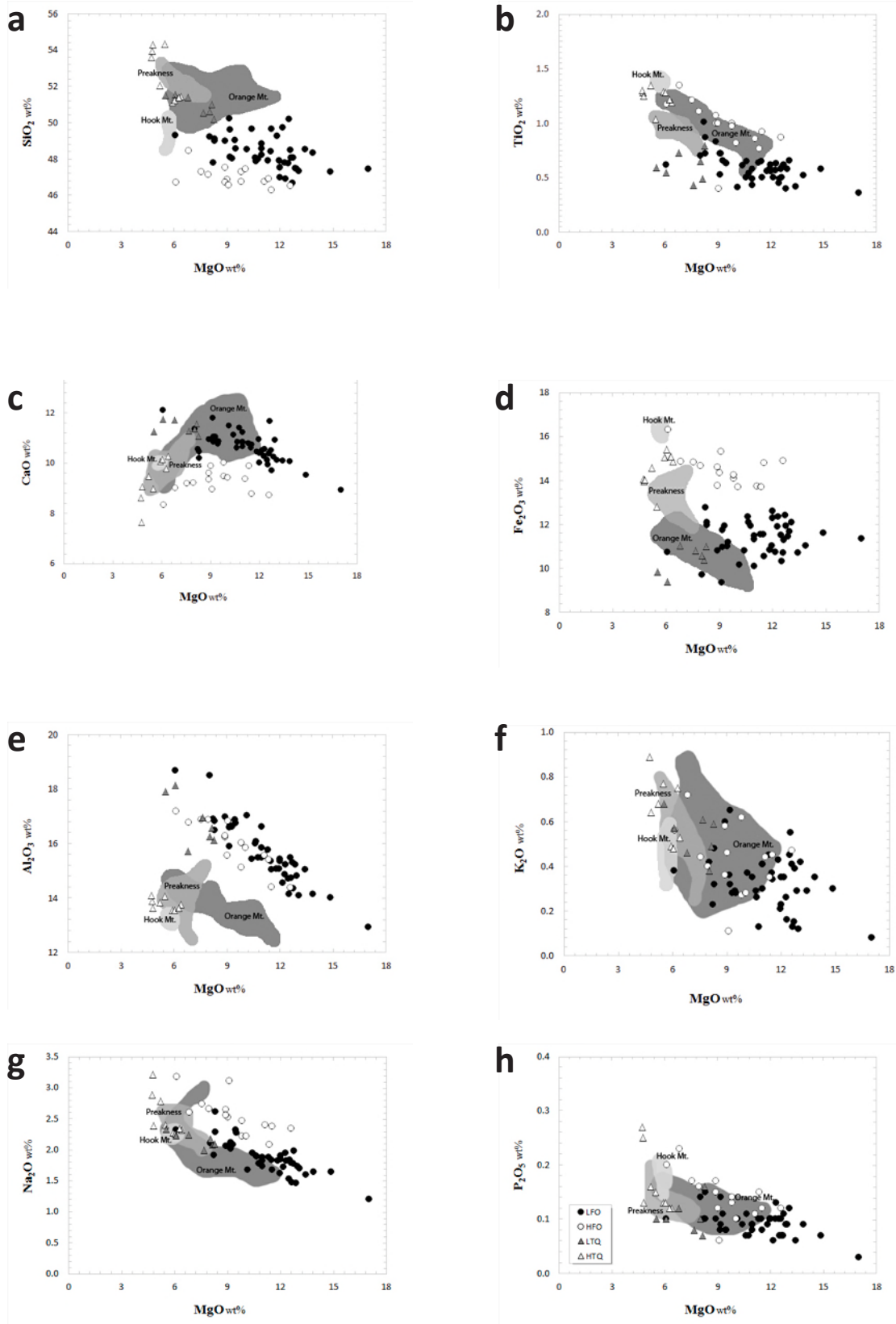


Figure 15.3 g-h: Major elements variation diagrams for ENA diabase samples and ENA flows, shown as grey fields for comparison.

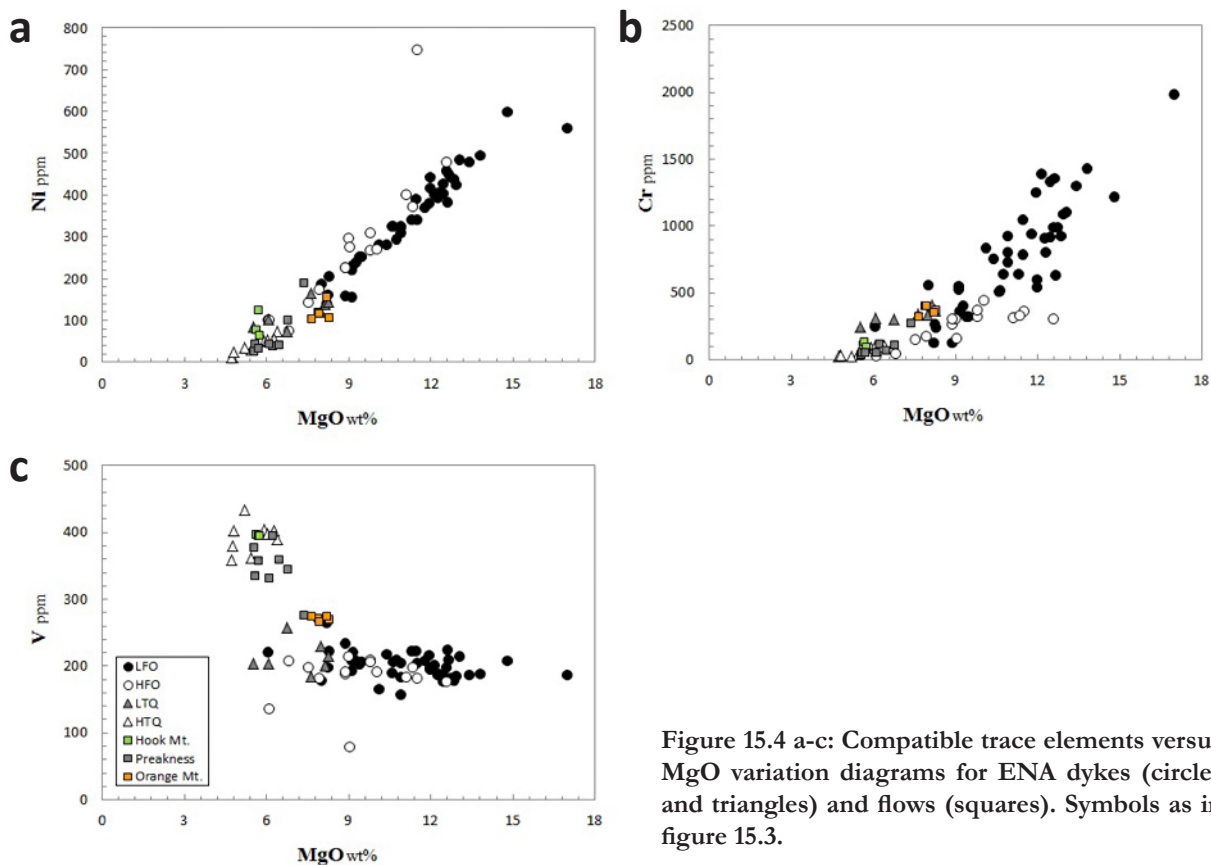


Figure 15.4 a-c: Compatible trace elements versus MgO variation diagrams for ENA dykes (circles and triangles) and flows (squares). Symbols as in figure 15.3.

Compatible trace elements show some discrepancies with Wiegand and Ragland's (1970) classification of Newark flows as well. Notably, Orange Mt. flows do not overlap HTQ compositions, being slightly richer in Ni (ca. 100 ppm) and Cr (ca. 400 ppm) and significantly depleted in V (ca. 270 ppm). Preakness flows show low Ni and Cr contents, overlapping HTQ compositions rather than LTQ ones, and this is most evident in their V content (300-400 ppm), perfectly corresponding to HTQ compositions. Hook Mt. flows do instead overlap compositions of HTQ dykes, in agreement with their HFTQ character.

Preakness and Hook Mt. flows share the same incompatible elements contents and patterns of the ENA dykes (Fig. 15.5 a), with similar Nb and Ti negative and Pb positive anomalies. On the contrary, Orange Mt. basalts do not show any negative Ti anomaly, and are slightly depleted in the less incompatible trace elements (i.e. from Ti to Lu). The same observations are valid for REE compositions (Fig. 15.5 b), i.e. ENA dykes, Preakness and Hook Mt. flows show homogeneous and rather flat REE patterns, while Orange Mt. samples show a more significant and smooth LREE/HREE fractionation (which is well visible on a plot of La/Yb vs Sm/Yb, Fig. 15.5 c).

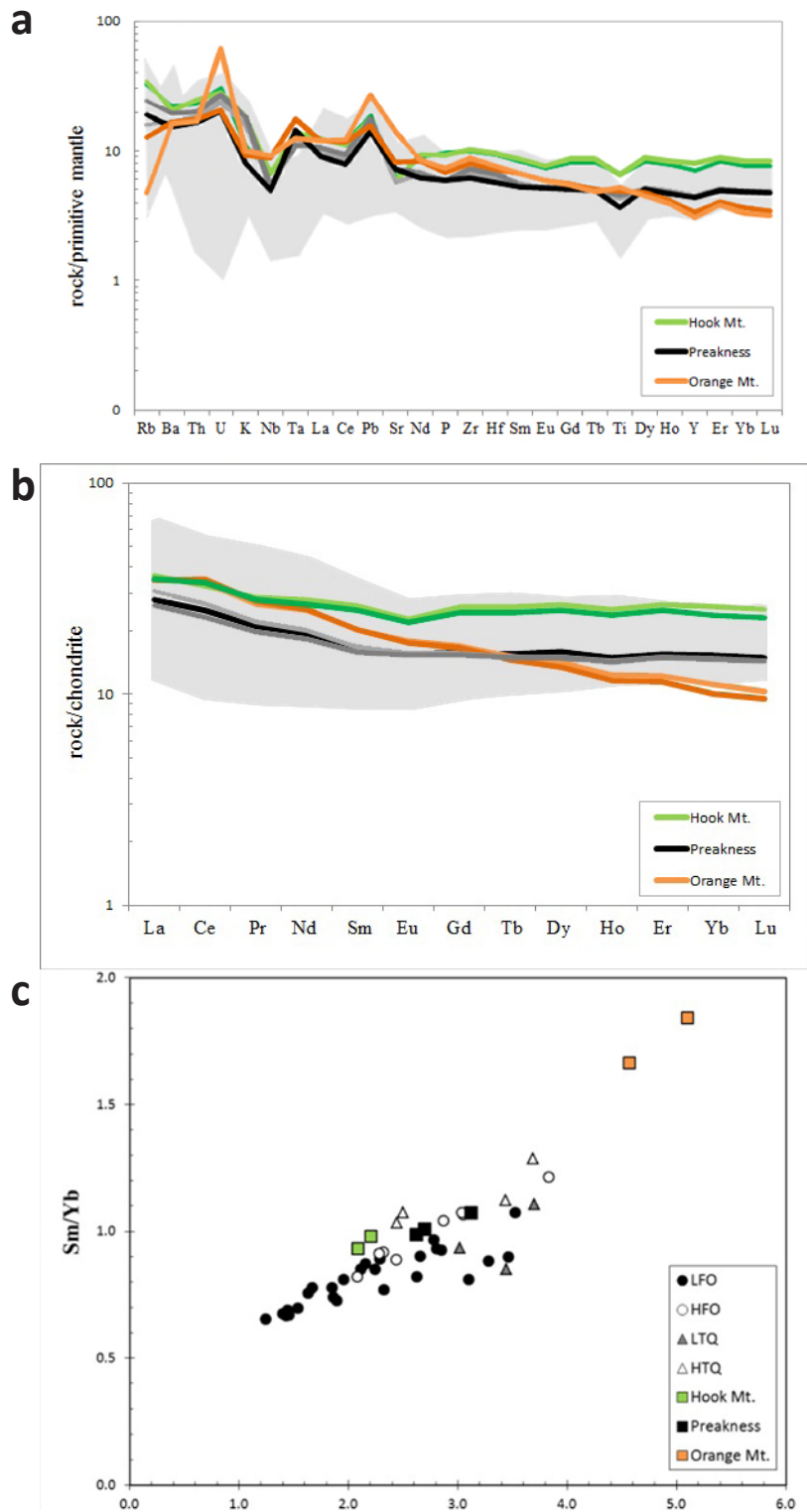


Figure 15.5 a-c: a) Spider diagrams showing primitive mantle normalized (Sun and McDonough, 1989) incompatible trace elements contents for 7 Newark flows. Grey field marks ENA dykes IE compositions for comparison. b) Spider diagram displaying chondrite-normalized (McDonough and Sun, 1995) REE contents for ENA dykes (grey shaded area) and flows (colored lines). c) La/Yb versus Sm/Yb compositions for ENA dykes and flows.

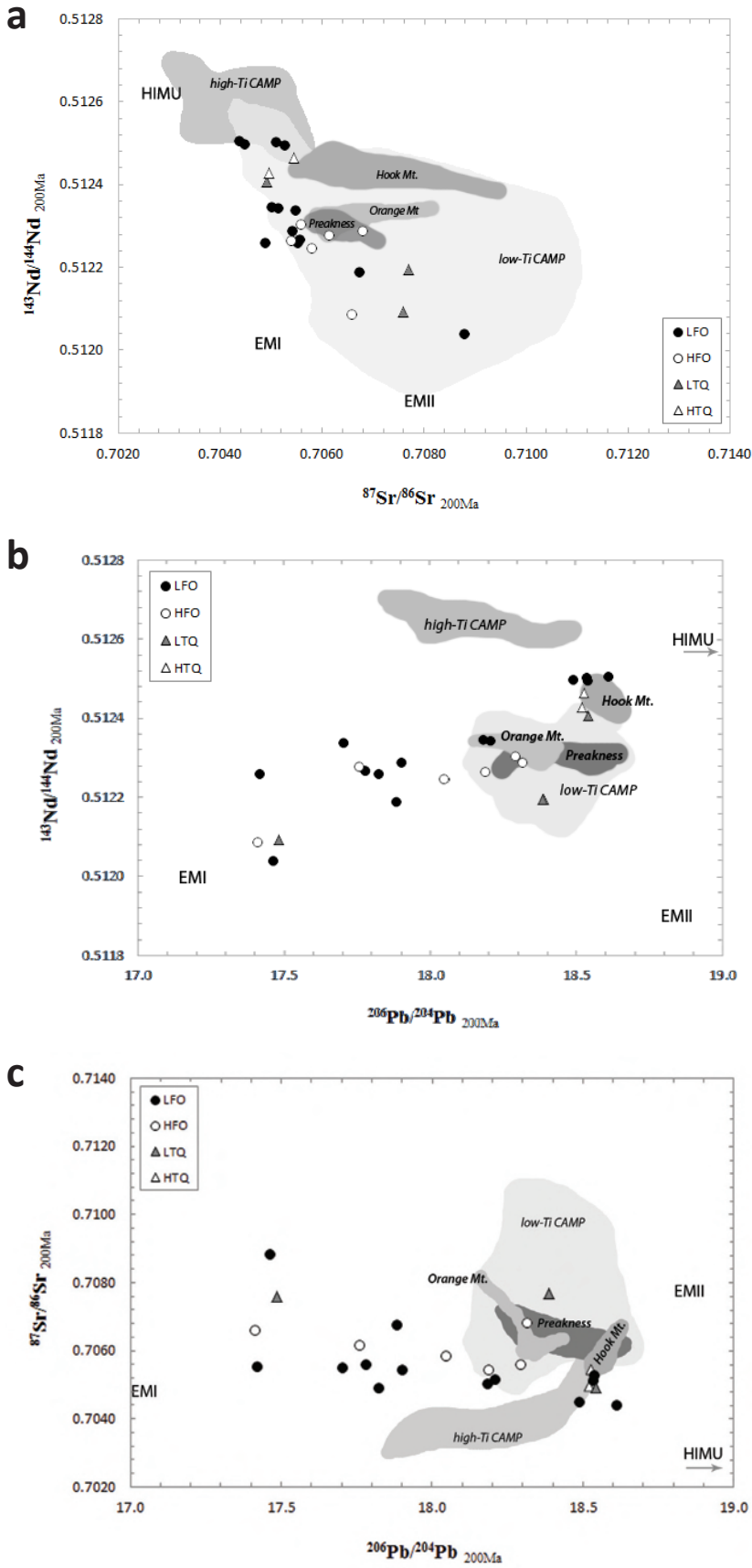


Figure 15.6 a-c: Sr-Nd (a), Nd-Pb (b) and Sr-Pb (c) isotopic spaces. ENA dykes data points are plotted with ENA flows fields for comparison. All the data are back-corrected to 200Ma.

Isotopic signatures for CAMP basaltic flows partially overlap those of ENA dykes, but extend outside the compositional fields formed by the dykes, though generally showing much reduced variations. In particular, at a given $^{143}\text{Nd}/^{144}\text{Nd}_i$ composition, Orange and Hook Mt. flows display more radiogenic Sr signatures (0.706-0.709), with respect to those shown by ENA dykes (0.704-0.706). ENA flows do not reach the low radiogenic Nd ratios shown by the dykes (0.5123-0.5124 vs 0.5125-0.5120). Preakness unit basalts show Sr-Nd-Pb signatures overlapping those of ENA dykes. Hook Mt. basalts show the most radiogenic Nd isotopic ratios, while Preakness and Orange Mt. basalts overlap at lower $^{143}\text{Nd}/^{144}\text{Nd}_i$. In Nd-Pb space, ENA flows cluster on the high $^{206}\text{Pb}/^{204}\text{Pb}_i$ - $^{143}\text{Nd}/^{144}\text{Nd}_i$ end of the array described by the dykes. In particular, Hook Mt. compositions are the highest in Nd and Pb ratios ($^{206}\text{Pb}/^{204}\text{Pb}_i$ 18.15-18.64), overlapping ENA dykes with the most radiogenic isotopic signatures i.e. the group of CS49 (cf. Chapter 13).

In both Pb-Pb isotopic spaces ENA flows plot on the highly-radiogenic end of the linear arrays described by ENA dykes, extending towards higher and very homogeneous $^{206}\text{Pb}/^{204}\text{Pb}$, $^{207}\text{Pb}/^{204}\text{Pb}$ (15.62-15.64) and $^{208}\text{Pb}/^{204}\text{Pb}$ (38.39-38.52) ratios. The most radiogenic isotopic compositions are reached by Hook Mt. basalts. In general, Pb/Pb isotopes show more enriched signatures for ENA flows than for ENA dykes.

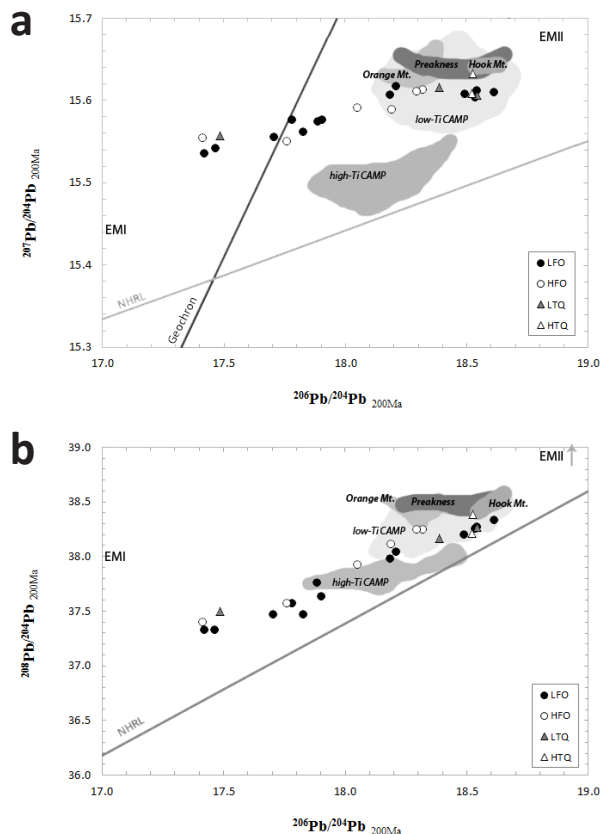


Figure 15.7 a-b: $^{207}\text{Pb}/^{204}\text{Pb}$ (a) and $^{208}\text{Pb}/^{204}\text{Pb}$ (b) plotted against $^{206}\text{Pb}/^{204}\text{Pb}$ isotopic signatures for ENA dykes (data points) and flows (grey areas). Fields for low-Ti and high-Ti CAMP rocks are shown as well for comparison. All the data are back-corrected to 200Ma.

Os isotopic signatures for Orange Mt. flows well overlap those observed for ENA dykes ($^{187}\text{Os}/^{188}\text{Os}$ 0.127-0.15, Fig. 15.8 a-c), with the only exception of a sample reaching more radiogenic signatures (0.207). Samples of the Preakness unit show distinctly higher Os isotopic ratios (0.187-0.260) with respect to the dykes, while Hook Mt. flows display intermediate signatures (0.146-0.170) that are nevertheless more enriched than those of the dykes. No distinct correlation appears between Os isotopes and Sr-Nd-Pb ones for the ENA flows, however the samples showing the most enriched Os signatures also display the most radiogenic $^{206}\text{Pb}/^{204}\text{Pb}$ ratios (Fig. 15.8 c).

With respect to mantle reservoirs (recalculated to 200Ma), ENA dykes and flows appear to plot between EMI and EMII compositions in Pb/Pb isotopic spaces, but the picture becomes more complex as Nd and Sr isotopes are considered, i.e. to explain high $^{144}\text{Nd}/^{143}\text{Nd}$ ratios, a different end-member must be invoked, either the DMM or the HIMU reservoir. The lowest $^{187}\text{Os}/^{188}\text{Os}$ signatures shown by ENA dykes and flows reflect those of the Primitive Upper Mantle reservoir (Shirey and Walker, 1998). Intermediate Os signatures overlap those of enriched mantle reservoirs (EMI, EMII and HIMU), while the most radiogenic ones trend towards a highly radiogenic reservoir i.e. the continental crust (cf. Chapter 14).

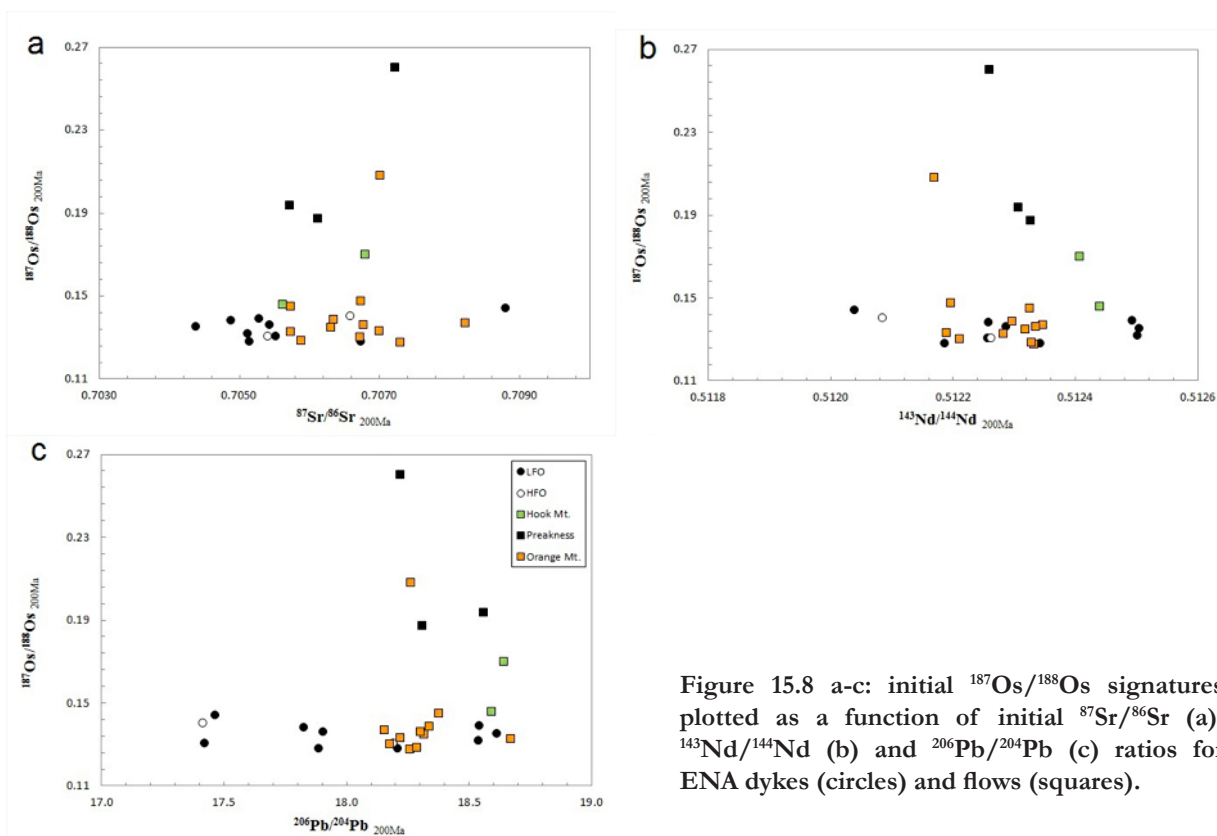


Figure 15.8 a-c: initial $^{187}\text{Os}/^{188}\text{Os}$ signatures plotted as a function of initial $^{87}\text{Sr}/^{86}\text{Sr}$ (a), $^{143}\text{Nd}/^{144}\text{Nd}$ (b) and $^{206}\text{Pb}/^{204}\text{Pb}$ (c) ratios for ENA dykes (circles) and flows (squares).

16 DISCUSSION

16.1 NORMATIVE GROUPS

Through major and trace element geochemistry, parental magmas of two different compositions can be envisaged for LFO and HFO ENA diabases, i.e. HFO magma type is enriched in Fe_2O_3 and I.E. with respect to LFO magma type. Modeling of closed-system differentiation shows that the correlations between major elements is controlled largely by fractionation of olivine, and, subsequently, of a late clinopyroxene + plagioclase assemblage. HTQ compositions may thus be achieved through $\sim 60\%$ fractional crystallization of both LFO- and HFO-type parental magmas. LTQ compositions are less straightforwardly interpreted as closed-system differentiates. However, an origin linked to magmatic evolution of an HFO parental magma-type can be ruled out with a certain confidence, HFO magma type being excessively CaO-depleted and TiO_2 -enriched. LTQ compositions can be reached through a fractional crystallization ruled mostly by olivine.

ENA flows have been previously classified (e.g., Wiegand and Ragland, 1971) as HTQ (Orange Mt.), LTQ (Preakness) and HFTQ (Hook Mt.) magma-types. However, from a comparison with the here studied dykes, no consistent compositional overlap appears among any of the flow and dyke groups, e.g., between HTQ dykes and Orange Mt. flows, and between LTQ dykes and Preakness flows. However, Preakness and Hook Mt. flows basalts were possibly derived by an LFO-type parental magma, while Orange Mt. appears chemically independent (e.g. more fractionated REE patterns, positive Ti anomaly).

16.2 MANTLE SOURCE

Since HFO and LFO dykes define two distinct liquid lines of descent and seem to refer to two different parental magmas, it may be possible that they require two different mantle sources. However, a broad overlap in isotopic traits is observed for the two dyke suites. Since the isotopic compositions of most analyzed dykes are probably not affected by significant crustal contamination (as previously discussed), it has to be considered that LFO and HFO parental magmas are issued from

a) the same mantle source, at different melting degrees, pressures or temperatures; or b) mantle sources with different mineralogy or major element compositions, yet sharing similar, heterogeneous, isotopic compositions.

a) The similar I.E. patterns (Nb, Ta, Ti negative and Pb positive anomalies) and isotopic signatures may be suggestive of a unique source. Anyway, a general, slight enrichment in I.E. is observed for HFO compared to LFO tholeiites that may lead to hypothesize their derivation from a lower degree of partial melting with respect to LFO tholeiites. Higher contents of Na and K of the HFO diabases (see Fig. 4.1) may support this hypothesis. However, there is a visible gap between HFO and LFO major elements compositions (e.g., in Fe, Ti, Ca), and if the difference between the two magma-types resides in the degree of partial melting, it would most probably lead to a continuous spectrum of compositions rather than to two separate groups. HFO samples are fewer than LFO ones (assuming this is not a sampling bias, and there is no way to rule it out), possibly reflecting lower volumes of primary magma produced, i.e. lower melting degree. There is no particular geographic localization for HFO vs LFO samples, so a possible drawback to this interpretation is the feasibility of melting a source at different degrees in the same restricted area, and separate the different partial melts obtained. It should be noted that the HFO diabases all belong to NW-oriented dykes (again assuming this not to be a sampling bias), that according to Ragland et al. (1983) are slightly older than N- and NE-trending ones, i.e. emplacement of low-degree melts could have occurred first, followed by higher-degree partial melts (possibly aided by an increase in temperature due to incipient continental extension). Estimated liquidus T (Table 12a) are slightly ($\sim 30^\circ$ C) lower for HFO magmas than for LFO ones at a given pressure. Melting of a similar source at different pressures seems unlikely, being at odds with observed major elements data (Chapter 13), e.g. higher Fe contents in HFO magmas would reflect melting at higher P, but this would not explain lower CaO contents.

b) Hinging on the different amount of CaO in rather undifferentiated magmas (Herzberg and Asimow, 2008) a second hypothesis arises of ENA dykes being issued from a mixed peridotitic-pyroxenitic source, where HFO magmas are pyroxenite-controlled, and LFO peridotite-controlled. This is supported also by a comparison with experimental melts issued from peridotitic and pyroxenitic mantle sources (Chapter 13) and by the high-Ni content in primitive olivine (Fo_{85-89}) pheno-

crysts (Chapter 8). However, supposing the presence of a mixed source raises several complications. If pyroxenite veins are supposed to coexist interlayered with lherzolite at the same pressure and temperature conditions, (e.g. as observed in the Ronda orogenic peridotite massif by Bodinier et al., 2008), they should melt at higher degree (at a given T) than the peridotite, given their more fertile character (lower solidus T). Still, if a slightly older age for HFO magmas is hypothesized, they may have been produced in an early phase, at relatively lower T of melting. Partial melting of the lherzolite would have started in a later phase, at higher mantle temperature. REE patterns (low La_{ch}/Yb_{ch}) for both magma types suggest formation in absence of residual garnet, thus either partial melts were issued from a source at a relatively shallow depth (in the spinel, rather than garnet stability field) or the extent of partial melting was high enough to consume the entire garnet budget. Partial melting at relatively low P may indeed have occurred in a lithospheric thinning context. Therefore, even if pyroxenites are generally thought to be garnet-bearing rocks, their partial melting at high degree (c. > 22%) would produce melts with relatively undifferentiated REE patterns, similar to those observed for HFO. In this sense, differences in major element geochemistry between HFO and LFO diabbases would reside in their origin from different mantle lithologies. To reconcile the similar REE patterns obtained, different melting degrees or mechanisms should be instead considered. However, this second process hardly reconciles similar I.E. patterns and the trace element enrichment in HFO tholeiites with respect to LFO, unless a slightly enriched character is supposed for the pyroxenite lithology. Pyroxenites are thought to represent the olivine-free reaction product of silica-rich melts (produced from eclogite) with peridotite (e.g. Yaxley and Green, 1998; Sobolev et al., 2005; Sobolev et al., 2007). In turn, eclogites are the high-pressure products of subducted oceanic crust, thus they should yield an I.E. depleted signature, typical of MORBs (Bodinier et al., 2008). However, oceanic crust may also show enriched (isotopic and trace element) compositions in itself or by hydrothermal alteration and reaction with subducted sediments (e.g., Plank and Langmuir, 1998; Yaxley and Green, 1998; Stracke et al., 2003; Peate et al., 2010; Koornef et al., 2012).

16.3 ENRICHED SIGNATURES

ENA diabase dykes share an enriched signature with the majority of low-Ti CAMP tholeiites, i.e. a positive Pb anomaly and generally enriched isotopic signatures, characteristically represented by high $\Delta 7/4$ values. Moreover, considerable isotopic heterogeneity is a common feature for low-Ti CAMP tholeiites. Previous studies on other areas of the CAMP recognized the sub continental lithospheric mantle as the most conceivable mantle source for low-Ti CAMP tholeiites (e.g. Pegram, 1990; Heatherington and Mueller, 1999; Cebrià et al., 2003; Merle et al., 2011), hinging on these enriched signatures as principal arguments. Indeed, because of the relatively short half-life of ^{235}U , high $^{207}\text{Pb}/^{204}\text{Pb}$ signatures reflect derivation from a very ancient component (Archean at least), that is, a reservoir that has been enriched in ^{235}U in the early history of the Earth and has evolved as a closed-system for a certain time. The sub continental lithospheric mantle, being isolated from asthenospheric convection, can be envisaged as the most likely repository of this high $\Delta 7/4$, EMI-like flavor, as in time it can evolve as a closed-system reservoir and reach isotopic characteristics far from those of a contemporaneous MORB mantle. Also, with respect to the convecting upper asthenosphere or a deep mantle reservoir, SCLM is more likely to be an isotopically heterogeneous source. This is entirely true, however, only for a SCLM constituting cratonic roots, while ENA SCLM is of much younger formation (Paleo-Proterozoic). Therefore, enriched domains must have been added to and incorporated within the ENA SCLM during a major geodynamic event. Pegram (1990) argues in favor of hybridization in sub-arc environment. Pre-Grenville subarc mantle was metasomatized by the slab-derived components, whose Pb isotopic traits were dominated by subducted sediments. Grenville continental collision (see Chapter 2) brought to the consolidation of these domains within the lithospheric roots of eastern North America. Eventually, during incipient rifting of Pangea, decompressional melting involved ENA lithospheric mantle. High $\Delta 7/4$ and negative Ta and Nb anomalies are thus explained without involving massive crustal contamination. In this view trace element compositions and isotopic ratios are controlled and buffered by melts issued from the enriched domains, while major element contents are not, and record the compositions of different mantle lithologies. Chemical evolution of the SCLM can thus be inferred by continental tholeiites geochemistry, basing on the approach followed also by e.g. Badger and Sinha (1989) and Murphy et al. (2007). Basing on Sm-Nd model ages and on U-Pb isochrones, Pegram

(1990), Heatherington and Mueller (1999) and Murphy et al. (2011) suggested derivation of ENA CAMP tholeiites from an SCLM of Grenville age ($\sim 1-0.9$ Ga). However, as Badger and Sinha (1989) pointed out, continental rift related tholeiites of ~ 700 Ma (Bakersville dykes and Catoctin Volcanic Province; Rankin, 1975; Goldberg et al. 1986) emplaced on the same area failed to record this enriched flavor. They thus argued that any event that included enriched domains in ENA SCLM should have occurred anywhere between 700 and 200 Ma. This time span is actually characterized by several orogenic phases (see Chapter 2), during which supra-subductive magmatism and arc accretion may have taken place, thus even if not strongly supported nor discarded by the new data here presented, this latter interpretation is however plausible.

Recycling of ancient subducted oceanic crust (\pm sediments) may result in pyroxenitic veining of the SCLM (Yaxley and Green, 1998; Sobolev et al, 2005; Sobolev et al., 2007), conveying EMI signatures to magmas eventually tapping the reservoir. Altered subducted oceanic crust may partially melt within the asthenosphere and subsequently crystallize in veins or conduits within lithospheric mantle during extensional phases (cf. Bodinier et al. 2008 and references therein). This type of oceanic crust recycling may have interested ENA lithospheric mantle during opening of the Iapetus ocean ($\sim 700-600$ Ma, see Chapter 2), thus transmitting enriched flavors to CAMP tholeiites but not to Catoctin-Bakersville ones. However, contrarily to SCLM enrichment in a sub arc environment, pyroxenitic veining via partial melts of subducted oceanic crust would not result in the negative Nb and positive Pb anomalies observed for ENA tholeiites (e.g. Weaver, 1991). Moreover, this would not directly explain the EMI-flavored Pb compositions.

In any case, EMI component is generally recognized to be conveyed by the recycling of oceanic crust accompanied by oceanic (pelagic) sediments (Zindler and Hart, 1986; Plank and Langmuir, 1998; Eisele et al., 2002; Salters and Sachi-Kocher, 2010) or, possibly, of subducted (lower) continental crust (e.g. Meyzen et al., 2005). Each of these enriched domains can have been plausibly included to the ENA SCLM during its complex geodynamic history, available to subsequent tapping by CAMP magmatism.

16.4 MANTLE PLUME?

The hypothesis of a mantle plume origin for CAMP magmatism has been investigated by several authors (May, 1971; Hill, 1991; Wilson, 1997), and it was suggested primarily by isotopic signatures and trace element ratios of magmas in Canada, Brazil, Liberia (Dupuy et al., 1988; Pe-Piper and Reynolds, 2000). Also, the oldest Atlantic oceanic crust was interpreted by Janney and Castillo (2001) to have plume-like signature. Cebrià et al. (2003) reconstructed an initial composition for the hypothetical Central Atlantic Plume (CAP) of $0.7028 \text{ }^{87}\text{Sr}/^{86}\text{Sr}$ and $0.5127 \text{ }^{143}\text{Nd}/^{144}\text{Nd}$, that is, higher in radiogenic Nd and unradiogenic Sr than all the CAMP rocks. Thus, to imply a mantle plume origin, a large extent of assimilation of either crust or lithospheric mantle must be accounted for. For reasons discussed in Chapter 14, crustal contamination has been interpreted to have had a negligible role in the petrogenesis of ENA diabases. Interaction of asthenospheric melts with enriched portions of the SCLM may produce the trace elements patterns and the enriched isotopic signatures observed in ENA tholeiites, as hypothesized by Merle et al. (2011) for CAMP tholeiites from the western Maranhão basin (Brazil). Direct occurrences of undifferentiated asthenospheric melts are however lacking in ENA, thus this latter hypothesis appears unlikely, unless for some reason no plume-issued melt could escape interaction with the lithospheric mantle. Anyway, since calculated mantle potential temperatures for ENA tholeiites (1470° - 1490° C) are $\sim 150^{\circ}$ C higher than those of the average ambient mantle (a difference too high to be explained with thermal insulation below Pangea supercontinent; Coltice et al., 2007), the involvement of a mantle plume as heat source cannot be ruled out. Nevertheless, other authors suggested that heat supply could be conveyed by the upper asthenosphere, due to lithospheric mantle delamination that followed the Alleghanian orogeny (Nelson, 1992; Levin et al., 2000).

17 CONCLUSIONS

The most likely scenario suggested for the petrogenesis of southern ENA diabase dykes and sills envisages a mixed source origin, i.e. a peridotitic mantle source veined by pyroxenites. Different major element characteristics of the two parental magma-types register the composition of the dominant source from which they are issued, i.e. either their pyroxenitic (HFO) or peridotitic (LFO) prevailing character. Contrarily, incompatible elements and isotopic systematics are controlled mainly by the pyroxenite. Therefore, the isotopic heterogeneity and the depleted I.E. character are invariably imparted by the pyroxenitic source to both the magma-types. The observed spinel-signature (poor fractionation of LREE/HREE) may be conveyed by the peridotite, implying a relatively low pressure (spinel stability field) equilibration of pyroxenite-derived melts with the hosting peridotite, and low pressure partial melting of peridotite-issued magmas. Co-variation trends in major elements compositions between the different diabbases are controlled by fractional crystallization, a closed-system differentiation mechanism possibly linking HTQ rocks to either LFO or HFO parental magma-types, and LFO rocks to LFO ones. Crustal assimilation up to 3-10% may answer for slight fluctuations in isotopic traits, but not for the vast spread of signatures observed. Therefore, an SCLM source is conceived for these magmatic bodies, being the reservoir that more reasonably explains both the isotopic enrichment and the heterogeneity observed. Indeed, different domains can be embedded within the SCLM through several geodynamic processes and can maintain their isotopic distinctiveness for a long time, isolated from the convective homogenization of the asthenosphere. ENA lithospheric mantle has undergone a complex geodynamic history, during which EMI-flavored domains can have been added in different ways. Accretion of mantle portions hybridized in a supra-subductive context or inclusion of recycled oceanic crust and sediments can have taken place during the geologic evolution of ENA area, which has alternatively behaved as passive or active margin and as suture zone of continental collisions. Conceivably, differences in the isotopic traits observed between southern ENA dykes and ENA flows intercalated to Newark supergroup basins can reside in the different lithotectonic evolution in which the two areas have been involved, i.e. EMI signature is most evident in the South, possibly reflecting a volumetric prevalence of recycled sediments (or isotopically equivalent domains) in the southern lithospheric mantle with

respect to the North. Even if no geochemical evidence for mantle plume related CAMP magmatism is recorded in the ENA area, the possible involvement of a mantle plume source is not straightforwardly ruled out. Relatively high mantle potential temperatures deduced from the investigated diabbases may indeed mirror the contribution of a mantle plume merely as heat supplier.

REFERENCES (PART I)

- ACKERMANN, H.D., BAIN, G.L., AND ZOHDY, A.A.R., 1976. Deep exploration of an east-coast Triassic basin using electrical resistivity. *Geology* **4**, 137-140.
- AIGNER-TORRES, M., BLUNDY, J., ULMER, P., AND PETTKE, T., 2007. Laser Ablation ICPMS study of trace element partitioning between plagioclase and basaltic melts: an experimental approach. *Contributions to Mineralogy and Petrology* **153**, 647-667.
- ALIBERT, C., 1985. A Sr-Nd isotope and REE study of late Triassic dolerites from the Pyrenees (France) and the Messajana dyke (Spain and Portugal). *Earth and Planetary Science Letters* **73**, 81-90.
- ANDERSEN, D.J., AND LINDSLEY, D.H., 1985. New (and final) models for the Ti-magnetite/ilmenite geothermometer and oxygen barometer. Abstract AGU 1985 Spring Meeting Eos Transactions. *American Geophysical Union* **66** (18), 416.
- ANDERSEN, D.J., LINDSLEY, D.H., AND DAVIDSON, P.M., 1993. QUILF: a Pascal program to assess equilibria among Fe-Mg-Ti oxides, pyroxenes, olivine and quartz. *Computers and Geosciences* **19**, 1333-1350.
- ANDERSON, D.L. 1998. The Edges of the Mantle. In: Gurnis, M., Wysession, M.E., Knittle, E., Buffett, B.A., eds., *The Core-Mantle Boundary Region*. *Geodynamics* **28**, American Geophysical Union, Washington, DC, 255-271.
- AYUSO, R.A., AND BEVIER, M.L., 1991. Regional differences in Pb isotopic compositions of feldspars in plutonic rocks of the Northern Appalachian Mountains, U.S.A., and Canada: A geochemical method of terrane correlation. *Tectonics* **10**, 191-212.
- BADGER, R.L., AND SINHA A.K., 1988. Age and Sr isotopic signature of the Catoctin volcanic province: Implications for subcrustal mantle evolution. *Geology* **16**, 692-695.
- BELL, H. III, 1988. Map showing Mesozoic diabase dykes in South Carolina described since 1960: *U.S. Geological Survey Miscellaneous Field Studies*, **Map MF-2030**, scale 1:250 000.
- BELL, H., BUTLER, J.R., HOWELL, D.E., AND WHEELER, W.H., 1974. Geology of the Piedmont and Coastal Plain near Pageland, South Carolina and Wadesboro, North Carolina: Carolina Geological Society fieldtrip guidebook, South Carolina State Development Board, Division of Geology, (South Carolina).
- BERTRAND, H., DOSTAL, J., AND DUPUY, C., 1982. Geochemistry of early Mesozoic tholeiites from Morocco. *Earth and Planetary Science Letters* **58**, 225-239.
- BEUTEL, E.K., NOMADE, S., FRONABARGER, A.K., AND RENNE, P.R., 2005. Pangea's complex breakup: A new rapidly changing stress field model. *Earth and Planetary Science Letters* **236**, 471-485.
- BIRCK, J.-L., ROY BARMAN, M., AND CAPMAS, F., 1997. Re-Os isotopic measurements at the femtomole level in natural samples. *Geostandards Newsletter* **21**, 19-27.
- BODINIER, J.-L., GARRIDO, C.J., CHANEFO, I., BRUGUIER, O., AND GERVILLA, F., 2008. Origin of Pyroxenite-Peridotite Veined Mantle by Refertilization Reactions: Evidence from the Ronda Peridotite (Southern Spain). *Journal of Petrology* **49**, 999-1025.
- BODINIER, J.-L., GARRIDO, C.J., CHANEFO, I., BRUGUIER, O., AND GERVILLA, F., 2008. Origin of Pyroxenite/Peridotite Veined Mantle by Refertilization Reactions: Evidence from the Ronda Peridotite (Southern Spain). *Journal of Petrology* **49**, 999-1025.
- BOHRSON, W.A., AND SPERA, F.J., 2001. Energy-Constrained Open-System Magmatic Processes II: Application of Energy-Constrained Assimilation-Fractional Crystallization (EC-AFC) Model to Magmatic Systems. *Journal of Petrology* **42**, 1019-1041.
- BRADLEY, D.C., 1982. Subsidence in late Paleozoic basins in the northern Appalachians. *Tectonics* **1**, 107-123.

- BURT, E.R., CARPENTER, P.A.III, MCDANIEL, R.D., AND WILSON, W.F., 1978. Diabase dykes of eastern Piedmont of North America. *North Carolina Geological Survey Information Circular* **23**, 12 p.
- BUTLER, J.R., AND FULLAGAR, P.D., 1978. Petrochemical and geochronological studies of plutonic rocks in the Southern Appalachians: III. Leucocratic adamellites of the Charlotte belt near Salisbury, North Carolina. *Geological Society of America Bulletin* **89**, 460-466.
- CAMPBELL, I. H., 2005. Large Igneous Provinces and the Mantle Plume Hypothesis. *Elements* **1**, 265-269.
- CARR, S.D., EASTON, R.M., JAMESON, R.A., AND CULSHAW, N. G. 2000. Geologic transect across the Grenville orogen of Ontario and New York. *Canadian Journal of Earth Sciences* **37**, 193-216.
- CARRIGAN, C.W., MILLER, C.F., FULLAGAR, P.D., BREAM, B.R., HATCHER, R.D. JR., AND COATH, C.D., 2003. Ion microprobe age and geochemistry of southern Appalachian basement, with implications for Proterozoic and Paleozoic reconstructions. *Precambrian Research* **120**, 1-36.
- CAWOOD, P.A., DUNNING, G.R., LUX, D., AND VAN GOOL, J.A.M., 1994. Timing of peak metamorphism and deformation along the Appalachian margin of Laurentia in Newfoundland: Silurian, not Ordovician. *Geology* **22**, 399-402.
- CEBRIÀ, J.M., LOPEZ-RUIZ, J., DOBLAS, M., MARTINS, L.T., AND MUNHA, J., 2003. Geochemistry of the Early Jurassic Messejana–Plasencia dyke (Portugal–Spain); implications on the origin of the Central Atlantic Magmatic Province. *Journal of Petrology* **44**, 547–568.
- CHAZOT, G., MENZIES, M.A., AND HARTE, B., 1996. Determination of partition coefficients between apatite, clinopyroxene, amphibole, and melt in natural spinel lherzolites from Yemen: Implications for wet melting of the lithospheric mantle. *Geochimica et Cosmochimica Acta* **60** (3), 423-437.
- CIRILLI, S., MARZOLI, A., TANNER, L., BERTRAND, H., BURATTI, N., JOURDAN, F., BELLINI, G., KONTAK, D., AND RENNE, P.R., 2009. Latest Triassic onset of the Central Atlantic Magmatic Province (CAMP) volcanism in the Fundy Basin (Nova Scotia): New stratigraphic constraints. *Earth and Planetary Science Letters* **286**, 514-525.
- CLARKE, D.B., MACDONALD, M.A., AND TATE, M.C., 1997. Late Devonian mafic-felsic magmatism in the Meguma Zone, Nova Scotia. *Geological Society of America Memoirs* **191**, 107-127.
- COLTICE, N., PHILLIPS, B.R., BERTRAND, H., RICARD, Y., AND REY, P., 2007. Global warming of the mantle at the origin of flood basalts over supercontinents. *Geology* **35**, 391-394.
- COOK, F.A., 1983. Some consequences of palinspastic reconstruction in the southern Appalachians. *Geology* **11**, 86-89.
- COURTILLOT, V., AND RENNE, P., 2003. On the ages of flood basalt events. *Comptes Rendus Geosciences* **335**, 113-140.
- COURTILLOT, V., JAUPART, C., MANIGHETTI, I., TAPPONNIER, P., AND BESSE, J., 1999. On causal links between flood basalts and continental breakup. *Earth and Planetary Science Letters* **166**, 177–195.
- CREASER, R.A., PAPANASTASSIOU, D.A., AND WASSERBURG, G.J., 1991. Negative thermal ion mass spectrometry of osmium, rhenium, and iridium. *Geochimica and Cosmochimica Acta* **55**, 397-401.
- CUMMINS, L.E., ARTHUR, J.D., AND RAGLAND, P.C., 1992. Classification and tectonic implications for early Mesozoic magma types of the Circum-Atlantic. In: Puffer J.H. and Ragland, P.C., eds., Eastern North American Mesozoic Magmatism. *Geological Society of America Special Paper* **268**, 119-135.
- DALLMEYER, R.D., WRIGHT, J.E., SECOR, D.T., AND SNOKE, A.W., 1986. Character of the Alleghanian orogeny in the southern Appalachians: Part II. Geochronological constraints on the tectonothermal evolution of the eastern Piedmont in South Carolina. *Geological Society of America Bulletin* **97**, 1329-1344.
- DAVIDSON, A., AND VAN BREEMEN, O., 2001. Baddeleyite U-Pb age of metadiabase near Key Harbour, Britt domain, Grenville Province, Ontario. Radiogenic Age and Isotopic Studies: Report 14. *Geological Survey of Canada, Current Research* **F7**, 11 p.
- DE BOER, J., AND SNIDER, F.G., 1979. Magnetic and chemical variations of Mesozoic diabase dikes from eastern North America: Evidence for a hotspot in the Carolinas. *Geological Society of America Bulletin* **90**, 185-198.

- DE MIN, A., PICCIRILLO, E.M., MARZOLI, A., BELLINI, G., RENNE, P.R., ERNESTO, M., AND MARQUES, L., 2003. The Central Atlantic Magmatic Province (CAMP) in Brazil: Petrology, Geochemistry, $^{40}\text{Ar}/^{39}\text{Ar}$ ages, paleomagnetism and geodynamic implications. In: Hames, W.E., McHone, J.G., Renne, P.R., Ruppel, C., eds., The Central Atlantic Magmatic Province: Insights from Fragments of Pangea. *AGU Geophysical Monographs* **136**, 209–226.
- DE PAOLO, D.J., 1981, Trace element and isotopic effects on combined wallrock assimilation and fractional crystallization. *Earth and Planetary Science Letters* **53**, 189–202.
- DE PAOLO, D.J., AND SIMS, K.W.W., 1997. Inferences about mantle magma sources from incompatible element concentration ratios in oceanic basalts. *Geochimica et Cosmochimica Acta* **61** (4), 765–784.
- DECKART, K., BERTRAND, H., AND LIEGEOIS, J.-P., 2005. Geochemistry and Sr, Nd, Pb isotopic composition of the Central Atlantic Magmatic Province (CAMP) in Guyana and Guinea. *Lithos* **82**, 289–314.
- DENNIS, A.J., SHERVAIS, J.W., MAULDIN, J., MAHER, H.D.JR., AND WRIGHT, J.E., 2004. Petrology and geochemistry of Neoproterozoic volcanic arc terranes beneath the Atlantic Coastal Plain, Savannah River Site, South Carolina. *Geological Society of America Bulletin* **116** (5–6), 572–593.
- DORAIS, M.J., WORKMAN, J., AND AGGARWAL, J., 2008. The petrogenesis of the Highlandcroft and Oliverian plutonic suites, New Hampshire: implications for the structure of the Bronson Hill terrane. *American Journal of Science* **308**, 73–99.
- DOSTAL, J., AND DUPUY, C., 1984. Geochemistry of the North Mountain Basalts (Nova Scotia, Canada). *Chemical Geology* **45**, 245–261.
- DOSTAL, J., AND DURNING, M., 1998. Geochemical constraints on the origin and evolution of early Mesozoic dikes in Atlantic Canada. *European Journal of Mineralogy* **10**, 79–93.
- DUNNING, G.R., AND HODYCH, J.P., 1990. U/Pb zircon and baddeleyite ages for the Palisades and Gettysburg sills of the northeastern United States: implications for the age of the Triassic/Jurassic boundary. *Geology* **18**, 795–798.
- DUPUY, C., MARSH, J., DOSTAL, J., MICHARD, A., AND TESTA, S., 1988. Asthenospheric and lithospheric sources for Mesozoic dolerites from Liberia (Africa): trace element and isotopic evidence. *Earth and Planetary Science Letters* **87**, 100–110.
- EISELE, J., SHARMA, M., GALER, S.J.G., Blichert-Toft, J., DEVEY, C.W., HOFMANN, A.W., 2002. The role of sediment recycling in EM-I inferred from Os, Pb, Hf, Nd, Sr isotope and trace element systematics of the Pitcairn hotspot. *Earth and Planetary Science Letters* **196**, 197–212.
- ERNESTO, M., RAPOSO, M.I.B., MARQUES, L.S., RENNE, P.R., DIOGO, L.A., AND DE MIN, A., 1999. Paleomagnetism, geochemistry and $^{40}\text{Ar}/^{39}\text{Ar}$ dating of the north-eastern Parana Magmatic Province: tectonic implications. *Journal of Geodynamics* **28**, 321–340.
- ERNST, R. E., BUCHAN, K. L., AND CAMPBELL, I. H., 2005. Frontiers in large igneous province research. *Lithos* **79**, 271–297.
- FULLAGAR, P.D., AND BUTLER, J.R., 1976. Petrochemical and geochronologic studies of plutons in the southern Appalachians: II, The Sparta granite complex, Georgia. *Geological Society of America Bulletin* **87**, 53–56.
- GAETANI, G.A., AND GROVE, T. L., 1998. The influence of water on melting of mantle peridotite. *Contributions to Mineralogy and Petrology* **131**, 323–346.
- GANGULI, P.M., KUNK, M.J., WINTSCH, R.P., DORAIS, M.J., AND SACKS, P.E., 1995. High precision sanidine $^{40}\text{Ar}/^{39}\text{Ar}$ results from Mesozoic rhyolite dikes near Lake Gaston, N.C. and VA. *Geological Society of America Abstracts* **27**, 45.
- GHIORSO, M.S., AND SACK, R.O., 1995. Chemical Mass Transfer in Magmatic Processes, IV. A Revised and Internally Consistent Thermodynamic Model for the Interpolation and Extrapolation of Liquid-Solid Equilibria in Magmatic Systems at Elevated Temperatures and Pressures. *Contributions to Mineralogy and Petrology* **119**, 197–212.
- GOLDBERG, S.A., BUTLER, J.R., AND FULLAGAR, P.D., 1986. The Bakersville dike swarm; geochronology and petrogenesis of late Proterozoic basaltic magmatism in the southern Appalachian Blue Ridge. *American Journal of Science* **286**, 403–430.

- GOWER, C.F., AND KROGH, T.E., 2002. A U-Pb geochronological review of the Proterozoic history of the eastern Grenville Province. *Canadian Journal of Earth Sciences* **39**, 795-829.
- GREENOUGH, J.D., JONES, L.M., AND MOSSMAN, D.J., 1989. Petrochemical and stratigraphic aspects of North Mountain Basalt from the north shore of the Bay of Fundy, Nova Scotia, Canada. *Canadian Journal of Earth Sciences* **26**, 2710-2717.
- GROSSMAN, J. N., GOTTFRIED, D., AND FROELICH, A. J., 1991. Geochemical data for Jurassic diabase associated with Early Mesozoic basins in the eastern United States, *U.S. Geological Survey, Open-File Report*, 91-322-K.
- HAMES, W.E., RENNE, P.R., AND RUPPEL, C., 2000. New evidence for geologically instantaneous emplacement of earliest Jurassic Central Atlantic magmatic province basalts on the North American margin. *Geology* **28**, 859-862.
- HAMES, W.E., SALTERS, V.J., MORRIS, D., AND BILLOR, M.Z., 2010. The Middle Jurassic flood basalts of southeastern North America. *Geological Society of America Abstracts with Programs* **42** (5), 196.
- HAMILTON, P.J., O'NIONS, R.K., BRIDGWATER, D., AND NUTMAN, A., 1983. Sm-Nd studies of Archaean metasediments and metavolcanics from West Greenland and their implications for the Earth's early history. *Earth and Planetary Science Letters* **62**, 263-272.
- HAMILTON, R.M., BEHRENDT, J.C., AND ACKERMANN, H.D., 1983. Land multichannel seismic-reflection evidence for tectonic features near Charleston, South Carolina. In: Gohn, G.S., ed., Studies related to the Charleston, South Carolina, earthquake of 1886—Tectonics and seismicity. *U.S. Geological Survey Professional Paper* **1313**, I1-I18.
- HATCHER R.D., AND GOLDBERG S.A., 1991. The Blue Ridge Geologic Province. In: Wright Horton, J. and Zullo, V.A., eds., The Geology of the Carolinas, Carolina Geologic Society Fiftieth Anniversary Volume, The University of Tennessee Press, Knoxville (Tennessee), 11-35.
- HATCHER, R.D., 2010. The Appalachian orogen: A brief summary. *Geological Society of America Memoirs* **206**, 1-19.
- HATCHER, R.D.JR., AND REPETSKI, J.E., 2007. The post-Knox unconformity: Product of global, not regional, processes. *Geological Society of America Abstracts with Programs* **39** (2), 8.
- HATCHER, R.D.JR., BREAM, B.R., AND MERSCHAT, A.J., 2007. Tectonic map of the southern and central Appalachians: A tale of three orogens and a complete Wilson cycle. In: Hatcher, R.D.Jr., Carlson, M.P., McBride, J.M., and Martínez Catalán, J.R., eds., 4-D Framework of Continental Crust. *Geological Society of America Memoirs* **200**, 595 p.
- HATCHER, R.D.JR., HOOPER, R.J., PETTY, S.M., AND WILLIS, J.D., 1984. Structure and chemical petrology of three southern Appalachian mafic-ultramafic complexes and their bearing upon the tectonics of emplacement and origin of Appalachian ultramafic bodies. *American Journal of Science* **284**, 484-506.
- HEATHERINGTON, A.L., AND MUELLER, P.A., 1991. Geochemical evidence for Triassic rifting in southwestern Florida. *Tectonophysics* **188**, 291-302.
- HEATHERINGTON, A.L., AND MUELLER, P.A., 1999. Lithospheric sources of North Florida, USA tholeiites and implications for the origin of the Suwannee terrain. *Lithos* **46**, 215-233.
- HEFFNER, D.M., KNAPP, J.H., AKINTUNDE, O.M., AND KNAPP, C.C., 2011. Preserved extent of Jurassic flood basalt in the South Georgia Rift: A new interpretation of the J horizon. *Geology*, doi:10.1130/G32638.1.
- HEINONEN, J.S., CARLSON, R.W., AND LUTTINEN, A.V., 2010. Isotopic (Sr, Nd, Pb, and Os) composition of highly magnesian dikes of Vestfjella, western Dronning Maud Land, Antarctica: A key to the origins of the Jurassic Karoo large igneous province. *Chemical Geology* **277**, 227-244.
- HERZBERG, C., 2006. Petrology and thermal structure of the Hawaiian plume from Mauna Kea volcano. *Nature* **444**, 605-609.
- HERZBERG, C., AND GAZEL, E., 2009. Petrological evidence for secular cooling in mantle plumes. *Nature* **458**, 619-623.
- HERZBERG, C., AND P.D. ASIMOW, 2008. Petrology of some oceanic island basalts: PRIMELT2.XLS software for primary magma calculation. *Geochemistry, Geophysics, Geosystems* **9**, Q09001.

- HIBBARD, J.P., STODDARD, E.F., SECOR, D.T., AND DENNIS A.J., 2002. The Carolina Zone: overview of Neoproterozoic to Early Paleozoic peri-Gondwanan terranes along the eastern flank of the southern Appalachians. *Earth-Science Reviews* **57**, 299-339.
- HIBBARD, J.P., VAN STAAL, C.R., AND MILLER, B.V., 2007. Links between Carolina, Avalonia and Ganderia in the Appalachian peri-Gondwanan realm. In: Sears, J., Harms, T., Evenchick, C., eds., Whence the Mountains? Inquiries into the Evolution of Orogenic Systems: A Volume in Honor of Raymond A. Price. *Geological Society of America Special Papers* **433**, 291-311.
- HIBBARD, J.P., VAN STAAL, C.R., AND RANKIN, D.W., 2007. A comparative analysis of pre-Silurian crustal building blocks of the northern and southern Appalachian orogeny. *American Journal of Science* **307**, 23-45.
- HIBBARD, J.P., VAN STAAL, C.R., AND RANKIN, D.W., 2010. Comparative analysis of the geological evolution of the northern and southern Appalachian orogen: Late Ordovician–Permian. *Geological Society of America Memoirs* **206**, 51-69.
- HILL, R.I., 1991. Starting plumes and continental break-up. *Earth and Planetary Science Letters* **104**, 398–416.
- HIROSE, K., AND KUSHIRO, I., 1993. Partial melting of dry peridotites at high pressures: Determination of compositions of melts segregated from peridotite using aggregates of diamond. *Earth and Planetary Science Letters* **114**, 477-489.
- HIRSCHMANN, M.M., KOGISO, T., BAKER, M.B., AND STOLPER, E.M., 2003. Alkalic magmas generated by partial melting of garnet pyroxenite. *Geology* **31**, 481-484.
- HODYCH, J.P., AND DUNNING, G.R., 1992. Did the Manicouagan impact trigger end-of-Triassic mass extinction? *Geology* **20**, 51–54.
- HOFFMANN, A., 1997. Mantle geochemistry the message from oceanic volcanism. *Nature* **385**, 219-229.
- HOLBROOK, W.S., AND KELEMEN, P.B., 1993. Large igneous province on the U.S. Atlantic margin and implications for magmatism during continental breakup. *Nature* **364**, 433-436.
- HOLM-DENOMA, C.S., AND DAS, R., 2010. Bimodal volcanism as evidence for Paleozoic extensional accretionary tectonism in the southern Appalachians. *Geological Society of America bulletin* **122**, 1220-1234.
- HORTON, J.W.JR., DRAKE, A.A., JR., AND RANKIN, D.W., 1989. Tectonostratigraphic terranes and their Paleozoic boundaries in the central and southern Appalachians. In: Dallmeyer, R.D., ed., Terranes in the Circum-Atlantic Paleozoic Orogens. *Geological Society of America Special Papers* **230**, 213-245.
- INGLE, S., MUELLER, P.A., HEATHERINGTON, A.L., AND KOZUCH, M., 2003. Isotopic evidence for the magmatic and tectonic histories of the Carolina Terrane: implications for stratigraphy and terrane affiliation. *Tectonophysics* **371**, 187-211.
- JOHNSTON, A.D., AND SCHWAB, B.E., 2004. Constraints on clinopyroxene/melt partitioning of REE, Rb, Sr, Ti, Cr, Zr, and Nb during mantle melting: First insights from direct peridotite melting experiments at 1.0 GPa. *Geochimica et Cosmochimica Acta* **68** (23), 4949-4962.
- JONES, L.M., AND WALKER, R.L., 1973. Rb-Sr whole-rock age of the Siloam Granite, Georgia: A Permian intrusive in the southern Appalachians. *Geological Society of America Bulletin* **84**, 3653-3658.
- JOURDAN, F., BERTRAND, H., SCHÄRER, U., Blichert-Toft, J., FÉRAUD, G., AND KAMPUNZU, A.B., 2007. Major and Trace Element and Sr, Nd, Hf, and Pb Isotope Compositions of the Karoo Large Igneous Province, Botswana–Zimbabwe: Lithosphere vs Mantle Plume Contribution. *Journal of Petrology* **48**, 1043-1077.
- JOURDAN, F., FÉRAUD, G., BERTRAND, H., WATKEYS, M.K., AND RENNE, P.R., 2008. $^{40}\text{Ar}/^{39}\text{Ar}$ ages of the sill complex of the Karoo large igneous province: implications for the Pliensbachian-Toarcian climate change. *Geochemistry, Geophysics, Geosystems* **9**, Q06009.
- JOURDAN, F., MARZOLI, A., BERTRAND, H., CIRILLI, S., TANNER, L.H., KONTAK, D.J., MCHONE, G., RENNE, P.R., AND BELLIENI, G., 2009. $^{40}\text{Ar}/^{39}\text{Ar}$ ages of CAMP in North America: implications for the Triassic–Jurassic boundary and the ^{40}K decay constant bias. *Lithos* **110**, 167-180.

- JOURDAN, F., MARZOLI, A., BERTRAND, H., COSCA, M., AND FONTIGNIE, D., 2003. The northernmost CAMP: $^{40}\text{Ar}/^{39}\text{Ar}$ age, petrology and Sr–Nd–Pb isotope geochemistry of the Kerforne dyke, Brittany, France. In: Hames, W.E., McHone, J.G., Renne, P.R., Ruppel, C., eds., *The Central Atlantic Magmatic Province: Insights from Fragments of Pangea. AGU Geophysical Monographs* **136**, 209–226.
- KELEMEN P.B., SHIMIZU N., AND DUNN T., 1993. Relative depletion of niobium in some arc magmas and the continental crust: Partitioning of K, Nb, La and Ce during melt/rock reaction in the upper mantle. *Earth and Planetary Science Letters* **120**, 111-134.
- KESHAV, S., GUDFINNSSON, G.H., SEN, G., AND FEI, Y., 2004. High-pressure melting experiments on garnet clinopyroxene and the alkalic to tholeiitic transition in ocean-island basalts. *Earth and Planetary Science Letters* **223**, 365-379.
- KING, P.B., 1961. Systematic pattern of Triassic dikes in the Appalachian region. *U.S. Geological Survey Professional Paper* **424** (B), 93-95.
- KINZLER, R.J., 1997. Melting of mantle peridotite at pressures approaching the spinel to garnet transition: application to mid-ocean ridge basalt petrogenesis. *Journal of Geophysical Research* **102**, 853-874.
- KNIGHT, K.B., NOMADE, S., RENNE, P.R., MARZOLI, A., BERTRAND, H., AND YOUNI, N., 2004. The central Atlantic magmatic province at the Triassic-Jurassic boundary: paleomagnetic and $^{40}\text{Ar}/^{39}\text{Ar}$ evidence from Morocco for brief, episodic volcanism. *Earth and Planetary Science Letters* **228**, 143-160.
- KOGISO, T., HIROSE, K., AND TAKAHASHI, E., 1998. Melting experiments on homogeneous mixtures of peridotite and basalt: application to the genesis of ocean island basalts. *Earth and Planetary Science Letters* **162**, 45-61.
- KOGISO, T., HIRSCHMANN, M.M., AND FROST, D.J., 2003. High-pressure partial melting of garnet pyroxenite: possible mafic lithologies in the source of ocean island basalts. *Earth and Planetary Science Letters* **216**, 603-617.
- KONTAK D.J., 2008. On the edge of CAMP: Geology and volcanology of the Jurassic North Mountain Basalt, Nova Scotia. *Lithos* **101**, 74-101.
- KOORNNEEF, J.M., STRACKE, A., BOURDON, B., MEIER, M.A., JOCHUM, K.P., STOLL, B., AND GRÖNVOLD, K., 2012. Melting of a Two-component Source beneath Iceland. *Journal of Petrology* **53**, 127-157.
- KOZUR, H.W., AND MOCK, R., 1991. New Middle Carnian and Rhaetian conodonts from Hungary and the Alps. Stratigraphic importance and tectonic implications for the Buda Mountains and adjacent areas. *Jahrbuch der Geologischen Bundesanstalt* **134**, 271-297.
- LEPAGE, L.D., 2003. ILMAT: an Excel worksheet for ilmenite–magnetite geothermometry and geobarometry. *Computers and Geosciences* **29**, 673-678.
- LEVIN, V., PARK, J., BRANDON, M.T., AND MENKE, W., 2000. Thinning of the upper mantle during late Paleozoic Appalachian orogenesis. *Geology* **28**, 239-242.
- LUDDEN, J., AND HYNES, A., 2000. The Abitibi-Grenville Lithoprobe project: two billion years of crust formation and recycling in the Precambrian Shield of Canada. *Canadian Journal of Earth Sciences* **37**, 459-476.
- LUDWIG, K.R., 2003. User's Manual for Isoplot 3.00, *Berkeley Geochronology Center Special Publication*, 74 p.
- MAHONEY, J.J., AND COFFIN, M.F., 1997. Large igneous provinces: continental, oceanic, and planetary flood volcanism. *Geophysical Monograph* **100**, 1–438.
- MARTIGNOLE, J., AND POUGET, P., 1994. A two-stage emplacement for the Cabonga allochthon (central part of the Grenville Province): Evidence for orthogonal and oblique collision during the Grenville orogeny. *Canadian Journal of Earth Sciences* **31**, 1714-1726.
- MARZOLI, A., BERTRAND, H., KNIGHT, K.B., CIRILLI, S., BURATTI, N., VERATI, C., NOMADE, S., RENNE, P.R., YOUNI, N., MARTINI, R., ALLENBACH, K., NEUWERTH, R., RAPAILLE, C., ZANINETTI, L., AND BELLINI, G., 2004. Synchrony of the Central Atlantic magmatic province and the Triassic-Jurassic boundary climatic and biotic crisis. *Geology* **32**, 973-976.

- MARZOLI, A., JOURDAN, F., PUFFER, J.H., CUPPONE, T., TANNER, L.H., WEEMS, R.E., BERTRAND, H., CIRILLI, S., BELLINI, G., AND DE MIN, A., 2011. Timing and duration of the Central Atlantic magmatic province in the Newark and Culpeper basins, eastern U.S.A. *Lithos* **122**, 175-188.
- MARZOLI, A., RENNE, P.R., PICCIRILLO, E.M., ERNESTO, M., BELLINI, G., AND DE MIN, A., 1999. Extensive 200-Million-Year-Old Continental Flood Basalts of the Central Atlantic Magmatic Province. *Science* **284**, 616-618.
- MAUCHE, R., FAURE, G., JONES, L.M., AND HOEFS, J., 1989. Anomalous isotopic compositions of Sr, Ar, and O in the Mesozoic diabase dikes of Liberia, West Africa. *Contributions to Mineralogy and Petrology* **101**, 12– 18.
- MAY, P.R., 1971. Pattern of Triassic diabase dikes around the North Atlantic in the context of predrift position of the continents. *Geological Society of America Bulletin* **82**, 1285–1292.
- MCBRIDE, J.H., NELSON, K.D., AND BROWN, L.D., 1989. Evidence and implications of an extensive Mesozoic rift basin and basalt/diabase sequence beneath the southeast Coastal Plain. *Geological Society of America Bulletin* **101**, 512–520.
- MCDONOUGH, W. F., AND SUN, S.-s., 1995. The composition of the Earth. *Chemical Geology* **120**, 223-254.
- MCDONOUGH, W.F., 1991. Chemical and isotopic systematics of continental lithospheric mantle. In: Meyer, H.O.A. and Leonardos, O.H. eds., *Kimberlites, Related Rocks and Mantle Xenoliths*. Companhia de Pesquisa de Recursos Minerais, Rio de Janeiro, (Brazil) **1**, 478-485.
- MC ELWAIN, J. C., BEERLING, D. J., AND WOODWARD, F. I., 1999. Fossil Plants and Global Warming at the Triassic-Jurassic Boundary. *Science* **285**, 1386-1390.
- MCHONE, J.G., 1996. Broad-terrace Jurassic flood basalts across northeastern North America. *Geology* **24**, 319-322.
- MCHONE, J.G., 2000. Non-plume magmatism and rifting during the opening of the central Atlantic Ocean. *Tectonophysics* **316**, 287-296.
- MCHONE, J.G., 2002. Volatile emissions of Central Atlantic Magmatic Province basalts: Mass assumptions and environmental consequences. In: Hames, W.E., McHone, J.G., Ruppel, C., and Renne, P., eds., *The Central Atlantic Magmatic Province*. *American Geophysical Union Monograph* **136**, 241-254.
- MCKENZIE, D., AND BICKLE, M.J., 1988. The volume and composition of melt generated by extension of the lithosphere. *Journal of Petrology* **29**, 625-679.
- MCELLEND, J.M., SELLECK, B.W., AND BICKFORD, M.E. 2010. Review of the Proterozoic evolution of the Grenville Province, its Adirondack outlier, and the Mesoproterozoic inliers of the Appalachians. In: Tollo, R.P., Bartholomew, M.J., Hibbard, J.P., Karabinas, P.M, eds., *From Rodinia to Pangea: The lithotectonic record of the Appalachian region*. *Geological Society of America Memoirs* **206**, 956 p.,
- MC SWEEN, H.Y., JR., SPEER, J.A., AND FULLAGAR, P.D., 1991. Plutonic rocks. In: Wright Horton, J. and Zullo, V.A., eds., *The Geology of the Carolinas*, Carolina Geologic Society Fiftieth Anniversary Volume (The University of Tennessee Press, Knoxville (Tennessee)), 109-126.
- MEISEL, T., WALKER, R.J., IRVING, A.J., AND LORAND, J.-P., 2001. Osmium isotopic compositions of mantle xenoliths: a global perspective. *Geochimica Cosmochimica Acta* **65**, 1311-1323.
- MERLE, R., MARZOLI, A., BERTRAND, H., REISBERG, L., VERATI, C., ZIMMERMANN, C., CHIARADIA, M., BELLINI, G., AND ERNESTO, M., 2011. $^{40}\text{Ar}/^{39}\text{Ar}$ ages and Sr–Nd–Pb–Os geochemistry of CAMP tholeiites from Western Maranhão basin (NE Brazil). *Lithos* **122**, 137-151.
- MEYZEN, C.M., LUDDEN, J.N., HUMLER, E., LUIS, B., TOPLIS, M.J., MÉVEL, C., AND STOREY, M., 2005. New insights into the origin and distribution of the DUPAL isotope anomaly in the Indian Ocean mantle from MORB of the Southwest Indian Ridge, *Geochemistry, Geophysics, Geosystems* **6**. Q11K11, doi:10.1029/2005GC000979.
- MORGAN, W.J., 1971. Convection plumes in the lower mantle. *Nature* **230**, 42–43.
- MORIMOTO, N., FABRIES, J., FERGUSON, A.K., GINZBURG, I.V., ROSS, M., SEIFERT, F.A., ZUSSMAN, J., AOKI, K., AND GOT-TARDI, G., 1988. Nomenclature of pyroxenes. *American Mineralogist* **73**, 1123-1133.

- MURPHY, J.B., VAN STAAL, C.R., AND KEPPIE, D., 1999. Middle to late Paleozoic Acadian orogeny in the northern Appalachians: A Laramide-style plume-modified orogeny. *Geology* **27** (7), 653-656.
- MURPHY, J.B., AND DOSTAL, J., 2007. Continental mafic magmatism of different ages in the same terrane: constraints on the evolution of an enriched mantle source. *Geology* **35**, 335-338.
- MURPHY, J.B., DOSTAL, J., GUTIÉRREZ-ALONSO, G., AND KEPPIE, J.D., 2011. Early Jurassic magmatism on the northern margin of CAMP: Derivation from a Proterozoic sub-continental lithospheric mantle. *Lithos* **123**, 158-164.
- NELSON, K.D., 1992. Are crustal thickness variations in old mountain belts like the Appalachians a consequence of lithospheric delamination? *Geology* **20**, 498-502.
- NOMADE, S., KNIGHT, K.B., BEUTEL, E., RENNE, P.R., VERATI, C., FÉRAUD, G., MARZOLI, A., YOUNI, N., AND BERTRAND, H., 2007. Chronology of the Central Atlantic Magmatic Province: Implications for the Central Atlantic rifting processes and the Triassic-Jurassic biotic crisis. *Palaeogeography, Palaeoclimatology, Palaeoecology* **244**, 326-344.
- ODOM, A.L., AND FULLAGAR, P.D., 1984. Rb-Sr whole rock and inherited zircon ages of the plutonic suite of the Crossnore Complex, southern Appalachians, and their implications regarding the time of opening of the Iapetus Ocean. In: The Grenville event in the Appalachians and related topics, (Bartolomew, M.J., ed.). *Geological Society of America Special Papers* **194**, 255-261.
- OH, J., AUSTIN, A., PHILLIPS, J.D., COFFIN, M.F., AND STOFFA, P.L., 1995. Seaward-dipping reflectors offshore the southeastern United States: Seismic evidence for extensive volcanism accompanying sequential formation of the Carolina Trough and Blake Plateau basin. *Geology* **23**, 9-12.
- OLSEN, P.E., KENT, D.V., ET-TOUHAMI, M., AND PUFFER, J., 2003. Cyclo-, Magneto-, and Bio-Stratigraphic Constraints on the Duration of the CAMP Event and its Relationship to the Triassic-Jurassic Boundary. In: The Central Atlantic Magmatic Province: Insights from fragments of Pangea. *Geophysical Monograph* **136**, 7-32.
- PÁLFY, J., MORTENSEN, J. K., CARTER, E. S., SMITH, P. L., FRIEDMAN, R. M., AND TIPPER, H. W., 2000. Timing the end-Triassic mass extinction: First on land, then in the sea? *Geology* **28**, 39-42
- PEATE, D.W., BREDDAM, K., BAKER, J.A., KURZ, M.D., BARKER, A.K., PRESTVIK, T., GRASSINEAU, N., AND SKOVGAARD, A.C., 2010. Compositional characteristics and spatial distribution of enriched Icelandic mantle components. *Journal of Petrology* **51**, 1447-1475.
- PEGRAM, W.J., 1990. Development of continental lithospheric mantle as reflected in the chemistry of the Mesozoic Appalachian Tholeiites, U.S.A. *Earth and Planetary Science Letters* **97**, 316-331.
- PE-PIPER, G., AND REYNOLDS, P.H., 2000. Early Mesozoic alkaline mafic dykes, southwestern Nova Scotia, Canada, and their bearing on Triassic-Jurassic magmatism. *Canadian Mineralogist* **38**, 217-232.
- PETTINGHILL, H.S., SINHA, A.K., AND TATSUMOTO, M., 1984. Age and origin of anorthosites, charnockites, and granulites in the Central Virginia Blue Ridge: Nd and Sr isotopic evidence. *Contributions to Mineralogy and Petrology* **85**, 279-291.
- PHILPOTTS, A.R., AND ASHER, P.M., 1993. Wallrock Melting and Reaction Effects Along the Higganum Diabase Dike in Connecticut - Contamination of a Continental Flood-Basalt Feeder. *Journal of Petrology* **34**, 1029-1058.
- PLANK, T., 2005. Constraints from thorium/lanthanum on sediment recycling at subduction zones and the evolution of the continents. *Journal of Petrology* **46**, 921-944.
- PLANK, T., AND LANGMUIR, C.H., 1998. The chemical composition of subducting sediment and its consequences for the crust and mantle. *Chemical Geology* **145**, 325-394.
- PLANK, T., LANGMUIR, C.H., 1998. The chemical composition of subducting sediment and its consequences for the crust and mantle. *Chemical Geology* **145**, 325-394.
- POLLOCK, J.C., AND HIBBARD, J.P., 2010. Geochemistry and tectonic significance of the Stony Mountain gabbro, North Carolina, Implications for the Early Paleozoic evolution of Carolina. *Gondwana Research* **17**, 500-515.

- POPENOE, P., AND ZEITZ, I., 1977. The nature of the geophysical basement beneath the Coastal Plain of South Carolina and the northeastern Georgia. In: Rankin, D.W., ed, Studies related to the Charleston, South Carolina, earthquake of 1886 – a preliminary report, *U.S Geological Survey Professional Paper* **1028**, 119-138.
- PUFFER, J.H., 1992. Eastern North American flood basalts in the context of the incipient breakup of Pangea. In: Puffer, J.H., Ragland, P.C., eds., Eastern North American Mesozoic Magmatism. *Geological Society of America Special Paper* **268**, 95–119.
- PUFFER, J.H., AND RAGLAND, P.C., 1992. Eastern North American Mesozoic Magmatism. *Geological Society of America Special Paper* **268**, 406 p.
- PUFFER, J.H., AND STUDENT, J.J., 1992. Volcanic structures, eruptive style, and post-eruptive deformation and chemical alteration of the Watchung flood basalts, New Jersey. In: Puffer J.H. and Ragland, P.C., eds., Eastern North American Mesozoic Magmatism. *Geological Society of America Special Paper* **268**, 261-278.
- PUFFER, J.H., BLOCK, K.A., AND STEINER, J.C., 2009. Transmission of flood basalts through a shallow crustal sill and the correlation of sill layers with extrusive flows: the Palisades intrusive system and the basalts of the Newark Basin, New Jersey, U.S.A. *Journal of Geology* **117**, 139–155.
- PUTIRKA, K., 2008. Thermometers and Barometers for Volcanic Systems. In: Putirka, K., and Tepley, F., eds., Minerals, Inclusions and Volcanic Processes. *Reviews in Mineralogy and Geochemistry, Mineralogical Society of America* **69**, 61-120.
- RAGLAND, P.C., HATCHER, R.D.JR., AND WHITTINGTON, D., 1983. Juxtaposed Mesozoic diabase dike sets from the Carolinas: A preliminary assessment. *Geology* **11**, 394-399.
- RAMPINO, M.R., SELF, S., AND STOTHERS, R.B., 1988. Volcanic winters, *Annual Reviews Earth and Planetary Science Letters* **16**, 73-99.
- RANKIN, D.W., 1975. The continental margin of eastern North America in the southern Appalachians: the opening and closing of the proto-Atlantic Ocean. *American Journal of Science* **275** (A), 298-336.
- RAUP, D. M., AND SEPKOSKI, J. J., 1982. Mass Extinctions in the Marine Fossil Record. *Science* **215**, 1501-1503.
- RENNE, P.R., MUNDIL, R., BALCO, G., MIN, K., AND LUDWIG, K.R., 2010. Joint determination of ^{40}K decay constants and $^{40}\text{Ar}^*/^{40}\text{K}$ for the Fish Canyon sanidine standard, and improved accuracy for $^{40}\text{Ar}/^{39}\text{Ar}$ geochronology. *Geochimica et Cosmochimica Acta* **74**, 5349-5367.
- ROBINSON, J.A.C., WOOD, B.J., AND BLUNDY, J.D., 1998. The beginning of melting of fertile and depleted peridotite at 1.5 GPa. *Earth and Planetary Science Letters* **155**, 97-111.
- RODGERS, J., 1971. The Taconic orogeny. *Geological Society of America* **82**, 1141-1178.
- ROEDER, P.L., AND EMSLIE, R.F., 1970. Olivine–liquid equilibrium. *Contributions to Mineralogy and Petrology* **29**, 275-289.
- ROY BARMAN, M., 1993. Mesure du rapport $^{187}\text{Os}/^{186}\text{Os}$ dans les basaltes et les peridotites: Contribution à la systématique ^{187}Re - ^{187}Os dans le manteaux, Université Thèse Paris VII, 268 p.
- RUDNICK, R.L., AND FOUNTAIN, D.M., 1995. Nature and composition of the continental crust -- a lower crustal perspective. *Reviews in Geophysics* **33**, 267-309.
- SAAL, A.E., RUNICK, R.L., RAVIZZA, G.E., AND HART, S.R., 1998. Re-Os isotope evidence for the composition, formation and age of the lower continental crust. *Nature* **393**, 58-61.
- SALTERS, V.J.M., AND SACHI-KOCHER, A., 2010. An ancient metasomatic source for the Walvis Ridge basalts. *Chemical Geology*, **273**, 151-157.
- SAMSON, S.D., COLER, D.G., AND SPEER, J.A., 1995. Geochemical and Nd-Sr-Pb isotopic composition of Alleghanian granites of the southern Appalachians: Origin, tectonic setting, and source characterization. *Earth and Planetary Science Letters* **134**, 359-376.

- SCHALTEGGER, U., GUEX, J., BARTOLINI, A., SCHOENE, B., AND OVTCHAROVA, M., 2008. Precise U–Pb age constraints for end-Triassic mass extinction, its correlation to volcanism and Hettangian post-extinction recovery. *Earth and Planetary Science Letters* **267**, 266-275.
- SCHENK, P.E., 1997. Sequence stratigraphy and provenance on Gondwana's margin: The Meguma zone (Cambrian to Devonian) of Nova Scotia, Canada. *Geological Society of America Bulletin* **109**, 395-409.
- SCHLISCHE, R.W., 2003. Progress in Understanding the Structural Geology, Basin Evolution, and Tectonic History of the Eastern North American Rift System. In: LeTourneau, P. and Olsen, P.E. eds., *The Great Rift Valleys of Pangea in the Eastern North America - volume One: Tectonics, Structure and Volcanism*, Columbia University Press, New York (New Jersey), 21-63.
- SCHOENE, B., CROWLEY, J.L., CONDON, D.J., SCHMIDT, M.D., AND BOWRING, S.A., 2006. Reassessing the uranium decay constants for geochronology using ID-TIMS U–Pb data. *Geochimica Cosmochimica Acta* **70**, 426–445.
- SCHOENE, B., GUEX, J., BARTOLINI, A., SCHALTEGGER, U., AND BLACKBURN, T.J., 2010. Correlating the end-Triassic mass extinction and flood basalt volcanism at the 100 ka level. *Geology* **38**, 387-390.
- SCHWAB, F.L., 1972. The Chilhowee Group and the Late Precambrian-Early Paleozoic sedimentary framework in the central and southern Appalachians, In: Lessing, P., Hayhurst, R.I., Barlow, J.A., Woodfork, L.D., eds., *Appalachian structures: Origin, evolution and potential for new exploration frontiers*, West Virginia University and West Virginia Geological and Economic Survey Seminar, Morgantown (West Virginia), 59-101.
- SCOTESE, C.R., BAMBACH, R.K., BARTON, C., VAN DER VOO, R., AND ZIEGLER, F.A., 1979. Paleozoic base maps. *Journal of Geology* **87**, 217-277.
- SECOR, D.T.JR., SNOKE, A.W., BRAMLETT, K.W., COSTELLO, O.P., AND KIMBRELL, O.P., 1986. Character of the Alleghanian orogeny in the southern Appalachians, part I: Alleghanian deformation in the eastern Piedmont of the South Carolina. *Geological Society of America Bulletin* **97**, 1319-1328.
- SELF, S., BLAKE, S., SHARMA, K., WIDDOWSON, M., AND SEPHTON, S., 2008. Sulfur and Chlorine in Late Cretaceous Deccan Magmas and Eruptive Gas Release. *Science* **319**, 1654-1657.
- SHIREY, S.B., AND WALKER, R.J., 1998. The Re-Os isotope system in cosmochemistry and high-temperature geochemistry. *Annual Reviews Earth and Planetary Science Letters* **26**, 423-500.
- SINHA, A.K., AND ZIETZ, I., 1982. Geophysical and geochemical evidence for a Hercynian magmatic arc, Maryland to Georgia. *Geology* **10**, 593-596.
- SMITH W.A., AND HARE, J.C., 1983. Paleomagnetic results from north-south and northwest trending diabase dykes from the Piedmont of North Carolina. *Geological Society of America Abstracts with Programs* **15**, 198 p.
- SMOLIAR, M.I., WALKER, R.J., AND MORGAN, J.W., 1996. Re-Os ages of Group IIA, IIIA, IVA, and IVB iron meteorites. *Science* **271**, 1099-1102.
- SOBOLEV, A.V., HOFMANN, A.W., KUZMIN, D.V., YAXLEY, G.M., ARNDT, N.T., CHUNG, S.-L., DANYUSHEVSKY, L.V., ELLIOTT, T., FREY, F.A., GARCIA, M.O., GURENKO, A.A., KAMENETSKY, V.S., KERR, A.C., KRIVOLUTSKAYA, N.A., MATVIENKOV, V.V., NIKOGOSIAN, I.K., ROCHOLL, A., SIGURDSSON, I.A., SUSHCHEVSKAYA, N.M., AND TEKLAY, M., 2007. The Amount of Recycled Crust in Sources of Mantle-Derived Melts. *Science* **316**, 412-417.
- SOBOLEV, A.V., HOFMANN, A.W., SOBOLEV, S.V., AND NIKOGOSIAN, I.K., 2005. *Nature* **434**, 590-597.
- SPERA, F.J., AND BOHRSON, W.A., 2001. Energy-Constrained Open-System Magmatic Processes I: General Model and Energy-Constrained Assimilation and Fractional Crystallization (EC-AFC) Formulation. *Journal of Petrology* **42**, 999-1018.
- STODDARD, E.F., 1992. A new suite of post-orogenic dikes in the eastern North Carolina Piedmont: Part II, Mineralogy and geochemistry. *Southeastern Geology* **32**, 119-142.
- STODDARD, E.F., DELOREY, C.M., MCDANIEL, R.D., DOOLEY, R.E., RESSETAR, R., AND FULLAGAR, P. D., 1986. A new suite of post-orogenic dikes in the eastern North Carolina Piedmont: Part I. Occurrence, petrography, paleomagnetism, and Rb/Sr geochronology. *Southeastern Geology* **27**, 1-12.

- STRACKE, A., BIZIMIS, M., AND SALTERS, V.J.M., 2003. Recycling oceanic crust: quantitative constraints. *Geochemistry, Geophysics, Geosystems* **4**. doi: 10.1029/2001GC000223.
- SUN, S.-S., AND McDONOUGH, W.F., 1989. Chemical and isotopic systematics of oceanic basalts: implications for mantle composition and processes. In: Saunders, A.D. and Norry, M.J., eds., *Magmatism in the Ocean Basins. Geological Society of London Special Publications* **42**, 313-345.
- TAYLOR, S.R., AND McLENNAN, S.M., 1995. The geochemical evolution of the continental crust. *Reviews in Geophysics* **33**, 241-265.
- TOLLO, R.P., AND GOTTFRIED, D., 1992. Petrochemistry of Jurassic basalt from eight cores, Newark basin, New Jersey. In: Puffer J.H. and Ragland, P.C., eds., *Eastern North American Mesozoic Magmatism. Geological Society of America Special Paper* **268**, 233-260.
- TOLLO, R.P., CORRIVEAU, L., McLELLAND, J., AND BARTHOLOMEW, M.J., 2004. Proterozoic tectonic evolution of the Grenville orogen in North America: An introduction. *Geological Society of America Memoirs* **197**, 1-18.
- ULMER, P., 1989. Partitioning of high field strength elements among olivine, pyroxenes, garnet and calc alkaline picobasalt: experimental results and an application. *Carnegie Institution of Washington Year Book* **1988-1989**, 42-47.
- VAN DER PLUJM, B.A., JOHNSON, R.J.E., AND VAN DER VOO, R., 1990. Early Paleozoic paleogeography and accretionary history of the Newfoundland Appalachians. *Geology* **18**, 898-901.
- VAN STAAL, C.R., MACNIOCALL, V., VALVERDE-VAQUERO, P., BARR, S.M., FYFFE, L.R., AND REUSCH, D.N., 2004. Ganderia, Avalonia, and the Salinic and Acadian orogenies. *Geological Society of America Abstracts with Programs* **36**, 128-129.
- VAN STAAL, C.R., WHALEN, J.B., MCNICOLI, V., PEHRSSON, S., LISSENBERG, C.J., ZAGOREVSKI, A., VAN BREEMEN, O., AND JENNER, G.A., 2007. The Notre Dame arc and the Taconic orogeny in Newfoundland. In: Hatcher, R.D.Jr., Carlson, M.P., McBride, J.H., and Martínez-Catalán, J.R., eds., *The 4-D Framework of Continental Crust. Geological Society of America Memoirs* **200**, doi: 10.1130/2007.1200 (26).
- VERATI, C., BERTRAND, H., AND FÉRAUD, G., 2005. The farthest record of the Central Atlantic Magmatic Province into West Africa craton: Precise $^{40}\text{Ar}/^{39}\text{Ar}$ dating and geochemistry of Taoudenni basin intrusives (northern Mali). *Earth and Planetary Science Letters* **235**, 391-407.
- VILLIGER, S., ULMER, P., AND MÜNTENER, O., 2004. Equilibrium and Fractional Crystallization Experiments at 0.7GPa; the Effect of Pressure on Phase Relations and Liquid Compositions of Tholeiitic Magmas. *Journal of Petrology* **45**, 2369-2388.
- VÖLKENING, J., WALCZYK, T., AND HEUMANN, K., 1991. Osmium isotope ratio determinations by negative thermal ionization mass spectrometry. *International Journal of Mass Spectrometry Ion Proceedings* **105**, 147-59.
- WARNER, R.D., SNIPES, D.S., HUGHES, S., WALKER, R.J., SCHMITT, R.A., AND STEINER, J.C., 1992. Geochemistry and petrology of Mesozoic dikes in South Carolina. In: Puffer, J.H. and Ragland, P.C., eds., *Eastern North America Mesozoic magmatism. Geological Society of America Special Papers* **268**, 333-346.
- WARNER, R.D., AND WASILEWSKI, P.J., 1985. Magnetic mineralogy of dolerite dykes. *Geological Society of America Abstracts with Programs* **17**, 141 p.
- WEIGAND, P.W., AND RAGLAND, P.C., 1970. Geochemistry of Mesozoic dolerite dikes from eastern North America. *Contributions to Mineralogy and Petrology* **29**, 195-214
- WHITE, R., AND MCKENZIE, D., 1989. Magmatism at Rift Zones: The Generation of Volcanic Continental Margins and Flood Basalts. *Journal of Geophysical Research* **94**, 7685-7729.
- WHITESIDE, J.H., OLSEN, P.E., KENT, D.V., FOWELL, S.J., AND ET-TOUHAMI, M., 2007. Synchrony between the Central Atlantic magmatic province and the Triassic-Jurassic mass-extinction event? *Palaeogeography, Palaeoclimatology, Palaeoecology* **244**, 345-367.
- WIGNALL, P.B., 2001. Large igneous provinces and mass extinctions. *Earth Science Reviews* **53**, 1-33.

- WILSON, M., 1997. Thermal evolution of the Central Atlantic passive margins: continental break-up above a Mesozoic superplume. *Journal of Geological Society of London* **154**, 491–495.
- WITHJACK, M.O., SCHLISCHE, R.W., AND OLSEN, P.E., 1998. Diachronous rifting, drifting, and inversion on the passive margin of central eastern North America: an analog for other passive margins. *American Association of Petroleum Geologists Bulletin* **82**, 817–835.
- WORKMAN, R.K., AND HART, S.R., 2005. Major and trace element composition of the depleted MORB mantle (DMM). *Earth and Planetary Science Letters* **231**, 53-72.
- WRIGHT HORTON, J., AND MCCONNELL, K.I., 1991. The Western Piedmont. In: Wright Horton, J. and Zullo, V.A., eds., *The Geology of the Carolinas, Carolina Geologic Society Fiftieth Anniversary Volume*, The University of Tennessee Press, Knoxville (Tennessee), 36-59.
- YAXLEY, G.M., AND GREEN, D.H., 1998. Reactions between eclogite and peridotite: mantle refertilisation by subduction of oceanic crust. *Schweizerische Mineralogische Petrographische Mitteilungen* **78**, 243–255.
- ZINDLER, A., AND HART, S., 1986. Chemical Geodynamics. *Annual Review of Earth and Planetary Science* **14**, 493-571.

PART II

LATEST TRIASSIC MARINE Sr ISOTOPIC VARIATIONS

1 OVERVIEW

Two large-scale events characterized the latest Triassic: 1) one of the main Phanerozoic biotic crises, which culminated at the Triassic–Jurassic boundary (TJB) at 201.31 ± 0.43 Ma (Schoene et al., 2010), but possibly started from the latest Norian or earliest Rhaetian, as a progressive reduction in the marine and terrestrial biota (Tanner et al., 2004); and 2) the emplacement of one of the largest igneous provinces, the Central Atlantic Magmatic Province (CAMP; Marzoli et al., 1999), centered at 200.0 ± 2.6 Ma (Marzoli et al., 2011; ages recalibrated after Renne et al., 2010) on a surface in excess of 10 million km² in Pangaea (Marzoli et al., 1999). Since CAMP eruptions straddled the TJB (Marzoli et al., 2004; Cirilli et al., 2009), volcanogenic pollution of the atmosphere may have triggered the end-Triassic extinction (McElwain et al., 1999; Hesselbo et al., 2002; Ruhl et al., 2011; Schaller et al., 2011).

As the onset of CAMP magmatism within the latest Triassic is poorly constrained, here we take an alternative approach to correlate the marine biostratigraphic time-scale (based on conodonts) with the magmatic event. This approach rests on the measure of Sr isotopic compositions of biostratigraphically well-constrained conodont samples of late Norian to latest Rhaetian age, i.e. *Mockina bidentata*, *Misikella hernsteini*–*Parvigondolella andrusovi*, *Misikella posthernsteini* and *Misikella ultima* Biozones (Kozur and Mock, 1991). The potential of Sr isotope stratigraphy hinges on the global homogeneity of the ⁸⁷Sr/⁸⁶Sr composition of the oceanic water, the residence time of Sr in seawater being far longer (e.g. 2.4 Ma; Jones and Jenkyns, 2001) than the ocean mixing time (about thousand years; Hodell et al., 1990). Henceforth, the ⁸⁷Sr/⁸⁶Sr composition of a single marine fossil sample of given age should reflect the global oceanic isotopic composition for that age (McArthur, 1998), given that the isotopic composition is not modified by alteration events. The new obtained ⁸⁷Sr/⁸⁶Sr variations are used to constrain the biostratigraphic age of CAMP magmatism, to constrain the end-Triassic time-scale and to evaluate the effects of CAMP on end-Triassic climate change and biological crisis.

2 METHODS

For Sr isotopic analyses, washed and crushed limestones (6-7 kg) were dissolved in 7% acetic acid and the insoluble residues sieved carefully with distilled water to retain a fraction between 104 and 825 μm , without density separation. Conodonts were handpicked under binocular microscope, selecting single elements without adhering sediment particles. Conodonts (40-60 elements per sample, corresponding to ~ 1 mg) were dissolved in sub-boiling distilled 6M HCl. Sr was separated from the matrix using a Sr-spec resin and was loaded on single Re filaments with a Ta oxide solution. Sr isotope ratios were measured on a Thermo Finnigan TRITON thermal ionization mass spectrometer at the Department of Mineralogy (University of Geneva, Switzerland) at a pyrometer-controlled temperature of 1480°C in static mode, using the virtual amplifier design to cancel out biases in gain calibration among amplifiers. $^{87}\text{Sr}/^{86}\text{Sr}$ values were corrected for internal fractionation using a $^{88}\text{Sr}/^{86}\text{Sr}$ value of 8.375209. Raw values were further corrected for external fractionation based on repeated measurements of the SRM987 standard for which a normalization value of $^{87}\text{Sr}/^{86}\text{Sr} = 0.710254$ was used. External reproducibility of the $^{87}\text{Sr}/^{86}\text{Sr}$ ratio for the SRM987 standard is 5 p.p.m. $^{87}\text{Sr}/^{86}\text{Sr}$ values are normalized to NBS 987 of 0.710254.

Samples	Location	CAI	Biozones (conodonts)	Analyzed species (EMPA)	Mean Sr (ppm)	$^{87}\text{Sr}/^{86}\text{Sr}$
K64	Lagonegro Basin (Italy) - Sasso di Castalda sec.	2.5	FAD <i>Mo. bidentata</i>			0.708136
K61	Lagonegro Basin (Italy) - Sasso di Castalda sec.	2.5	<i>Mo. bidentata</i>			0.708121
NR2	Sicilian Basin (Italy) - Pizzo Mondello sec.	1	<i>P. andruscovi</i> , <i>Mo. bidentata</i>	<i>Mocikina bidentata</i>	1983	0.707935
RAE 3-1	Mamonia Complex (Cyprus)	1	<i>P. andruscovi</i> , <i>Mo. bidentata</i>			0.707928
KE3	Lagonegro Basin (Italy) - Sasso di Castalda sec.	2.5	FAD <i>M. bernsteini</i>	<i>Mocikina bidentata</i>	2147	0.708236
NR59	Sicilian Basin (Italy) - Pizzo Mondello sec.	1	<i>M. bernsteini</i> , <i>P. andruscovi</i>	<i>Misikella bernsteini</i>	1853	0.707975
PR.12	Lagonegro Basin (Italy) - Pignola-Abricola sec.	2.5	<i>Misikella bernsteini</i>			0.708264
IKZ1	Lagonegro Basin (Italy) - Sasso di Castalda sec.	2.5	<i>M. bernsteini</i> , trans <i>M. bernsteini/postbernsteni</i>			0.708176
REV 4 18m	Mamonia Complex (Cyprus) - Locality REV 4	1	FAD <i>Misikella postbernsteni</i>			0.707985
REV 3-1	Mamonia Complex (Cyprus) - Locality REV-3	1	<i>Misikella postbernsteni</i>			0.707892
REV 4 8m	Mamonia Complex (Cyprus) - Locality REV 4	1	<i>M. postbernsteni</i> , <i>M. keessenensis</i>			0.707893
J18c	Bergamasc Alps (Italy) - Costa Imagna sec.	2	<i>M. postbernsteni</i> , <i>M. keessenensis</i>	<i>Misikella bernsteini</i>	1558	0.707846
PG38	Sicilian Basin (Italy) - Pizzo Mondello sec.	1	FAD <i>Misikella ultima</i>	<i>Misikella postbernsteni</i>	1973	0.707774
PG41	Sicilian Basin (Italy) - Pizzo Mondello sec.	1	<i>Misikella ultima</i>	<i>Misikella postbernsteni</i>	2459	0.707777
PG16	Sicilian Basin (Italy) - Pizzo Mondello sec.	1	<i>Misikella ultima</i>	<i>Misikella postbernsteni</i>	1989	0.707759
REV 4-30m	Mamonia Complex (Cyprus) - Locality REV-4	1	<i>Misikella ultima</i>			0.707936
PR3	Lagonegro Basin (Italy) - Pignola-Abricola sec.	1.5	<i>M. ultima</i> , <i>M. konaci</i>	<i>Misikella postbernsteni</i>	1753	0.708049
PR2	Lagonegro Basin (Italy) - Pignola-Abricola sec.	1.5	<i>M. ultima</i> , <i>M. konaci</i>	<i>Misikella postbernsteni</i>	2493	0.708026
PR1	Lagonegro Basin (Italy) - Pignola-Abricola sec.	1.5	<i>M. ultima</i> , <i>M. konaci</i>	<i>Misikella postbernsteni</i>	1541	0.708074

Table 2a. Measured $^{87}\text{Sr}/^{86}\text{Sr}$ compositions of biogenic apatite from late Norian to latest Rhaetian conodont samples. The stratigraphic position, conodont alteration index (CAI) and conodont association of the analysed samples are described in detail in Fähræus and Ryley (1989), Giordano et al. (2010), Muttoni et al. (2010) and Mazza and Rigo (2012).

3 RESULTS

We analyzed 19 conodont biogenic apatite samples from sections belonging to the Tethyan realm (Table 2a). In particular, the $^{87}\text{Sr}/^{86}\text{Sr}$ composition of the analyzed conodonts is considered to reflect the global seawater isotopic composition of the latest Norian (*Mockina bidentata* and *Misikella hernsteini*–*Parvigondolella andrusovi* Biozones), early Rhaetian (*Misikella posthernsteini* Biozone) and late Rhaetian (*Misikella ultima* Biozone). The advantages of analyzing conodont samples are represented by a) conodont fossils being the most reliable biostratigraphic tools for the latest Triassic (Giordano et al., 2010); b) the high Sr (and low Rb) content of the apatite constituting these fossils; c) the possibility to check the state of preservation of conodonts considering their CAI (Conodont Alteration Index), which should be lower than 2.5 for the original Sr isotopic composition to be maintained (Ebneht et al., 1997; Korte et al., 2003).

Electron Microprobe analyses were performed on 10 conodonts, representative of different CAI values observed from the analyzed stratigraphic sections (cf. Appendix VI). Sr contents averaged for each sample range from ~ 1500 to 2500 p.p.m., in agreement with compositions of previously analyzed conodont apatites considered not to be altered by diagenetic overprint and weathering (Ebneht et al., 1997; Korte et al., 2003; Trotter and Eggins, 2006). Sr contents (p.p.m.) show no correlation with $^{87}\text{Sr}/^{86}\text{Sr}$ or with CAI values (Fig. 3.2 a) indicating that no major contribution of diagenetic Sr was added to the conodont samples. Nonetheless, conodonts yielding CAI of 2.5 are probably altered being characterized by higher $^{87}\text{Sr}/^{86}\text{Sr}$ ($\sim 2 \times 10^{-4}$) values compared with coeval low CAI samples, but preserve relative fluctuations in the original signal, apparently mimicking the trend defined by coeval samples with $\text{CAI} \leq 2$ (Fig. 3.2 c), similarly noticed by Bertram et al. (1992) and Ebneht et al. (1997) for Palaeozoic conodonts. However, for the quantification of the isotopic shifts, only samples with $\text{CAI} \leq 2$ were considered.

Previously published $^{87}\text{Sr}/^{86}\text{Sr}$ data for Triassic fossils (conodonts and brachiopods) show a global drop in Sr isotopic ratio during the latest Triassic (Korte et al., 2003; Cohen and Coe, 2007 and references therein). Largely consistent with these data, our new results are focused on the latest Triassic and refine with high resolution the details of the marine $^{87}\text{Sr}/^{86}\text{Sr}$ variations from the late

Norian to the TJB, highlighting two main significant shifts (Fig. 3.1 a, Table 2a). The first occurs just after the base of the Rhaetian stage, here defined as the FAD (First Appearance Datum) of conodont *Misikella posthernsteini* (Giordano et al., 2010; Fig. 3.1 a, c) and is marked by a rapid drop from relatively high (0.70798) to lower $^{87}\text{Sr}/^{86}\text{Sr}$ values (~ 0.70777 at the base of the *Misikella ultima* Biozone). The second $^{87}\text{Sr}/^{86}\text{Sr}$ shift starts within the latest Rhaetian when the Sr isotopic values rise again to relatively high values, up to 0.70807 (upper *Misikella ultima* Biozone). Later, the seawater Sr isotopic curve shows a long negative trend from the earliest to the middle Lower Jurassic, i.e. Hettangian–Pliensbachian/Toarcian (e.g. Jones et al., 1994; Jones and Jenkins, 2001).

The $^{87}\text{Sr}/^{86}\text{Sr}$ isotopic curve observed for our conodont samples is mimicked by the seawater $^{187}\text{Os}/^{188}\text{Os}$ curve for the Rhaetian illustrated by Cohen and Coe (2002) and Kuroda et al. (2010) (Fig. 3.1 b), who documented a decreasing trend of $^{187}\text{Os}/^{188}\text{Os}$ starting from the lowest Rhaetian and then an abrupt increase in the latest Rhaetian, which in turn is followed by a stable phase from the TJB to the late Hettangian. Notably, the Sr and Os isotopic shifts are biostratigraphically correlated considering the coeval occurrences of the Tethyan conodont *Misikella posthernsteini* and the North American conodont *Epigondolella mosheri* A at the base of the radiolarian *Propavicingula moniliformis* Assemblage Zone (Giordano et al., 2010), corresponding to *Haeckelicyrtium breviora* Zone for Japan (Carter, 2007), and the global disappearance of the bivalve genus *Monotis*, after a short period of dwarfism (as a possible response to a period of global perturbation; McRoberts et al., 2008). The calibration between the base of the radiolarian *Globolaxtorum tozeri* Zone and the occurrence of conodont *Misikella ultima* is shown in Pálffy et al. (2007), (Fig. 3.1 c).

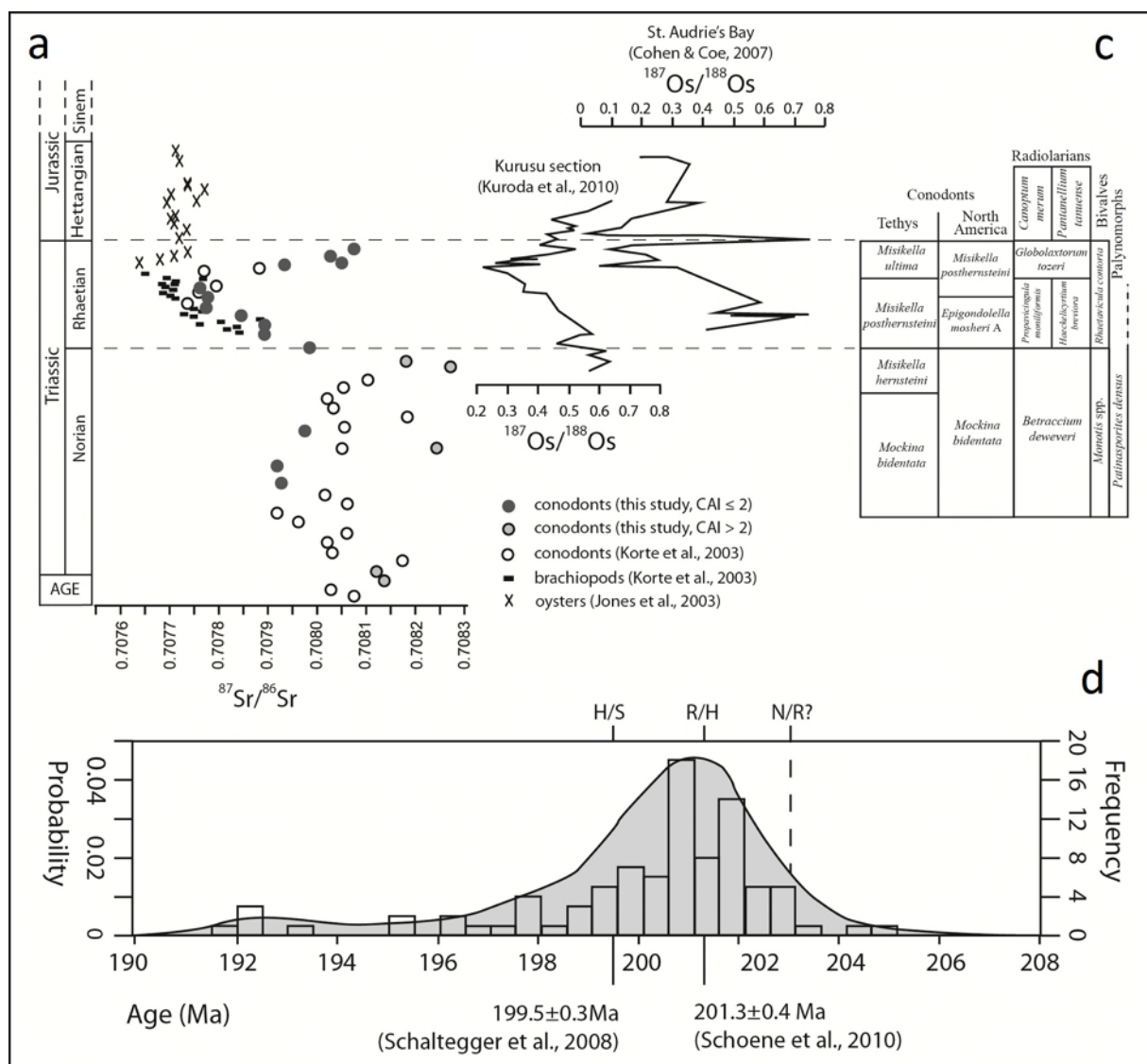


Figure 3.1: (a) Sr isotopic variations of Norian to Hettangian fossils. Dark grey circles: our conodont $^{87}\text{Sr}/^{86}\text{Sr}$ data, CAI \leq 2; black contoured grey circles: our conodont $^{87}\text{Sr}/^{86}\text{Sr}$ data, CAI > 2; open circles and black rectangles represent conodonts and brachiopods respectively of Korte et al. (2003); crosses are oysters from Jones et al. (1994). (b) Marine sediment $^{187}\text{Os}/^{188}\text{Os}$ are from previous studies (Cohen and Coe, 2002; Kuroda et al., 2010). (c) Biostratigraphical calibrations after Giordano et al. (2010), Carter (2007) and Pálffy et al. (2007). (d) Relative probability and frequency distribution of $^{40}\text{Ar}/^{39}\text{Ar}$ plateau ages of CAMP basalts (Marzoli et al., 2011 and references therein). Note the peak activity occurring between c. 202 and 200 Ma. Ages are recalculated considering newly defined K decay constant and monitor values (Renne et al., 2010) and are thus directly comparable to the U/Pb zircon ages for the TJB (201.31 \pm 0.43 Ma; Schoene et al., 2010), and the Hettangian/Sinemurian boundary (199.5 \pm 0.24 Ma; Schaltegger et al., 2008).

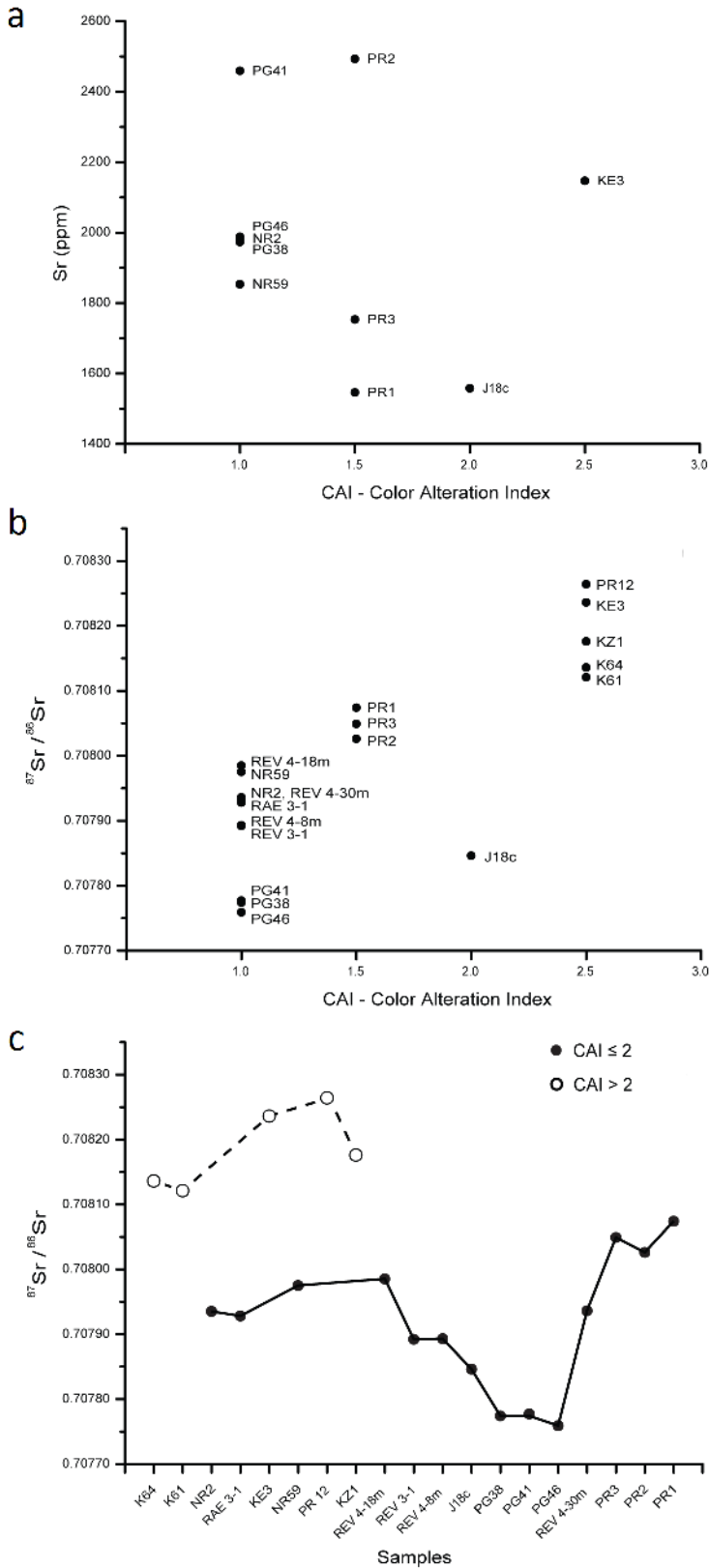


Figure 3.2: Sr content (p.p.m.) and $^{87}\text{Sr}/^{86}\text{Sr}$ vs. conodont alteration index (CAI) (a and b, respectively). (c) Samples with CAI > 2 (open circles) are shown to mimic the trend drawn by coeval samples with CAI ≤ 2 (black circles), although at slightly higher $^{87}\text{Sr}/^{86}\text{Sr}$. In (c), samples are plotted in stratigraphic order with oldest left.

4 DISCUSSION

The variations in the Sr and Os isotopic curves are well correlated for the period between the latest Norian and the TJB, despite the different residence times of the two elements in oceanic waters (the residence time of Sr being at least one order of magnitude longer than that of Os). Therefore, the global perturbations affecting contemporaneously the isotopic balance of both the systems are most likely attributed to abrupt and intense large-scale events. In detail, the progressive drop of Sr and Os marine compositions recorded from the base of the Rhaetian may suggest a reduction in the contribution to the oceans from old continental crust-derived material with high $^{87}\text{Sr}/^{86}\text{Sr}$ and $^{187}\text{Os}/^{188}\text{Os}$, i.e. a reduction in the global run-off. Following calculations of Jones and Jenkins (2001), the observed negative shift may be compatible with a reduction of 15–20% in global run-off. This in turn would imply a significant drop in global temperature that may have been triggered by a catastrophic event, such as a bolide impact or a LIP emplacement and possible associated volcanogenic SO_2 emissions (e.g. Wignall, 2001; Self et al., 2008). Notably, no major asteroid impact is known for the Late Triassic, after that forming the c. 214 Ma Manicougan crater (cf. Jourdan et al., 2009a). Instead, SO_2 release from basalt eruptions may have reduced global temperatures with a consequent decrease in rainfall, but also enhanced the weathering rate through the acidification of the fallout. Presumably, these two effects would tend to balance out, not affecting the Sr flux. Therefore, a short-term drop in run-off is not a likely mechanism to explain the Sr isotopic negative shift.

An alternative scenario is that the earliest-Rhaetian $^{87}\text{Sr}/^{86}\text{Sr}$ and $^{187}\text{Os}/^{188}\text{Os}$ drop may be due to a change in the isotopic signature of the sedimentary source, most likely attributed to a magmatic origin, i.e. either to enhanced hydrothermal activity at Mid-Ocean ridges, or to chemical weathering of young juvenile mantle-derived basalts (Jones and Jenkyns, 2001; Cohen and Coe, 2007). Significant changes in oceanic crust production rates at Mid-Ocean ridges cannot be documented for the Late Triassic and in any case would affect the Sr marine budget for time-scales of several Ma (e.g. Jones and Jenkyns, 2001; Cohen and Coe, 2007). Therefore, even if we cannot completely rule out the presence of any yet undocumented LIP (e.g. an oceanic plateau) during the Late Triassic, in accordance with previous studies (Cohen and Coe, 2007; Kuroda et al., 2010), we propose to attribute

the source of low $^{87}\text{Sr}/^{86}\text{Sr}$ and $^{187}\text{Os}/^{188}\text{Os}$ to chemical alteration/weathering of juvenile basalts belonging to the only remarkable volcanic event known in the Late Triassic, the continental emplacement of the CAMP. The influence of the CAMP on the global ocean Sr isotopic composition can be modelled considering reasonable estimates for the volume of the CAMP (~ 2 million km^3 ; Marzoli et al., 1999), the mean Sr isotopic composition of the basalts (~ 0.705) and their Sr concentration (~ 200 p.p.m.; e.g. Merle et al., 2011). Based on the dynamic response model (Hodell et al., 1990) and on the equilibrium isotopic mass balance calculation used by Jones and Jenkyns (2001), and considering the riverine, hydrothermal and diagenetic Sr fluxes as constant, weathering and erosion of 8% of the total volume of CAMP rocks could explain the difference between the high $^{87}\text{Sr}/^{86}\text{Sr}$ value of the Norian (~ 0.70798) and the low Rhaetian $^{87}\text{Sr}/^{86}\text{Sr}$ value (0.70777). Similar calculations were performed in previous studies (Cohen and Coe, 2007; Kuroda et al., 2010) to assess the role of the CAMP in changing seawater $^{187}\text{Os}/^{188}\text{Os}$. We note that a rapid weathering of CAMP basalts, shortly after their emplacement, is consistent also with the indistinguishable $^{40}\text{Ar}/^{39}\text{Ar}$ alteration and magmatic crystallization ages for CAMP basalts (Jourdan et al., 2009b) as well as with rapidly fluctuating atmospheric CO_2 values responding to CAMP eruption and weathering cycles (Schaller et al., 2011). In a period of rather stable climate (Preto et al., 2010), weathering of the first CAMP basalts acted as a source of unradiogenic Sr and Os, driving early Rhaetian seawater towards lower Sr and Os isotopic ratios (Fig. 3.1 a). The subsequent late Rhaetian recovery (positive shift, Fig. 3.2 c) of seawater $^{87}\text{Sr}/^{86}\text{Sr}$ and $^{187}\text{Os}/^{188}\text{Os}$ has been interpreted as an enhancement of rainfall on ancient continental crust (Cohen and Coe, 2007; Kuroda et al., 2010), as would be consistent with strongly increased global temperatures observed at the TJB (e.g. Ruhl et al., 2011). While sharing this interpretation, we propose furthermore that this late Rhaetian increase of seawater $^{87}\text{Sr}/^{86}\text{Sr}$ may be probably magnified by the contemporaneous sedimentary cover of CAMP lava flows (as observed in the Circum-Atlantic Mesozoic basins of Morocco, Eastern North America and Brazil; e.g. Olsen et al., 2002; Marzoli et al., 2004; Merle et al., 2011) and that it may possibly reflect a transient stasis of CAMP eruptions. Even if not detectable by the $^{40}\text{Ar}/^{39}\text{Ar}$ age data for CAMP basalts, due to the c. 1 Ma resolution of this dating method, brief periods of volcanic quiescence (of c. 300 ka; Whiteside et al., 2007) have been documented for the Newark basin CAMP lava flows (e.g. Olsen et al., 2002) and are consistent with palaeomagnetic data suggesting that CAMP basalts erupted as successive intense brief pulses (Knight et al., 2004).

5 EVIDENCES FOR A RHAETIAN ONSET OF THE CAMP

Our interpretation is that the negative Sr isotopic shift at the beginning of the Rhaetian was triggered by the CAMP, thus implying that CAMP activity started close to the NRB. Previous to this study, the biostratigraphic calibration of the CAMP was based on palynological associations, in particular, on the distribution of the sporomorph *Patinasporites densus*, which has been documented to disappear in the upper Norian–lowermost Rhaetian in several sections worldwide from different palaeoclimatic belts of both Southern and Northern hemispheres (Cirilli et al., 2009). In this sense, at least the oldest Moroccan CAMP lava flows, resting on *P. densus*-bearing sediments (Marzoli et al., 2004), and the CAMP lava pile from the Fundy basin (Canada), emplaced below strata containing a Rhaetian palynological assemblage (Cirilli et al., 2009), are constrained to be Rhaetian in age, as also confirmed by conchostracan biostratigraphy (Kozur and Weems, 2010).

The backward repositioning of the CAMP onset close to the NRB, as suggested by our new $^{87}\text{Sr}/^{86}\text{Sr}$ analyses (and consistent with the $^{187}\text{Os}/^{188}\text{Os}$ data of Kuroda et al., 2010), does not contrast the common idea of a causal link between the CAMP event and the TJB biotic turnover. Instead, it suggests the extension of its trigger role on the entire latest Triassic biotic crisis, emphasizing its step-wise style (Tanner et al., 2004) and is largely consistent with models predicting the environmental effects of CAMP basalts and their trigger effect on Late Triassic atmospheric CO_2 injections (McElwain et al., 1999; Bonis et al., 2010; Ruhl and Kürschner, 2011; Ruhl et al., 2011; Schaller et al., 2011), which then led to a global warming event and perturbations of global biogeochemical cycles (e.g. Beerling and Berner, 2002; Ruhl et al., 2011).

As $^{40}\text{Ar}/^{39}\text{Ar}$ ages recalibrated with newly proposed decay constant and fluence monitor values (Renne et al., 2010) can be directly compared with the U/Pb zircon age of the TJB (201.31 ± 0.43 Ma; Schoene et al., 2010), we can estimate the maximum time possibly elapsed between the NRB (i.e. the onset of the negative Sr and Os isotopic shifts) and the TJB, and thus the duration of the end-Triassic biotic crisis and of the Rhaetian stage. The relative probability plot (Fig. 3.1 d) of all available $^{40}\text{Ar}/^{39}\text{Ar}$ plateau ages (Marzoli et al., 2011) shows that a significant portion of CAMP rocks may have been emplaced before the TJB as the peak of CAMP magmatism has an age comprised

between c. 202 and 200 Ma, whereas any activity before c. 203 Ma was probably of minor volume. The Sr (and Os) isotopic curve and particularly the negative shift observed during the earliest Rhaetian require emplacement and erosion of a significant volume of the CAMP already from the NRB. This poses a maximum age for the onset of the peak activity of CAMP at the NRB of about 203 Ma and, consequently, a maximum duration of c. 1.7 Ma for the Rhaetian and the end-Triassic biological turnover.

REFERENCES (PART II)

- BEERLING, D.J. AND BERNER, R.A., 2002. Biogeochemical constraints on the Triassic-Jurassic boundary carbon cycle event. *Global Biogeochemical Cycles* **16**, 1036-1048.
- BERTRAM, C.J., ELDERFIELD, H., ALDRIDGE, R.J., AND CONWAY MORRIS, S., 1992. $^{87}\text{Sr}/^{86}\text{Sr}$, $^{143}\text{Nd}/^{144}\text{Nd}$ and REEs in Silurian phosphatic fossils. *Earth and Planetary Science Letters* **113**, 239-249.
- BONIS, N.R., VAN KONIJNENBURG-VAN CITTERT J.H.A., AND KÜRSCHNER, W.M., 2010. Changing CO₂ conditions during the end-Triassic inferred from stomatal frequency analysis on *Lepidopteris ottonis* (Goeppert) Schimper and *Ginkgoites taeniatus* (Braun) Harris. *Palaeogeography, Palaeoclimatology, Palaeoecology* **295**, 146-161.
- CARTER, E.S., 2007. Global distribution of Rhaetian radiolarian faunas and their contribution to the definition of the Triassic-Jurassic boundary. In: Lucas, S.G. and Spielmann, J.A., eds., *The Global Triassic. New Mexican Museum of Natural History and Science Bulletin* **41**, 27-31.
- CIRILLI, S., MARZOLI, A., TANNER, L., BERTRAND, H., BURATTI, N., JOURDAN, F., BELLINI, G., KONTAK, D., AND RENNE, P.R., 2009. Latest Triassic onset of the Central Atlantic Magmatic Province (CAMP) volcanism in the Fundy Basin (Nova Scotia): New stratigraphic constraints. *Earth and Planetary Science Letters* **286**, 514-525.
- COHEN, A.S. AND COE, A.L., 2002. New geochemical evidence for the onset of volcanism in the Central Atlantic magmatic province and environmental change at the Triassic-Jurassic boundary. *Geology* **30**, 267-270.
- COHEN, A.S. AND COE, A.L., 2007. The impact of the Central Atlantic Magmatic Province on climate and on the Sr- and Os-isotope evolution of seawater. *Palaeogeography, Palaeoclimatology, Palaeoecology* **244**, 374-390.
- EBNETH, S., DIENER, A., BUHL, D., AND VEIZER, J., 1997. Strontium isotope systematics of conodonts: Middle Devonian, Eifel Mountains, Germany. *Palaeogeography, Palaeoclimatology, Palaeoecology* **132**, 79-96.
- FAHREUS, L.E. AND RYLEY, C., 1989. Multielement species of *Misikella* Kozur and Mock, 1974 and *Axiiothes* n. gen. (Conodonta) from the Mamonia Complex (Upper Triassic), Cyprus. *Canadian Journal of Earth Sciences* **26**, 1255-1263.
- GIORDANO, N., RIGO, M., CIARAPICA, G., AND BERTINELLI, A., 2010. New biostratigraphical constraints for the Norian/Rhaetian boundary: data from Lagonegro Basin, Southern Apennines, Italy. *Lethaia* **43**, 573-586.
- HELSELBO, S.P., ROBINSON, S.A., SURLYK, F., AND PIASECKI, S., 2002. Terrestrial and marine extinction at the Triassic-Jurassic boundary synchronized with major carbon-cycle perturbation: A link to initiation of massive volcanism? *Geology* **30**, 251-254.
- HODELL, D.A., MEAD, G.A., AND MUELLER, P.A., 1990. Variation in the strontium isotopic composition of seawater (8 Ma to present): Implications for chemical weathering rates and dissolved fluxes to the oceans. *Chemical Geology: Isotope Geoscience section* **80**, 291-307.
- JONES, C.E., JENKYN, H.C., AND HELSELBO, S.P., 1994. Strontium isotopes in Early Jurassic seawater. *Geochimica et Cosmochimica Acta* **58**, 1285-1301.
- JONES, C.E. AND JENKYN, H.C., 2001. Seawater strontium isotopes, oceanic anoxic events, and seafloor hydrothermal activity in the Jurassic and Cretaceous. *American Journal of Science* **301**, 112-149.
- JOURDAN, F., RENNE, P.R., AND REIMOLD, W.U., 2009. An appraisal of the ages of terrestrial impact structures. *Earth and Planetary Science Letters* **286**, 1-13.
- JOURDAN, F., MARZOLI, A., BERTRAND, H., CIRILLI, S., TANNER, L.H., KONTAK, D.J., MCHONE, G., RENNE, P.R., AND BELLINI, G., 2009. $^{40}\text{Ar}/^{39}\text{Ar}$ ages of CAMP in North America: Implications for the Triassic-Jurassic boundary and the ^{40}K decay constant bias. *Lithos* **110**, 167-180.

- KNIGHT, K.B., NOMADE, S., RENNE, P.R., MARZOLI, A., BERTRAND, H., AND YOUNI, N., 2004. The Central Atlantic Magmatic Province at the Triassic–Jurassic boundary: paleomagnetic and $^{40}\text{Ar}/^{39}\text{Ar}$ evidence from Morocco for brief, episodic volcanism. *Earth and Planetary Science Letters* **228**, 143-160.
- KORTE, C., KOZUR, H.W., BRUCKSCHEN, P., AND VEIZER, J., 2003. Strontium isotope evolution of Late Permian and Triassic seawater. *Geochimica et Cosmochimica Acta* **67**, 47-62.
- KOZUR, H.W., AND MOCK, R., 1991. New Middle Carnian and Rhaetian conodonts from Hungary and the Alps. Stratigraphic importance and tectonic implications for the Buda Mountains and adjacent areas. *Jahrbuch der Geologischen Bundesanstalt* **134**, 271-297.
- KOZUR, H.W., AND WEEMS R.E., 2010. The biostratigraphic importance of conchostracans in the continental Triassic of the northern hemisphere. In: Lucas, S.G., ed., *The Triassic Timescale. Geological Society of London, Special Publications* **334**, 315-417.
- KURODA, J., HORI, R.S., SUZUKI, K., GROCKE, D.R., AND OHKOUCHI, N., 2010. Marine osmium isotope record across the Triassic–Jurassic boundary from a Pacific pelagic site. *Geology* **38**, 1095-1098.
- MARZOLI, A., RENNE, P.R., PICCIRILLO, E.M., ERNESTO, M., BELLINI, G., AND DE MIN, A., 1999. Extensive 200-Million-Year-Old Continental Flood Basalts of the Central Atlantic Magmatic Province. *Science* **284**, 616-618.
- MARZOLI, A., BERTRAND, H., KNIGHT, K.B., CIRILLI, S., BURATTI, N., VERATI, C., NOMADE, S., RENNE, P.R., YOUNI, N., MARTINI, R., ALLENBACH, K., NEUWERTH, R., RAPAILLE, C., ZANINETTI, L., AND BELLINI, G., 2004. Synchrony of the Central Atlantic magmatic province and the Triassic–Jurassic boundary climatic and biotic crisis. *Geology* **32**, 973-976.
- MARZOLI, A., JOURDAN, F., PUFFER, J.H., CUPPONE, T., TANNER, L.H., WEEMS, R.E., BERTRAND, H., CIRILLI, S., BELLINI, G., AND DE MIN, A., 2011. Timing and duration of the Central Atlantic magmatic province in the Newark and Culpeper basins, eastern U.S.A. *Lithos* **122**, 175-188.
- MAZZA, M. AND RIGO, M., 2012. Taxonomy and stratigraphic record of the Upper Triassic conodonts of the Pizzo Mondello section (Western Sicily, Italy), GSSP candidate for the base of the Norian. *Rivista Italiana di Paleontologia e Stratigrafia* **118**/1.
- MCCARTHER, J.M., 1998. Strontium isotope stratigraphy. In: Doyle, P. and Bennet, M.R., eds., *Unlocking the Stratigraphical Record. Advances in modern stratigraphy*, John Wiley and Sons, Chichester, UK, 221-241.
- MCELWAIN, J.C., BEERLING, D.J., AND WOODWARD, F.I., 1999. Fossil Plants and Global Warming at the Triassic–Jurassic Boundary. *Science* **285**, 1386-1390.
- MCCROBERTS C.A., KRYSSTYN L., AND SHEA A., 2008. Rhaetian (Late Triassic) *Monotis* (Bivalvia: Pectinoida) from the eastern Northern Calcareous Alps (Austria) and the end-Norian crisis in pelagic faunas. *Palaeontology* **51**, 721–735.
- MERLE, R., MARZOLI, A., BERTRAND, H., REISBERG, L., VERATI, C., ZIMMERMANN, C., CHIARADIA, M., BELLINI, G., AND ERNESTO, M., 2011. $^{40}\text{Ar}/^{39}\text{Ar}$ ages and Sr–Nd–Pb–Os geochemistry of CAMP tholeiites from Western Maranhão basin (NE Brazil). *Lithos* **122**, 137-151.
- MUTTONI, G., KENT, D.V., JADOU, F., OLSEN, P.E., RIGO, M., GALLI, M.T., AND NICORA, A., 2010. Rhaetian magneto-biostratigraphy from the Southern Alps (Italy): Constraints on Triassic chronology. *Palaeogeography, Palaeoclimatology, Palaeoecology* **285**, 1-16.
- OLSEN, P.E., KENT, D.V., SUES, H.D., KOEBERL, C., HUBER, H., MONTANARI, A., RAINFORTH, E.C., FOWELL, S.J., SZAJNA, M.J., AND HARTLINE, B.W., 2002. Ascent of Dinosaurs Linked to an Iridium Anomaly at the Triassic–Jurassic Boundary. *Science* **296**, 1305-1307.
- PÁLFY, J., DEMÉNY, A., HAAS, J., CARTER, E.S., GÖRÖG, Á., HALÁSZ, D., ORAVECZ-SCHEFFER, A., HETÉNYI, M., MÁRTON, E., ORCHARD, M.J., OZSVÁRT, P., VETO, I., AND ZAJZON, N., 2007. Triassic–Jurassic boundary events inferred from integrated stratigraphy of the Csovár section, Hungary. *Palaeogeography, Palaeoclimatology, Palaeoecology* **244**, 11-33.
- PRETO, N., KUSTATSCHER, E., AND WIGNALL, P.B., 2010. Triassic climates - State of the art and perspectives. *Palaeogeography, Palaeoclimatology and Palaeoecology* **290**, 1-10.

- RENNE, P.R., MUNDIL, R., BALCO, G., MIN, K., AND LUDWIG, K.R., 2010. Joint determination of ^{40}K decay constants and $^{40}\text{Ar}^*/^{40}\text{K}$ for the Fish Canyon sanidine standard, and improved accuracy for $^{40}\text{Ar}/^{39}\text{Ar}$ geochronology. *Geochimica et Cosmochimica Acta* **74**, 5349-5367.
- RUHL, M., AND KÜRSCHNER, W. M., 2011. Multiple phases of carbon cycle disturbance from large igneous province formation at the Triassic-Jurassic transition. *Geology* **39**, 431-434.
- RUHL, M., BONIS, N.R., REICHAERT, G.J., SINNINGHE DAMSTÉ, J.S., AND KÜRSCHNER, W.M., 2011. Atmospheric carbon injection linked to end-Triassic mass extinction. *Science* **333**, 430-434.
- SCHALLER, M.F., WRIGHT, J.D., AND KENT, D.V., 2011. Atmospheric $p\text{CO}_2$ Perturbations associated with the Central Atlantic Magmatic Province. *Science* **331**, 1404-1409.
- SCHALTEGGER, U., GUEX, J., BARTOLINI, A., AND OVTCHAROVA, M., 2008. Precise U-Pb age constraints for end-Triassic mass extinction, its correlation to volcanism and Hettangian post-extinction recovery. *Earth and Planetary Science Letters* **267**, 266-275.
- SCHOENE, B., GUEX, J., BARTOLINI, A., SCHALTEGGER, U., AND BLACKBURN, T.J., 2010. Correlating the end-Triassic mass extinction and flood basalt volcanism at the 100 ka level. *Geology* **38**, 387-390.
- SELF, S., BLAKE, S., SHARMA, K., WIDDOWSON, AND M., SEPHTON, S., 2008. Sulfur and Chlorine in Late Cretaceous Deccan Magmas and Eruptive Gas Release. *Science* **319**, 1654-1657.
- TANNER, L.H., LUCAS, S.G., AND CHAPMAN, M.G., 2004. Assessing the record and causes of Late Triassic extinctions. *Earth-Science Reviews* **65**, 103-139.
- TROTTER, J.A. AND EGGINS, S.M., 2006. Chemical systematics of conodont apatite determined by laser ablation ICPMS. *Chemical Geology* **233**, 196-216.
- WHITESIDE, J.H., OLSEN, P.E., KENT, D.V., FOWELL, S.J., AND ET-TOUHAMI, M., 2007. Synchrony between the Central Atlantic magmatic province and the Triassic-Jurassic mass-extinction event? *Palaeogeography, Palaeoclimatology and Palaeoecology* **244**, 345-367.
- WIGNALL, P.B., 2001. Large igneous provinces and mass extinctions. *Earth-Science Reviews* **53**, 1-33.

APPENDICES

APPENDIX I - METHODS

A1.1 SAMPLE PREPARATION

Samples were reduced in size and separated from alteration crusts and surfaces with a steel and diamond disk miter saw. Smaller portions of rock were then crushed under a hand screw-press, covering the crushing surfaces with two plexiglass tablets (1x10x10 cm) to protect the samples from steel contamination. New plexiglass gaskets were used for each sample. The obtained chips were sieved to reach a 1.6-2 mm grain separate. A portion of the separate was finely ground in agate mill to obtain a fine powder for XRF and ICP-MS analyses, while a second batch of material for isotopic analyses was carefully hand-picked under binocular microscope, choosing only fresh and fractured chips, avoiding those with saw-cut surfaces, alteration coatings and any other possible source of contamination or alteration. Around 2g of this separate were then repeatedly rinsed with distilled water in ultrasonic bath, to clean them from any handling-derived dirt and to eliminate stuck dust and powder. Dried chips were subsequently finely ground with an agate mortar and pestle, both carefully rinsed and cleaned (with diluted HCl and deionized water) before and after every sample. Pure silica was crushed before each sample, to guarantee a deep cleaning and purification of the agate surface, and this operation was followed by pre-contamination of the mortar by grinding a small batch of the sample itself and blowing it with compressed air before crushing the sample.

A1.2 X-RAY FLUORESCENCE

To measure the Loss On Ignition (LOI), rock powder of each sample was weighted on a high precision scale (± 0.0003 g), using a Pt crucible as a container, previously brought to incandescence on an acetylene torch, to evaporate any possible hand-grease or water condensed on Pt walls, that would affect the accuracy of the weighting. During weighting procedures, Pt vessels were kept closed in glass silica driers to prevent any hydration. To measure LOI at 110°C, samples in their vessels were then kept in furnace overnight at 110°C, and subsequently re-weighted. To measure LOI at 1000°C, samples were subsequently heated in muffle for 5 hours at 1100°C, and re-weighted. Due to changes in the Fe oxidation state during ignition, after ignition samples might be heavier, thus resulting in a negative LOI at 1000°C. The algebraic sum of LOI at 110°C and LOI at 1000°C gives the total LOI.

A fraction of the ignited sample powder is then mixed with $\text{Li}_2\text{B}_4\text{O}_7$ powder, in a proportion of 0.65 g : 6.5 g. After careful homogenization of the two components, the mixture is heated to melting at $\sim 1150^\circ\text{C}$ with a propan-methan fuelled melting torch and quenched in disks in Pt vessels, to obtain a homogeneous glass disk.

XRF analyses were then performed using a WDS Philips PW2400 device, equipped with a Rh X-ray tube. Precision is around $\pm 0.6\%$ for major elements and $\pm 3\%$ for trace elements. Accuracy within 0.5% is guaranteed for Si, while for all the other major elements accuracy is within 3%. Accuracy under 5% is achieved for trace elements. Rilevability limits are within 0.2% for Si, within 0.01% for Al, Mg and Na and within 0.005% for Ti, Fe, Mn, Ca, K and P. Limits for trace elements, in ppm, are: Sc = 5, V = 5, Cr = 6, Co = 3, Ni = 3, Cu = 3, Zn = 3, Ga = 5, Rb = 3, Sr = 3, Y = 3, Zr = 3, Nb = 3, Ba = 10, La = 10, Ce = 10, Nd = 10, Pb = 5, Th = 3, U = 3.

A1.3 Sr-Nd-Pb ISOTOPES

Sample powders were carefully weighted (150 mg) and dissolved in sub-boiling distilled 6M HCl and 8M HNO₃. Sr was separated twice from the matrix by chromatography using a Sr-spec resin and was loaded on single Re filaments with a Ta oxide solution as activator. Nd elution and separation required REE-spec resin and Pb separation required TRU-spec.

Sr-Nd-Pb isotope ratios were measured on a Thermo Finnigan TRITON thermal ionization mass spectrometer at the Department of Mineralogy (University of Geneva, Switzerland) at a pyrometer-controlled temperature of 1480°C in static mode, using the virtual amplifier design to cancel out biases in gain calibration among amplifiers. ⁸⁷Sr/⁸⁶Sr values were corrected for internal fractionation using a ⁸⁸Sr/⁸⁶Sr value of 8.375209. Raw values were further corrected for external fractionation based on repeated measurements of the SRM987 standard for which a normalization value of ⁸⁷Sr/⁸⁶Sr = 0.710254 was used. External reproducibility of the ⁸⁷Sr/⁸⁶Sr ratio for the SRM987 standard is 5 ppm. ⁸⁷Sr/⁸⁶Sr values are normalized to NBS 987 of 0.710254.

A1.4 Os ISOTOPES

Sample powder was carefully weighted (0.5 g, within ± 0.00003 precision) and set in a quartz vial. Samples were then double-spiked (for Re and Os), according to the previously estimated quantities. Indeed, given the MgO wt% and the type of rock that was going to be analyzed, an empirical estimation is assessed of which spike was needed (several Re and Os spikes are available, with different concentrations of the element, diluted in HNO₃) and in which quantity. Spikes were added as following:

1. Samples >12 wt% MgO: **spike Os 0.05 ppb**, 0.14g (~7 drops)
2. Samples 10-12 wt% MgO: **spike Os 0.05 ppb**, 0.10g (~5 drops)
3. Samples <10 wt% MgO: **spike Os 0.05 ppb**, 0.07g (~4 drops)
4. Blank: **spike Os 0.05 ppb**, 1 drop.

1. All samples: **spike Re 3.5 ppb**, 0.14g (~6 drops)
2. Blank: **spike Re 3.5 ppb**, 1 drop.

Spike containers are refrigerated, thus a re-equilibration with the clean room temperature was needed before weighting them. 'Differential' weighting of the wanted spike quantity was calculated as the weight difference between the full spike tank and its weight after spiking the sample.

Aqua regia as 5 ml HNO₃ 16N and 1.5 ml HCl 7N was then added to the vials, and they were sealed with Teflon tape and an apposite quartz cap. Vials with both samples and blanks were heated in oven to support the dissolution in acid. Temperature was step-wise increased to reach 300°C, maintained for 5 hours and subsequently gradually lowered. Heating was carried out in a pressure chamber, where high pressure (N₂ pumped up to 100 bar) was maintained to prevent vials opening.

Once cooled, the samples were poured (carefully recovering all the material) in big Teflon beakers for the Os extraction procedure (following Birck et al., 1997). 2ml Br₂ were added and tightly screw-capped beakers were heated at 120°C, for 3 hours on the heating plate. If any leaking occurs, Os is lost (it is volatile) and the procedure must be restarted completely. After cooling, Br₂ was extracted with a siringe and a Teflon tip, and poured in a second, smaller beaker. Distilled water was added, to prevent any Br₂ from evaporating. Full recovering of the sample is guaranteed by pouring 1 more ml Br₂, in the big beaker and repeating the heating to perform a second extraction. All the water, floating upon the Br₂, was then removed from the smaller beaker and 0.5 ml HBr were added. HBr

serves as a reducer for Os, thus impeding its evaporation during the Br₂ elimination. Teflon elbows were screw-secured as a connection between the sample-bearing small becker and a second, water-filled similar becker. Samples were thus mildly (40°-50° C) heated overnight in a bee-hive oven, with the empty becker facing outside. All the Br₂ evaporates, passes through the Teflon elbow, and condenses into the second becker, where the water protects it from covering the inverse path. Br₂ and water were trashed, and the remaining of the sample was recovered.

Samples were further evaporated on hot plate at 48-80°C, paying attention not to dry them up totally, for a last drop is necessary in order to transfer the sample. The last drop was recovered with a syringe, placed on the reversed cap of a small becker and dried up completely on a hot plate. Micro-distillation (Roy Barman, 1993) was then performed covering the dried sample with a droplet of Cr^{VI} (red) in H₂SO₄, placing a drop of HBr at the bottom of the becker, closing it and wrapping it in tin foil. The closed beckers were thus heated overturned on hot plate for 4 hours at 110°C. Cr^{VI} oxidizes Os, which can thus evaporate and condense on the HBr drop above it. HBr reduces Os into metallic state, preventing its evaporation during the drying procedure. Once totally dried, the samples were ready to be loaded onto Pt filaments for the TIMS.

A small Teflon tipped syringe (rinsed thrice with distilled water) was used to load samples on the Pt filaments. XXX was used as activator. Pt filaments were electrically heated to incandescence to lose all possible humidity, then mildly heated as the sample was deposited (loaded) in small droplets. Care must be taken in loading all the sample on a small, punctual spot along the filament.

A different extraction procedure was followed for Re. Residues from Br₂ extractions in the big beckers were dried on the hot plate and redissolved in 0.4 N HNO₃. Undissolved residues were eliminated through centrifugation. Extraction proceeded by chemical elution using AG1 X8 anion exchange resin columns. Re concentrations were then measured by ICP-MS.

Distilled, ultra-pure acids and reactants were used throughout the above described procedure.

Washing procedures for clean-room glassware:

1. Quartz vials were washed under abundant water, to eliminate insoluble residues after dissolution in hot aqua regia. Vials were half filled with 50% HNO_3 , all the vials were dipped in water in a big becker and boiled. After ultrasonic bath, a second washing in 50% HNO_3 was required, and, where necessary (coatings still stuck to the vial internal walls) in HF. After careful rinsing with distilled water, the vials were air-dried and stored.
2. Small beckers were washed with water and half-filled with HBr. After 24 hours heating in bee-hive oven, beckers were emptied, rinsed with water and dipped in boiling HNO_3 for 48 hours.
3. Big beckers were rinsed with water and heated on hot plate with HBr overnight.
4. Teflon tips were washed with water, then placed in column under 9:1 water-HBr solution and heated for 24 hours.
5. Teflon elbows were rinsed in water, then dipped in HBr in a closed container and heated for 48 hours on hot plate under hood.

APPENDIX II - SAMPLES COORDINATES AND FIELD NOTES

Sample	Latitude	Longitude	Altitude	Trend	Country rock
Georgia					
CS1	N 33° 11' 40.6	W 84° 41' 99.7	267 m	NW	off basin
CS2	N 33° 11' 40.6	W 84° 41' 99.7	267 m	NW	off basin
CS3	N 33° 14' 08.3	W 84° 42' 55.2	300 m	NW	off basin
CS4	N 33° 14' 08.3	W 84° 42' 55.2	300 m	NW	off basin
CS5	N 33° 56' 46.9	W 83° 42' 04.5	240 m	NW	off basin
CS6	N 33° 57' 49.2	W 83° 43' 08.4	255 m	NW	off basin
CS7	N 33° 54' 49.1	W 83° 38' 43.0	278 m	NW	off basin
CS8	N 33° 54' 49.1	W 83° 38' 43.0	278 m	NW	off basin
CS9	N 34° 45' 20.6	W 83° 29' 33.0		NW	off basin
CS10	N 34° 41' 59.9	W 83° 24' 58.8	472 m	NW	off basin
South Carolina					
CS11	N 34° 36' 51.3	W 81° 43' 26.1	166 m	NW	off basin in medium-grained biotite metagranite
CS12	N 34° 41' 01.8	W 82° 04' 05.5		NW	off basin in medium-grained biotite metagranite
CS13	N 34° 41' 01.8	W 82° 04' 05.5		NW	off basin in medium-grained biotite metagranite
CS14	N 34° 39' 27.4	W 82° 01' 55.8	210 m	NW	off basin in biotite gneiss / amphibolite gneiss
CS15	N 34° 08' 25.1	W 81° 07' 09.5	88 m	NW	off basin in Neoproterozoic-Cambrian (Emory formation)
CS16	N 34° 09' 44.7	W 81° 06' 54.4	96 m	NW	off basin in Neoproterozoic quartz-feldspar crystal tuff (Persimmon Fork Formation)
CS17	N 34° 09' 59.9	W 81° 06' 02.8	100 m	NW	off basin in Neoproterozoic quartz-feldspar crystal tuff (Persimmon Fork Formation)
CS18	N 34° 11' 16.1	W 81° 06' 26.3	85 m	NW	off basin in Neoproterozoic felsic to intermediate tuffs (Persimmon Fork Formation)
CS19	N 34° 11' 38.0	W 81° 06' 47.7	106 m	NW	off basin in Neoproterozoic felsic to intermediate tuffs (Persimmon Fork Formation)
CS20	N 34° 12' 42.4	W 81° 06' 03.1	103 m	NW	off basin in Neoproterozoic felsic to intermediate tuffs (Persimmon Fork Formation)
CS21	N 34° 12' 41.4	W 81° 05' 41.8	76 m	NW	off basin in Neoproterozoic felsic to intermediate tuffs (Persimmon Fork Formation)
CS22	N 34° 12' 26.8	W 81° 03' 12.8	118 m	NW	off basin
CS23	N 34° 38' 52.9	W 80° 31' 01.7	135 m	NW	off basin
CS24	N 34° 38' 52.9	W 80° 31' 01.7	135 m	NW	off basin
CS25	N 34° 45' 03.1	W 80° 30' 17.4	127 m	NW	off basin
CS26	N 34° 12' 26.9	W 81° 03' 13.2	109 m	NW	off basin
CS27	N 34° 32' 40.3	W 80° 27' 00.5	72 m	NW	off basin
CS28	N 34° 39' 08.0	W 80° 31' 00.8	140 m	NW	off basin
CS29	N 34° 39' 38.5	W 80° 30' 07.1	150 m	NW	off basin
CS30	N 34° 44' 11.2	W 80° 35' 01.3		NW	off basin
CS31	N 34° 44' 21.3	W 80° 35' 0.0	159 m	NW	off basin
CS32	N 34° 23' 53.9	W 80° 51' 05.5	90 m	NW	off basin
CS33	N 34° 23' 25.6	W 80° 49' 34.3	87 m	NW	off basin
CS35	N 34° 29' 16.0	W 80° 56' 07.3	98 m	E-W	off basin
CS36	N 34° 31' 18.4	W 80° 55' 28.8	147 m	NW?	off basin
CS37	N 34° 48' 02.0	W 80° 18' 39.3	126 m	NW	off basin
CS38	N 34° 46' 26.6	W 80° 04' 41.4	82 m	NW	off basin
CS39	N 34° 46' 26.6	W 80° 04' 41.4	82 m	NW?	off basin

Sample	Latitude	Longitude	Altitude	Trend	Country rock
North Carolina					
CS41	N 34° 56' 14.4	W 79° 49' 15.0	20 m	NW	off basin
CS42	N 35° 04' 40.2	W 79° 56' 50.2	70 m	NW	in basin
CS43	N 35° 04' 56.5	W 79° 57' 24.4	65 m	NW	in basin
CS44	N 35° 04' 23.6	W 79° 55' 4.0	69 m	NW	in basin
CS45	N 35° 13' 37.6	W 79° 50' 27.1	92 m	N-S	in basin
CS46	N 35° 06' 47.9	W 79° 48' 15.1	159 m	N-S	in basin
CS47	N 35° 04' 32.0	W 79° 50' 16.3	106 m	N-S	in basin
CS48	N 35° 04' 14.9	W 79° 50' 37.7	92 m	N-S	in basin
CS49	N 36° 06' 46.6	W 78° 46' 02.4	76 m	sill	in basin
CS50	N 36° 06' 46.6	W 78° 46' 02.4	76 m	sill	in basin
CS51	N 36° 06' 46.6	W 78° 46' 02.4	76 m	N-S	in basin
CS52	N 36° 06' 43.0	W 78° 46' 05.4	101 m	N-S	in basin
CS54	N 35° 45' 54.1	W 79° 03' 08.1		N-S	off basin
CS55	N 35° 45' 48.1	W 79° 02' 47.3	123 m	NW	off basin mixed epiclastic-pyroclastic
CS56	N 35° 50' 83.6	W 79° 02' 16.6		N-S	off basin Chatham group lithofacies Association II
CS57	N 35° 50' 11.0	W 79° 00' 47.9	99 m	N-S	off basin Chatham group lithofacies Association I (metasediments)
CS59	N 36° 07' 23.7	W 80° 30' 32.5	219 m	E-W	off basin
CS60	N 36° 07' 23.7	W 80° 30' 32.5		N30E	off basin
CS61	N 36° 09' 18.8	W 80° 23' 46.9		NE	off basin
CS62	N 36° 09' 26.7	W 80° 23' 40.1	250 m	NE	off basin
Virginia					
CS63	N 36° 39' 42.8	W 79° 35' 40.2	222 m	NW	in basin
CS64	N 36° 39' 37.4	W 79° 34' 34.5		N-S	off basin
CS66	N 36° 49' 12.9	W 79° 25' 08.1	219 m	NW	off basin
CS67	N 36° 56' 18.1	W 79° 27' 16.2	276 m	NW	
CS68	N 36° 54' 03.7	W 78° 43' 53.2	95 m	NW	in basin
CS69	N 37° 17' 29.5	W 78° 26' 17.8	124 m	N-S	off basin
CS70	N 37° 20' 13.7	W 78° 25' 18.3	106 m	NW	in basin
CS71	N 37° 17' 54.7	W 78° 27' 04.9	136 m	NE	off basin
CS72	N 37° 18' 07.4	W 78° 27' 03.9	127 m	NW	off basin
CS73	N 37° 17' 43.6	W 78° 27' 38.4	111 m	N-S	off basin
CS75	N 36° 53' 05.6	W 77° 35' 14.5	76 m	NW	off basin
CS76	N 36° 52' 08.5	W 77° 37' 22.8	57 m	NW	
CS77	N 37° 49' 53.9	W 77° 27' 52.3	72 m	N-S	in basin
CS78	N 37° 50' 40.6	W 77° 30' 37.0	60 m	NW	in basin
CS79	N 38° 13' 23.3	W 78° 49' 31.6	351 m	NW	off basin
CS80	?	?	---	sill	in Culpeper basin

APPENDIX III - DATA TABLES: GEOCHEMISTRY OF ENA DYKES

Sample	CS13	CS14	CS15	CS16	CS18	CS19	CS25	CS27	CS28	CS29	CS31	CS33	CS35	CS36	CS37
Normative group	LFO	LFO	LFO	LFO	LFO	LFO	LFO	LFO	LFO	LFO	LFO	LFO	LFO	LFO	LFO
Dyke trend	NW	NW	NW	NW	NW	NW	NW	NW	NW	NW	NW	NW	E-W	NW	NW
State	SC	SC	SC	SC	SC	SC	SC	SC	SC	SC	SC	SC	SC	SC	SC
SiO ₂	49.61	47.34	49.26	48.48	47.30	48.39	50.18	49.74	48.05	48.06	49.64	48.00	47.89	48.06	48.53
TiO ₂	0.72	0.66	0.56	0.58	0.58	0.65	0.49	0.50	0.62	0.50	0.61	0.54	0.58	0.50	0.42
Al ₂ O ₃	15.89	14.09	15.08	15.48	14.00	15.34	14.15	14.56	14.35	15.99	15.44	15.47	15.07	14.73	15.05
Fe ₂ O ₃	10.97	12.10	10.84	10.71	11.61	11.53	10.31	10.74	11.93	12.36	10.81	11.93	11.04	11.30	10.71
MnO	0.17	0.18	0.17	0.17	0.18	0.18	0.17	0.17	0.17	0.18	0.17	0.18	0.17	0.18	0.17
MgO	9.15	13.07	11.81	12.60	14.83	11.47	12.49	12.15	12.76	10.61	10.40	10.76	11.96	12.62	13.43
CaO	10.84	10.12	10.47	10.38	9.53	10.62	9.95	10.52	9.70	10.62	11.13	11.41	10.95	11.67	10.11
Na ₂ O	2.02	1.70	1.82	1.79	1.64	1.84	1.84	1.72	1.98	1.91	1.95	1.78	1.62	1.48	1.60
K ₂ O	0.65	0.42	0.43	0.41	0.30	0.37	0.55	0.35	0.39	0.29	0.35	0.13	0.21	0.13	0.29
P ₂ O ₅	0.14	0.12	0.09	0.10	0.07	0.10	0.07	0.06	0.11	0.07	0.09	0.07	0.10	0.07	0.06
Tot	100.16	99.80	100.53	100.70	100.04	100.49	100.20	100.51	100.06	100.59	100.59	100.27	99.59	100.74	100.37
Mg# (0.13)	65.5	71.1	71.3	72.8	74.4	69.4	73.4	72.0	70.9	66.2	68.7	67.3	71.2	71.8	74.1
alkali (Na ₂ O + K ₂ O)	2.67	2.12	2.25	2.20	1.94	2.21	2.39	2.07	2.37	2.20	2.30	1.91	1.83	1.61	1.89
L.O.I. at 110°C	0.18	0.24	0.48	0.35	0.23	0.34	0.38	0.67	0.19	0.34	0.33	0.33	0.38	0.19	0.34
L.O.I.	0.64	0.24	1.42	0.46	0.89	1.00	0.26	1.25	-0.39	0.63	0.31	0.86	0.88	0.80	0.90
L.O.I. _{tot}	0.82	0.48	1.89	0.81	1.12	1.35	0.64	1.92	-0.20	0.97	0.65	1.18	1.26	1.00	1.24
Sc	30	24	24	22	21	26	26	27	21	28	31	28	28	32	23
V	207	213	208	197	208	222	186	201	181	189	218	208	216	223	186
Cr	523	1105	941	984	1215	784	1328	1390	990	509	752	638	1249	1356	1296
Co	48	63	58	57	70	56	53	58	59	63	49	61	60	61	63
Ni	220	484	369	457	599	390	425	399	443	325	279	292	379	382	479
Cu	84	87	74	68	75	88	59	68	72	89	78	95	69	88	56
Zn	95	101	88	83	92	90	86	84	99	100	87	93	89	87	85
La	9.75	7.65		5.53			6.17		4.74		5.12	2.81			3.79
Ce	20.1	15.8		11.5			13.1		10.0		11.2	6.2			8.3
Pr	2.74	2.16		1.54			1.78		1.40		1.56	0.88			1.12
Nd	11.5	9.1		6.7			7.6		6.4		7.0	4.3			5.1
Sm	2.97	2.49		1.88			2.14		1.80		2.06	1.48			1.45
Eu	0.95	0.83		0.66			0.66		0.73		0.73	0.60			0.52
Gd	3.77	3.34		2.48			2.61		2.47		2.83	2.27			1.98
Tb	0.70	0.63		0.47			0.49		0.47		0.53	0.47			0.40
Dy	4.77	4.47		3.35			3.51		3.30		3.80	3.42			2.88
Ho	1.06	0.99		0.75			0.79		0.75		0.86	0.81			0.67
Er	2.99	2.87		2.15			2.30		2.21		2.48	2.32			2.01
Tm	0.44	0.42		0.33			0.34		0.33		0.38	0.35			0.30
Yb	2.77	2.69		2.08			2.22		2.11		2.43	2.26			2.00
Lu	0.45	0.42		0.33			0.36		0.35		0.39	0.36			0.32
Ba	177	124		99			118		172		98	47			106
Th	1.18	0.91		1.19			1.47		0.43		0.87	0.18			0.70
Nb	3.29	2.35		2.29			2.64		1.84		2.38	1.27			1.41
Y	27.1	25.8		19.5			20.0		19.1		21.7	20.4			17.3
Hf	2.28	1.77		1.39			1.66		1.17		1.44	0.95			0.98
Ta	0.19	0.13		0.16			0.20		0.12		0.17	0.08			0.09
U	0.23	0.15		0.31			0.41		0.11		0.25	0.03			0.20
Pb	3.21	2.27		2.11			2.91		1.68		1.88	0.73			1.76
Rb	18.7	13.8		11.8			14.9		7.5		8.5	6.3			7.4
Cs	2.92	1.71		4.13			1.10		0.59		1.19	13.74			0.27
Sr	120.8	86.9		118.1			85.5		128.3		108.1	104.2			86.5
Sc	44.3	43.4		38.2			36.9		35.0		39.2	47.1			39.9
Zr	84.6	65.9		49.8			58.9		41.6		50.2	32.1			35.5
Re (ppt)		881							626		725				
Os (ppt)		924							415		419				
⁸⁷ Sr/ ⁸⁶ Sr _{200Ma}		0.706738							0.705434		0.704487				
¹⁴³ Nd/ ¹⁴⁴ Nd _{200Ma}		0.51219							0.51229		0.51250				
ε Nd _{200Ma}		-3.79							-1.82		2.26				
²⁰⁶ Pb/ ²⁰⁴ Pb _{200Ma}		17.886							17.904		18.491				
²⁰⁷ Pb/ ²⁰⁴ Pb _{200Ma}		15.574							15.577		15.608				
²⁰⁸ Pb/ ²⁰⁴ Pb _{200Ma}		37.759							37.633		38.199				
¹⁸⁷ Os/ ¹⁸⁵ Os _{200Ma}		0.128							0.136						
Δ 7/4		14.46							14.47		11.23				
Δ 8/4		50.75							35.93		21.66				
⁸⁷ Sr/ ⁸⁶ Sr _{measured}		0.708040							0.705913		0.705131				
¹⁴³ Nd/ ¹⁴⁴ Nd _{measured}		0.51240							0.51251		0.51273				
²⁰⁶ Pb/ ²⁰⁴ Pb _{measured}		18.012							18.028		18.756				
²⁰⁷ Pb/ ²⁰⁴ Pb _{measured}		15.581							15.583		15.621				
²⁰⁸ Pb/ ²⁰⁴ Pb _{measured}		38.015							37.795		38.502				

Sample	CS38	CS39	CS41	CS42	CS43	CS45	CS47	CS48	CS49	CS51	CS55	CS56	CS57	CS59	CS60
Normative group	LFO	LFO	LFO	LFO	LFO	LFO	LFO	LFO	LFO	LFO	LFO	LFO	LFO	LFO	LFO
Dyke trend	NW	NW	NW	NW	NW	N-S	N-S	N-S	sill	N-S	NW	N-S	N-S	E-W	NE
State	SC	SC	NC	NC	NC	NC	NC	NC	NC	NC	NC	NC	NC	NC	NC
SiO ₂	49.30	46.98	47.44	46.91	49.11	48.21	48.83	49.21	50.23	48.09	48.98	46.67	47.79	47.88	47.52
TiO ₂	0.62	0.56	0.58	0.63	0.87	0.58	0.49	0.70	0.53	0.72	0.72	0.61	0.57	0.65	0.62
Al ₂ O ₃	18.68	15.36	14.82	15.22	16.48	15.48	16.62	18.49	16.60	16.65	16.83	15.31	14.87	16.07	15.42
Fe ₂ O ₃	10.74	12.62	11.68	12.34	11.95	11.49	10.09	9.72	9.34	11.75	12.10	12.43	11.90	12.09	12.28
MnO	0.17	0.19	0.17	0.18	0.18	0.18	0.16	0.15	0.16	0.18	0.19	0.18	0.18	0.18	0.18
MgO	6.09	11.99	12.95	12.32	8.28	10.94	10.94	8.03	9.12	9.17	8.30	12.69	12.27	10.64	12.00
CaO	12.12	10.02	10.92	10.57	10.20	11.22	10.66	11.37	11.79	11.05	10.46	10.51	10.27	10.84	10.41
Na ₂ O	2.32	1.91	1.73	1.83	2.29	1.83	1.88	2.11	2.04	2.12	2.62	1.78	1.95	1.89	1.85
K ₂ O	0.38	0.35	0.12	0.16	0.48	0.30	0.41	0.42	0.36	0.32	0.32	0.15	0.26	0.26	0.23
P ₂ O ₅	0.10	0.10	0.09	0.13	0.15	0.08	0.09	0.14	0.08	0.09	0.10	0.07	0.10	0.11	0.10
Tot	100.52	100.08	100.50	100.29	99.99	100.31	100.17	100.34	100.25	100.14	100.62	100.40	100.16	100.61	100.61
Mg# (0.13)	56.4	68.4	71.6	69.4	61.2	68.4	71.2	65.3	69.0	64.0	61.0	69.9	70.1	66.7	69.0
alkali (Na ₂ O + K ₂ O)	2.70	2.26	1.85	1.99	2.77	2.13	2.29	2.53	2.40	2.44	2.94	1.93	2.21	2.15	2.08
L.O.I. at 110°C	0.33	0.36	0.54	0.43	0.50	0.32	0.32	0.33	0.36	0.52	0.39	0.37	0.20	0.21	0.12
L.O.I.	0.62	0.68	1.24	0.65	0.53	0.17	0.59	0.15	0.22	0.40	0.37	0.48	0.34	0.77	0.43
L.O.I. _{tot}	0.95	1.04	1.78	1.08	1.03	0.49	0.91	0.47	0.58	0.92	0.76	0.85	0.54	0.98	0.55
Sc	19	36	22	15	16	29	13	19	25	23	23	33	28	29	28
V	220	197	184	188	197	204	157	178	192	220	221	208	186	206	195
Cr	243	542	1087	801	263	918	799	556	546	357	235	624	902	511	595
Co	40	68	57	63	55	60	54	48	45	56	48	65	64	62	66
Ni	99	441	424	404	159	322	309	186	154	230	205	449	393	324	416
Cu	92	102	75	81	65	80	50	75	56	92	99	101	61	96	79
Zn	92	100	92	98	105	93	85	85	76	95	101	95	97	98	100
La			3.07	3.18				4.90	4.76	5.21	5.61		4.32	3.59	3.49
Ce			6.7	7.1				10.8	10.7	11.3	12.2		9.6	7.9	7.6
Pr			0.95	1.06				1.53	1.49	1.57	1.68		1.34	1.10	1.09
Nd			4.5	5.0				7.0	6.5	7.1	7.6		6.1	5.2	5.0
Sm			1.39	1.54				1.91	1.92	2.19	2.33		1.71	1.71	1.62
Eu			0.58	0.65				0.81	0.68	0.86	0.87		0.63	0.69	0.67
Gd			2.01	2.27				2.46	2.53	3.18	3.26		2.37	2.61	2.51
Tb			0.40	0.48				0.48	0.50	0.63	0.65		0.48	0.54	0.52
Dy			2.93	3.46				3.41	3.43	4.48	4.57		3.44	3.83	3.71
Ho			0.67	0.80				0.76	0.79	1.04	1.03		0.80	0.88	0.86
Er			2.00	2.33				2.21	2.26	2.96	3.02		2.32	2.58	2.48
Tm			0.30	0.36				0.34	0.35	0.45	0.45		0.36	0.39	0.38
Yb			2.00	2.28				2.14	2.20	2.82	2.87		2.32	2.49	2.44
Lu			0.32	0.36				0.35	0.34	0.45	0.47		0.37	0.40	0.38
Ba			85	89				194	103	131	129		155	66	71
Th			0.18	0.17				0.45	0.52	0.32	0.54		0.23	0.49	0.47
Nb			1.78	1.72				2.05	1.86	1.91	2.43		1.74	1.53	1.52
Y			17.4	20.4				19.4	20.1	26.0	26.4		20.3	22.6	21.9
Hf			0.93	0.90				1.13	1.33	1.46	1.74		1.11	1.07	1.02
Ta			0.13	0.12				0.13	0.13	0.12	0.14		0.11	0.10	0.10
U			0.03	0.04				0.11	0.11	0.08	0.09		0.07	0.12	0.12
Pb			0.79	0.78				1.62	1.43	1.48	1.98		1.21	1.40	1.32
Rb			4.8	2.5				7.9	6.1	5.7	4.5		4.4	12.3	8.4
Cs			4.90	0.23				0.71	0.27	0.42	0.21		0.22	2.88	1.46
Sr			97.0	114.0				182.3	148.0	138.7	147.6		139.7	95.2	87.6
Sc			39.1	40.8				35.0	42.1	42.6	36.6		39.8	41.6	40.0
Zr			32.6	31.2				39.1	49.6	52.0	62.7		40.6	35.2	34.4
Re (ppt)			880					503		1024			911		1011
Os (ppt)			452					276		132			258		310
⁸⁷ Sr/ ⁸⁶ Sr _{200Ma}			0.705524					0.705567	0.704381	0.705490	0.705275		0.704884		0.705147
¹⁴³ Nd/ ¹⁴⁴ Nd _{200Ma}			0.512226					0.51227	0.51250	0.51234	0.51249		0.51226		0.51234
ε Nd _{200Ma}			-2.41					-2.22	2.42	-0.86	2.20		-2.38		-0.74
²⁰⁶ Pb/ ²⁰⁴ Pb _{200Ma}			17.421					17.781	18.612	17.706	18.541		17.827		18.211
²⁰⁷ Pb/ ²⁰⁴ Pb _{200Ma}			15.535					15.577	15.609	15.555	15.611		15.561		15.617
²⁰⁸ Pb/ ²⁰⁴ Pb _{200Ma}			37.329					37.571	38.332	37.465	38.266		37.465		38.039
¹⁸⁷ Os/ ¹⁸⁸ Os _{200Ma}			0.131					0.135	0.135	0.139	0.139		0.138		0.128
Δ 7/4			15.60					15.82	10.08	14.46	11.06		13.79		15.22
Δ 8/4			64.01					44.63	20.26	43.06	22.27		28.51		39.51
⁸⁷ Sr/ ⁸⁶ Sr _{measured}			0.705935					0.705926	0.704719	0.705827	0.705528		0.705141		0.705933
¹⁴³ Nd/ ¹⁴⁴ Nd _{measured}			0.51250					0.51248	0.51274	0.51258	0.51274		0.51248		0.51260
²⁰⁶ Pb/ ²⁰⁴ Pb _{measured}			17.489					17.911	18.767	17.813	18.631		17.931		18.392
²⁰⁷ Pb/ ²⁰⁴ Pb _{measured}			15.539					15.583	15.617	15.560	15.616		15.567		15.626
²⁰⁸ Pb/ ²⁰⁴ Pb _{measured}			37.472					37.748	38.568	37.604	38.443		37.588		38.269

Sample	CS61	CS62	CS63	CS64	CS68	CS70	CS71	CS72	CS73	CS75	CS76	CS79	CS80
Normative group	LFO	LFO	LFO	LFO	LFO	LFO	LFO	LFO	LFO	LFO	LFO	LFO	LFO
Dyke trend	NE	NE	NW	N-S	NW	NW	NE	NW	N-S	NW	NW	NW	NW
State	NC	NC	VA	VA	VA	VA	VA	VA	VA	VA	VA	VA	VA
SiO ₂	48.35	48.01	49.04	48.56	49.63	48.53	48.57	47.47	47.76	48.97	47.79	47.91	47.45
TiO ₂	0.52	0.66	0.64	0.63	0.50	0.41	0.43	0.40	0.45	0.83	1.01	0.64	0.36
Al ₂ O ₃	14.13	16.61	16.88	16.74	15.05	17.02	15.83	15.22	14.70	16.98	16.90	15.77	12.94
Fe ₂ O ₃	11.04	11.92	10.99	11.19	10.54	10.16	11.33	11.46	11.50	10.81	12.76	11.55	11.34
MnO	0.17	0.18	0.17	0.17	0.17	0.16	0.17	0.17	0.17	0.19	0.20	0.18	0.17
MgO	13.84	9.28	9.43	9.49	11.50	10.14	10.94	12.87	12.46	8.89	8.21	11.31	16.99
CaO	10.08	11.04	10.77	10.86	10.74	11.49	10.85	10.25	10.12	10.94	10.57	10.80	8.94
Na ₂ O	1.65	2.08	2.32	2.28	1.68	1.68	1.73	1.46	1.53	2.06	1.92	1.88	1.20
K ₂ O	0.35	0.28	0.29	0.28	0.34	0.37	0.41	0.29	0.45	0.60	0.23	0.45	0.08
P ₂ O ₅	0.09	0.11	0.08	0.08	0.08	0.10	0.09	0.09	0.10	0.10	0.10	0.10	0.03
Tot	100.22	100.17	100.61	100.28	100.23	100.06	100.35	99.68	99.24	100.37	99.69	100.59	99.50
Mg# (0.13)	74.1	63.9	66.1	65.9	71.3	69.4	68.7	71.9	71.2	65.2	59.4	69.0	77.3
alkali (Na ₂ O + K ₂ O)	2.00	2.36	2.61	2.56	2.02	2.05	2.14	1.75	1.98	2.66	2.15	2.33	1.28
L.O.I. at 110°C	0.20	0.18	0.20	0.28	0.43	0.42	0.34	0.55	0.38	0.36	0.25	0.36	3.42
L.O.I.	0.44	0.09	0.76	0.89	1.31	0.87	0.43	1.97	1.03	2.23	2.08	1.04	4.64
L.O.I. _{tot}	0.64	0.27	0.96	1.17	1.74	1.29	0.77	2.52	1.41	2.59	2.33	1.40	8.06
Sc	23	31	16	18	29	12	26	32	30	17	22	21	32
V	187	208	202	205	204	165	182	177	176	233	264	222	185
Cr	1429	402	319	321	1046	828	725	920	913	122	124	637	1983
Co	65	56	52	48	57	50	58	65	59	52	55	56	67
Ni	494	237	252	252	340	280	324	437	402	158	140	338	558
Cu	67	93	94	90	37	46	73	64	50	81	95	80	24
Zn	92	99	88	90	89	88	97	95	98	93	108	94	81
La	5.04	3.89	4.24	4.19	6.19	6.56	7.16		7.92			7.02	
Ce	10.8	8.5	9.4	9.1	12.9	13.7	14.7		16.0			14.6	
Pr	1.44	1.19	1.30	1.28	1.74	1.85	1.99		2.15			2.01	
Nd	6.3	5.6	6.2	6.0	7.3	7.7	8.2		8.9			8.7	
Sm	1.67	1.79	1.97	1.95	1.94	1.77	1.87		2.06			2.33	
Eu	0.61	0.71	0.77	0.75	0.66	0.55	0.58		0.62			0.80	
Gd	2.31	2.76	2.89	2.76	2.49	2.03	2.24		2.33			3.04	
Tb	0.45	0.57	0.57	0.57	0.49	0.38	0.43		0.45			0.58	
Dy	3.26	4.00	4.08	4.00	3.50	2.73	3.17		3.17			4.04	
Ho	0.75	0.94	0.94	0.92	0.81	0.65	0.75		0.74			0.91	
Er	2.18	2.75	2.70	2.67	2.39	1.99	2.30		2.27			2.64	
Tm	0.33	0.41	0.41	0.40	0.37	0.31	0.36		0.35			0.40	
Yb	2.17	2.68	2.60	2.51	2.36	2.00	2.31		2.29			2.50	
Lu	0.35	0.43	0.41	0.41	0.38	0.34	0.38		0.38			0.40	
Ba	125	92	86	82	127	162	160		167			160	
Th	0.60	0.51	0.42	0.43	0.96	0.60	0.69		0.69			0.69	
Nb	1.88	1.67	1.96	1.92	1.93	2.25	2.16		2.63			2.54	
Y	19.2	24.0	23.8	23.1	20.7	16.6	19.4		19.4			23.2	
Hf	1.16	1.13	1.46	1.42	1.50	1.22	1.36		1.54			1.68	
Ta	0.11	0.11	0.12	0.12	0.13	0.14	0.13		0.16			0.16	
U	0.14	0.13	0.08	0.07	0.19	0.12	0.14		0.10			0.12	
Pb	1.79	1.47	1.49	1.49	2.13	2.00	2.40		3.00			2.06	
Rb	9.2	6.7	6.3	7.6	7.7	8.3	12.2		13.9			10.8	
Cs	2.06	0.36	0.48	0.73	0.50	0.54	1.42		2.97			0.56	
Sr	100.5	94.8	128.7	127.8	105.1	103.2	84.4		87.7			117.7	
Sc	39.4	42.2	37.2	37.1	42.1	37.2	41.2		38.4			41.4	
Zr	42.1	38.2	50.9	49.3	55.1	47.6	52.8		59.0			64.8	
Re (ppt)				983					854				
Os (ppt)				164					213				
⁸⁷ Sr/ ⁸⁶ Sr _{200Ma}		0.705023		0.705113					0.708802				
¹⁴³ Nd/ ¹⁴⁴ Nd _{200Ma}		0.51234		0.51250					0.51204				
ε Nd _{200Ma}		-0.71		2.36					-6.67				
²⁰⁶ Pb/ ²⁰⁴ Pb _{200Ma}		18.185		18.537					17.464				
²⁰⁷ Pb/ ²⁰⁴ Pb _{200Ma}		15.607		15.603					15.542				
²⁰⁸ Pb/ ²⁰⁴ Pb _{200Ma}		37.975		38.251					37.323				
¹⁸⁷ Os/ ¹⁸⁸ Os _{200Ma}				0.132					0.144				
Δ 7/4		14.47		10.29					15.76				
Δ 8/4		36.20		21.31					58.21				
⁸⁷ Sr/ ⁸⁶ Sr _{measured}		0.705601		0.705603					0.710105				
¹⁴³ Nd/ ¹⁴⁴ Nd _{measured}		0.51260		0.51276					0.51222				
²⁰⁶ Pb/ ²⁰⁴ Pb _{measured}		18.357		18.633					17.531				
²⁰⁷ Pb/ ²⁰⁴ Pb _{measured}		15.616		15.608					15.545				
²⁰⁸ Pb/ ²⁰⁴ Pb _{measured}		38.201		38.438					37.469				

Sample	CS5	CS6	CS7	CS8	CS9	CS10	CS11	CS17	CS20	CS21	CS22	CS26	CS32	CS54
Normative group	HFO	HFO	HFO	HFO	HFO	HFO	HFO	HFO	HFO	HFO	HFO	HFO	HFO	HFO
Dyke trend	NW	NW	NW	NW	NW	NW	NW	NW	NW	NW	NW	NW	NW	NW
State	GA	GA	GA	GA	GA	GA	SC	SC	SC	SC	SC	SC	SC	NC
SiO ₂	47.28	47.53	46.88	46.76	46.52	46.29	46.71	47.27	46.76	47.12	46.70	46.90	48.43	47.43
TiO ₂	1.00	1.00	1.00	0.86	0.87	0.92	1.17	1.21	0.97	1.11	1.07	0.77	1.35	0.82
Al ₂ O ₃	15.11	16.23	15.57	15.57	14.37	14.41	17.19	16.87	16.01	16.87	16.29	15.41	16.76	15.83
Fe ₂ O ₃	14.10	13.78	14.36	13.73	14.89	14.80	16.31	14.83	14.26	14.67	14.61	13.69	14.86	13.70
MnO	0.19	0.18	0.19	0.18	0.19	0.19	0.19	0.20	0.20	0.20	0.19	0.19	0.20	0.20
MgO	9.82	8.90	9.02	11.11	12.59	11.52	6.13	7.56	9.82	7.95	8.88	11.36	6.84	10.05
CaO	9.49	9.61	9.90	9.37	8.72	8.79	8.35	9.19	10.03	9.21	9.35	9.88	9.01	9.44
Na ₂ O	2.47	2.65	2.53	2.40	2.35	2.38	3.18	2.74	2.22	2.66	2.56	2.09	2.60	2.22
K ₂ O	0.62	0.58	0.46	0.44	0.47	0.45	0.56	0.44	0.27	0.40	0.36	0.35	0.72	0.28
P ₂ O ₅	0.13	0.15	0.12	0.11	0.12	0.12	0.20	0.17	0.14	0.16	0.17	0.15	0.23	0.10
Tot	100.21	100.61	100.03	100.53	101.09	99.87	99.99	100.48	100.68	100.35	100.18	100.79	101.00	100.07
Mg# (0.13)	61.3	59.5	58.9	64.8	65.8	63.9	46.1	53.7	61.1	55.2	58.1	65.4	51.2	62.6
alkali (Na ₂ O + K ₂ O)	3.09	3.23	2.99	2.84	2.82	2.83	3.74	3.18	2.49	3.06	2.92	2.44	3.32	2.50
L.O.I. at 110°C	0.14	0.19	0.17	0.20	0.18	0.21	0.28	0.41	0.31	0.31	0.40	0.41	0.34	0.42
L.O.I.	0.26	-0.19	-0.03	-0.01	0.05	0.68	1.64	-0.01	0.91	-0.15	-0.18	0.45	-0.16	0.81
L.O.I. _{tot}	0.40	0.00	0.14	0.20	0.23	0.89	1.92	0.41	1.22	0.16	0.22	0.86	0.17	1.23
Sc	34	24	32	24	35	30	10	18	25	18	20	27	17	27
V	209	188	214	183	176	181	136	197	206	181	191	197	206	192
Cr	319	258	299	308	299	361	24	145	370	170	304	325	43	437
Co	66	53	66	68	74	75	61	60	66	62	67	65	51	67
Ni	307	226	295	399	479	747	99	141	266	172	226	372	75	270
Cu	134	96	150	136	138	146	57	62	96	63	72	109	37	103
Zn	116	108	114	106	112	110	128	124	111	120	116	105	126	109
La			8.27		7.79		7.95	10.42		9.92	9.43	5.96	15.51	
Ce			17.4		16.0		16.9	21.8		20.9	19.8	12.7	33.0	
Pr			2.44		2.17		2.36	2.99		2.85	2.69	1.79	4.46	
Nd			10.8		9.3		10.6	13.0		12.4	11.8	8.1	19.4	
Sm			3.27		2.84		3.18	3.64		3.51	3.42	2.35	4.91	
Eu			1.24		1.06		1.24	1.30		1.27	1.19	0.89	1.58	
Gd			4.89		4.10		4.44	4.83		4.59	4.57	3.29	5.77	
Tb			0.95		0.81		0.85	0.89		0.86	0.87	0.65	1.07	
Dy			6.62		5.69		5.88	6.15		5.94	5.90	4.59	7.06	
Ho			1.44		1.25		1.29	1.32		1.29	1.27	1.03	1.55	
Er			3.99		3.50		3.68	3.70		3.59	3.59	2.97	4.33	
Tm			0.59		0.51		0.55	0.55		0.52	0.53	0.45	0.64	
Yb			3.57		3.20		3.49	3.42		3.27	3.29	2.86	4.05	
Lu			0.57		0.51		0.57	0.55		0.53	0.52	0.45	0.64	
Ba			163		137		206	239		161	152	161	314	
Th			0.92		1.46		0.49	0.95		0.93	0.93	0.22	1.17	
Nb			3.01		3.03		4.68	5.83		5.45	4.94	2.25	7.37	
Y			37.1		32.1		33.8	33.7		32.4	32.8	26.5	39.3	
Hf			2.53		2.02		2.14	2.65		2.51	2.40	1.61	3.39	
Ta			0.18		0.21		0.29	0.37		0.36	0.31	0.12	0.41	
U			0.15		0.31		0.08	0.16		0.15	0.14	0.04	0.21	
Pb			2.59		2.61		1.68	1.87		1.81	1.69	1.50	3.41	
Rb			11.8		20.4		18.1	9.9		6.5	6.8	6.8	12.8	
Cs			0.30		1.01		0.75	1.96		0.66	0.67	1.19	1.68	
Sr			108.2		119.1		217.9	194.6		169.9	174.0	109.5	265.1	
Sc			45.8		42.4		29.5	33.5		33.0	35.1	39.9	38.5	
Zr			90.3		71.1		79.2	96.0		92.0	89.2	57.5	129.2	
Re (ppt)					1368							1167		
Os (ppt)					905							436		
⁸⁷ Sr/ ⁸⁶ Sr _{200Ma}			0.706140		0.705409			0.706795			0.705585	0.706583	0.705815	
¹⁴³ Nd/ ¹⁴⁴ Nd _{200Ma}			0.51228		0.51226			0.51229			0.51230	0.51209	0.51225	
ε Nd _{200Ma}			-2.05		-2.31			-1.81			-1.53	-5.76	-2.63	
²⁰⁶ Pb/ ²⁰⁴ Pb _{200Ma}			17.761		18.190			18.318			18.294	17.414	18.050	
²⁰⁷ Pb/ ²⁰⁴ Pb _{200Ma}			15.550		15.589			15.613			15.610	15.555	15.591	
²⁰⁸ Pb/ ²⁰⁴ Pb _{200Ma}			37.572		38.109			38.241			38.246	37.400	37.921	
¹⁵⁷ Os/ ¹⁸⁸ Os _{200Ma}					0.130							0.140		
Δ 7/4			13.37		12.63			13.59			13.65	17.59	14.32	
Δ 8/4			47.19		49.00			46.78			50.21	71.95	47.23	
⁸⁷ Sr/ ⁸⁶ Sr _{measured}			0.707041		0.706818			0.707215			0.705905	0.707097	0.706212	
¹⁴³ Nd/ ¹⁴⁴ Nd _{measured}			0.51251		0.51251			0.51251			0.51253	0.51232	0.51245	
²⁰⁶ Pb/ ²⁰⁴ Pb _{measured}			17.877		18.427			18.482			18.455	17.462	18.172	
²⁰⁷ Pb/ ²⁰⁴ Pb _{measured}			15.556		15.601			15.621			15.619	15.557	15.597	
²⁰⁸ Pb/ ²⁰⁴ Pb _{measured}			37.798		38.472			38.571			38.603	37.490	38.141	

Sample	CS23	CS24	CS30	CS44	CS52	CS53	CS77
Normative group	LTQ	LTQ	LTQ	LTQ	LTQ	LTQ	LTQ
Dyke trend	NW	NW	NW	NW	NW	sill	N-S
State	SC	SC	SC	NC	NC	NC	VA
SiO ₂	51.53	51.49	50.99	50.18	51.37	50.60	50.55
TiO ₂	0.55	0.59	0.49	0.79	0.73	0.65	0.43
Al ₂ O ₃	18.13	17.90	16.57	16.13	15.72	16.26	16.95
Fe ₂ O ₃	9.38	9.84	10.38	11.01	11.02	10.58	10.80
MnO	0.16	0.15	0.17	0.17	0.19	0.17	0.17
MgO	6.07	5.53	8.14	8.25	6.77	8.00	7.64
CaO	11.74	11.26	11.58	11.07	11.71	11.36	11.28
Na ₂ O	2.23	2.33	2.09	2.10	2.24	2.18	2.00
K ₂ O	0.57	0.68	0.49	0.59	0.46	0.38	0.61
P ₂ O ₅	0.10	0.10	0.07	0.16	0.12	0.10	0.08
Tot	100.46	99.87	100.97	100.45	100.33	100.28	100.51
Mg# (0.13)	59.6	56.1	64.1	63.0	58.3	63.3	61.7
alkali (Na ₂ O + K ₂ O)	2.80	3.01	2.58	2.69	2.70	2.56	2.61
L.O.I. at 110°C	0.45	0.53	0.30	0.38	0.39	0.79	0.82
L.O.I.	0.43	0.18	0.13	0.15	0.33	0.83	0.86
L.O.I. _{tot}	0.87	0.70	0.43	0.53	0.72	1.63	1.67
Sc	24	21	24	23	36	27	25
V	204	203	201	216	258	231	185
Cr	310	241	406	364	299	334	344
Co	37	38	50	50	39	43	44
Ni	101	84	139	145	75	120	165
Cu	68	75	56	74	84	69	76
Zn	82	84	85	97	92	87	94
La	7.41			9.65			8.35
Ce	15.5			20.1			17.2
Pr	2.04			2.70			2.23
Nd	8.7			11.8			8.9
Sm	2.29			2.88			2.06
Eu	0.74			1.00			0.55
Gd	2.88			3.42			2.34
Tb	0.55			0.64			0.45
Dy	3.87			4.30			3.23
Ho	0.87			0.96			0.77
Er	2.56			2.75			2.32
Tm	0.38			0.41			0.36
Yb	2.45			2.61			2.43
Lu	0.40			0.42			0.40
Ba	147			287			210
Th	1.62			0.65			2.01
Nb	2.80			3.27			3.60
Y	22.3			24.3			19.9
Hf	1.68			1.95			1.52
Ta	0.20			0.18			0.23
U	0.43			0.10			0.30
Pb	3.13			2.60			3.30
Rb	13.8			10.2			19.7
Cs	1.02			0.23			0.45
Sr	138.9			196.0			108.0
Sc	40.3			41.9			42.3
Zr	60.9			74.1			58.0
Re (ppt)							
Os (ppt)							
⁸⁷ Sr/ ⁸⁶ Sr _{200Ma}	0.70492			0.70760			0.70769

Sample	CS1	CS2	CS3	CS4	CS46	CS50	CS66	CS67	CS69
Normative group	HTQ	HTQ	HTQ	HTQ	HTQ	HTQ	HTQ	HTQ	HTQ
Dyke trend	NW	NW	NW	NW	N-S	sill	NW	NW	N-S
State	GA	GA	GA	GA	NC	NC	VA	VA	VA
SiO ₂	51.10	51.25	51.41	51.37	54.33	52.06	53.94	53.58	54.28
TiO ₂	1.29	1.28	1.19	1.22	1.04	1.35	1.28	1.30	1.25
Al ₂ O ₃	13.55	13.55	13.75	13.63	14.06	13.84	13.88	14.08	13.63
Fe ₂ O ₃	15.07	15.40	14.85	15.08	12.81	14.58	13.95	14.07	14.01
MnO	0.23	0.22	0.24	0.23	0.23	0.23	0.24	0.22	0.21
MgO	5.93	6.02	6.39	6.28	5.46	5.19	4.76	4.74	4.80
CaO	10.07	10.15	10.29	9.80	8.99	9.48	7.66	8.64	9.06
Na ₂ O	2.28	2.27	2.32	2.34	2.40	2.79	3.21	2.89	2.39
K ₂ O	0.49	0.48	0.53	0.75	0.77	0.68	1.17	0.89	0.64
P ₂ O ₅	0.13	0.13	0.12	0.12	0.15	0.16	0.25	0.27	0.13
Tot	100.14	100.75	101.09	100.82	100.24	100.36	100.34	100.68	100.40
Mg# (0.13)	47.3	47.1	49.5	48.7	49.3	44.8	43.7	43.4	43.8
alkali (Na ₂ O + K ₂ O)	2.77	2.75	2.85	3.09	3.17	3.47	4.38	3.78	3.03
L.O.I. at 110°C	0.20	0.20	0.29	0.27	1.05	0.56	0.43	0.57	0.52
L.O.I.	-0.27	-0.19	0.03	-0.17	0.39	0.42	1.32	0.86	0.22
L.O.I. _{tot}	-0.06	0.01	0.31	0.10	1.44	0.98	1.75	1.42	0.75
Sc	36	32	29	37	41	53	52	37	44
V	404	398	390	402	362	433	379	359	402
Cr	92	88	104	95	41	26	23	22	36
Co	47	45	45	47	46	42	38	35	45
Ni	52	54	73	54	30	36	11	10	23
Cu	107	90	72	82	51	142	10	11	36
Zn	125	125	117	119	111	126	121	124	124
La		8.53		7.98	10.16				11.91
Ce		18.3		17.2	22.2				24.9
Pr		2.56		2.42	3.00				3.31
Nd		11.6		10.9	13.1				14.1
Sm		3.66		3.37	3.55				3.90
Eu		1.24		1.21	1.17				1.28
Gd		4.83		4.59	4.14				4.74
Tb		0.92		0.87	0.76				0.89
Dy		6.21		5.89	5.03				5.98
Ho		1.34		1.26	1.08				1.29
Er		3.73		3.57	2.97				3.71
Tm		0.55		0.52	0.44				0.56
Yb		3.41		3.27	2.75				3.47
Lu		0.56		0.52	0.43				0.57
Ba		135		134	192				165
Th		1.92		1.80	2.04				2.98
Nb		4.28		3.98	4.06				5.33
Y		34.9		32.9	27.3				33.4
Hf		2.70		2.53	2.54				2.93
Ta		0.28		0.26	0.29				0.38
U		0.52		0.49	0.63				0.85
Pb		3.30		2.94	3.86				4.87
Rb		15.1		31.0	17.7				20.7
Cs		0.55		0.88	0.62				0.50
Sr		117.7		127.1	209.8				143.4
Sc		50.6		45.9	44.1				49.4
Zr		95.2		88.6	94.6				106.4
Re (ppt)									
Os (ppt)									
⁸⁷ Sr/ ⁸⁶ Sr _{200Ma}		0.70545			0.70496				
¹⁴³ Nd/ ¹⁴⁴ Nd _{200Ma}		0.51246			0.51243				
ε Nd _{200Ma}		1.62			0.93				
²⁰⁶ Pb/ ²⁰⁴ Pb _{200Ma}		18.526			18.520				
²⁰⁷ Pb/ ²⁰⁴ Pb _{200Ma}		15.633			15.609				
²⁰⁸ Pb/ ²⁰⁴ Pb _{200Ma}		38.384			38.210				
¹⁸⁷ Os/ ¹⁸⁵ Os _{200Ma}									
Δ 7/4		13.37			11.05				
Δ 8/4		35.88			19.20				
⁸⁷ Sr/ ⁸⁶ Sr _{measured}		0.70651			0.70566				
¹⁴³ Nd/ ¹⁴⁴ Nd _{measured}		0.51271			0.51264				
²⁰⁶ Pb/ ²⁰⁴ Pb _{measured}		18.842			18.847				
²⁰⁷ Pb/ ²⁰⁴ Pb _{measured}		15.649			15.626				
²⁰⁸ Pb/ ²⁰⁴ Pb _{measured}		38.764			38.554				

APPENDIX IV - NORMATIVE COMPOSITIONS OF ENA DYKES

Sample	CIPW group	Quartz	Plagioclase	Orthoclase	Nepheline	Leucite	Kalsilite	Corundum	Diopside	Hypersthene	Wollastonite	Olivine
CS1	HTQ	5.67	45.02	2.90	0	0	0	0	19.72	17.3	0	0
CS2	HTQ	5.49	44.72	2.84	0	0	0	0	19.91	17.58	0	0
CS3	HTQ	4.52	45.14	3.13	0	0	0	0	20.29	17.94	0	0
CS4	HTQ	4.39	44.39	4.43	0	0	0	0	19.22	18.38	0	0
CS46	HTQ	9.71	45.92	4.61	0	0	0	0	15.15	16.67	0	0
CS50	HTQ	5.39	47.16	4.02	0	0	0	0	18.87	15.21	0	0
CS66	HTQ	6.55	47.47	6.97	0	0	0	0	13.6	16.28	0	0
CS67	HTQ	7.48	47.42	5.26	0	0	0	0	15.16	15.43	0	0
CS69	HTQ	11.00	45.05	3.78	0	0	0	0	16.17	15.16	0	0
CS23	LTQ	3.16	56.75	3.37	0	0	0	0	16.05	15.29	0	0
CS24	LTQ	3.57	56.55	4.08	0	0	0	0	15.45	14.69	0	0
CS30	LTQ	1.05	51.92	2.90	0	0	0	0	18.17	20.37	0	0
CS44	LTQ	0.55	50.79	3.49	0	0	0	0	17.05	21.45	0	0
CS52	LTQ	3.16	50.66	2.72	0	0	0	0	21.04	15.92	0	0
CS53	LTQ	1.25	52.16	2.25	0	0	0	0	18.01	20.23	0	0
CS77	LTQ	1.30	52.50	3.60	0	0	0	0	16.19	20.68	0	0
CS5	HFO	0	49.62	3.66	0	0	0	0	14.57	9.41	0	14.33
CS6	HFO	0	53.30	3.43	0	0	0	0	13	8.32	0	13.68
CS7	HFO	0	51.67	2.72	0	0	0	0	15.19	7.97	0	13.93
CS8	HFO	0	50.95	2.60	0	0	0	0	12.41	7.69	0	18.46
CS9	HFO	0	47.13	2.78	0	0	0	0	12.26	7.6	0	21.83
CS10	HFO	0	48.00	2.72	0	0	0	0	12.67	9.1	0	18.97
CS11	HFO	0	58.56	3.37	0	0	0	0	7.66	8.04	0	12.49
CS17	HFO	0	55.97	2.60	0	0	0	0	9.87	12.57	0	9.8
CS20	HFO	0	51.88	1.60	0	0	0	0	12.92	12.49	0	12.72
CS21	HFO	0	55.82	2.36	0	0	0	0	9.6	12.85	0	10.44
CS22	HFO	0	54.02	2.13	0	0	0	0	10.94	11.09	0	12.97
CS26	HFO	0	49.40	2.07	0	0	0	0	13.22	12.04	0	15.51
CS32	HFO	0	53.96	4.25	0	0	0	0	9.18	19.9	0	3.14
CS54	HFO	0	51.65	1.65	0	0	0	0	11.21	17.88	0	9.78
CS13	LFO	0	49.78	3.84	0	0	0	0	16.59	21.19	0	2.11
CS14	LFO	0	44.45	2.48	0	0	0	0	16.06	16.35	0	13.79
CS15	LFO	0	47.19	2.54	0	0	0	0	15.74	21.63	0	6.89
CS16	LFO	0	48.17	2.42	0	0	0	0	14.28	17.64	0	11.51
CS18	LFO	0	44.17	1.77	0	0	0	0	13.53	17.46	0	16.71
CS19	LFO	0	48.25	2.19	0	0	0	0	15.7	18.26	0	9.1
CS25	LFO	0	44.53	3.25	0	0	0	0	16.2	25.19	0	5.23
CS27	LFO	0	45.64	2.07	0	0	0	0	16.69	25.28	0	4.56
CS28	LFO	0	46.25	2.30	0	0	0	0	14.79	16.82	0	13.18
CS29	LFO	0	50.51	1.71	0	0	0	0	14.58	17.44	0	9.24
CS31	LFO	0	48.92	2.07	0	0	0	0	17.89	21.23	0	3.8
CS33	LFO	0	49.18	0.77	0	0	0	0	18.06	17.76	0	7.83
CS35	LFO	0	47.51	1.24	0	0	0	0	16.55	20.23	0	8.25
CS36	LFO	0	45.72	0.77	0	0	0	0	19.44	18.19	0	9.87
CS37	LFO	0	46.77	1.71	0	0	0	0	13.42	22.2	0	10.29
CS38	LFO	0	59.21	2.25	0	0	0	0	16.38	15.49	0	0.59
CS39	LFO	0	48.87	2.07	0	0	0	0	13.58	13.38	0	15.26
CS41	LFO	0	47.13	0.71	0	0	0	0	17.06	14.67	0	14.02
CS42	LFO	0	48.61	0.95	0	0	0	0	15.11	13.68	0	14.75
CS43	LFO	0	53.11	2.84	0	0	0	0	13.34	21.54	0	1.91
CS45	LFO	0	48.88	1.77	0	0	0	0	17.76	16.43	0	8.85
CS47	LFO	0	51.89	2.42	0	0	0	0	13.36	19.26	0	7.51
CS48	LFO	0	57.80	2.48	0	0	0	0	12.74	18.9	0	2.18
CS49	LFO	0	52.57	2.13	0	0	0	0	18.45	20.75	0	0.84
CS51	LFO	0	53.25	1.89	0	0	0	0	15.65	15.02	0	7.45
CS55	LFO	0	55.53	1.89	0	0	0	0	14.61	13.86	0	7.22
CS56	LFO	0	48.63	0.89	0	0	0	0	14.78	12.55	0	16.39
CS57	LFO	0	47.87	1.54	0	0	0	0	15.52	15.57	0	12.97
CS59	LFO	0	50.70	1.54	0	0	0	0	14.88	16.92	0	9.2
CS60	LFO	0	48.85	1.36	0	0	0	0	14.39	16	0	12.63
CS61	LFO	0	44.33	2.07	0	0	0	0	15.5	20.08	0	11.99
CS62	LFO	0	53.10	1.65	0	0	0	0	15.31	15.79	0	7.4
CS63	LFO	0	54.50	1.71	0	0	0	0	14.59	15.86	0	7.15
CS64	LFO	0	54.17	1.65	0	0	0	0	15.18	14.38	0	8.35
CS68	LFO	0	46.99	2.01	0	0	0	0	16.26	26.08	0	2.91
CS70	LFO	0	52.36	2.19	0	0	0	0	14.99	19.49	0	5.51
CS71	LFO	0	49.09	2.42	0	0	0	0	15.36	20	0	7.17
CS72	LFO	0	47.02	1.71	0	0	0	0	13.1	21.5	0	10.66
CS73	LFO	0	45.54	2.72	0	0	0	0	14.35	21.93	0	9.28
CS75	LFO	0	52.97	3.55	0	0	0	0	14.78	17.56	0	4.62
CS76	LFO	0	53.71	1.36	0	0	0	0	12.25	24.06	0	0.83
CS79	LFO	0	49.25	2.66	0	0	0	0	15.79	13.92	0	11.89
CS80	LFO	0	40.38	0.47	0	0	0	0	11.69	27.25	0	14.45

APPENDIX V - PETROGRAPHY OF SAMPLED ENA DYKES

Sample	Olivine	Plagioclase	Clinopyroxene	Pigeonite	Orthopyroxene	Texture	Grain size	Alteration	Notes
CS1	x	x	x	x		intergranular-subophitic	M-F	AA	abundant oxides, glomeroporphyritic cpx
CS2	x	x	x	x		intergranular-subophitic	M	SA	abundant oxides
CS3	x	x	x	x		subophitic, porphyritic	F	A	abundant oxides
CS4		x	x	x		intergranular-subophitic	F	A	
CS5	x	x	x	x		holocrystalline, ophitic	M-C	AA	
CS6	x	x	x	x		holocrystalline, ophitic	M-C	SA	fresh plagioclases
CS7	x	x	x	x		intergranular	M	T	
CS8	x	x	x	x		holocrystalline, ophitic	M-C	SA	biotite
CS9	x	x	x	x		interstitial	M	A	
CS10	x	x	x	x		intergranular	M	A	
CS11	x	x	x	x		intergranular-porphyritic	M	AA	
CS12	x	x	x	x		holocrystalline, equigranular	M-C	AA	
CS13	x	x	x	x		holocrystalline	M-C	SA	
CS14	x	x	x	x		intergranular-porphyritic	M-F	T	
CS15	x	x	x	x		interstitial	M	A	M in olivines
CS16	x	x	x	x		holocrystalline, equigranular	M-C	A	
CS17	x	x	x	x		holocrystalline, equigranular	M	SA	
CS18	x	x	x	x		holocrystalline, equigranular	M-F	A	
CS19	x	x	x	x		holocrystalline, ophitic	M-C	T	
CS20	x	x	x	x		interstitial	M	A	small olivines
CS21	x	x	x	x		holocrystalline, equigranular	M	SA	zoned plagioclases
CS22	x	x	x	x		holocrystalline, equigranular	M	T	
CS23	x	x	x	x		holocrystalline, equigranular	M-C	SA	zoned plagioclases, altered olivines
CS24	x	x	x	x		holocrystalline, equigranular	M	A	altered olivines
CS25	x	x	x	x		holocrystalline, equigranular	M-C	SA	
CS26	x	x	x	x		interstitial-porphyritic	M-C	SA	zoned plagioclases, M in olivines
CS27	x	x	x	x		holocrystalline, equigranular	M-C	SA	
CS28	x	x	x	x		porphyritic	C olivines	T	
CS29	x	x	x	x		interstitial	M-F	A	altered olivines
CS30	x	x	x	x		holocrystalline, equigranular	M-C	SA	
CS31	x	x	x	x		holocrystalline, equigranular	M	T	abundant oxides, fresh plagioclases
CS32	x	x	x	x		holocrystalline, equigranular	M-F	SA	
CS33	x	x	x	x		intergranular	F	SA	
CS35	x	x	x	x		holocrystalline, equigranular	M-C	AA	altered olivines
CS36	x	x	x	x		interstitial-porphyritic	M-F	A	
CS37	x	x	x	x		holocrystalline, ophitic	C	SA	
CS38	x	x	x	x		holocrystalline, ophitic	C	SA	zoned plagioclases

Sample	Olivine	Plagioclase	Clinopyroxene	Pigeonite	Orthopyroxene	Texture	Grain size	Alteration	Notes
CS39	x	x	x			holocrystalline, equigranular	M-C	A	altered olivines
CS41	x	x	x			intersertal-porphyritic	F	A	
CS42	x	x	x			holocrystalline, equigranular	M-C	U	
CS43	x	x	x			intersertal	M-F	AA	biotite, altered olivines
CS44	x	x	x	x		intergranular	F	AA	altered olivines
CS45	x	x	x			holocrystalline, ophitic	M	A	abundant oxides
CS46	x	x	x	x		intersertal	M-C	A	
CS47	x	x	x			holocrystalline, subophytic	C	U	
CS48	x	x	x		x	holocrystalline, subophytic	M-C	U	
CS49	x	x	x		x	holocrystalline, equigranular	C	U	MI in olivines, fresh plagioclases
CS50	x	x	x	x		holocrystalline, cumulitic	VC	AA	coarse oxides, graphic tetures
CS51	x	x	x			intergranular	M-F	A	small olivines
CS52	x	x	x			holocrystalline, ophitic	M-C	A	small, altered olivines
CS53	x	x	x			porphyritic	C plagioclases	A	biotite
CS54	x	x	x			intergranular	M-F	A	biotite
CS55	x	x	x			intergranular	M-C	U	sieve structures
CS56	x	x	x			intergranular-porphyritic	F	SA	
CS57	x	x	x			porphyritic	C olivines	U	MI in skeletal olivines
CS59	x	x	x			intersertal	M	U	MI in olivines
CS60	x	x	x			porphyritic	M olivines + cpx	U	
CS61	x	x	x			intergranular-porphyritic	M-C olivines + cpx	SA	
CS62	x	x	x			intergranular, subophitic	M	U	
CS63	x	x	x			intersertal	M	U	small cpx
CS64	x	x	x			intersertal-porphyritic	M-C	U	
CS66	x	x	x	x		holocrystalline	M	AA	
CS67	x	x	x	x		holocrystalline, equigranular	M-C	AA	
CS68	x	x	x			intergranular	M-C	A	
CS69	x	x	x	x		holocrystalline, equigranular	M-C	AA	
CS70	x	x	x			holocrystalline, equigranular	M-C	SA	
CS71	x	x	x			intergranular	M	A	
CS72	x	x	x			intersertal	M-C	A	
CS73	x	x	x			intersertal-porphyritic	M-F	SA	
CS75	x	x	x	x		intersertal	M	AA	
CS76	x	x	x			intersertal	M	AA	
CS77	x	x	x			intersertal-porphyritic, seriate	C olivines	A	MI in olivines
CS79	x	x	x			holocrystalline, equigranular	M	A	
CS80	x	x	x	x		intersertal	M-C	AA	altered olivines

APPENDIX VI - EMPA ANALYSES OF CONODONT SAMPLES

Sr content (ppm) measured by electronic microprobe (CAMECA SX50, IGG-CNR of Padova), run at 10 nA and 20 kv, for 10 conodonts. Conodont elements were included in epoxy and polished. Analyzed species, Sr content for each data point, minimum and maximum Sr content (ppm), number of data points, statistical mean and median (ppm) are here reported for each sample.

NR2	
<i>P. andrusovi, Mo. bidentata</i>	
Analysis	Sr ppm
NR2-r-r1_1	1531.50
NR2-r-r1_2	1602.54
NR2-r-r1_3	1885.84
NR2-r-r1_4	1816.49
NR2-r-r1_5	1923.04
NR2-r-r1_6	2208.03
NR2-r-r1_7	2812.68
NR2-r-r1_8	1353.91
NR2-r-r1_9	676.53
NR2-r-r1_10	1743.76
NR2-r-r1_11	2529.39
NR2-r-r1_12	3380.97
NR2-r-r1_13	1745.45
NR2-r-r1_14	1424.95
NR2-r-r1_15	1887.53
NR2-r-r2_1	1958.56
NR2-r-r2_2	2386.47
NR2-r-r2_3	2100.63
NR2-r-r2_4	1282.88
NR2-r-r2_5	2243.55
NR2-r-r2_6	1602.54
NR2-r-r2_7	2670.61
NR2-r-r2_8	2350.11
NR2-r-r2_9	2315.43
NR2-r-r2_10	2172.52
NR2-r-r2_11	2492.18
NR2-r-r2_12	1460.47
NR2-r-r2_13	1959.41
NR2-r-r2_14	1710.78
NR2-r-r2_15	2279.07
min	676.53
MAX	3380.97

# analyses	30
Mean	1983.59
Median	1940.80
St. Dev.	533.26

NR59	
<i>M. bernsteini, P. andrusovi</i>	
Analysis	Sr ppm
NR59-r-r1_1	1816.49
NR59-r-r1_2	1923.89
NR59-r-r1_3	2065.12
NR59-r-r1_4	2492.18
NR59-r-r1_5	748.41
NR59-r-r1_6	1390.27
NR59-r-r1_7	1994.08
NR59-r-r1_8	2280.76
NR59-r-r1_9	1319.24
NR59-r-r1_10	1780.97
NR59-r-r1_11	1139.96
NR59-r-r1_12	1460.47
NR59-r-r1_13	2314.59
NR59-r-r1_14	1887.53
NR59-r-r1_15	1424.95
NR59-r-r2_1	1282.03
NR59-r-r2_2	2527.70
NR59-r-r2_3	1495.98
NR59-r-r2_4	2314.59
NR59-r-r2_5	1495.98
NR59-r-r2_6	2315.43
NR59-r-r2_7	1709.09
NR59-r-r2_8	1424.95
NR59-r-r2_9	2279.07
NR59-r-r2_10	3453.70
min	748.41
MAX	3453.70

# analyses	25
Mean	1853.50
Median	1816.49
St. Dev.	572.20

KE3	
<i>FAD M. bernsteini</i>	
Analysis	Sr ppm
KE3-r-r1_1	1426.64
KE3-r-r1_2	2032.14
KE3-r-r1_3	2812.68
KE3-r-r1_4	1782.66
KE3-r-r1_5	2314.59
KE3-r-r1_6	1994.08
KE3-r-r1_7	391.54
KE3-r-r1_8	1495.98
KE3-r-r1_9	2136.15
KE3-r-r1_10	2669.77
KE3-r-r1_11	2812.68
KE3-r-r1_12	1567.86
KE3-r-r1_13	2243.55
KE3-r-r1_14	2137.00
KE3-r-r1_15	1603.38
KE3-r-r2_1	2314.59
KE3-r-r2_2	2669.77
KE3-r-r2_3	1531.50
KE3-r-r2_4	819.45
KE3-r-r2_5	1709.94
KE3-r-r2_6	2740.80
KE3-r-r2_7	1497.67
KE3-r-r2_8	3065.54
KE3-r-r2_9	2957.29
KE3-r-r2_10	2602.96
KE3-r-r2_11	784.78
KE3-r-r2_12	2350.11
KE3-r-r2_13	2528.54
KE3-r-r2_14	2742.49
KE3-r-r2_15	2599.58
KE3-1	1816.49
KE3-2	2600.42
KE3-3	1709.09
KE3-4	2705.29
KE3-5	2350.11
KE3-6	2670.61
KE3-7	2314.59
KE3-8	1139.96
KE3-9	3665.96
KE3-10	2564.06
KE3-11	2208.03
KE3-12	2103.17
KE3-13	2138.69
min	391.54
MAX	3665.96

# analyses	43
Mean	2147.03
Median	2243.55
St. Dev.	661.93

J18c*M. posthernsteini, M. koessenensis*

Analysis	Sr ppm
J18c-r-r1_1	1319.24
J18c-r-r1_2	1605.07
J18c-r-r1_3	1818.18
J18c-r-r1_4	1355.60
J18c-r-r1_5	1140.80
J18c-r-r1_6	1033.40
J18c-r-r1_7	1673.57
J18c-r-r1_8	1780.97
J18c-r-r1_9	2243.55
J18c-r-r1_10	1460.47
J18c-r-r1_11	1353.91
J18c-r-r1_12	1140.80
J18c-r-r1_13	1638.05
J18c-r-r1_14	1318.39
J18c-r-r1_15	1246.51
J18c-r-r2_1	1246.51
J18c-r-r2_2	1531.50
J18c-r-r2_3	1211.84
J18c-r-r2_4	2137.84
J18c-r-r2_5	2171.67
J18c-r-r2_6	2243.55
J18c-r-r2_7	605.50
J18c-r-r2_8	1424.95
J18c-r-r2_9	1961.10
J18c-r-r2_10	749.26
J18c-r-r2_11	2708.67
J18c-r-r2_12	2246.09
J18c-r-r2_13	1105.29
J18c-r-r2_14	1568.71
J18c-r-r2_15	1710.78
min	605.50
MAX	2708.67

# analyses	30
Mean	1558.39
Median	1495.98
St. Dev.	480.80

PG38*FAD Misikella ultima*

Analysis	Sr ppm
PG38-r-r1_1	1140.80
PG38-r-r1_2	2174.21
PG38-r-r1_3	3140.80
PG38-r-r1_4	2209.73
PG38-r-r1_5	2281.61
PG38-r-r1_6	1034.25
PG38-r-r1_7	1602.54
PG38-r-r1_8	1460.47
PG38-r-r1_9	1390.27
PG38-r-r1_10	1104.44
PG38-r-r1_11	2100.63
PG38-r-r1_12	3062.16
PG38-r-r1_13	2315.43
PG38-r-r1_14	1602.54
PG38-r-r1_15	819.45
PG38-r-r2_1	2208.03
PG38-r-r2_2	1317.55
PG38-r-r2_3	2350.11
PG38-r-r2_4	1496.83
PG38-r-r2_5	2740.80
PG38-r-r2_6	2599.58
PG38-r-r2_7	1602.54
PG38-r-r3_1	2032.14
PG38-r-r3_2	1995.77
PG38-r-r3_3	1142.49
PG38-r-r3_4	2141.23
PG38-r-r3_5	2497.25
PG38-r-r3_6	2494.71
PG38-r-r3_7	1818.18
PG38-r-r3_8	677.38
PG38-r-r3_9	1924.74
PG38-r-r3_10	1212.68
PG38-r-r4_1	3206.77
PG38-r-r4_2	2100.63
PG38-r-r4_3	1852.01
PG38-r-r4_4	1780.97
PG38-r-r4_5	2705.29
PG38-r-r4_6	2848.20
PG38-r-r4_7	1567.86
PG38-r-r4_8	2955.60
PG38-r-r4_9	1567.02
PG38-r-r4_10	2601.27
min	677.38
MAX	3206.77

# analyses	42
Mean	1973.26
Median	2013.95
St. Dev.	653.65

PG41*Misikella ultima*

Analysis	Sr ppm
PG41-r-r1_1	2954.76
PG41-r-r1_2	1389.43
PG41-r-r1_3	2243.55
PG41-r-r1_4	4163.21
PG41-r-r1_5	2990.27
PG41-r-r1_6	1747.15
PG41-r-r1_7	2317.12
PG41-r-r1_8	1319.24
PG41-r-r1_9	2461.73
PG41-r-r1_10	1853.70
PG41-r-r1_11	3067.23
PG41-r-r1_12	1784.36
PG41-r-r1_13	1712.47
PG41-r-r1_14	3206.77
PG41-r-r1_15	1819.87
PG41-r-r1_16	3171.25
PG41-r-r1_17	3096.83
PG41-r-r1_18	3985.62
PG41-r-r1_19	1033.40
PG41-r-r1_20	1674.42
PG41-r-r2_1	2352.64
PG41-r-r2_2	2103.17
PG41-r-r2_3	1532.35
PG41-r-r2_4	1674.42
PG41-r-r2_5	1389.43
PG41-r-r2_6	605.50
PG41-r-r2_7	1604.23
PG41-r-r2_8	1104.44
PG41-r-r2_9	1674.42
PG41-r-r2_10	1923.04
PG41-r-r2_11	2100.63
PG41-r-r2_12	3452.01
PG41-r-r2_13	1425.79
PG41-r-r2_14	2067.65
PG41-r-r2_15	2854.97
PG41-r-r2_16	3281.18
PG41-r-r2_17	3672.73
PG41-r-r2_18	7974.63
PG41-r-r2_19	5524.74
PG41-r-r2_20	2069.34
min	605.50
MAX	7974.63

# analyses	40
Mean	2459.49
Median	2084.99
St. Dev.	1333.32

PG46		PR3		PR2		PR1	
<i>Misikella ultima</i>		<i>M. ultima, M. kovacsi</i>		<i>M. ultima, M. kovacsi</i>		<i>M. ultima, M. kovacsi</i>	
Analysis	Sr ppm	Analysis	Sr ppm	Analysis	Sr ppm	Analysis	Sr ppm
PG46-1	1976.32	PR3-1	1829.18	PR2-1	2067.65	PR1-1	1429.18
PG46-2	1901.90	PR3-2	1326.00	PR2-2	2990.27	PR1-2	1391.97
PG46-3	2299.37	PR3-3	2759.41	PR2-3	2565.75	PR1-3	2567.44
PG46-4	1293.02	PR3-4	1899.37	PR2-4	2171.67	PR1-4	1675.26
PG46-5	2979.28	PR3-r-r1_1	1863.00	PR2-5	2669.77	PR1-5	890.49
PG46-6	2727.27	PR3-r-r1_2	1076.53	min	2067.65	PR1-6	641.86
PG46-7	1867.23	PR3-r-r1_3	646.09	MAX	2990.27	PR1-7	1533.19
PG46-8	1758.99	PR3-r-r1_4	1149.26			PR1-8	2314.59
PG46-9	2047.36	PR3-r-r1_5	1471.46	# analyses	5	PR1-9	1318.39
PG46-10	2368.71	PR3-r-r1_6	1184.78	Mean	2493.02	PR1-10	1176.32
PG46-11	1330.23	PR3-r-r1_7	2153.07	Median	2565.75	PR1-11	1531.50
PG46-12	2047.36	PR3-r-r1_8	1041.01	St. Dev.	376.83	PR1-12	1282.88
PG46-13	1831.71	PR3-r-r1_9	1939.11			PR1-13	2351.80
PG46-14	1545.03	PR3-r-r1_10	1973.78			min	641.86
PG46-15	2729.81	PR3-r-r1_11	1578.01			MAX	2567.44
PG46-16	2047.36	PR3-r-r1_12	1757.29				
PG46-17	934.46	PR3-r-r1_13	2652.85			# analyse	13
PG46-18	1615.22	PR3-r-r1_14	2115.86			Mean	1546.53
PG46-19	2370.40	PR3-r-r1_15	2904.02			Median	1429.18
PG46-20	2082.88	PR3-5	1220.30			St. Dev.	565.88
PG46-21	2011.84	PR3-6	2044.82				
min	934.46	PR3-r-r2_1	1256.66				
MAX	2979.28	PR3-r-r2_2	2585.20				
		PR3-r-r2_3	2690.91				
# analyses	21	PR3-r-r2_4	1901.90				
Mean	1988.85	PR3-r-r2_5	1436.79				
Median	2011.84	PR3-r-r2_6	1149.26				
St. Dev.	497.37	PR3-r-r2_7	682.45				
		PR3-r-r2_8	2476.11				
		PR3-r-r2_9	1542.49				
		PR3-r-r2_10	2404.23				
		PR3-r-r2_11	2189.43				
		PR3-r-r2_12	1938.27				
		PR3-r-r2_13	1005.50				
		PR3-r-r2_14	1472.30				
		PR3-r-r2_15	431.29				
		PR3-7	789.85				
		PR3-R-R3_1	1636.36				
		PR3-R-R3_2	3132.35				
		PR3-R-R3_3	996.19				
		PR3-R-R3_4	2063.42				
		PR3-R-R3_5	1210.15				
		PR3-R-R3_6	2385.62				
		PR3-R-R3_7	2563.21				
		PR3-R-R3_8	2065.12				
		PR3-R-R3_9	2208.03				
		PR3-R-R3_10	1958.56				
		PR3-R-R3_11	2385.62				
		PR3-R-R3_12	926.85				
		PR3-R-R3_13	2136.15				
		PR3-R-R3_14	1282.88				
		PR3-R-R3_15	1674.42				
		min	431.29				
		MAX	3132.35				
		# analyses	52				
		Mean	1753.13				
		Median	1846.09				
		St. Dev.	638.93				